



University
of Glasgow

<https://theses.gla.ac.uk/>

Theses Digitisation:

<https://www.gla.ac.uk/myglasgow/research/enlighten/theses/digitisation/>

This is a digitised version of the original print thesis.

Copyright and moral rights for this work are retained by the author

A copy can be downloaded for personal non-commercial research or study,
without prior permission or charge

This work cannot be reproduced or quoted extensively from without first
obtaining permission in writing from the author

The content must not be changed in any way or sold commercially in any
format or medium without the formal permission of the author

When referring to this work, full bibliographic details including the author,
title, awarding institution and date of the thesis must be given

Enlighten: Theses

<https://theses.gla.ac.uk/>
research-enlighten@glasgow.ac.uk

**A STUDY OF IMAGING MODES IN THE SCANNING
TRANSMISSION ELECTRON MICROSCOPE**

BY YONGJIE SU

**submitted for the degree of M.Sc at the faculty
of science of the University of Glasgow**

April 1989

© 1989 YONGJIE SU

ProQuest Number: 10999254

All rights reserved

INFORMATION TO ALL USERS

The quality of this reproduction is dependent upon the quality of the copy submitted.

In the unlikely event that the author did not send a complete manuscript and there are missing pages, these will be noted. Also, if material had to be removed, a note will indicate the deletion.



ProQuest 10999254

Published by ProQuest LLC (2018). Copyright of the Dissertation is held by the Author.

All rights reserved.

This work is protected against unauthorized copying under Title 17, United States Code
Microform Edition © ProQuest LLC.

ProQuest LLC.
789 East Eisenhower Parkway
P.O. Box 1346
Ann Arbor, MI 48106 – 1346

DECLARATION

I hereby certify that I am the author of this thesis, that I have consulted all the cited references and done the work in this thesis, and that the work has not been previously presented for any higher degree.

Yongjie Su

April, 1989

ACKNOWLEDGEMENTS

This thesis would not have been possible without the help of many others who have contributed to this work. Foremost I would like to thank my supervisor, Professor J.N. Chapman, for his constant encouragement and all the fruitful advice throughout the project. I would like to thank Professor R.P. Ferrier for his encouragement and providing facilities within the Solid State Group in the Department of Physics and Astronomy at the University of Glasgow.

I would also like to thank Mr.P. McColgan for his helpful discussion for this work, and Dr.S. McVitie and Mr.G.J. Sinclair for their practical help in using computers.I must thank Mr.H. Gong for his remote help on the computer image simulation aspect. Thanks are also extended to Mr.W. Chen, Mr.Y.C. Ge, Mr. Y.S. Guo, and Mr. F.J. Martin for their useful discussions on particular topics.

In addition, I would like to thank Mr. J. Simms and Miss. M. Low and the departmental IBM computer group for their kindly given me help in many ways.

I wish to express my thanks to Professor Henry. H.Y.Wong , Dr. K.C. Li, the University of Shantou, and the Higher Education Bureau of Guangdong Province for provided opportunity to study at Glasgow University.

Finally, I wish to express my thanks to my parents for their unflinching support and encouragement to seek a higher education.

This thesis is dedicated to my wife.

ABSTRACT

The efficiency of transmitted electron utilization is low in the standard phase contrast imaging mode in the scanning transmission electron microscope (STEM). This leads to serious difficulties when, for example, radiation sensitive material is under investigation. A significant improvement is achieved by using the differential phase contrast (DPC) imaging mode in STEM where a non-rotationally symmetric detector system is employed. To systematically investigate image formation in the DPC mode, a two-dimensional calculation of the DPC transfer function for an aberrated STEM imaging system is undertaken. The results show that the effect of spherical aberration increases markedly with the semiangle of the objective aperture, and a properly chosen defocus is necessary to balance the effect. From the calculations the optimum instrumental parameters pertaining to the VG-HB 5 STEM at Glasgow University are provided. Further improvement in efficiency is achieved by the use of a segmented annular detector leading to a modified DPC imaging mode. Variation of the annular detector geometry can lead to either a high signal-to-noise ratio or a flat DPC transfer function and signal-to-noise ratio band. In addition, computer image simulation techniques provide a flexible way to select conditions for imaging radiation sensitive material. Both the DPC and modified DPC modes are used in a set of simulations applicable to small pigmentary particles. Of particular interest are the topography and internal structure of the particles. The results substantiate the transfer function calculations.

NOMENCLATURE

- C_s ----- spherical aberration coefficient
- C_t ----- $C_t = I_m/I_p$
- C_r ----- $C_r = (S/N)_m$
- D_a ----- area of beams overlap on the detector in DPC mode
- $D(\mathbf{r}_d)$ ----- detector response function
- d_z ----- defocus
- E_0 ----- accelerating voltage
- $E(\mathbf{r}), E(\mathbf{r}_0)$ ----- quadratic factors
- e ----- absolute value of charge on the electron
- f ----- focal length
- $h(\mathbf{r})$ ----- specimen transmittance
- I_d ----- total signal current on annular detector
- I_m ----- maximum differential signal current on detector
- I_p ----- total current in the electron probe
- j ----- electron current density
- k ----- spatial frequency
- k_{xr}, k_{yr} ----- normalized spatial frequencies
- M ----- magnification
- n_0 ----- number of detected electrons
- $P(\mathbf{k})$ ----- Fourier transform of the objective aperture function
- R ----- distance from specimen to detector plane
- R_d ----- $R_d = \alpha_H/\alpha_s$
- \mathbf{r} ----- coordinates in the relevant planes

$S(\mathbf{r})$ ----- image signal

S/N ----- signal-to-noise

$T(\mathbf{k})$ ----- transfer function

$t(x)$ ----- thickness of the specimen

∇t ----- thickness gradient of the specimen

$t(\mathbf{r})$ ----- point-spread function

$V(x)$ ----- inner potential function

$w(\mathbf{k})$ ----- phase shift caused by C_s and d_z

z ----- coordinate along the optic axis

α_s ----- semi-angle subtended by objective aperture

α_H ----- semi-angle subtended by the circular hollow zone in the
detector centre

$\Phi(\mathbf{r}), \phi(\mathbf{r})$ ----- phase excursion

ε ----- specimen orientation with respect to detector

$\Psi(\mathbf{r}), \psi(\mathbf{r})$ ----- wave function

Λ ----- specimen periodicity

λ ----- electron wavelength

θ ----- scattering angle

θ_B ----- Bragg angle

γ, γ' ----- geometrical factors

τ ----- dwell time

δ ----- linear dimension

η ----- brightness of the source

CONTENTS

DECLARATION

ACKNOWLEDGEMENTS

ABSTRACT

NOMENCLATURE

	PAGE
INTRODUCTION	1
CHAPTER 1 IMAGING IN THE TRANSMISSION ELECTRON MICROSCOPE	3
1.1 Introduction to electron microscopy	
1.2 Image formation in the conventional transmission electron microscope (CTEM)	
1.2.1 Basic image formation	
1.2.2 Phase problem and weak phase/amplitude approximation	
1.2.3 The phase contrast image	
1.2.4 Phase contrast transfer function	
1.3 Image formation in the scanning transmission electron microscope (STEM)	
1.3.1 STEM	
1.3.2 Image formation in STEM and the reciprocity principle	
1.4 Assessment of efficiency of electron utilization	

CHAPTER 2 IMAGING OF BEAM SENSITIVE
MATERIALS IN THE TRANSMISSION
ELECTRON MICROSCOPE 25

- 2.1 Introduction
- 2.2 Beam sensitive materials and radiation damage
- 2.3 Methods for reducing radiation damage
- 2.4 Phthalocyanine pigments

CHAPTER 3 DIFFERENTIAL PHASE CONTRAST 31
IMAGING IN STEM

- 3.1 Introduction
- 3.2 Principles of DPC image formation
- 3.3 The efficiency of DPC detection
- 3.4 The DPC transfer function
 - 3.4.1 The effects of defocus
 - 3.4.2 The effects of the objective aperture size
- 3.5 Calculation of two-dimensional DPC transfer
 - 3.5.1 Computer programme description
 - 3.5.2 Results and conclusion

CHAPTER 4 OPTIMIZATION OF DETECTOR CONFIGURATION 46

- 4.1 Introduction
- 4.2 Modified DPC transfer function and signal-to-noise ratio
- 4.3 Computed results and discussion

4.4 Summary and conclusion

CHAPTER 5	SIMULATION OF DPC AND MODIFIED DPC IMAGE	53
5.1	Introduction	
5.2	Mathematical treatment	
5.3	Computer image simulation	
5.4	Background information on Cl-Cu PC particles	
5.5	Image simulation of "model" Cl-Cu PC particles	
5.5.1	Edge images of the particle	
5.5.2	Lattice fringe images of the particle	
5.6	Simulated images using annular detectors	
5.7	Summary and conclusion	
CHAPTER 6	CONCLUSIONS AND SUGGESTIONS FOR FURTHER WORK	65
6.1	Conclusions	
6.2	Suggests for further work	
REFERENCES		69
APPENDIX 1	FIGURES 1	
APPENDIX 2	FIGURES 2	
APPENDIX 3	COMPUTER PROGRAMME	

INTRODUCTION

This thesis is concerned with imaging in the scanning transmission electron microscope (STEM). In particular the differential phase contrast (DPC) mode is of interest and attention is focused on the phase contrast transfer function and the efficiency of electron utilisation. The latter is of the greatest importance when radiation sensitive specimens are to be investigated. In addition to the standard DPC imaging mode, which involves the use of a split or quadrant detector, the effect of modifying the detector geometry by the introduction of a circular hole is considered. A number of advantages are found to accrue through the use of the resulting annular quadrant detector. Further details of the thesis content, on a chapter by chapter basis, are given below.

In Chapter 1, the basic theory of phase contrast for weak phase objects in the conventional transmission electron microscope (CTEM) and the STEM is described. In both instances, expressions are derived relating to the efficiency of electron utilization.

Interest has centred on the efficiency of electron utilisation as one important application of electron imaging is to study the topography and internal structure of pigmentary particles, many of which are radiation sensitive.

Radiation damage is a major problem when trying to obtain high resolution information from such specimens. The particles of interest here are phthalocyanine pigments and studies of them using standard CTEM and STEM imaging modes are reviewed in Chapter 2. Several methods to reduce the radiation damage, which

are based either on improving the operational conditions or minimizing the beam sensitivity of the sample itself chemically or physically, are described. It is realized that a possible way to minimize the required radiation dose is to seek alternative imaging modes with a more efficient utilisation of electrons.

In Chapter 3, the DPC imaging mode in the STEM is introduced and the principles of DPC image formation for weak phase objects are given. Thereafter the high efficiency of DPC imaging is proved in section 3.3. To study DPC imaging in greater detail, expressions for the phase contrast are derived and calculations performed pertaining to an aberrated objective lens with parameters applicable to the VG-HB5 STEM at Glasgow University. As the imaging characteristics show an orientational dependence, full two-dimensional computations were undertaken and extensive results are presented and discussed in section 3.5.

Further study, concerned with the optimisation of the detector configuration, is described in Chapter 4. The idea of using an annular split detector and annular quadrant detector is introduced and the imaging characteristics are shown to be attractive. In particular, when the geometry is carefully chosen a high signal-to-noise ratio with an acceptable contrast transfer can be obtained over a wide spatial frequency range.

In Chapter 5 image simulations of small particles are undertaken. In section 5.3 both edge and lattice fringe DPC images of the particles are examined under practical operational conditions. The simulation programme is then extended to encompass the modified DPC imaging mode where annular detectors are employed, and some significant results are presented in section 5.4.

Chapter 1

Imaging in the Transmission Electron Microscope

1.1. Introduction to Electron Microscopy

It is commonly said that the microscope has a limit of resolution of approximately $c\lambda/F$. This was first explained by Ernst Abbe who was engaged in the design of light microscopes. Here c is a constant lying between 0.6 and 0.8, and F is the numerical aperture* of the objective lens. Obviously the resolution can be improved either by decreasing the wavelength λ or by increasing the numerical aperture, F . With a light microscope, we are limited to a resolution of the order of 300 nm, since the shortest visible wavelength is about 400 nm and the highest numerical aperture is about 1.4.

In order to find suitable radiation of shorter wavelength charged particles, and in particular electrons, were considered, as it had been suggested by Louis de Broglie in the 1920's that a wavelength should be associated with material particles. When electrons are accelerated to a high speed by allowing them to pass through a potential difference, E_0 , λ can be expressed as (Born and Wolf, 1959)

$$\lambda = 1.2 / E_0^{1/2} \quad (1.1)$$

*The numerical aperture is defined by $F=n_0\sin\theta_0$, where n_0 is the refractive index of the medium between the specimen and the objective lens and θ_0 is the semi-angle subtended at the specimen by the objective lens.

Here λ is in nm and E_0 in volts. In addition, electrons offer advantages over x - rays because, whilst the x-rays do have wavelengths of the order of angstroms, they are not able to be focused. It was first realized by Busch in 1926 that axially symmetric electrostatic and magnetic fields act as lenses for charged particles. In principle one can use either electrostatic or magnetic lenses to focus a beam of electrons. Practical instruments, however, exclusively employ magnetic lenses as they can be made with smaller defects, (for instance, spherical and chromatic aberration, as well as astigmatism), than electrostatic lenses (Hawkes, 1972).

A schematic showing the magnetic lenses and other components in a typical conventional transmission electron microscope (CTEM) is given in Fig.(1.1). The source of electrons is traditionally a hairpin filament or a pointed thermionic cathode enclosed within a cylindrical shield carrying a negative potential (range of 50 ~ 200 kV), through which the electrons are accelerated. They are emitted at an extremely high speed from the electron gun. A good electron gun should have high brightness (probe current density per unit solid angle) and a small virtual source diameter. Two new source guns, one using a LaB_6 cathode and the other being a field emission electron gun (FEG), have hence been developed. A FEG requires no heating and has a very high brightness of the order of $10^9 \text{ A}\cdot\text{cm}^{-2}\cdot\text{s}\cdot\text{r}^{-1}$ and a small virtual source diameter ($< 0.01\mu\text{m}$). Thus it is very suitable for use in the scanning transmission electron microscopes (see. section 1.3).

The electrons leave the gun as a fine diverging beam and then are concentrated into a very small beam by a pair of

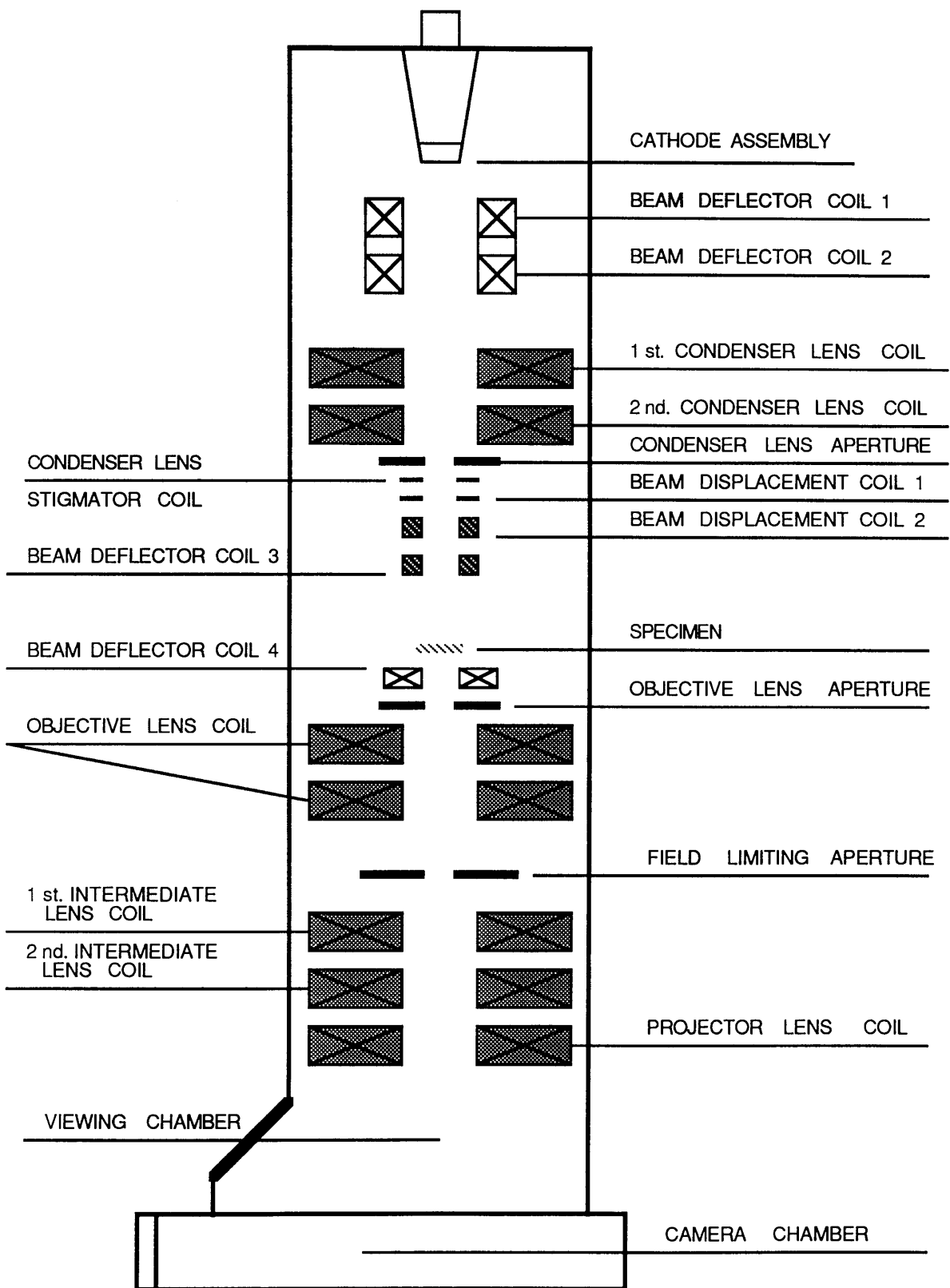


Fig. 1.1. Schematic of the column cross section of the JEM-100C CTEM

magnetic condenser lenses. The first lens is a strong one and is used to form a beam of diameter $\leq 1 \mu\text{m}$ close to its back focal plane; the second lens with 1 ~ 2 times magnification controls the area of the specimen illuminated. Such a double condenser lens system allows flexibility in the area of specimen illuminated and the angle subtended by the source. This is particularly important when dealing with radiation sensitive specimens where damage is a serious problem.

The details of electrons interacting with a specimen are complicated. When a very thin specimen ($\sim 10 \text{ nm}$) is introduced, normally no, or only one, scattering event occurs as an incident electron passes through the specimen as the mean free path of an electron with 100 keV energy is usually greater than 10 nm. Multiple scattering, however, may happen within a thicker specimen. The required structural information is carried by the electrons leaving the specimen after interacting with it. These can include forward-scattered and backscattered electrons.

In the transmission electron microscope (TEM) the transmitted electron beam after the specimen can be considered as comprising three components. These are:

- 1) Elastically scattered electrons

Broadly speaking, elastic scattering deals with the incident electrons colliding directly with the atomic nucleus, and corresponds to large-angle scattering. The energy transfer for the electrons scattering is negligible.

- 2) Inelastically scattered electrons

Inelastic electron scattering events occur when the incident electrons interact with orbital electrons in the atom. It corresponds to small-angle scattering, involving a loss of energy as the electrons are

transmitted through the specimen.

3) Unscattered electrons

These are undeviated in transmission through the specimen. The unscattered component may interfere with the elastic component, for instance, in phase contrast electron microscopy. This is discussed later in section 1.2.3.

The objective lens is the only lens which contributes significantly to the spherical aberration of the optical system and in which the electrons are reasonably steeply inclined to the optic axis. This makes the objective lens the most critical component in the microscope. The intermediate and projector lenses magnify the intermediate image that the objective lens produces and, by varying their strengths simultaneously, a wide range of magnifications can be obtained. The other purpose of these lenses is to alter the mode of operation of the microscope. For example, in the image-forming mode the final image plane can be arranged to be conjugate to a plane near the lower surface of the specimen, (Fig.1.2). On the other hand, by adjusting the lens currents it may be made conjugate to the image-side focal plane of the objective. This is important as the diffraction pattern is formed at, or in the vicinity of, this focal plane and its visualisation is essential in the examination of crystalline materials.

The final image is examined on a fluorescent screen through a lead-glass window. The specimen is usually scrutinized at low magnification, with any interesting features being brought to the centre of the screen. The magnification is then increased until the image showing the required detail is obtained.

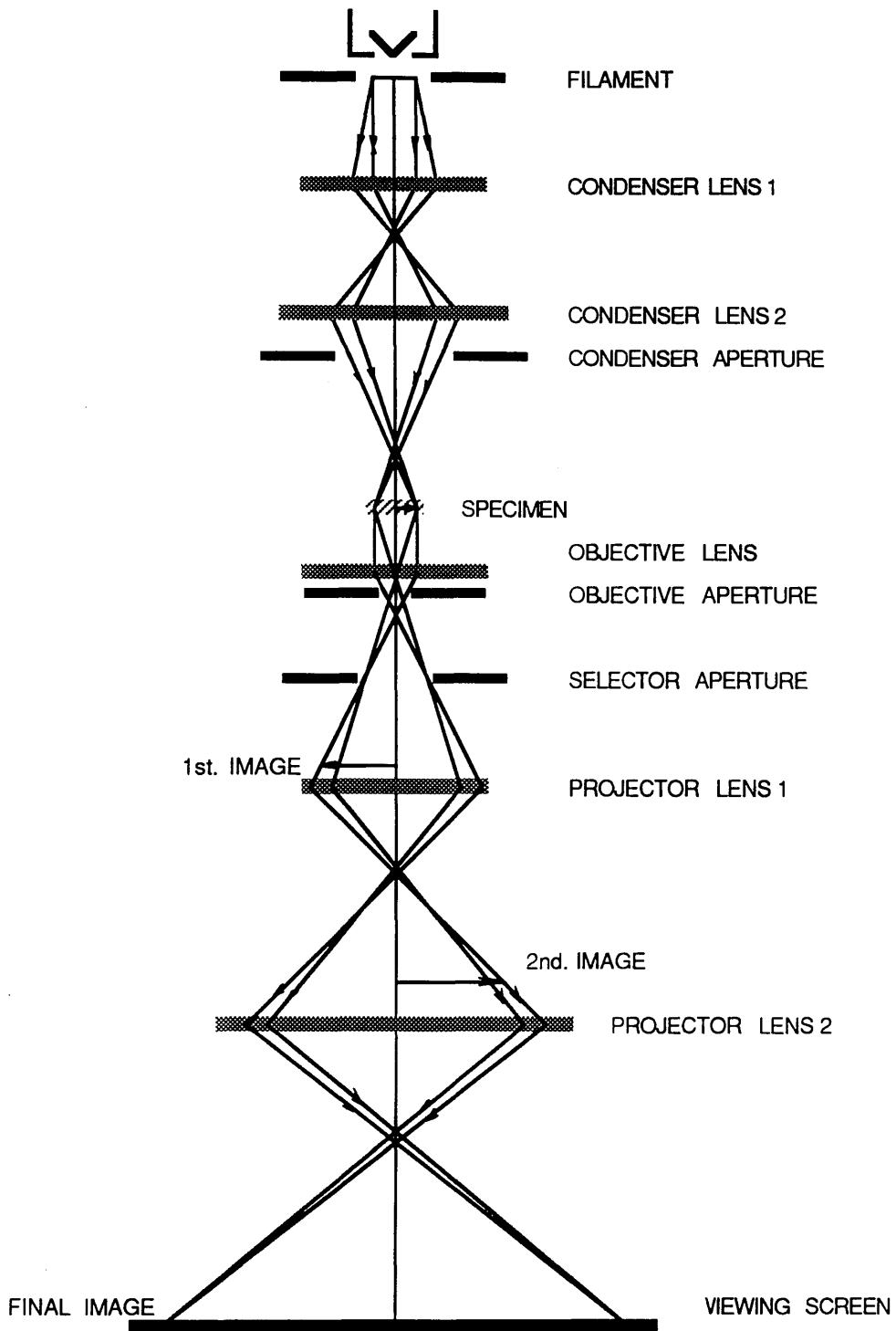


Fig.1.2. Ray diagram for a complete CTEM

1.2. Image formation in the Conventional Transmission Electron Microscope

1.2.1. Basic image formation

Consider a composite system consisting of a coherent illuminating system, a specimen and an image-formation system. Before deriving the relation between the electron wave functions in conjugate planes, it is convenient to denote the position coordinates in the object plane by $\mathbf{r}_0 = (x_0, y_0)$ and \mathbf{r}'_0 , and those in the image plane by \mathbf{r}_i and \mathbf{r}'_i . The wave function $\psi(\mathbf{r})$, which describes the electron wave in a plane downstream from the object plane can be related to that at the object plane, ψ_0 , by the following formula

$$\psi(\mathbf{r}) = \int t(\mathbf{r}, \mathbf{r}_0) \psi_0(\mathbf{r}_0) d\mathbf{r}_0 \quad (1.1)$$

The function $t(\mathbf{r}, \mathbf{r}_0)$ is the point-spread or impulse-response function relating the wave function $\psi(\mathbf{r})$ to $\psi_0(\mathbf{r}_0)$. If the imaging conditions are isoplanatic, which is generally true for small objects close to optic axis, $t(\mathbf{r}, \mathbf{r}_0) = t(\mathbf{r} - \mathbf{r}_0)$, and we obtain (Hawkes, 1978)

$$t(\mathbf{r}, \mathbf{r}_0) = \{E(\mathbf{r}_0) / ME(\mathbf{r})\} t(\mathbf{r} / M - \mathbf{r}_0) \quad (1.2)$$

where M denotes the magnification, and $E(\mathbf{r})$, $E(\mathbf{r}_0)$ are quadratic factors,

$$E(\mathbf{r}) = \exp\{(i\pi\gamma / \lambda M) \mathbf{r} \cdot \mathbf{r}\}$$

$$E(\mathbf{r}_0) = \exp\{(i\pi\gamma' / \lambda) \mathbf{r}_0 \cdot \mathbf{r}_0\}$$

Here γ, γ' are geometrical factors; in practice $E(\mathbf{r}_0)$ can often be replaced by unity ($\gamma' \approx 0$).

In order to incorporate the effects due to the aperture function, the wave function in the image plane is conveniently obtained in two stages by inserting the expression giving the wave function $\psi_a(\mathbf{r}_a)$ in the aperture plane in terms of $\psi_0(\mathbf{r}_0)$ into Eqn.(1.1). Then the wave function at the image plane is related to that in the intermediate plane by

$$\psi_i(\mathbf{r}_i) = \int t(\mathbf{r}_i, \mathbf{r}_a) \psi_a(\mathbf{r}_a) d\mathbf{r}_a \quad (1.3)$$

The function $t(\mathbf{r}_i, \mathbf{r}_a)$ is of the form

$$t(\mathbf{r}_i, \mathbf{r}_a) = \exp\{i\pi [\gamma \mathbf{r}_i \mathbf{r}_i / M - \gamma' \mathbf{r}_a \mathbf{r}_a] / \lambda\} t(\mathbf{r}_i / M - \mathbf{r}_a) \quad (1.4)$$

Substituting for $\psi_a(\mathbf{r}_a)$ in Eqn.(1.3) with the aid of Eqn.(1.1), we find

$$\psi_i(\mathbf{r}_i) = [1 / ME(\mathbf{r}_i)] \int t(\mathbf{r}_i / M - \mathbf{r}_0) \psi_0(\mathbf{r}_0) E(\mathbf{r}_0) d\mathbf{r}_0 \quad (1.5)$$

The function, t , is the Fourier transform of the objective aperture function, $T'(\mathbf{r}_a)$, as

$$t(\mathbf{r}_i / M - \mathbf{r}_0) = [1 / \lambda^2 f^2] \int T'(\mathbf{r}_a) \exp\{2\pi i(\mathbf{r}_i / M - \mathbf{r}_0) \mathbf{r}_a / \lambda f\} d\mathbf{r}_a \quad (1.6)$$

in which f is the objective focal length. The function $T'(\mathbf{r}_a)$ is equal to zero outside the objective aperture and is given by the

phase shift within the aperture. This phase shift is dominated by two main factors, the third order spherical aberration, C_s , and the defocus, d_z , which is defined as a distance from the real specimen plane to the plane conjugate to the final image if the specimen plane is not quite conjugate to the final image plane. We have

$$T(\mathbf{r}_a) = p'(\mathbf{r}_a) \exp[-i w'(\mathbf{r}_a)] \quad (1.7)$$

in which

$$\begin{aligned} p'(\mathbf{r}_a) &= 0 && \text{outside the aperture} \\ &1 && \text{inside the aperture} \end{aligned} \quad (1.8)$$

The phase shift, w , is given by

$$w'(\mathbf{r}_a) = (2\pi / \lambda) \{ C_s (\mathbf{r}_a \cdot \mathbf{r}_a)^2 / 4f^4 - d_z \mathbf{r}_a \cdot \mathbf{r}_a / 2f^2 \} \quad (1.9)$$

The expressions may become simpler if we introduce the spatial frequency coordinate

$$\mathbf{k} = \mathbf{r}_a / \lambda f \quad (1.10)$$

with $w(\mathbf{k}) = w'(\lambda f \mathbf{k})$ and $p(\mathbf{k}) = p'(\lambda f \mathbf{k})$ as usual, we find Eqn.(1.6) becomes

$$t(\mathbf{r}_i / M - \mathbf{r}_0) = \int T(\mathbf{k}) \exp\{2\pi i (\mathbf{r}_i / M - \mathbf{r}_0) \cdot \mathbf{k}\} d\mathbf{k} \quad (1.11)$$

whilst Eqn.(1.9) becomes (Hawkes,1978)

$$w(\mathbf{k}) = (2\pi / \lambda) \{ C_s(\mathbf{k}\mathbf{k})^2 \lambda^4 / 4 - dz \lambda^2 \mathbf{k}\mathbf{k} / 2 \} \quad (1.12)$$

We note that if we write

$$\Psi_0(\mathbf{k}) = \int \psi_0(\mathbf{r}_0) \exp(-2\pi i \mathbf{k} \mathbf{r}_0) d\mathbf{r}_0 \quad (1.13)$$

$$T(\mathbf{k}) = \int t(\mathbf{r}) \exp(-2\pi i \mathbf{k} \mathbf{r}) d\mathbf{r} \quad (1.14)$$

$$\Psi_i(\mathbf{k}) = (1/M^2) \int \psi_i(\mathbf{r}_i) \exp(-2\pi i \mathbf{k} \mathbf{r}_i / M) d\mathbf{r}_i \quad (1.15)$$

then Eqn.(1.5) becomes (neglecting quadratic terms)

$$\Psi_i(\mathbf{k}) = (1/M) T(\mathbf{k}) \Psi_0(\mathbf{k}) \quad (1.16)$$

This equation tells us that the coherent wave is transferred linearly between the object and final image plane in CTEM. The function, $T(\mathbf{k})$, describes the spatial frequency response of the imaging system, and by which the specimen, represented by the spatial frequency spectrum of the wave leaving the object, Ψ_0 , is thus filtered.

1.2.2. Phase problem and weak phase/amplitude approximation

We find Eqn.(1.16) relates the wave function in the image plane to that in the object plane by a linear modulation function, but the equation is not directly useful for the task of extracting information from the final image quantitatively.

In an attempt to quantitatively examine the information from electron images the phase problem must be considered. Firstly it is

only the electron current density, proportional to the square modulus of the electron wave function, which can be detected and measured in either a diffraction or image plane. Secondly both amplitude and phase contrast will in general be present in the same image and it is frequently difficult to separate their contributions.

A direct attempt to solve the phase problem is discussed by Misell (1978), which is applicable to thin specimens. Central to it is the approximation $|\psi_s(\mathbf{r})| \ll 1$, where $\psi_s(\mathbf{r})$ describes the effect of the specimen on the incident electron beam and represents the projection of the specimen structure onto a plane $\mathbf{r} = (x, y)$.

The amplitude and phase of the wave that emerges from the specimen will be different from those of the incident wave, since it has been modulated on passing through the specimen. The parallel incident beam corresponds to a disturbance

$$\psi(\mathbf{r}) = A(\mathbf{r}) \exp(2\pi i z / \lambda) \quad (1.17)$$

Here z denotes the direction in which the wave is travelling. $A(\mathbf{r})$ denotes the constant amplitude, and there is no loss of generality in normalizing this to unity, i.e. $A(\mathbf{r}) = 1$. The specimen may be characterized by its transmittance, $h(\mathbf{r})$, which measures the change in amplitude and phase between the incident wave and the emergent wave at any point, and can be expressed as

$$h(\mathbf{r}) = [1 - a(\mathbf{r})] \exp[i\phi(\mathbf{r})] \quad (1.18)$$

where $a(\mathbf{r})$ and $\phi(\mathbf{r})$ are real functions, and $0 \leq a(\mathbf{r}) \leq 1$.

Under the conditions described above where only a small fraction of the incident electrons are scattered the phase shift ϕ is generally appreciably less than unity, so that

$$\phi(\mathbf{r}) \ll 1 \quad (1.19)$$

and we can write

$$h(\mathbf{r}) \approx 1 - a(\mathbf{r}) + i\phi(\mathbf{r}) \quad (1.20)$$

This is known as the weak phase approximation. The quadratic and higher order terms in $\phi(\mathbf{r})$ are small compared to the lower order ones and have been neglected.

1.2.3. The phase contrast image

Image contrast is often defined in terms of the variation in image intensity relative to the mean intensity of the image. There are two main contrast mechanisms. The first one is considered to be aperture contrast (Hawkes, 1972). Some electrons are intercepted by the objective aperture and their absence from the beam produces contrast, because electrons are scattered differentially outside the objective aperture from regions of the specimen with different density. The contrast thus depends on the angular distribution of the scattered electrons and the size of the objective aperture. It increases with increasing specimen thickness and decreasing size of the objective aperture.

The other mechanism is through phase contrast, which results from the interference of the unscattered and the elastically scattered

electrons. These are shifted in phase by the effect of the spherical aberration of the objective lens and the defocus.

We concentrate on this contrast mechanism and return to Eqn. (1.20) with the $a(\mathbf{r})$ term omitted. Taking the Fourier transform of this equation yields

$$H(\mathbf{k}) = \delta(\mathbf{k}) + i\Phi(\mathbf{k}) \quad (1.21)$$

Substituting Eqn.(1.21) into Eqn.(1.16) with the aid of Eqn.(1.17), we obtain

$$\Psi_i(\mathbf{k}) = (1/M) T(\mathbf{k}) [\delta(\mathbf{k}) + i\Phi(\mathbf{k})] \quad (1.22)$$

Substituting Eqn(1.17) into Eqn(1.22) and taking the Fourier transform yields

$$\Psi_i(\mathbf{r}) = (1/M) \int p(\mathbf{k}) \exp[iw(\mathbf{k})] [\delta(\mathbf{k}) + i\Phi(\mathbf{k})] \exp(2\pi i \mathbf{k} \mathbf{r}) d\mathbf{k} \quad (1.23)$$

so that

$$M^2 \Psi_i \Psi_i^* = [1 + \int p e^{iw} (i\Phi) \exp(2\pi i \mathbf{k} \mathbf{r}) d\mathbf{k}] [1 + \int p e^{-iw} (-i\Phi^*) \exp(-2\pi i \mathbf{k} \mathbf{r}) d\mathbf{k}] \quad (1.24)$$

With the fact of $\Phi(\mathbf{k}) = \Phi^*(-\mathbf{k})$, and neglecting the quadratic term, we have

$$M^2 \Psi_i \Psi_i^* = 1 + 2 \int p(\mathbf{k}) \Phi(\mathbf{k}) \sin w(\mathbf{k}) \exp [2\pi i \mathbf{k} \mathbf{r}] d\mathbf{k} \quad (1.25)$$

The quantity $M^2 \Psi_i \Psi_i^*$ is proportional to the electron current

density at the image plane, and we write

$$j = M^2 \psi_i \psi_i^* \quad (1.26)$$

Inverting Eqn.(1.25), we get the intensity in the image plane as

$$I(\mathbf{k}) = \delta(\mathbf{k}) + 2 p(\mathbf{k}) \Phi(\mathbf{k}) \sin w(\mathbf{k}) \quad (1.27)$$

The spatial frequency spectrum of the phase structure of the specimen is therefore modulated by the phase contrast transfer function of $\sin w(\mathbf{k})$.

1.2.4 Phase contrast transfer function

Spatial frequency components in a weak phase object are imaged with a contrast proportional to the phase contrast transfer function, $-\sin w(\mathbf{k})$. Expressed alternatively the contribution to the image contrast of diffracted beam amplitudes for a particular range of spatial frequency is modulated by this function. The form of the function is shown in Fig.(1.3), for 100 kV electrons, $C_s = 3.3$ mm and several values of defocus. The reasons why the particular parameter values were chosen is clarified later; for now they serve to illustrate the general features of conventional phase contrast imaging.

With in-focus ($d_z = 0$) operating condition the function $w(\mathbf{k})$ is completely determined by the lens aberration as shown in Eqn.(1.12); its significance increases at higher spatial frequencies. It

is apparent that low spatial frequency components of the object do not contribute to the in-focus phase contrast image. At higher spatial frequencies negative contrast appears, and thereafter the sign of the contrast oscillates.

Introduction of non-zero values of defocus still generally results in the phase contrast transfer function oscillating. However, it is possible to identify an optimum defocus, the Schezer defocus which for the assumed conditions is -110 nm. The curve indicates that with such a value of defocus the transfer function is close to unity over a large range of spatial frequencies without contrast reversals.

The characteristic features of the phase contrast transfer function imply that by altering the defocus value d_z one can tune the electron microscope to emphasise detail of a particular spatial frequency for a weak phase specimen.

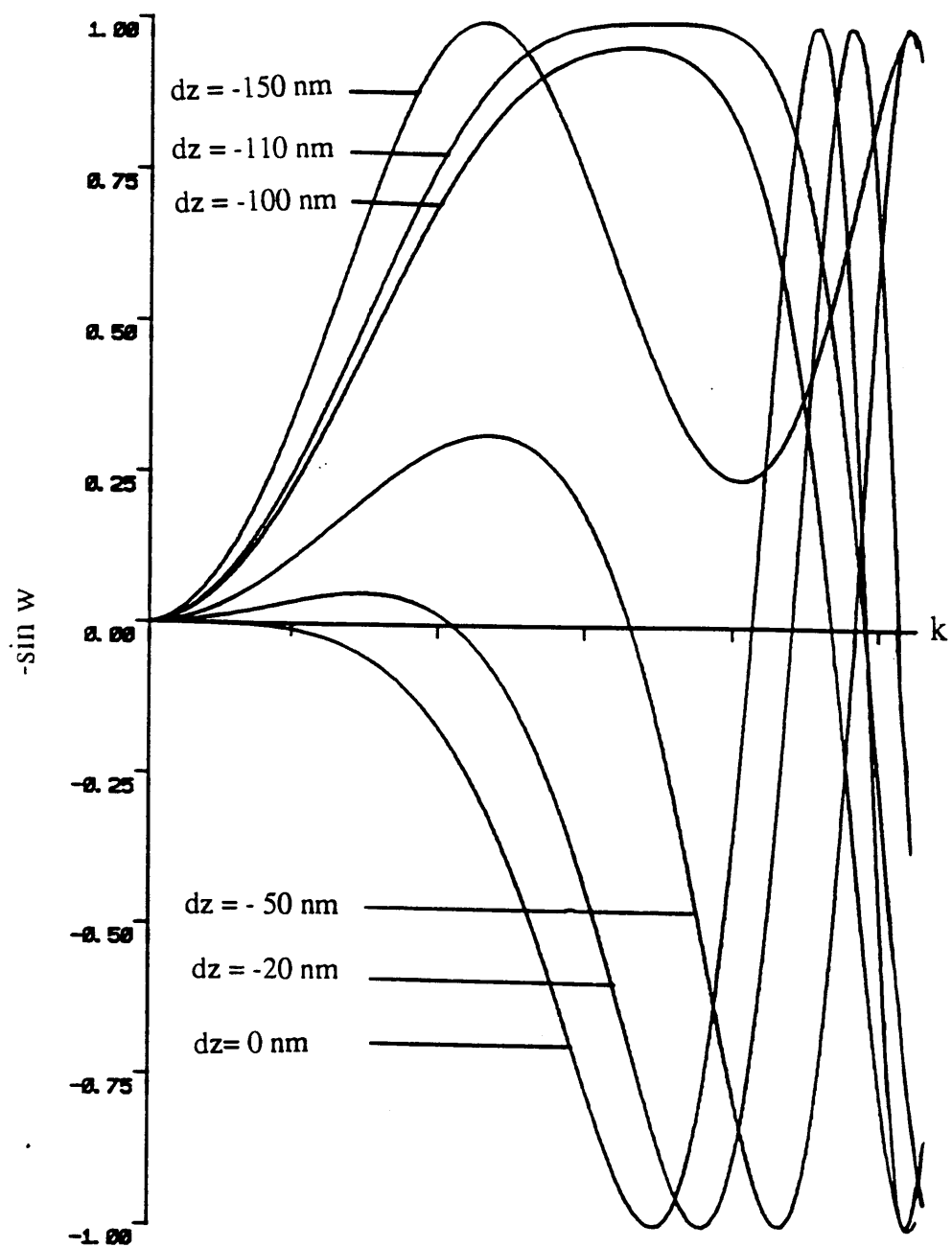


Fig.1.3. The phase contrast transfer function, for 100 kV, $C_s = 3.3 \text{ mm}$, and the indicated values of d_z

1.3. Image Formation in Scanning Transmission Electron Microscope

1.3.1. STEM

Scanning transmission electron microscopes, derived from the original design of Crewe et al. (1968), have proved to be highly versatile, offering high spatial resolution capabilities both for imaging and for microanalysis. This is due to the flexibility in their illumination and particularly in their detection systems which allows the use of a large number of the signals generated from the interaction between the incident probe and the specimen.

A schematic layout of the extended VG-HB5 STEM column at Glasgow University is shown in Fig.(1.4). The optical system of it essentially consists of a high brightness electron source, a condenser-objective probe lens (Crewe and Wall 1970) and a detector. The source is a field emission gun (FEG), which allows the use of probes ~ 0.5 nm in diameter carrying current ~ 0.2 nA. Of course, to realise high resolution, the instrument has to be used in the transmission mode, and the specimen must be very thin. The probe forming lens forms a demagnified image of the source, and the focused probe is fixed or scanned in a raster pattern across the specimen plane, which is thus approximately conjugate to the source plane. Various signals resulting from the interaction of this primary beam of electrons with the sample are collected and measured with suitable detectors, which may be located in a plane conjugate to the entrance or exit pupil of the probe-forming lens. The

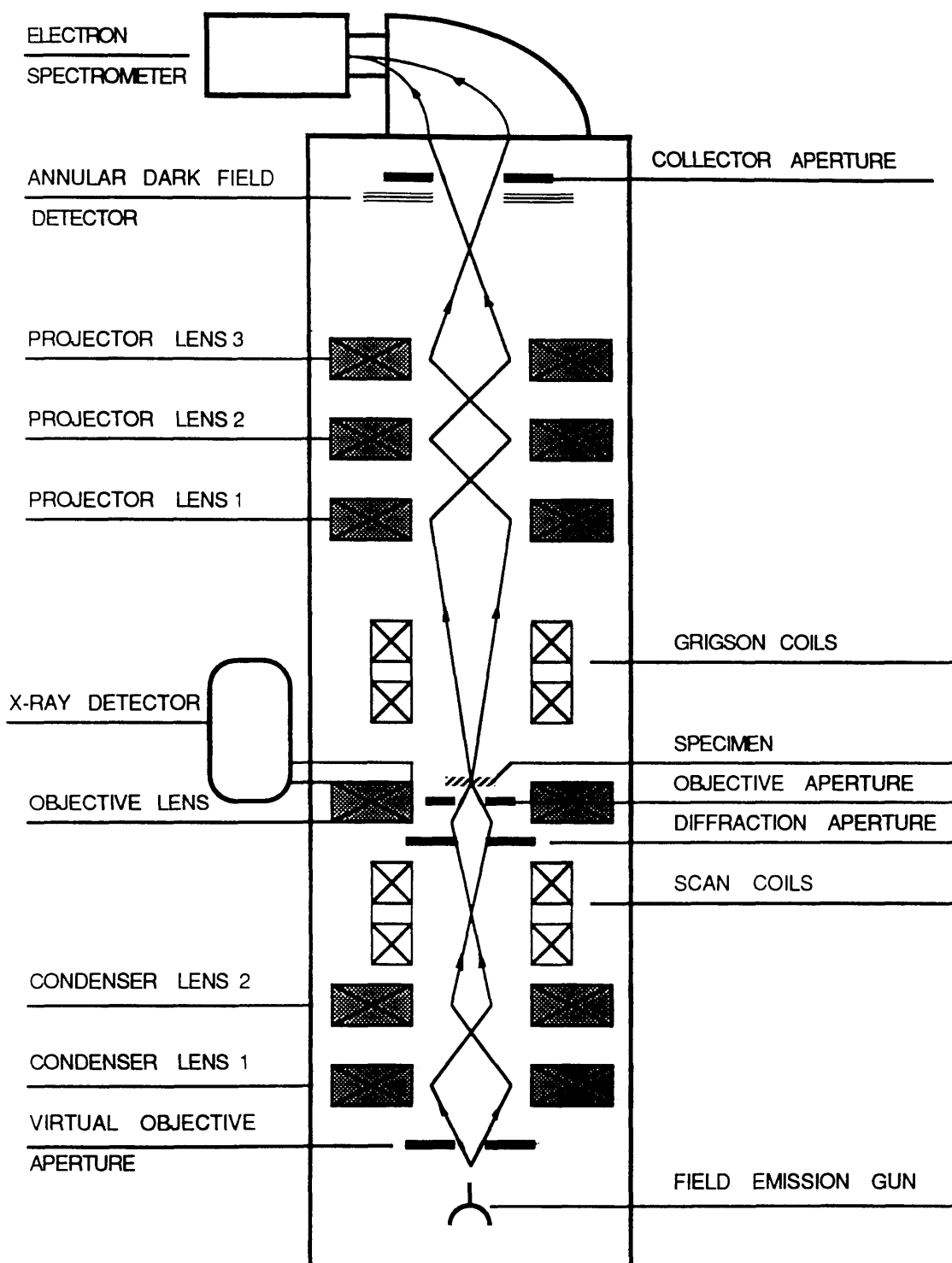


Fig.1.4. Schematic drawing of the main components of the Glasgow University STEM

electrical outputs are amplified, may or may not be digitized, and then applied to the control electrode of a synchronously scanned display oscilloscope.

The STEM instruments have been shown to offer significant advantages over CTEMs which include

1) A variety of detector configurations is available and their effects lead to a wider range of imaging modes than are available in the usual CTEM cases. The basic STEM instrument often has two detectors. The small on-axis or bright field detector collects the unscattered electrons, the majority of those inelastically scattered and a fraction of the elastically scattered electrons. The annular detector allows the unscattered and inelastically scattered electrons to pass through the centre of the detector into an electron spectrometer, where the inelastic component can be separated from the unscattered component, and an inelastic image formed simultaneously with the elastic image collected on the annulus of the detector. Moreover, the possibility exists of using split or quadrant detector in bright field, which allows multi-channel signals to be extracted and processed separately in an on-line computer (Burge et al, 1980).

2) The sequential nature of the STEM image signal collection simplifies the attachment of on-line computer facilities and allows the direct digitization of image data. This is often preferable to photography and photographic scanning particularly when image processing is required. Image processing may be sub-divided into four principal activities: (a) restoration (b) data compression and picture encoding (c) image enhancement (d) feature extraction and classification.

1.3.2. Image formation in STEM and the reciprocity principle

Consider the STEM image formation system illustrated in Fig.(1.5), and the notation in Fig.(1.6). For convenience we introduce a vector notation, $\mathbf{r} = (x, y)$ with different subscripts to distinguish the different planes of interest. If the probe is centred on a point \mathbf{r}_0 then the wave emerging from the specimen is related to that before specimen by

$$\psi(\mathbf{r}, \mathbf{r}_0) = h(\mathbf{r}) \psi_0(\mathbf{r} - \mathbf{r}_0) \quad (1.28)$$

in which constant factors have been neglected. The equation shows that at the object the amplitude and phase of the illuminating beam are modulated by the complex specimen transmission function $h(\mathbf{r})$. In the detector plane (subscript d), the signal depends on both the current density distribution and the detector response function. We represent the latter by a function $D(\mathbf{r}_d)$, which characterizes the shape and any position-dependent variation in sensitivity of the detector. The image signal generated while the probe is located at the point \mathbf{r}_0 is thus proportional to

$$S(\mathbf{r}_0) = \int |\Psi_d(\mathbf{r}_d, \mathbf{r}_0)|^2 D(\mathbf{r}_d) d\mathbf{r}_d \quad (1.29)$$

We can write the wave function in the detector plane as

$$\Psi_d(\mathbf{r}_d, \mathbf{r}_0) = \int \psi(\mathbf{r}, \mathbf{r}_0) \exp(-2\pi i \mathbf{r}_d \mathbf{r} / \lambda R) d\mathbf{r} \quad (1.30)$$

in which R is the distance between detector and specimen, so that

$$S(\mathbf{r}_0) = \int \psi(\mathbf{r}, \mathbf{r}_0) \psi^*(\mathbf{r}', \mathbf{r}_0) D(\mathbf{r}_d)$$

$$\exp\{-2\pi i \mathbf{r}_d(\mathbf{r} - \mathbf{r}') / \lambda R\} d\mathbf{r} d\mathbf{r}' d\mathbf{r}_d \quad (1.31)$$

or in the form of

$$S(\mathbf{r}_0) = \int \psi(\mathbf{r}, \mathbf{r}_0) \psi^*(\mathbf{r}', \mathbf{r}_0) D'[(\mathbf{r} - \mathbf{r}') / \lambda R] d\mathbf{r} d\mathbf{r}' \quad (1.32)$$

where

$$D'(\mathbf{p}) = \int D(\mathbf{r}_d) \exp(-2\pi i \mathbf{p} \mathbf{r}_d) d\mathbf{r}_d \quad (1.33)$$

Introducing the specimen transmittance, we find that the signal is given by

$$S(\mathbf{r}_0) = \int \psi_0(\mathbf{r} - \mathbf{r}_0) \psi_0^*(\mathbf{r} - \mathbf{r}'_0) h(\mathbf{r}) h^*(\mathbf{r}') D'[(\mathbf{r} - \mathbf{r}') / \lambda R] d\mathbf{r} d\mathbf{r}' \quad (1.34)$$

The relation between the signal detected and the specimen transmittance $h(\mathbf{r})$ may be determined for any given geometry by inserting the appropriate form of $D(\mathbf{r}_d)$ in Eqn. (1.34).

We now consider the particular case of a small on-axial detector in bright-field STEM and establish the reciprocity theorem. The Helmholtz reciprocity theorem (Cowley, 1969) states

that a point source at any point B producing a certain amplitude in the recording plane at A will produce the same amplitude at B when placed at A. We can thus think of a STEM as being equivalent to a CTEM with the directions of motion of the electrons reversed. The reversibility is clear in Fig.1.7, where the two microscope

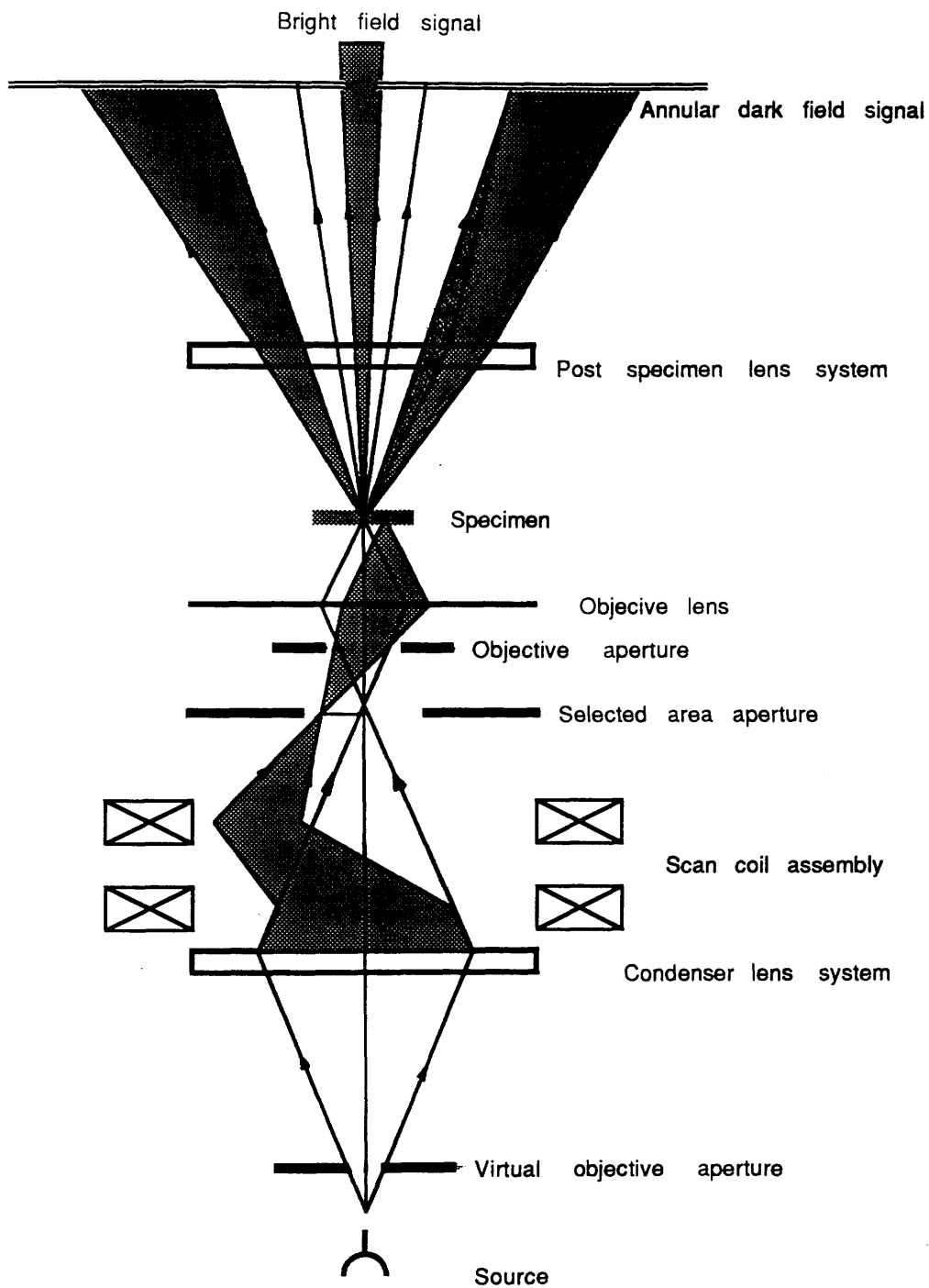


Fig. 1.5 Ray diagram of image mode in a STEM

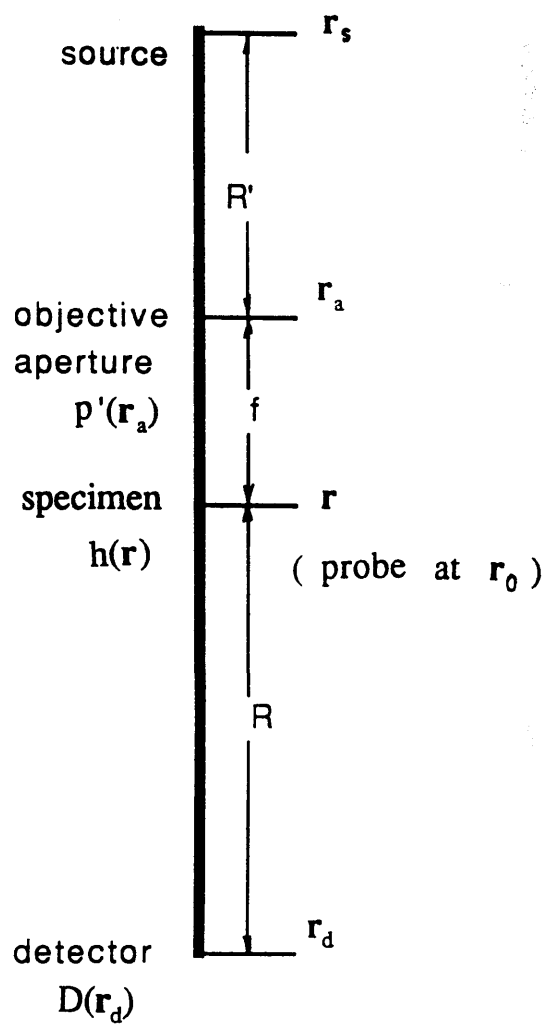


Fig.1.6. Definition of the notation in a STEM imaging system

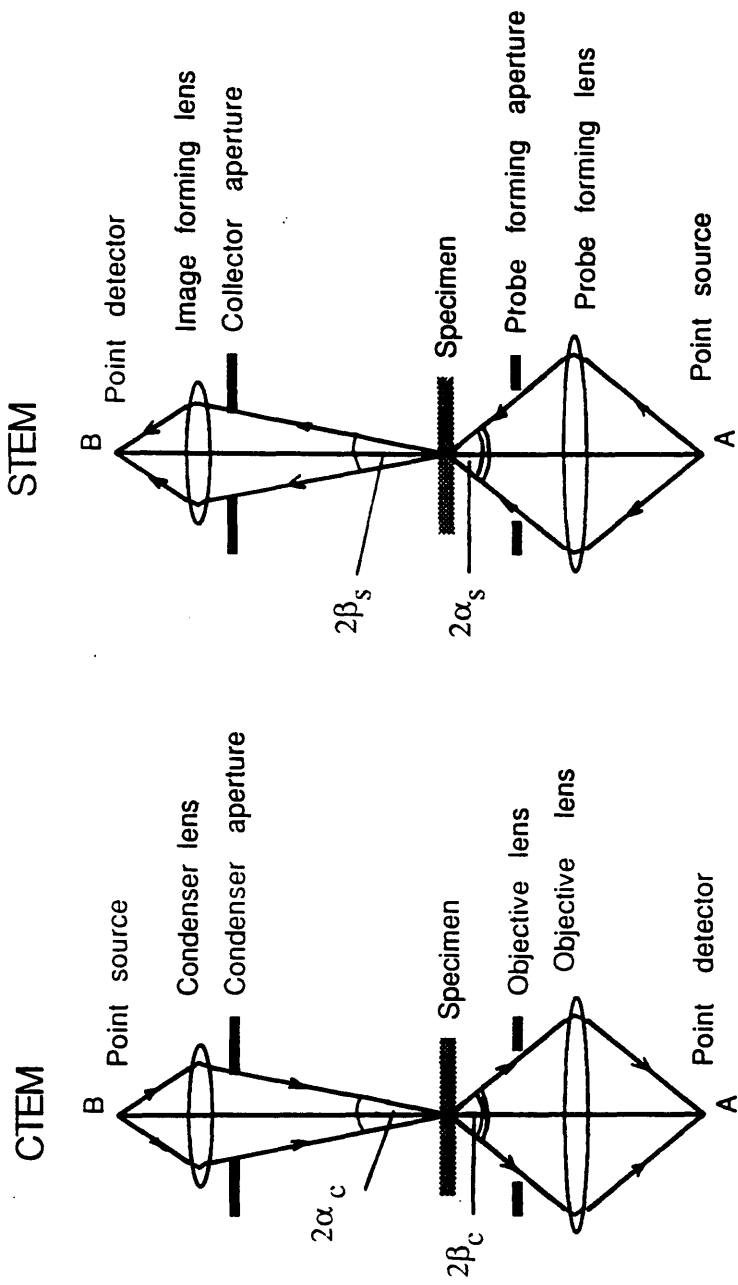


Fig.1.7. Diagram showing the principles of reciprocity applied to CTEM and STEM

diagrams differ only in the direction of the arrows. However, some necessary conditions must be fulfilled.

1) the specimen and the field in the magnetic lens must be inverted

2) the lenses must have equivalent properties

3) the angular conditions at the specimen have to be equivalent, that is $\alpha_s = \beta_c$ and $\alpha_c = \beta_s$

4) strictly, only elastically scattered electrons should contribute to the image

Returning to bright-field image formation in STEM, the response function for a very small on-axial detector can be treated as a delta function, so that $D'[(\mathbf{r} - \mathbf{r}') / \lambda R]$ is constant and Eqn.(1.34) becomes

$$S(\mathbf{r}_0) = \int \psi_0(\mathbf{r} - \mathbf{r}_0) \psi_0^*(\mathbf{r}' - \mathbf{r}_0) h(\mathbf{r}) h^*(\mathbf{r}') d\mathbf{r} d\mathbf{r}' \quad (1.35)$$

We take the alternative form of this equation as

$$S(\mathbf{r}_0) = \int H(\mathbf{k}) \Psi_0(\mathbf{k}) H^*(\mathbf{k}') \Psi_0^*(\mathbf{k}') \exp [2\pi i (\mathbf{k} - \mathbf{k}') \mathbf{r}_0] d\mathbf{k} d\mathbf{k}' \quad (1.36)$$

For the case of a weak phase object, we use the approximation which has been expressed in Eqn.(1.21), and obtain

$$\begin{aligned} S(\mathbf{r}_0) &= \int [\delta(\mathbf{k}) + i\Phi_0(\mathbf{k})] [\delta(\mathbf{k}') - i\Phi_0^*(\mathbf{k}')] \Psi_0(\mathbf{k}) \Psi_0^*(\mathbf{k}') \\ &\quad \exp[2\pi i (\mathbf{k} - \mathbf{k}') \mathbf{r}_0] d\mathbf{k} d\mathbf{k}' \\ &= [1 + i \int \Phi_0(\mathbf{k}) \Psi_0(\mathbf{k}) \exp(2\pi i \mathbf{k} \mathbf{r}_0) d\mathbf{k}] \\ &\quad [1 - i \int \Phi_0^*(\mathbf{k}') \Psi_0^*(-\mathbf{k}') \exp(-2\pi i \mathbf{k}' \mathbf{r}_0) d\mathbf{k}'] \end{aligned} \quad (1.37)$$

The quadratic term represents the dark-field case which we do not discuss here , and is ignored. The Fourier transform of Eqn.(1.37) then is expressed by

$$S(\mathbf{k}) = \delta(\mathbf{k}) + i\Phi_0(\mathbf{k}) \Psi_0(\mathbf{k}) - i\Phi_0^*(-\mathbf{k}) \Psi_0^*(-\mathbf{k}) \quad (1.38)$$

Recalling that the wave before the specimen is associated with the electron microscope imaging condition and contains terms arising from the wave aberrations of the objective lens, we then have

$$\Psi_0(\mathbf{k}) = p(\mathbf{k}) \exp[iw(\mathbf{k})] \quad (1.39)$$

So that the signal current which is contributed on the detector plane finally takes the form

$$\begin{aligned} S(\mathbf{k}) &= \delta(\mathbf{k}) + i\Phi_0(\mathbf{k}) [\Psi_0(\mathbf{k}) - \Psi_0^*(-\mathbf{k})] \\ &= \delta(\mathbf{k}) + 2\Phi_0(\mathbf{k}) p(\mathbf{k}) \sin w(\mathbf{k}) \end{aligned} \quad (1.40)$$

Thus the spatial frequency spectrum of the detector current $S(\mathbf{k})$ is essentially the same form as that of the CTEM, a zero-order term and a linear term.

1.4. Assessment of efficiency of electron utilization

In practice the phase contrast imaging mode in TEM is widely used in investigating the structure of both amorphous and

crystalline specimens. However, one problem we deal with is that some organic specimens are sensitive to damage by radiation during observation. This is further discussed in Chapter 2. It is therefore necessary to consider the efficiency of the imaging modes of both CTEM and STEM from the point of view of electron utilization.

It is desirable to estimate a minimum radiation dose required to record a clear image with a reasonable value of the signal-to-noise ratio, S/N . The signal S here is defined as resulting from the elastic scattering of electrons by the specimen, whilst the noise N arises from statistical fluctuations in the number of electrons from one image element to the next, and the inelastic scattering by the specimen. Image contrast is defined in terms of the modulation of the image intensity divided by the average background intensity, and the modulation is assumed to be caused totally by the elastic scattering from the specimen.

We have shown that with the weak-phase approximation in bright-field CTEM, the image intensity $j(\mathbf{r})$ is given in Eqn(1.27) by writing

$$j(\mathbf{r}) = 1 - 2\phi(\mathbf{r}) * q(\mathbf{r}) \quad (1.41)$$

where the asterisk denotes a convolution of two functions, and $q(\mathbf{r})$ is the inverse Fourier transform of $p(\mathbf{k})\sin[w(\mathbf{k})]$. Thus the image transform depends on the transform of the object structure $\phi(\mathbf{r})$ multiplied by the microscope function $\sin[w(\mathbf{k})]$. The contributions to the background intensity arise from the unscattered beam which is unity in Eqn.(1.40), and the inelastic scattering, which has little effect for the weakly scattering objects under consideration here. As

an approximation the signal, S , is proportional to 2ϕ (Misell,1978), and we have

$$S_{\max} = 2\phi_0 n_0 \quad (1.42)$$

where ϕ_0 is the maximum phase excursion and n_0 is the number of detected electrons on a pixel of the detector, that is

$$n_0 = \eta_0 \pi \alpha_c^2 \delta^2 \tau / e \quad (1.43)$$

in which η_0 is brightness of the source . δ is the linear dimension of a pixel referred back to the object plane and τ is the recording time.

The noise is calculated by the addition of the statistical fluctuations and substrate noise. In the absence of a support film, N is $\sqrt{n_0}$, so that

$$\begin{aligned} (S/N)_{\max} &= 2\phi_0 n_0 / (n_0)^{1/2} = 2\phi_0 (n_0)^{1/2} \\ &= 2\phi_0 (\eta_0 \pi \alpha_c^2 \delta^2 \tau / e)^{1/2} \end{aligned} \quad (1.44)$$

We note that in the approximations used here all the electrons going through the specimen reach the image recording plane in the CTEM.

In STEM the maximum signal collected by the detector can be expressed as

$$S_{\max} = 2 \phi_0 \beta_s^2 I_p \tau / (\alpha_s^2 e) \quad (1.45)$$

where I_p is the total electron current in the probe, that is

$$I_p = \eta_0 \delta^2 \pi \alpha_s^2 \quad (1.46)$$

It should be noted that the factor $(\beta_s/\alpha_s)^2$ represents the ratio

of the number of electrons collected to those incident on the specimen. The noise can be expressed as

$$N = [\beta_s^2 I_p \tau / (\alpha_s^2 e)]^{1/2} \quad (1.47)$$

Thus if β_s is the same as α_c in the CTEM we will have a maximum signal-to-noise exactly the same as that in the CTEM, namely

$$(S/N)_{\max} = 2\phi_0 (\eta_0 \pi \beta_s^2 \delta^2 \tau / e)^{1/2} \quad (1.48)$$

However, we should realise that for good phase contrast α_s and β_s should be small and whilst we pay no severe price for this in CTEM, where essentially all electrons striking the specimen proceed to the image, the same is not true in STEM. We have noted that in the latter case the number of electrons incident on the specimen exceeds those collected by $(\beta_s/\alpha_s)^2$ with particularly serious consequences for imaging radiation sensitive material. This then is one of the motivations for seeking alternative STEM imaging techniques of the kind introduced in Chapter 3.

Chapter 2

Imaging of Beam Sensitive Materials in the Transmission Electron Microscope

2.1. Introduction

Electron microscopy has proved a powerful technique for investigating small crystalline particles. Recent studies have demonstrated that to resolve lattice fringes with a periodicity of ~ 0.1 nm is becoming increasingly routine (Reimer, 1984). Further, high resolution images allow the crystal structure of, for example, epitaxially prepared films to be established and defects observed and identified.

Some instrumental considerations of imaging in the transmission electron microscope have been discussed in Chapter 1. However, with many specimens the full instrumental potential cannot be realised. For example, all organic specimens are sensitive to damage by the electron beam so that erroneous conclusions may easily be drawn from the resulting micrographs. Degradation of an organic crystalline particle in the electron beam can involve changes in both the size and shape of the particles under examination as well as eliminating information about their internal structure. Thus it is difficult with these materials to take high resolution images.

Copper phthalocyanine (Cu PC) and chlorinated copper phthalocyanine (Cl-Cu PC) are important organic crystals and in many ways are typical of radiation sensitive materials. They have been studied using TEM by many authors. However attempts to

obtain images involving the finer lattice fringes (0.3 ~ 0.5 nm) are hampered due to the problem of radiation damage.

Many efforts have been made to minimize radiation damage to the specimens, and some of these are summarized in the remainder of this chapter. It is realized that all investigations of materials of this kind will benefit from imaging modes in which the utilisation of electrons is as efficient as possible. This provided part of the incentive for developing the modes discussed in Chapter 3 and 4.

2.2 Beam sensitive materials and radiation damage

A characteristic dose is generally used as a measure of the sensitivity of a material to the effect of electron irradiation. In the case of crystalline material it is often taken as the dose necessary to reduce diffraction spot intensities to $1/e$ of their initial value. In order to record a bright field image with a resolution of ~ 0.2 nm a typical dose on the specimen of $\sim 1 \text{ C} \cdot \text{cm}^{-2}$ is required, and this is much greater than the characteristic dose of $\leq 0.1 \text{ C} \cdot \text{cm}^{-2}$ for the majority of organic materials, so it is doubtful whether a direct observation of the molecular structure of these materials can be achieved safely by electron imaging. That such images have been obtained of Cl-Cu PC reflects its higher stability, the critical dose being $\sim 10 \text{ C} \cdot \text{cm}^{-2}$.

During image formation the specimen is continuously irradiated by highly energetic charged electrons (typically 100 KeV). When these electrons pass through a thin specimen they may either be

unaffected, elastically scattered, or inelastically scattered. The energy transfer from electrons to the molecules in specimen should be considered in the interaction between beam and the specimen; it is significant when the inelastic electron scattering is concerned.

It is realized that the inelastic electron scattering, where the incident electron interacts with an orbital electron in the atom, is the main cause of radiation damage in organic specimens (Cosslett, 1978). This is generally because the energy transfer in this kind of scattering can be large ^{due to} the equal masses of the two particles involved in the collision, and leads to many results like atomic or molecular excitation ^{tot} or ionization, as well as displacement of an atom.

The initial causes of radiation damage to the organic materials are usually K-shell ionizations. A molecule which has been excited by the energy dissipated from the primary beam may liberate the energy by breaking selected bonds, forming initial radicals. Secondary reactions can lead to lattice disruption. Crosslinking can occur when a very reactive aromatic radical reacts with its adjacent molecule, resulting in a loss of resonance energy. Degradation may take place in many ways, producing degraded products. Meanwhile, recombination tends to give a stable product which preserves the lattice structure.

2.3 Methods for reducing radiation damage

Two strategies can be adopted to minimize the effects of radiation damage. One is to sidestep the problem somehow without actually reducing the radiation sensitivity of the sample. The other is to

actually reduce the sensitivity to the incident electron beam. The minimum exposure technique is used to record the required detail with the smallest number of electrons wasted during microscope manipulation. The simplest way is that focusing and astigmatism correction are carried out on a field of little interest and the region to be recorded is then quickly brought under electron illumination and photographed. In CTEMs equipped with 'minimum exposure packages' a set of beam-deflection coils (Hobbs,1984) are energized for this purpose. Beam deflection may be coupled with the second approach of focussing the beam to brightly illuminate a small expendable area, just off the recording field, in which the operations like focussing and tilting can be effected before more uniformly illuminating the desired area. More efficient recording media such as fast photographic emulsions can sometimes be used effectively. High voltage operation is based on the fact that the energy lost by an electron per unit mass thickness traversed decreases as its velocity is increased by raising the accelerating voltage. The frequency of both inelastic and elastic scattering events are less at high voltage but the former tend to decrease more rapidly than the latter (Salih et.al., 1974). Low temperature operation is used because some organic specimens are much less sensitive to radiation damage when kept at low temperature during microscopy (Cosslett,1978^b). A specimen surrounded with a solid or liquid medium helps to preserve its ultrastructure during electron irradiation. This may be due to simple mechanical confinement preventing the displacement of molecular fragments formed by irradiation. Coating a specimen with a thin layer of evaporated carbon or aluminum has an obvious stabilizing effect of reducing the rate of mass loss(Salih et.al.,1974).

2.4. Phthalocyanine pigments

The phthalocyanines, introduced in section 2.1, are of importance as colouring agents when in pigmentary form and the comments below pertain to this as well as to the epitaxial form more familiar to electron microscopists. The phthalocyanines have a common molecular structure, shown in Fig. 2.1, in which the central position marked as metal atom, M, is copper for the most widely used industrial pigments. Other elements can occupy this position and even two hydrogen atoms can make the molecule stable in the absence of a co-ordinating metal. The copper phthalocyanine and metal free derivatives are blue in colour, but this may be changed to green by substitution of a halogen for the peripheral hydrogen atoms in the positions marked A in Fig.2.1. A range of substitutions is possible up to a maximum value of 16 by synthesizing the molecule with chlorinated reactants to change the colour hue and strength of the pigment. Industrial chlorination levels attained typically involve substitution of 14 ~ 15 chlorine atoms per molecule. The effectiveness of a pigment in colouring a medium depends largely upon the pigment size and how well the pigments are dispersed.

Study of the detailed topography and internal structure of phthalocyanine pigments must be achieved using a dose $< 1 \text{ C}\cdot\text{cm}^{-2}$ for Cl-Cu PC pigments. Thus imaging modes which allow both topography (potholes, facets steps) and internal structure to be revealed simultaneously are required. Furthermore, as already noted, the efficiency of electron utilisation must be high. In Chapter 5 calculations directly relevant to investigations of pigments and

using the most promising imaging modes developed in Chapter 3 and 4 are presented.

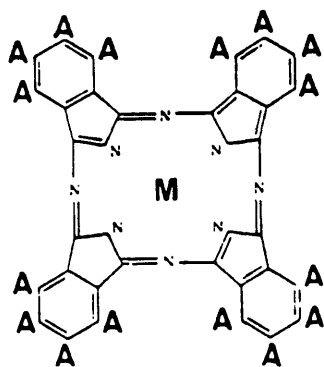


Fig.2.1. The phthalocyanine molecule. M is the co-ordinating metal atom with halogen substitution at A.

Chapter 3

Differential Phase Contrast Imaging in STEM

3.1. Introduction

Phase contrast in the transmission electron microscope is frequently produced by the interference of the unscattered incident wavefront and the elastically scattered wavefront. According to the Helmholtz reciprocity principle, discussed in section 1.3.2, a point detector can be used in the STEM for collecting an axially centred portion of the transmitted beam, to obtain a bright field phase contrast image (Cowley,1969), identical to that formed in the CTEM. Such a small detector, however, collects only a small fraction of the total electron flux so that signal currents are low (section 1.4). Acceptable signal to noise ratios can then only be obtained through long exposure times. This is frequently impractical due to contamination or drift; for radiation sensitive specimens the consequences are even more severe in that serious damage occurs before sufficient electrons are collected from each point on the specimen.

This situation can be improved by enlarging the detector radius (as defined by the collector aperture) until an acceptable detected electron current is reached. However, a single large detector implies a low coherence and therefore poor phase contrast transfer (Cowley, 1975). In addition, the noise is related to the detector area so that the signal-to-noise ratio is by no means a monotonically

increasing function of detector size. It is therefore of importance to seek a compromise between the contrast and electron current falling on the detector when attempting to obtain a high resolution image. Theory has predicted that an optimum bright-field detector exists for any given set of instrumental parameters (Cowley, 1978). However, even so standard phase contrast microscopy in STEM represents an inefficient use of electrons and there is incentive to study alternative imaging modes.

Flexible detection methods are possible in STEM, so the use of different detector configurations has attracted much attention (Burge and Toorn^{vov}, 1980). In particular, both phase contrast transfer and the signal-to-noise ratio can be influenced by varying the detector configuration. One attractive scheme comprises a large axial bright-field detector divided into two independent semicircular detectors (Dekkers and de Lang, 1974). However, the split detector is insensitive to phase variations parallel to the split. To solve this problem a bright-field detector divided into four quadrants can be used (Rose, 1977). The signals of interest from such a detector are the difference signals from opposite quadrants, as these, to a very good approximation, relate linearly to orthogonal components of the phase gradient of the specimen transmittance. For this reason the imaging mode is known as differential phase contrast (DPC) microscopy. A further development is the first moment detector system which represents an ideal DPC image system (Waddell and Chapman, 1979) but has not yet been achieved due to the technical difficulties in detector construction. Morrison and Chapman (1983) have compared these three systems and concluded that the more easily realised split and opposite quadrant (OQ) detectors both

offer viable alternatives to the first moment detector in permitting quantitative image interpretation to be undertaken.

It should be noted that if an image is formed from the sum signal, rather than from difference signal, the result is an incoherent bright-field image so that amplitude information can be obtained using different combinations of the same signals (Dekkers and de Lang, 1977).

In this chapter, discussion centres on the extraction of phase information and expressions for the DPC transfer function are derived. In an aberration free system it is easy to calculate this for both split and OQ detectors and the result can be expressed in terms of overlap areas between the unscattered bright-field cone and that due to a diffracted beam. However, in practice both spherical aberration and defocus are important and must be included in any complete description. In this case, the phase difference between the direct beam and a diffracted beam over the overlapped area is no longer constant, so the transfer functions must be calculated numerically. Results have been presented previously for the functions either along the x-axis scan direction (Dekkers and de Lang, 1977) or fully in two dimensions but with an aberration free system (Rose, 1977). A more systematic quantitative calculation of general applicability has been undertaken for the geometries so far discussed by Morrison and Chapman (1983). With the detector response functions appropriate for both split and OQ detectors, two-dimensional transfer functions are calculated in this chapter to obtain complete information on the DPC transfer properties. To help relate to practical operation conditions, lens aberrations and other parameters appropriate to the VG HB5 are chosen. These can then be used in the analysis of experimental DPC

images acquired using the Glasgow University Vacuum Generators HB-5 STEM which has been equipped with a commercial Centronic QD -100 quadrant photodiode detector.

DPC imaging is used in the study of magnetic and semiconductor materials and in studying the topography and internal structure of particles. It is the latter which is of greatest interest here and, in Chapter 5 , an image simulation technique for small particles using the DPC imaging mode is described.

3.2. Principles of DPC image formation

The contrast with which we are concerned arises through the overlap (and subsequent interference) of beams diffracted from the specimen with the unscattered beam. Consider a weakly scattering object in which the phase varies sinusoidally with periodicity Λ and in which the maximum phase excursion $\phi_0 \ll 1$. Under these conditions the specimen transmittance can be represented by

$$h(x) = 1 + i\phi_0 \sin(2\pi x / \Lambda) \quad (3.1)$$

If the specimen is illuminated by a coherent probe, subtending an angle α_s , there emerge from the specimen three beams, the direct beam B_0 and two diffracted beams B_{-1} and B_{+1} (Fig.3.1). To ensure that there is some overlap between the beams the condition $2\alpha_s > \theta$ must be fulfilled where θ is the characteristic scattering angle from an object of periodicity Λ and is given by λ/Λ .

The objective aperture is placed at the focal point of the objective lens. The half-angle of the cone of light is α_s . The distance from the specimen to the detector plane is R . The detector plane is at a distance R from the specimen.

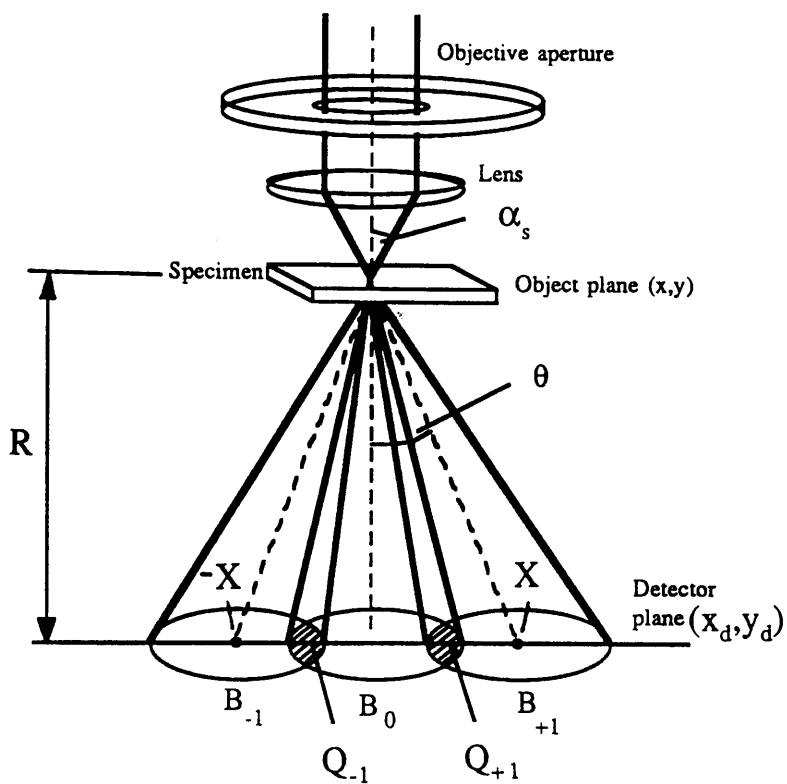


Fig.3.1. Schematic representation of a convergent-beam diffraction pattern in the STEM

We denote the area of overlap which occurs in the detection plane situated a distance R away by Q_{-1} and Q_{+1} (Fig.3.1). The complex amplitude in this plane, Ψ_d , can be written as (Dekkers and de Lang, 1977)

$$\begin{aligned}\Psi_d(x_0, x_d, y_d) = \Psi_0(x_d, y_d) + \frac{1}{2} \phi_0 \Psi_0(x_d + X, y_d) e^{2i\pi x_0/\Lambda} \\ - \frac{1}{2} \phi_0 \Psi_0(x_d - X, y_d) e^{-2i\pi x_0/\Lambda}\end{aligned}\quad (3.2)$$

where the last two terms in Eqn.(3.2) represent the two diffracted beams, which are centred a distance $X = R\theta$ away from the axial point.

Suppose that there are no aberrations in the probe forming system and the specimen is in focus. The amplitude and phase of Ψ_d can be treated as constant within the bright-field cone and zero elsewhere, so that $\Psi_0(x_d, y_d) = A_0$. With the term in ϕ_0^2 neglected, the intensity in Q_{-1} is given by

$$\begin{aligned}I_{-1} &= A_0^2 \left(1 + \frac{1}{2} \phi_0 e^{i2\pi x_0/\Lambda}\right) \left(1 + \frac{1}{2} \phi_0 e^{-i2\pi x_0/\Lambda}\right) \\ &= A_0^2 [1 + \phi_0 \cos(2\pi x_0 / \Lambda)]\end{aligned}\quad (3.3)$$

while that in Q_{+1} by

$$I_{+1} = A_0^2 [1 - \phi_0 \cos(2\pi x_0 / \Lambda)] \quad (3.4)$$

It can be seen that interference in these two areas is in antiphase. Thus by dividing the detector into two semicircular areas, and subtracting the signal falling on one half of the detector from that on the other, a resulting signal $S(x)$ is obtained

such that

$$S(x) \propto 2 A_0^2 \phi_0 D_a \cos(2\pi x_0 / \Lambda) \quad (3.5)$$

where D_a denotes the area of an overlap region. Thus the signal recorded as the electron probe scans across the specimen is directly proportional to the phase gradient of the specimen transmittance function.

The total current I_p incident on the detector plane is proportional to $\pi\alpha_s^2$. Thus the ratio of the information containing current from the detector to the current in the probe, $I(x)/I_p$, and its corresponding maximum value I_m/I_p are

$$I(x)/I_p = 2 \phi_0 D_a \cos(2\pi x_0 / \Lambda) / (\pi\alpha_s^2) \quad (3.6)$$

and

$$I_m/I_p = 2 \phi_0 D_a / (\pi\alpha_s^2) \quad (3.7)$$

In this expression D_a is an area in angle-space so that $D_a/(\pi\alpha_s^2)$ presents the fraction of the bright field cone which is involved in an overlap.

Each pixel of the image is produced in a time sequential manner, and hence the maximum signal expressed as a number of electrons is given by

$$S_{\max} = 2 \phi_0 \tau I_p D_a / (\pi\alpha_s^2 e) \quad (3.8)$$

The noise N will relate to the sum of the variances of the total signals from each half-detector

$$N = [(I_p \tau / 2e)_R + (I_p \tau / 2e)_L]^{1/2} = (I_p \tau / e)^{1/2} \quad (3.9)$$

The maximum signal-to-noise is then given by

$$(S/N)_m = 2 \phi_0 D_a (I_p \tau / e)^{1/2} / (\pi \alpha_s^2) \quad (3.10)$$

In practice both spherical aberration and defocus have to be taken into account. This can be done by replacing $\Psi_0(x_d, y_d) = A_0$ by $\Psi_0(x_d, y_d) = A_0 e^{i w(\mathbf{k})}$, where $w(\mathbf{k})$ is defined in Eqn.(1.12) and $\mathbf{k} = \mathbf{r}_d / \lambda R$.

As a result of this phase factor, the phase difference between the undeflected beam B_0 and the diffracted beams B_{-1} and B_{+1} varies with the position in the overlap area. Specifically for the left-hand area the phase difference is

$$\Delta w(k_x, k_y)_l = w(k_x + \kappa, k_y) - w(k_x, k_y) \quad (3.11)$$

where $\kappa = X / \lambda R$. For the right-hand area it is

$$\Delta w(k_x, k_y)_r = \Delta w(-k_x, k_y)_l \quad (3.12)$$

The intensity in Q_{-1} becomes

$$\begin{aligned} I_1 &= A_0^2 \left[1 + \frac{1}{2} \phi_0 e^{i(2\pi x_0 / \Lambda + \Delta w)} \right] \left[1 + \frac{1}{2} \phi_0 e^{-i(2\pi x_0 / \Lambda + \Delta w)} \right] \\ &= A_0^2 [1 + \phi_0 \cos(2\pi x_0 / \Lambda + \Delta w)] \end{aligned} \quad (3.13)$$

and that in Q_{+1}

$$I_r = A_0^2 [1 - \phi_0 \cos(2\pi x_0 / \Lambda + \Delta w)] \quad (3.14)$$

Thus the corresponding maximum difference signal from equivalent elements on the two detectors is reduced from a value proportional to $2A_0^2\phi_0$ to one proportional to $2A_0^2\phi_0\cos\Delta w$ and instead of simply multiplying by the overlap area it is necessary to integrate $\cos \Delta w$ over this area. We then obtain, as the expression equivalent to Eqn.(3.7) one in which D_a is replaced by

$$\int_{D_a} \cos [w(k_x + \kappa, k_y) - w(k_x, k_y)] dk_x dk_y .$$

As the angular extent of the probe is defined by an aperture subtending a half-angle α_s , it is convenient to express all the spatial frequencies as a function of the aperture cut-off α_s/λ . Thus $k = (\alpha_s/\lambda)k_r$, so two dimensionless variables k_{xr} and k_{yr} can be introduced as normalized spatial frequencies in the x and y directions respectively. Thus Eqn.(3.7) becomes

$$I_m / I_p = (2\phi_0 / \pi) \int_{D_a} \cos [w(k_{xr}, k_{yr}) - w(k_{xr} - \kappa_r, k_{yr})] dk_{xr} dk_{yr} \quad (3.15)$$

where $\kappa_r = \lambda / (\alpha_s \Lambda) = \theta / \alpha_s$, For Eqn.(3.15) to be applicable, the overlap area must not disappear which necessitates the condition $\kappa_r < 2$.

3.3. The efficiency of DPC detection

The efficiency of electrons utilization in standard CTEM and STEM have been discussed in section 1.4. It is found that the conditions of the reciprocity principle are strict and in practice the condition $\beta_s = \alpha_c$ is not satisfied in STEM (Fig.1.7). If it is, it leads to a low detection efficiency and poor signal-to-noise ratio.

In the DPC mode the detection efficiency depends on $D_a/(\pi\alpha_s^2)$ (in the aberration-free case). Thus, relative to that of standard STEM, the efficiency in DPC STEM is $D_a/(\pi\beta_s^2)$ times.

The signal-to-noise ratio in DPC STEM is known from Eqn.(3.10) and can be rewritten in the form

$$(S/N)_{\max} = 2 \phi_0 [\eta_0 D_a^2 \delta^2 \tau / (\pi \alpha_s^2 e)]^{1/2} \quad (3.16)$$

Here η_0 and δ have been defined in section 1.4. Comparing Eqn(3.16) to Eqn(1.48) we know the maximum signal-to-noise ratio in DPC STEM is $D_a/(\pi\alpha_s\beta_s)$ times that in standard STEM. With $\beta_s \approx \alpha_s/10$, it suggests the DPC mode is again superior.

3.4. The DPC transfer function

Further analysis of the DPC imaging mode for weak phase objects can be achieved through a study of how phase objects of

different periodicities are imaged. We define a transfer function as the right hand side of Eqn.(3.15) divided by ϕ_0 . Initially it is assumed that the orientation of the phase object is parallel to the line which divides the detector into two halves (Fig.3.2); this orientation is the optimum one for the transfer of phase information (see. section.3.5).

For an aberration-free system the transfer function is proportional to the areas Q_{-1} and Q_{+1} in Fig.(3.1). However, we note that at lower spatial frequency the two diffracted beams themselves overlap, and as their contributions to the phase signal are in antiphase, signal cancellation occurs and no phase information can be derived from electrons falling on these portions of the detector (Fig.3.3). Thus, the efficiency of phase information transfer falls at low and high spatial frequency and for an aberration-free system the maximum DPC transfer is achieved around a reduced spatial frequency of $k_{xr} \approx 0.9$ as shown in Fig.(3.4). A similar shaped curve is obtained for a quadrant detector albeit with a lower maximum value for I_m/I_p , reflecting its smaller collection area. However, if the signal-to-noise ratio is calculated it is apparent that this is not significantly reduced using a quadrant detector compared with use of a split one (Fig.3.5). This is because although less signal is collected by the quadrant detector the noise is reduced by a factor of 0.7 as the electron noise is proportional to the square root of the illuminated area of the detector.

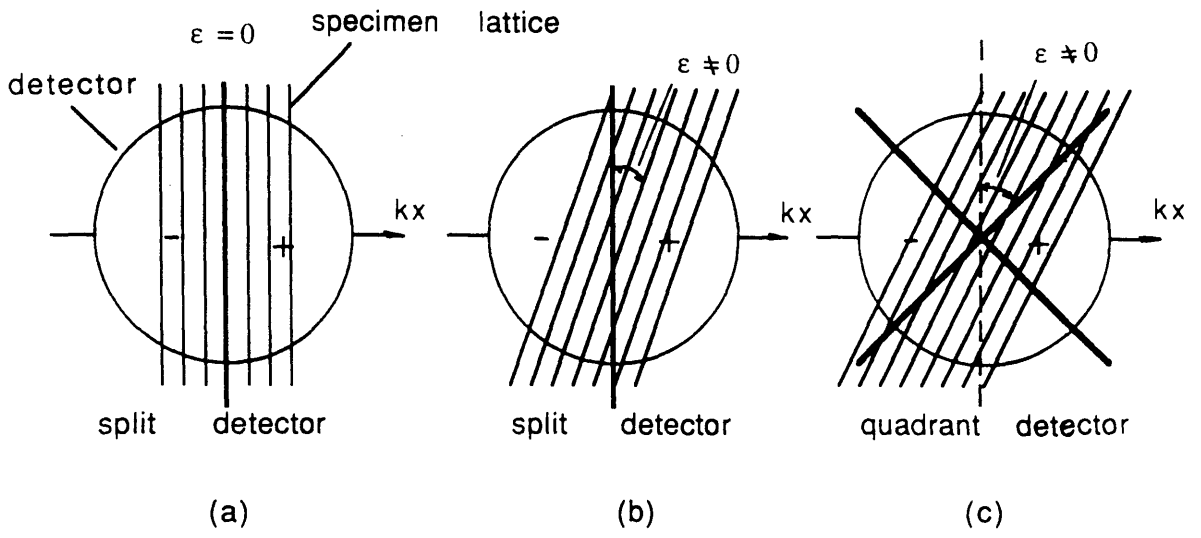


Fig.3.2. Schematic of the orientations of specimen with detector

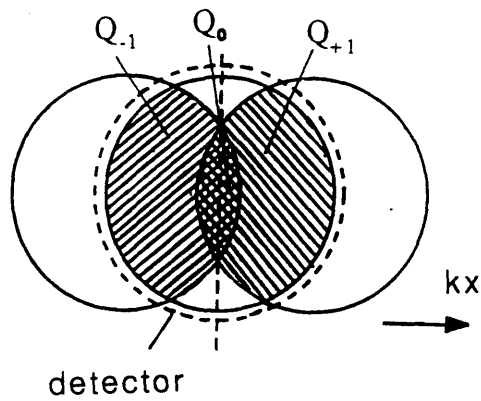


Fig.3.3. Schematic representation of the overlapped areas on a split detector at low spatial frequency. The phase information can be derived from Q_{-1} and Q_{+1} , but cancellation occurs at Q_0 .

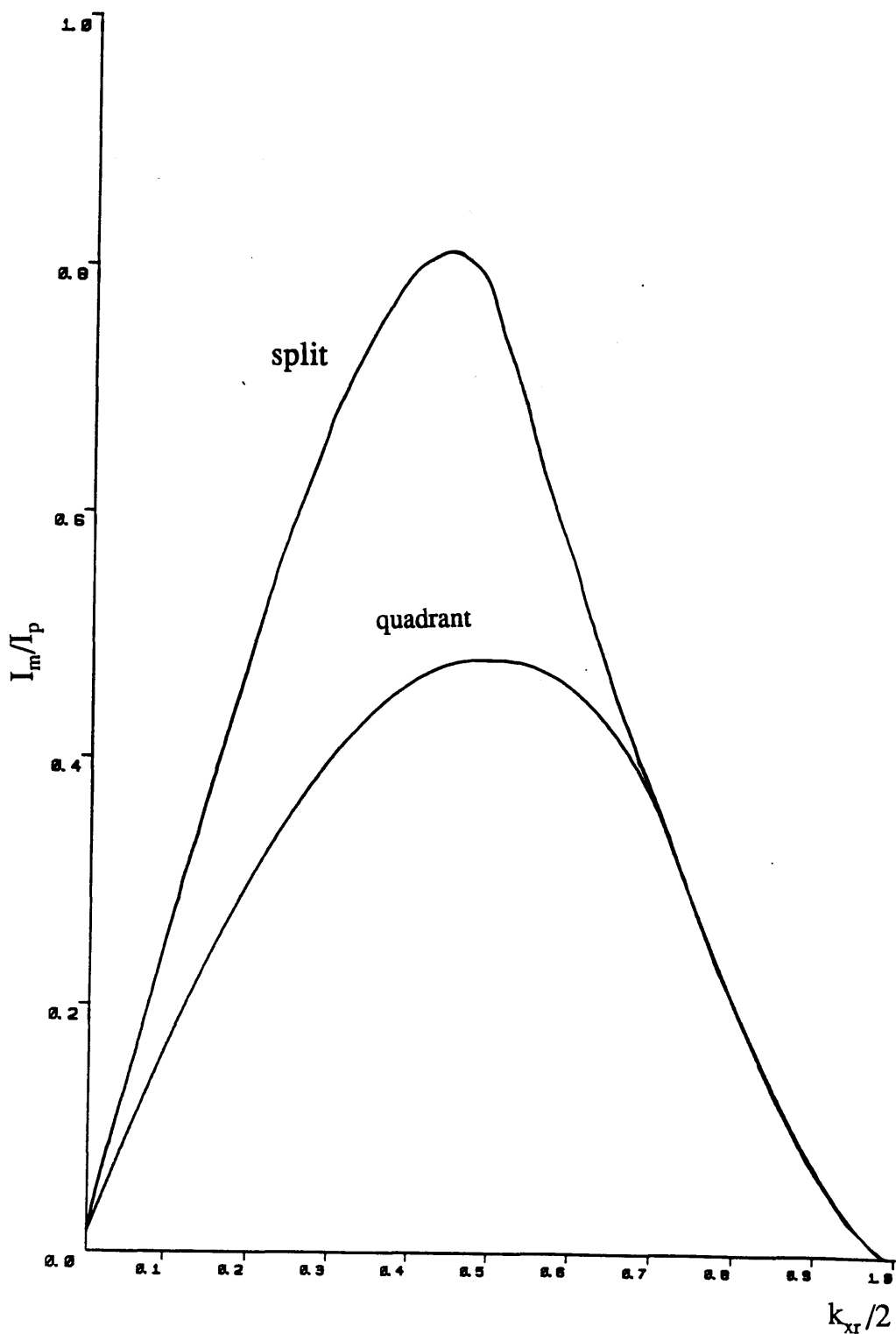


Fig.3.4. DPC transfer along the k_{xr} -axis for both split and quadrant detectors in an aberration-free system

Note: In this and subsequent figures 'DPC transfer' should read 'Phase transfer as derived from the DPC imaging mode.'

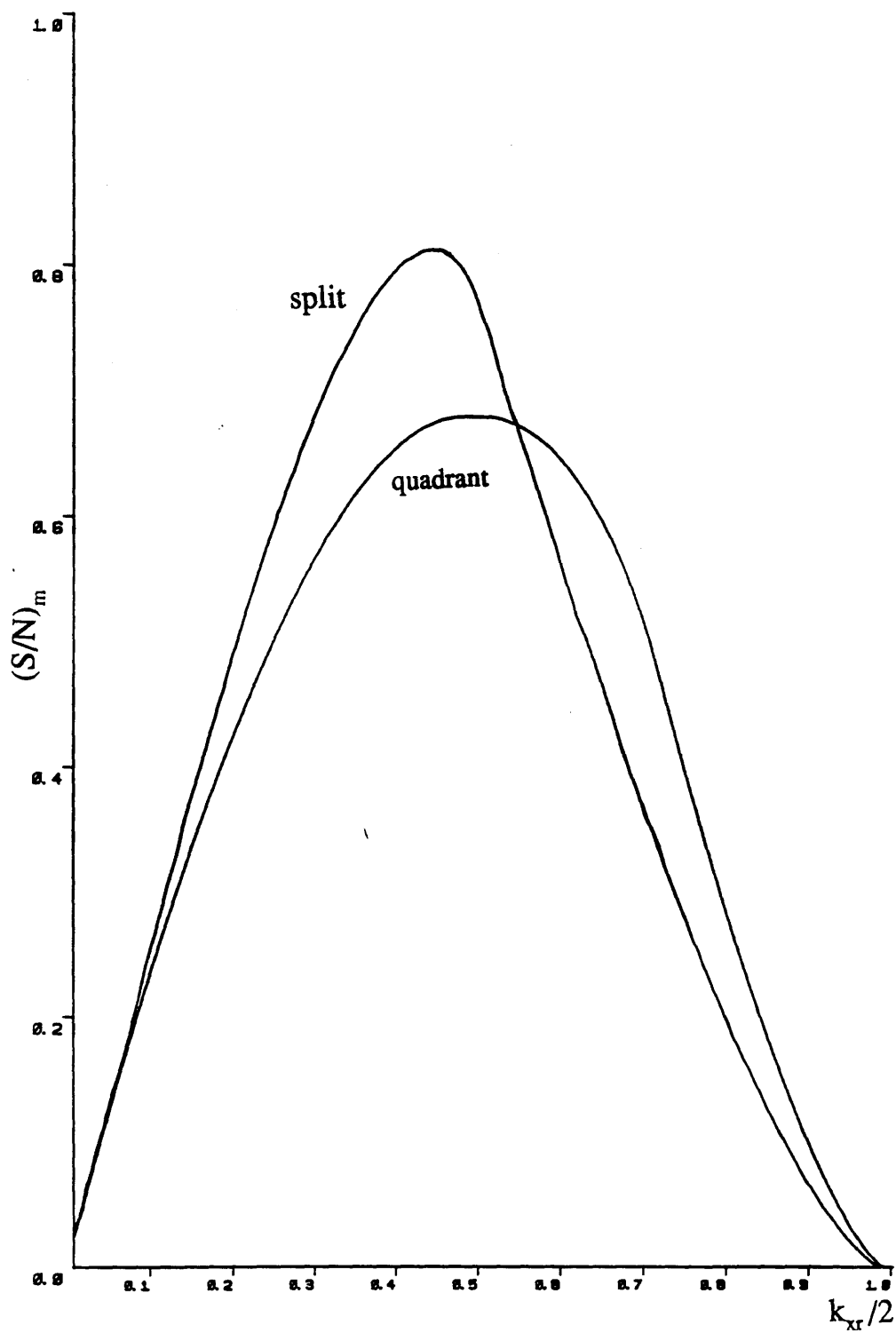


Fig.3.5. The signal-to-noise ratio for DPC imaging in an aberration-free system using both split and quadrant detectors

3.4.1. The effects of defocus

In any real microscope spherical aberration will have to be taken into consideration. In the VG-HB5 STEM at Glasgow University the objective lens has a value of $C_s = 3.3$ mm. In addition a value must be selected for α_s and initially we select $\alpha_s = 8.32$ mrad (obtained in practice using a $50\text{ }\mu\text{m}$ objective aperture). This is close to the optimum value defined by $1.41(\lambda/C_s)^{1/4}$. We have calculated I_m/I_p under these conditions for a variety of defocus values and some results for a split detector are shown in Fig.(3.6). For comparison the result for the aberration free system is repeated. It is clear that transfer of phase information is less efficient but that there is no oscillation in the sign of the transfer function as is the case in standard phase contrast imaging where contrast reversal occurs at high spatial frequencies. The optimum defocus is found to be close to the Scherzer defocus of $-1.15(C_s\lambda)^{1/2}$, a value of -110 nm for the system under consideration.

3.4.2. The effects of the objective aperture size

Other objective apertures used to define the probe angle in the VG-HB5 STEM at Glasgow University are $25\mu\text{m}$, $50\mu\text{m}$, and $100\mu\text{m}$. However, the computer calculation shows that the DPC transfer is by no means improved with the increase in the aperture size, the effect of spherical aberration increasing markedly with α_s . Fig.3.7 shows DPC transfer using three values of α_s whilst C_s remains constant at 3.3 mm. The image produced using a small

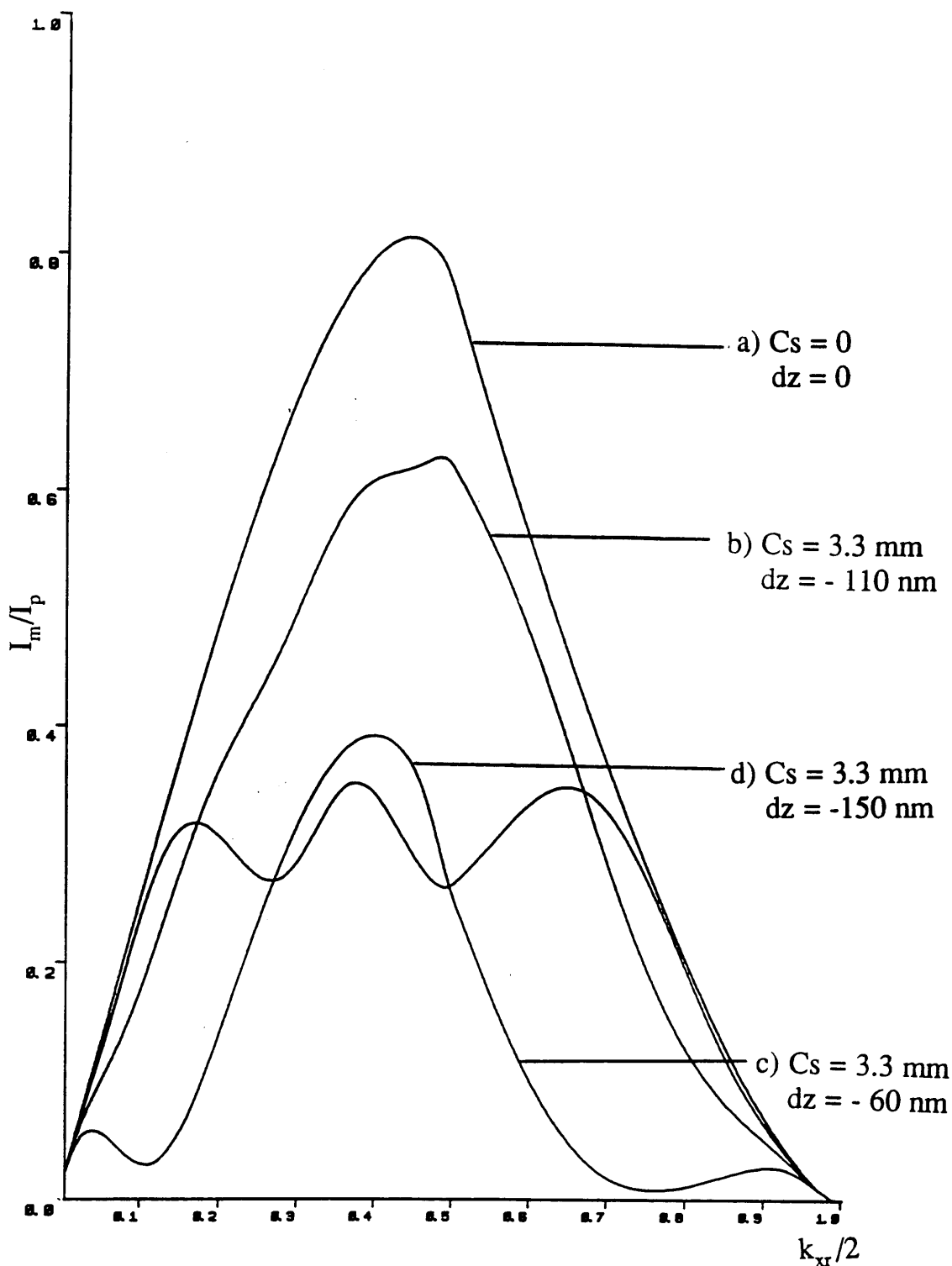


Fig.3.6. Comparison of DPC transfer using (a) a perfect lens and in-focus operation, and (b) to (d) a lens effected by spherical aberration $C_s = 3.3$ mm, under three values of defocus. In all cases, $\alpha_s = 8.32 \text{ mrad}$ and a split detector is used.

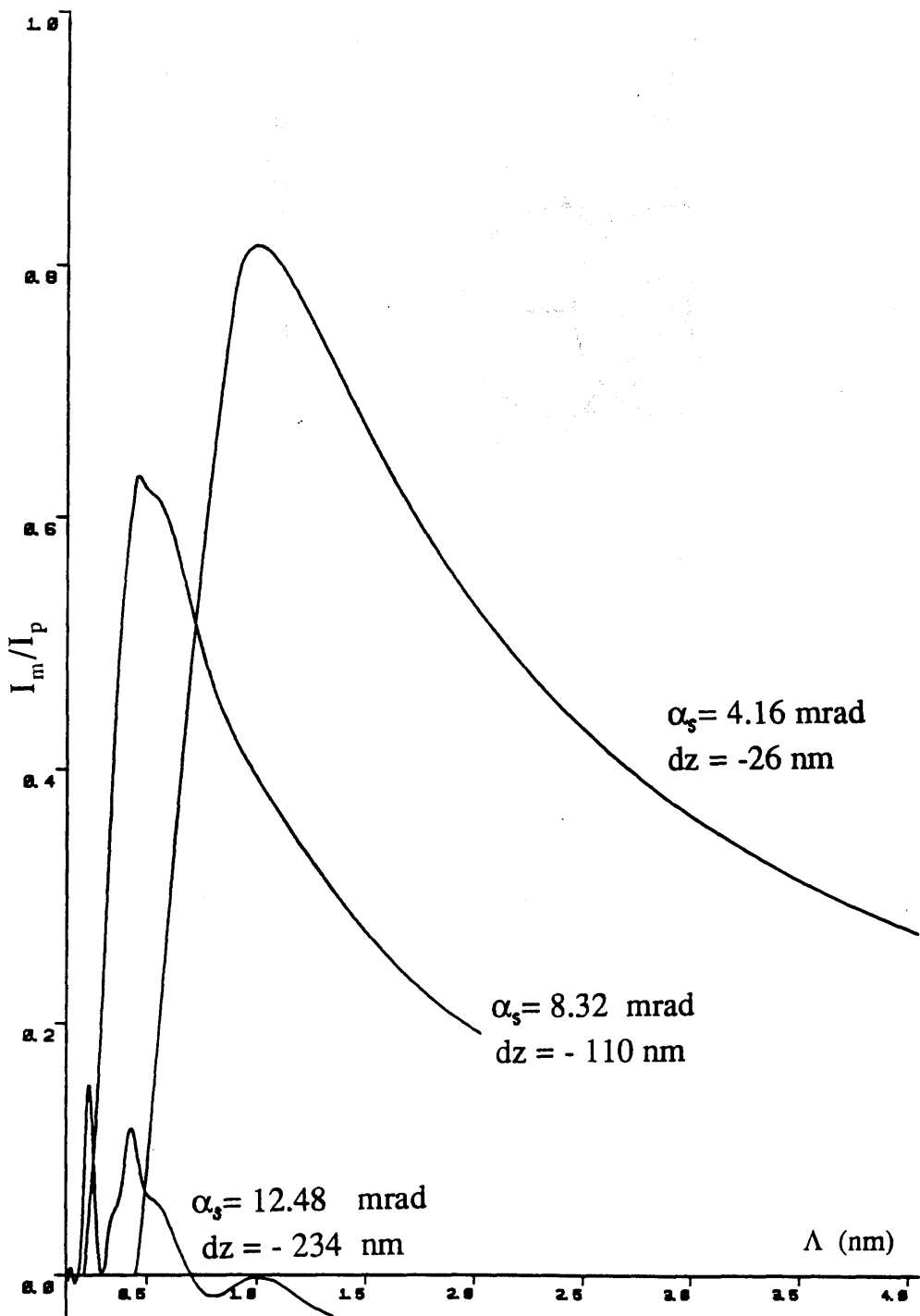


Fig.3.7. Calculated DPC transfer for different aperture sizes and optimum defoci with a split detector, and $C_s = 3.3$ mm

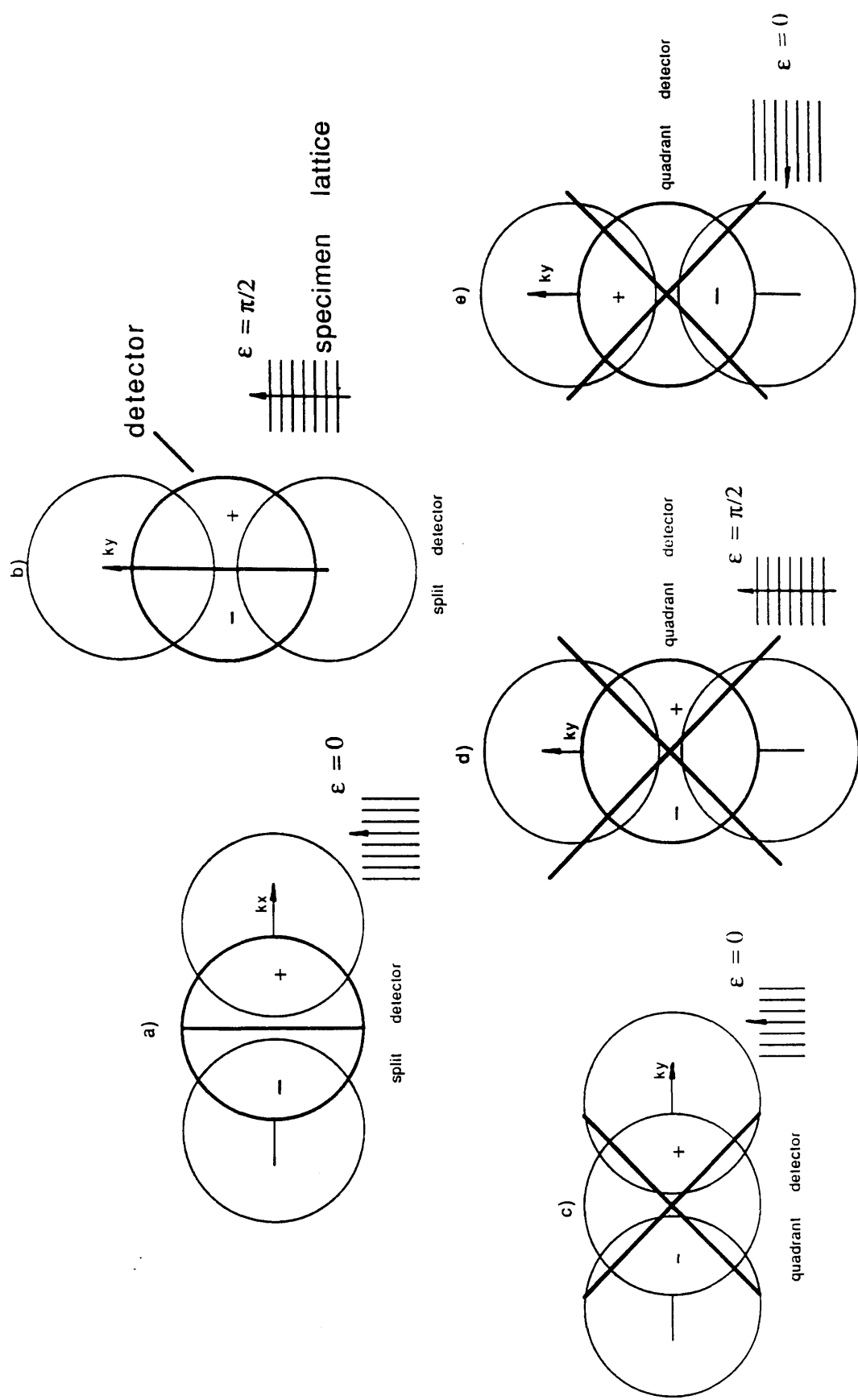


Fig.3.8. Schematic of the orientation in split / quadrant detectors and its effects on the signal detection

aperture of $\alpha_s = 4.16$ mrad suffers least from spherical aberration, and hence the transfer function remains high over a wide region of spatial frequency (or as shown in the figure periodicities in real space). Obviously, a larger aperture with $\alpha_s = 8.32$ mrad is advantageous in the case where a specimen with smaller periodicities is under investigation, but the signal level is lower for values of $\Lambda > 0.8$ nm. Using a larger aperture still, for instance, $\alpha_s = 12.48$ mrad, leads generally to very poor quality images, and would only be viable with a better probe forming lens.

3.5. Calculation of two-dimensional DPC transfer

A split detector has an antisymmetric response function about $k_{xr}=0$, that is

$$\begin{aligned} D(k_{xr}) &= -1, k_{xr} < 0 \\ &= 0, k_{xr} = 0 \\ &= 1, k_{xr} > 0 \end{aligned} \tag{3.17}$$

Similarly, as shown in Fig.(3.8), a quadrant detector also displays an antisymmetric response about $k_{xr} = 0$. The anisotropy of the detector response results in DPC transfer being sensitive to the orientation of the specimen with respect to the detector. The calculation of I_m/I_p as a function of real space periodicity with varied orientations, defined by ϵ (Fig.3.2), from 0 to $\pi/2$ is plotted in Fig.(3.9). The contrast decreases as ϵ increases from zero, and drops to zero when it becomes $\pi/2$. This simply means no

information from an orientation perpendicular to the split of the detector is transferred. In the quadrant detector, however, the situation can be changed when the orientation reaches $\pi/2$. By employing the other pair of quadrants instead of the original two ones (Fig.3.8e) the contrast transfer will be equivalent to that shown in Fig.3.8c.

Further study is concerned with using a computer programme to calculate the two-dimensional differential phase contrast transfer for an aberrated STEM using both split and quadrant detectors.

3.5.1. Computer programme description

The simple geometric calculation of DPC transfer function is satisfactory if the system is assumed to be aberration free (Morrison, 1981), as the phase difference between the zero order beam and the first order beam is always constant over the interference areas. In an attempt to examine it in the conditions corresponding to the practical operation of the VG-HB5 STEM at Glasgow University, a computer programme has been written (see Appendix 3) which allows great flexibility in the detector configuration, and allows the DPC transfer function and signal-to-noise ratio to be explored over the entire spatial frequency domain. It is written in Fortran level 77. Normally the spatial frequency plane is divided into 100×100 elements and it takes less than five minutes to complete the calculation in the IBM-4361-5 mainframe (VM/P system) computer. Use of a greater number of elements provides no more useful information but leads to an increase in the computing time. The

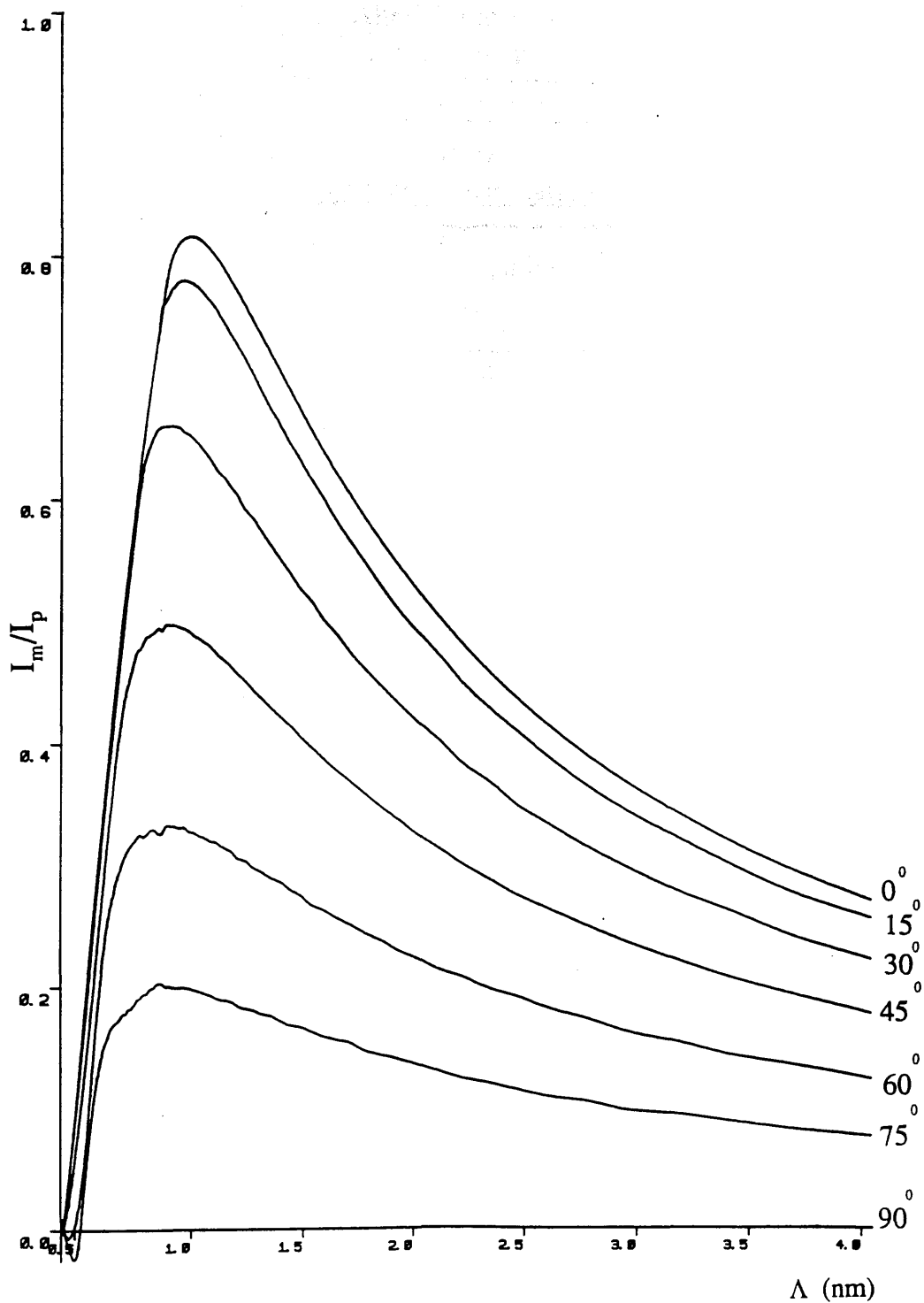


Fig. 3.9. The DPC transfer for different angles ϵ defined in Fig.(3.8) with a split detector, and $C_s = 3.3$ mm, $d_z = -26$ nm, $\alpha_s = 4.16$ mrad

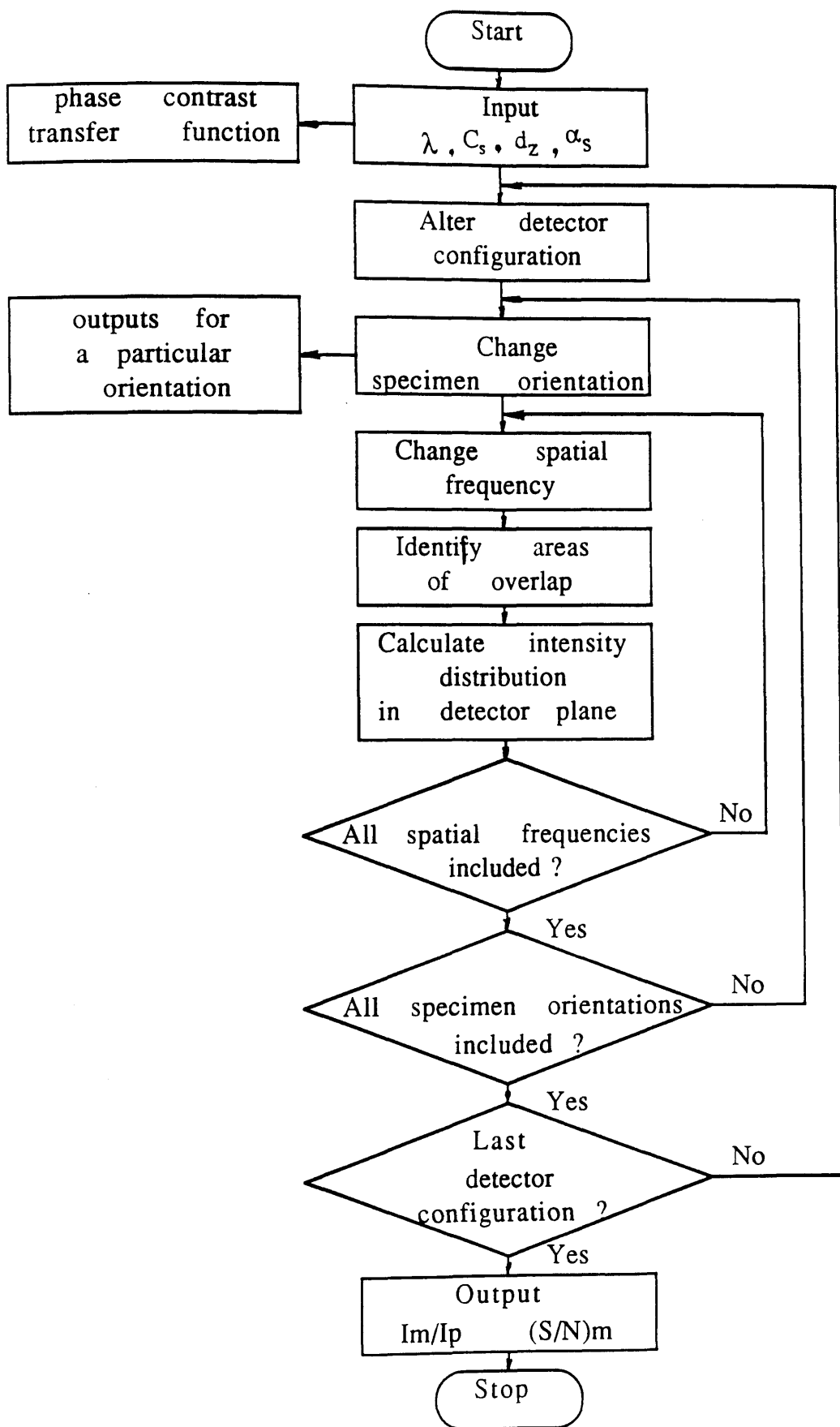


Fig.3.10. Block diagram of the computer programme for DPC transfer calculation

following points about the programme (block diagram shown in Fig.3.10) should be noted.

1. Coherent illumination using 100 kV electrons is assumed.
2. The detector can be assumed to be either a spot detector, in which case the subroutine PCTF is used, or a detector with an antisymmetric response function.
3. In the latter case either split or quadrant detectors can be chosen. In addition the annular split and quadrant detectors, which are the subject of Chapter 4, can also be simulated.
4. The orientation of the specimen with respect to the detector can be given any angle between 0 and $\pi/2$.
5. The transfer function I_m/I_p was defined in section 3.4, and the signal-to-noise ratio in the calculation is defined as I_m/I_p divided by the detector area. they are calculated over the spatial frequency range $0 \leq k_{xr} \leq 2$, and $0 \leq k_{yr} \leq 2$, corresponding to the region where there is complete overlap to separation of the interfering beams.
6. The results are displayed in the form of three dimensional and contours plots to aid visualisation.

3.5.2. Results and conclusion

We have plotted out some results from the two-dimensional DPC transfer calculation in Fig.(3.10 ~ 3.17). Here four values of Δf are taken in conjunction with appropriately chosen defocus values. An objective lens of $C_s = 3.3$ mm, and radiation with wave length $\lambda = 3.7$ pm are used. In both the three-dimensional and contour plots, only the transfer function for $k_{xr} > 0$ is shown; that for $k_{xr} < 0$ can be generated by recalling that the detector response function is antisymmetric. From the calculations we note

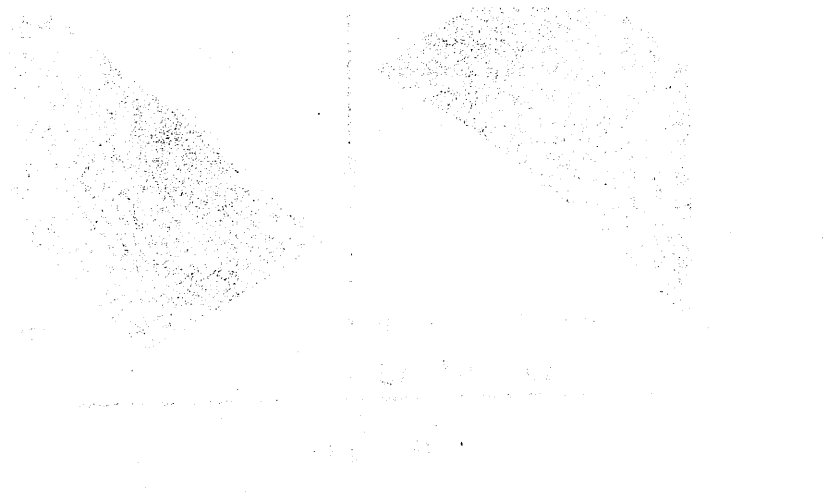
-The DPC transfer and the signal-to-noise ratio achieve their optimum values close to $k_{yr} = 0$. This corresponds to the situations shown in Fig.3.8a for the split detector and Fig.3.8c for the quadrant detector.

- The DPC transfer function is less sensitive to defocus for small values of α_s .

- The optimum transfer is obtained using a defocus which satisfies

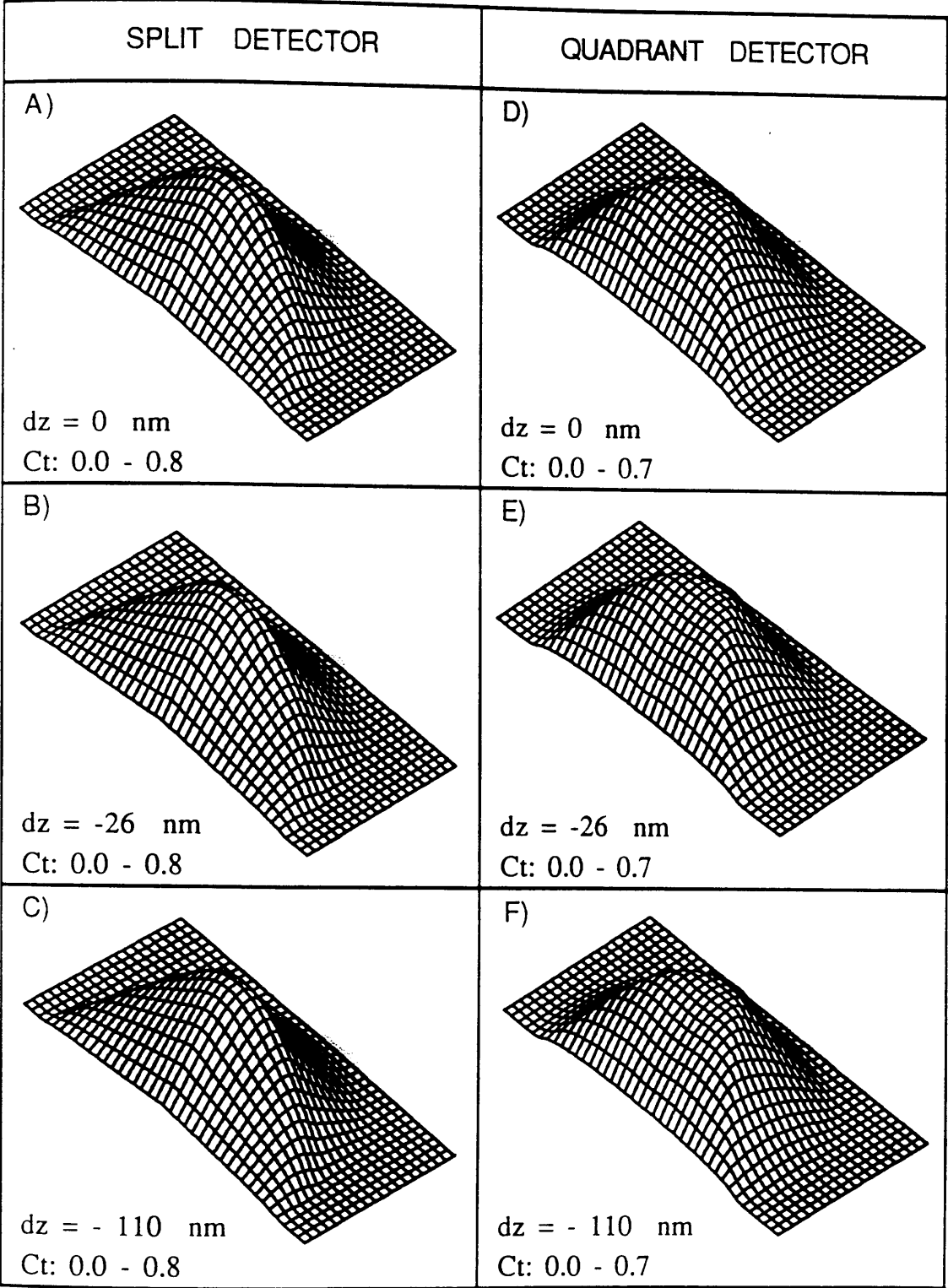
$$d_z = (\alpha_{opt} / \alpha_s)^2 d_{zs} \quad (3.20)$$

in which d_{zs} is the Scherzer defocus for the optimum aperture size, α_{opt} , which is 8.32 mrad for $C_s = 3.3$ mm. Thus the optimum transfer is approached with $d_z = -26$ nm for $\alpha_s = 4.16$ mrad, and $d_z = -234$ nm for $\alpha_s = 12.48$ mrad.



$$\alpha_s = 4.16 \text{ mrad}$$

$$Ct = I_m/I_p$$

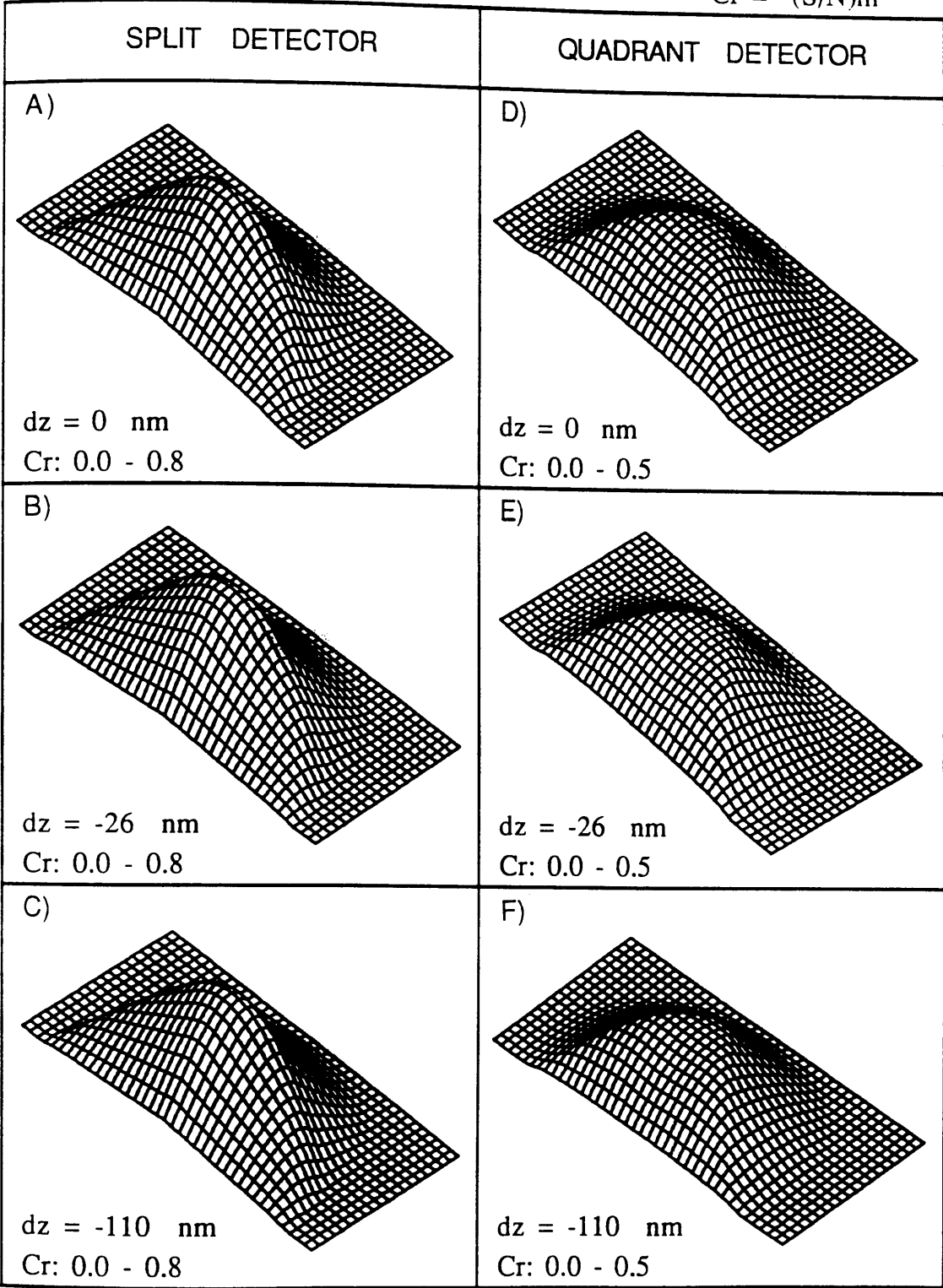


$\begin{matrix} & Ct & \\ k_y r & \downarrow & k_x r \end{matrix}$

Fig. 3.11. Three-dimensional plots of DPC transfer function

$$\alpha_s = 4.16 \text{ mrad}$$

$$Cr = (S/N)m$$

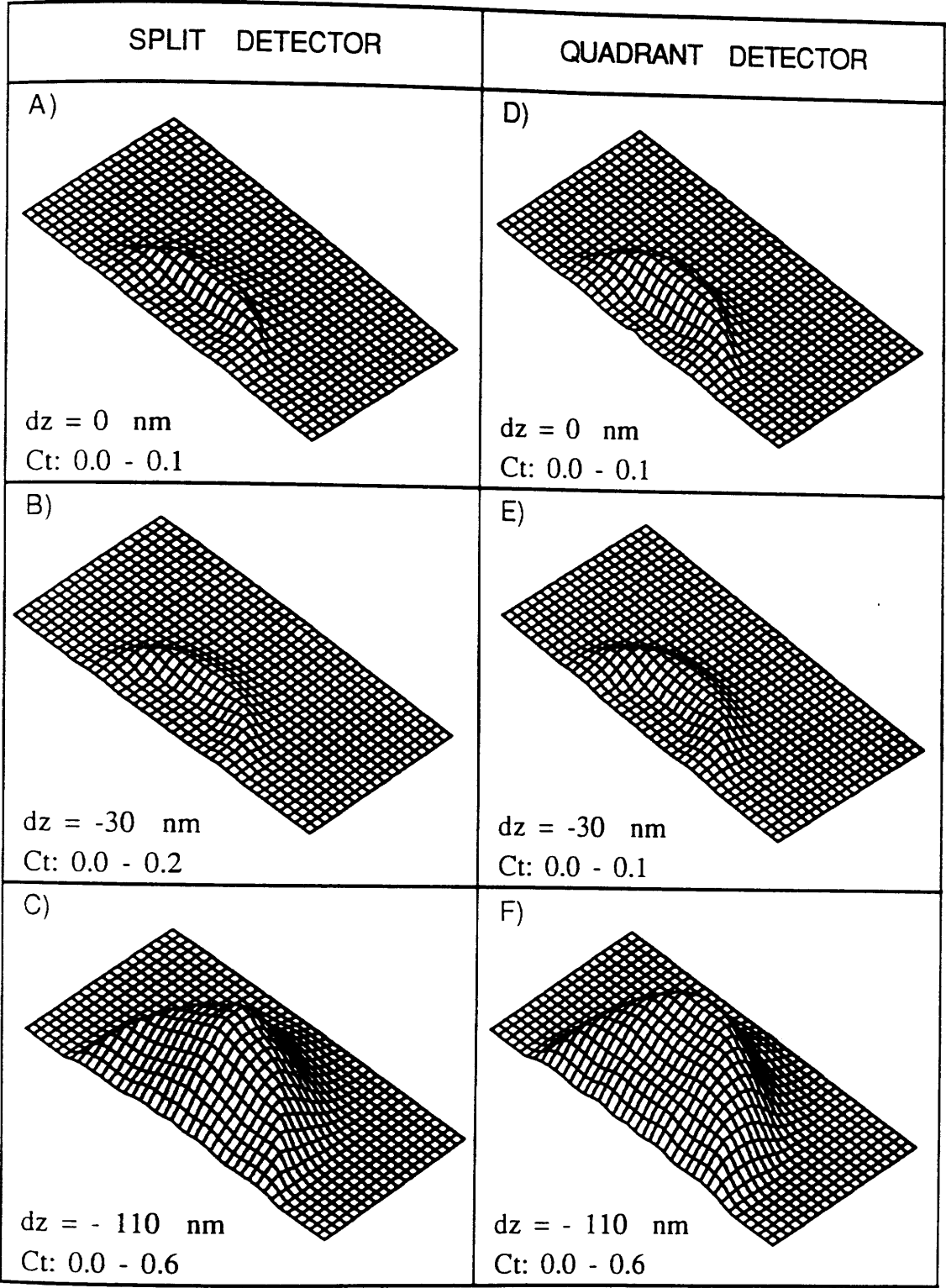


Cr
 \downarrow
 $k_y r \quad k_x r$

Fig. 3.12. Three-dimensional plots of signal-to-noise ratio in DPC transfer

$$\alpha_s = 8.32 \text{ mrad}$$

$$C_t = I_m/I_p$$



$\begin{matrix} & C_t \\ k_y r & \downarrow & k_x r \end{matrix}$

Fig. 3.13. Three-dimensional plots of DPC transfer function

$$\alpha_s = 8.32 \text{ mrad}$$

$$Cr = (S/N)_m$$

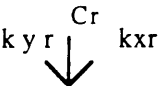
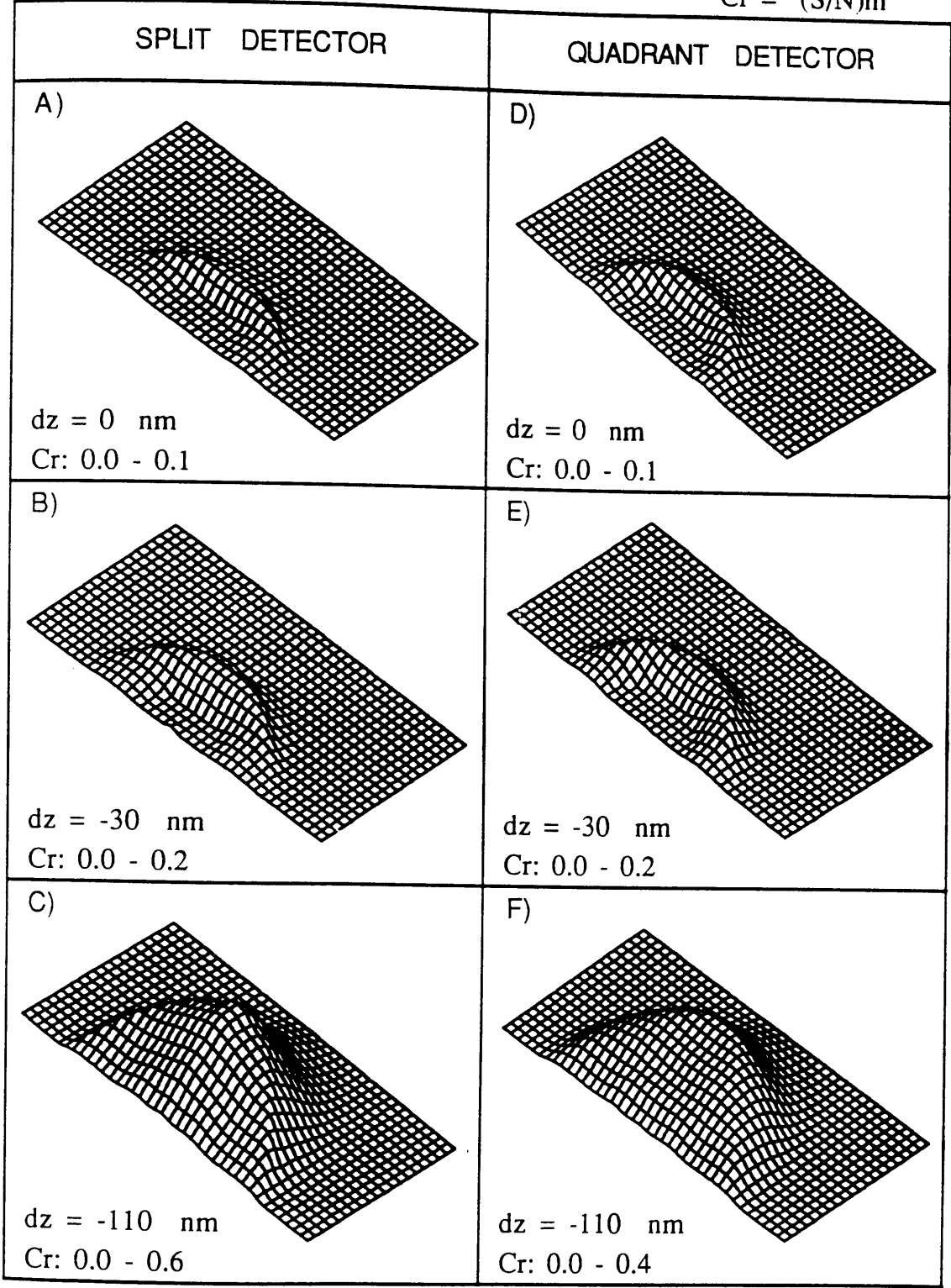


Fig. 3.14. Three-dimensional plots of signal-to-noise ratio in DPC transfer

$$\alpha_s = 12.48 \text{ mrad}$$

$$Ct = \text{Im}/I_p$$

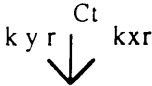
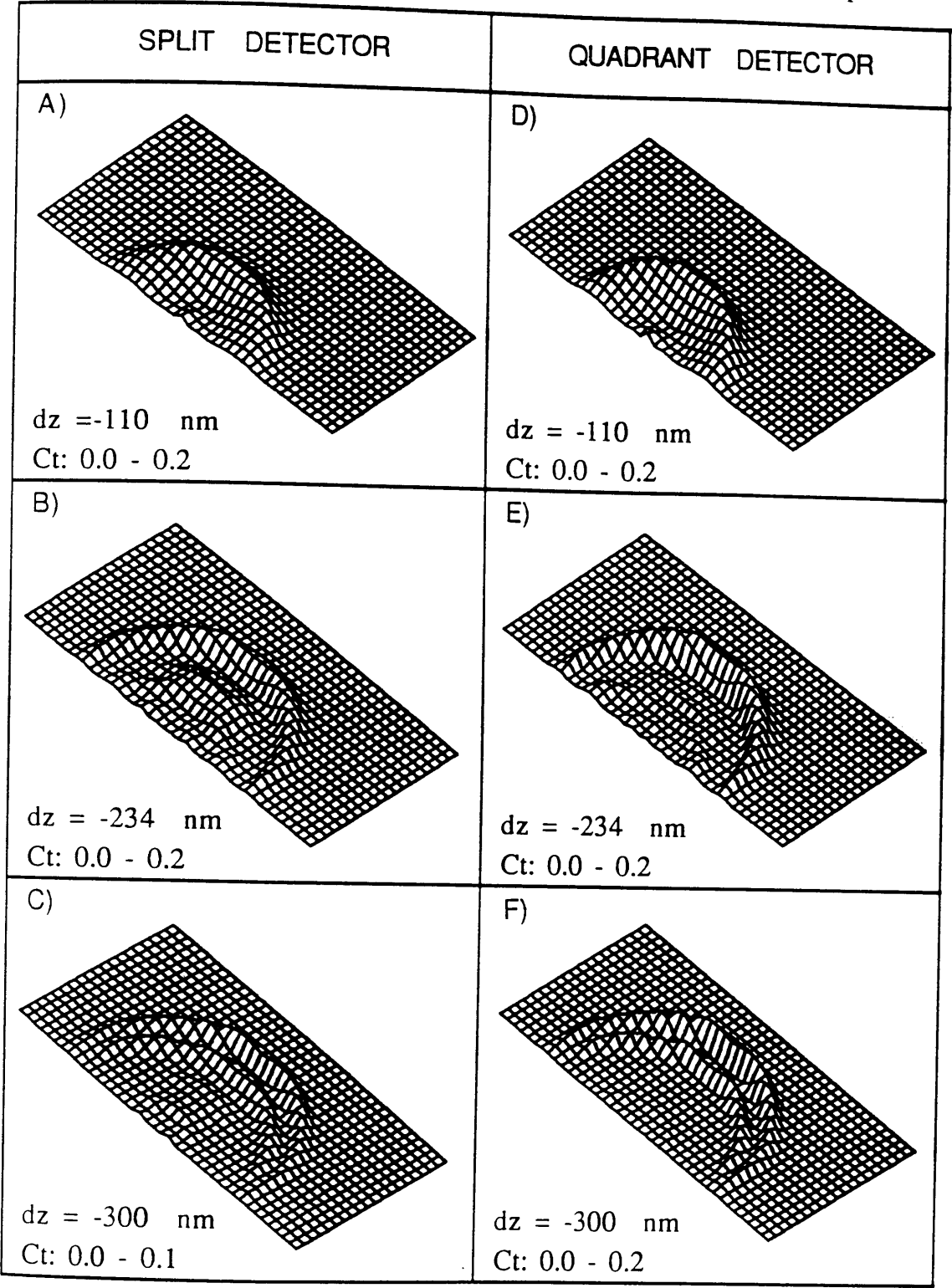
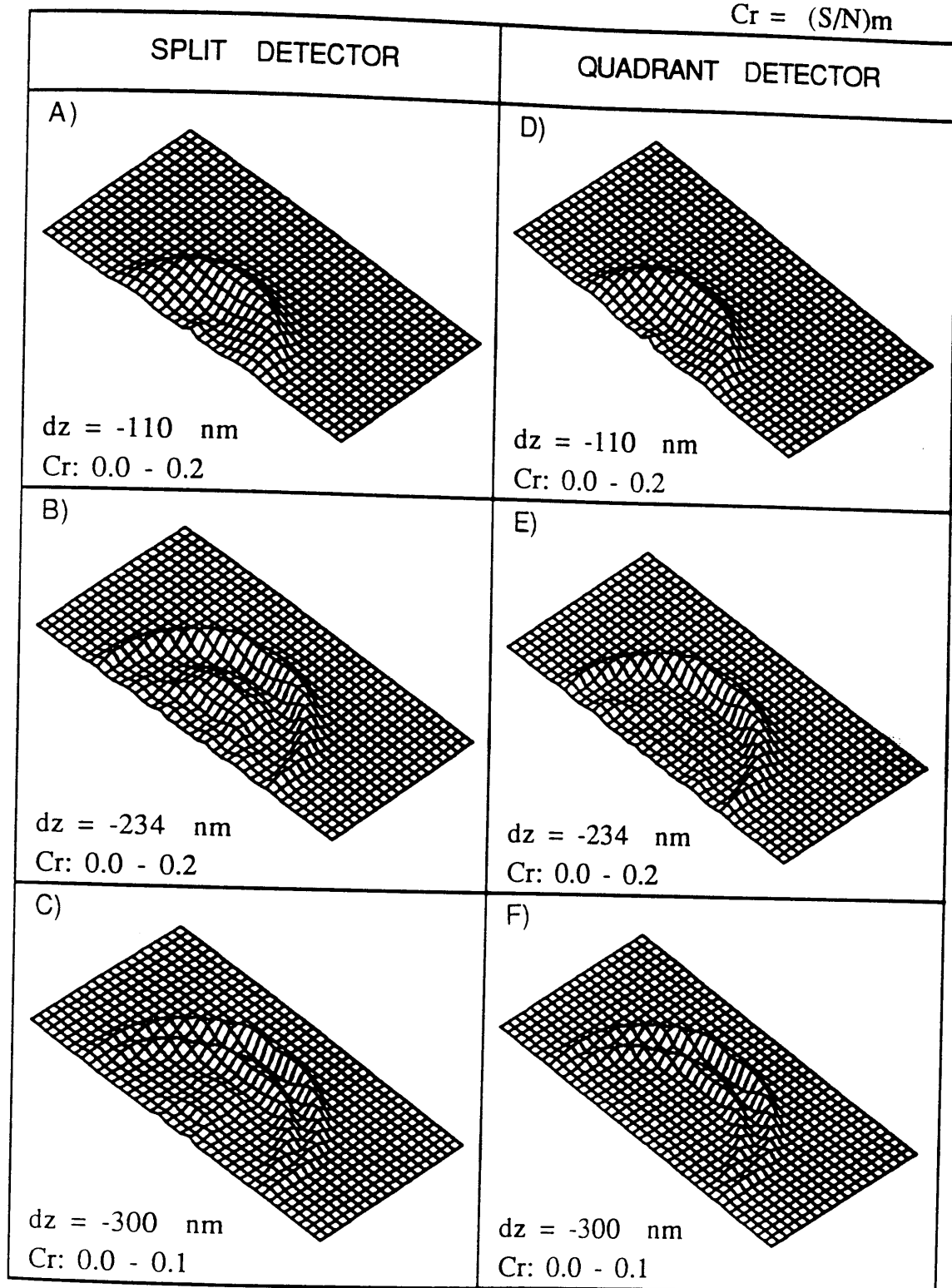


Fig. 3.15. Three-dimensional plots of DPC transfer function

$$\alpha_s = 12.48 \text{ mrad}$$

$$Cr = (S/N)m$$

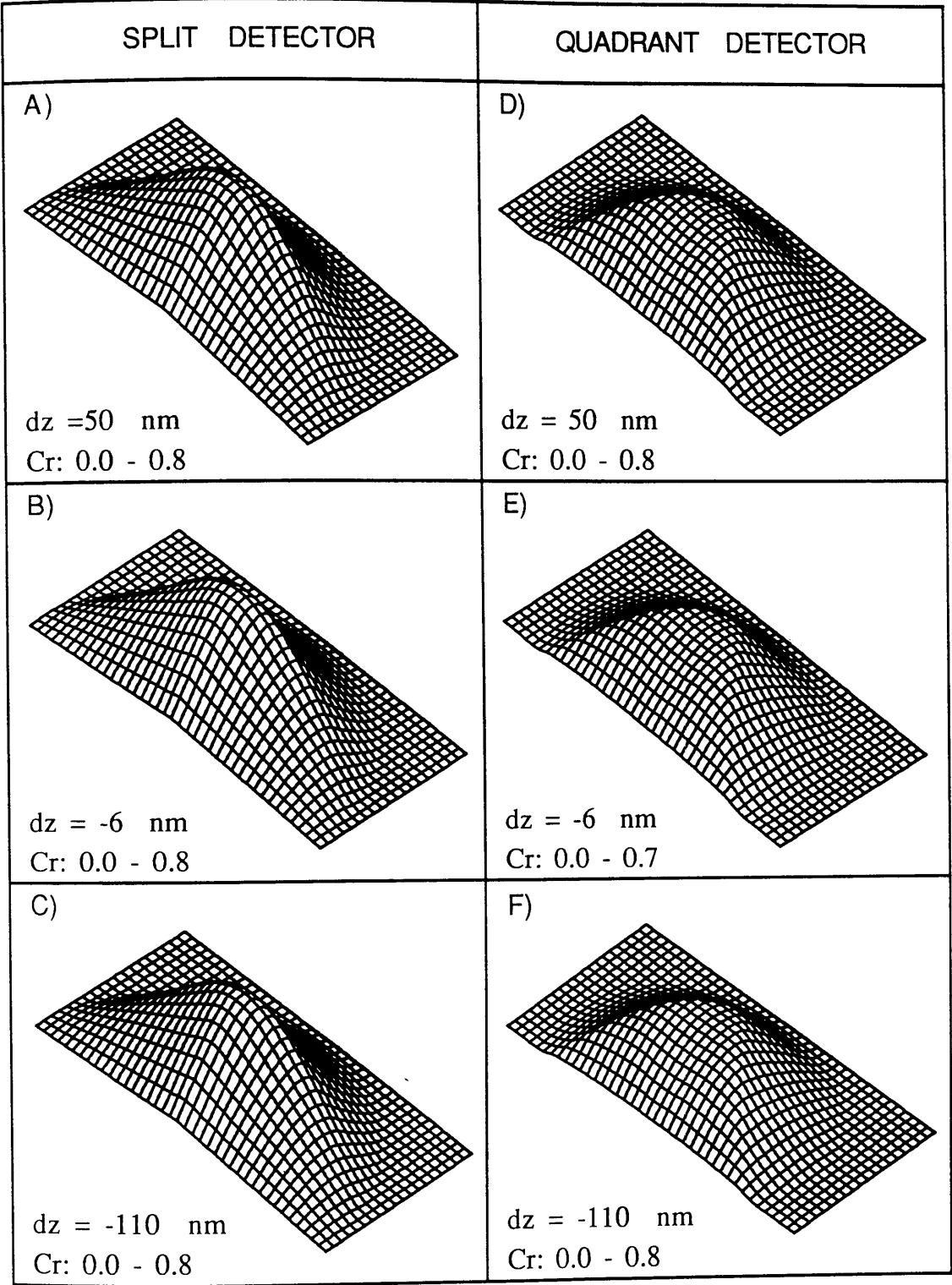


Cr
 \downarrow
 $k_y r \quad k_x r$

Fig. 3.16. Three-dimensional plots of signal-to-noise ratio in DPC transfer

$$\alpha_s = 2.08 \text{ mrad}$$

$$Cr = (S/N)_m$$



Cr
 \downarrow
 $k_y r \quad k_x r$

Fig. 3.18. Three-dimensional plots of signal-to-noise ratio in DPC transfer

Chapter 4

Optimization of detector configuration

4.1. Introduction

Beside the split detector and quadrant detector which we have discussed in Chapter 3, various other detector configurations can be used in the STEM. A possibility suggested by Rose (1973) is one which consists of a central disc and two annuli all within the bright-field cone. It produces an image with a higher signal-to-noise ratio than a single spot detector. Further, it offers good contrast over a wide region of spatial frequency (Burge et.al.,1980). More recent developments of detector configurations for phase contrast imaging in STEM have employed detector arrays, e.g. one consisting of 32 annuli and 128 channels (Haider et.al.,1988).

In this Chapter, we attempt to combine the advantages from the simple annular detector with those from the normal split / quadrant detectors. With attention particularly concentrating in improving the signal-to-noise ratio, the two-dimensional DPC transfer function is calculated again for two modified detector configurations : the annular split (AS) detector and the annular quadrant (AQ) detector. The same computer programme described in Chapter 3 is used here. It allows the configurations of AS and AQ detectors to be carefully chosen and optimized under specified experimental conditions.

4.2. Modified DPC transfer function and signal-to-noise ratio

It has been shown in Fig.(3.1) that at high spatial frequency the regions of overlap between the straight through and diffracted beams occur over small parts of the detector surface distant from the detector centre. On the other hand, when the spatial frequency is low there is overlap between both diffracted beams themselves leading to cancellation of the information carrying signals in these regions (Fig.3.3). In both cases the implication is that the part of the detector near the centre is redundant for collecting useful signals but nonetheless contributes to the total noise.

An annular quadrant detector has a geometry shown in Fig.(4.1), in which α_H is the semiangle subtended by the circular hollow zone in the detector centre. The transfer function for this modified differential phase contrast imaging mode is once again proportional to I_m/I_p and can be calculated as in section 3.4. However, it should be noted that as different values of α_H are considered here so the effective overlap areas, e.g. Q_{+1} and Q_{-1} in Fig.(3.3), which contribute to I_m vary.

We are particularly interested in the signal-to-noise ratio in the modified DPC imaging mode. It is known that the electron noise is proportional to the square root of the total current detected, so that if an annular split detector is considered, the noise for an annular split detector can be expressed by

$$N = (I_d \tau / e)^{1/2} \quad (4.1)$$

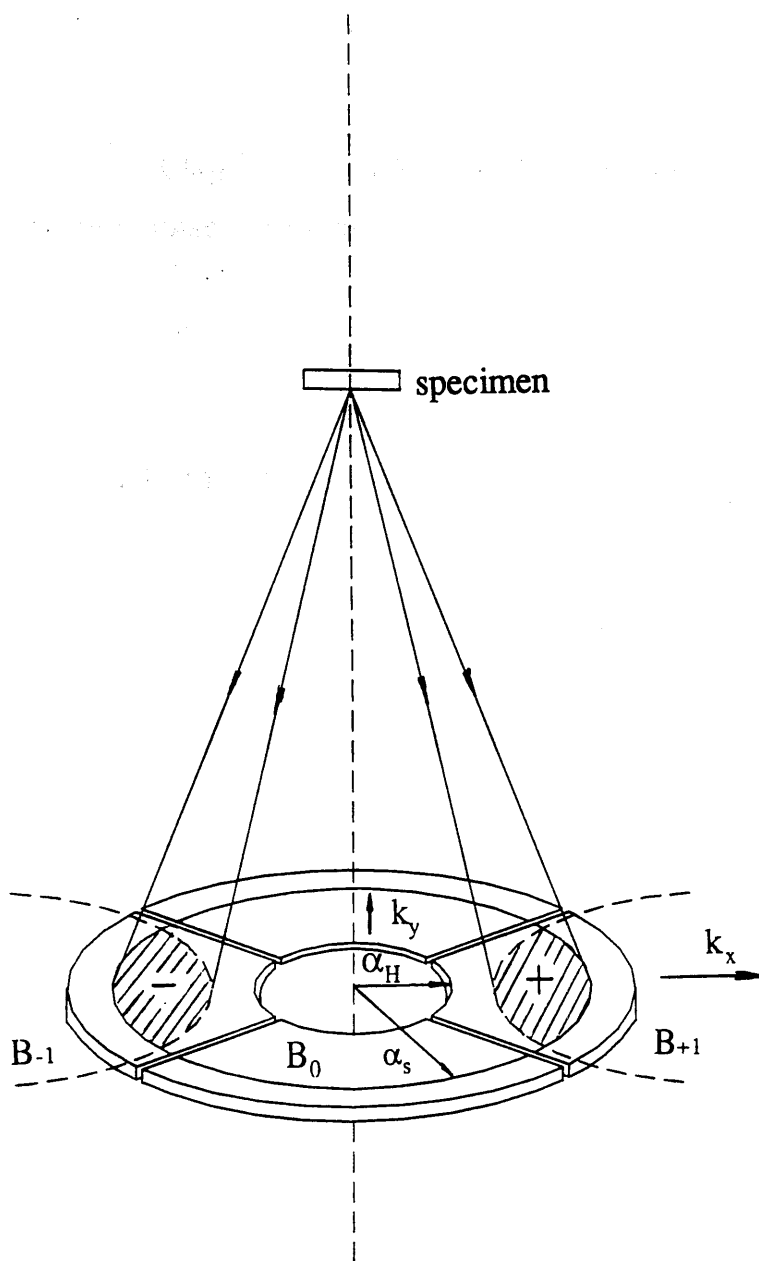


Fig.4.1. Schematic diagram of an annular quadrant detector and the effects of the convergent beams

Here I_d is the total current collected by the annular detector, which can be further expressed as

$$I_d = I_p (1 - \alpha_H^2 / \alpha_s^2) \quad (4.2)$$

If we define $R_d^2 = (\alpha_H / \alpha_s)^2$ and combine Eqn.(4.1) and Eqn.(4.2) together the noise becomes

$$N = [I_p \tau (1 - R_d^2) / e]^{1/2} \quad (4.3)$$

We have expressed the maximum signals collected by the detector for an aberration-free STEM imaging system in Eqn.(3.8) and it can also be further expressed for an aberrated imaging system as

$$S_{\max} = [2\phi_0 \tau I_p / (\pi e)] \int_{D_a'} \cos \Delta w \, dk_{xr} dk_{yr} \quad (4.4)$$

where D_a' is the detected overlap area, i.e. the overlap area when allowance is made for the fact that $\alpha_H \neq 0$.

Thus the signal-to-noise ratio when using an split annular detector becomes

$$(S/N)_m = (2\phi_0 / \pi) (I_p \tau / e)^{1/2} (1 - R_d^2)^{-1/2} \int_{D_a'} \cos \Delta w \, dk_{xr} dk_{yr} \quad (4.5)$$

In Eqn.(4.3) it is clear that by removing the central part from the normal split detector the noise is decreased (for an annular detector, $0 < R_d < 1$). This means that although less signals carrying useful information are detected as R_d increases, the signal-to-noise ratio will not necessarily monotonically decrease. In other words,

as is shown in Eqn.(4.5), beside the phase shift, $w(k_r)$, the signal-to-noise ratio is strongly influenced by R_d .

Similarly, with an AQ detector which has half the area of an AS detector , we write the total current collected by the detector as

$$I_d = \frac{1}{2} I_p (1 - R_d^2) \quad (4.6)$$

The noise in this case then is

$$N = [I_p \tau (1 - R_d^2) / (2e)]^{1/2} \quad (4.7)$$

Thus we get the signal-to-noise ratio when using an annular quadrant detector as

$$(S/N)_m = 1.41 (2\phi_0/\pi) (I_p \tau/e)^{1/2} (1 - R_d^2)^{-1/2} \int_{\Omega} \cos \Delta w \, dk_{xr} dk_{yr} \quad (4.8)$$

4.3. Computed results and discussion

In the modified DPC imaging mode I_m/I_p and $(S/N)_m$ depend not only on the objective aperture size, the lens aberration and the defocus, but also on the value R_d . Some results of calculations are presented in Fig.(4.2-4.8); they are plotted out with either I_m/I_p or $(S/N)_m$ against the real space periodicity Λ , and ^{are} all concerned with the case of $\varepsilon = 0$, except in Fig.(4.8), and a fixed value for C_s of 3.3 mm. The optimum values of defocus, which have been discussed in Chapter 3, were chosen for each relevant objective aperture size.

For each set of instrumental parameters five different detector geometries are considered in the calculations, forming a family of curves in each figure. In addition, three-dimensional plots and the corresponding contours of typical results are shown in Appendix 2.

The results show a general feature that when $R_d = 0.2$ both I_m/I_p and $(S/N)_m$ are very close to those obtained from a normal detector geometry ($R_d = 0$). This means that as would be expected, removing a small portion of the central disc from a normal detector has little effect on the DPC transfer. An increase in R_d means that the diameter of the inner annulus of the detector is enlarged and the active area of the detector is reduced. Although less of the information carrying signal is detected in this case the noise is significantly diminished. This is the reason why the signal-to-noise ratio does not decrease rapidly with increasing R_d . Indeed, it is apparent that very significant gains in signal-to-noise ratio are obtained when studying slowly varying phase objects.

With $R_d = 0$, the standard configuration, there is normally a marked peak in the DPC transfer function. An AS detector, however, can provide a comparatively stable transfer function and signal-to-noise ratio over a wide band of periodicity. This becomes more significant when R_d is in the range of 0.6 - 0.8 (Fig.4.2). The effect is even more pronounced in the case of the AQ detector where essentially flat DPC transfer bands and flat signal-to-noise ratio bands appear if $\alpha_s = 4.16$ mrad (Fig.4.3). We should note that the extremities of the flat band regions are not exactly the same in the two cases. Furthermore it is again apparent that these bands are broadened as R_d increases. Figures 4.4 and 4.5 show that a similar form of results is obtained when α_s is increased to 8.32 mrad. Significant

differences are that peak transfer occurs at smaller periodicities and that, whilst $(S/N)_m$ remains approximately constant over a wide range of spatial frequency, the increased effect of spherical aberration leads to a significant departure from flatness.

The calculations for a big objective aperture size, $\alpha_s = 12.48$ mrad, are shown in Fig.(4.6 - 4.7). With the chosen defocus a sharp peak appears at $\Lambda \sim 0.3$ nm for a given AQ detector, whilst more peaks appear around $\Lambda \sim 0.2 - 0.5$ nm for an AS detector, although both transfer and signal-to-noise ratio are very poor. Clearly, once again, imaging with an aperture of this size should only be performed with a lens with a smaller spherical aberration coefficient.

We know from Chapter 3 that the information obtained using a normal quadrant detector with an one dimensional specimen with an orientation of $\varepsilon = \pi/4 + \varepsilon'$ ($0 \leq \varepsilon' \leq \pi/4$) are equivalent to those with an orientation of $\varepsilon = \pi/4 - \varepsilon'$. It should be noted that when using such a detector in practice, images from the two pairs of opposite quadrants can be used simultaneously. (Fig.3.8d,e). Thus the extreme case of interest is when a specimen has an orientation of $\varepsilon = \pi/4$ (Fig.4.8) instead of $\varepsilon = \pi/2$. With $\varepsilon = \pi/4$ both the DPC transfer function and signal-to-noise ratio assume their minimum values, there being a monotonic decrease from $\varepsilon = 0$ to $\varepsilon = \pi/4$; this is a disadvantage of the DPC imaging mode.

This remains true in the annular detector cases. On the other hand, comparing the results in Fig.(4.3) with those in Fig.(4.8), we note that both I_m/I_p and $(S/N)_m$ are reduced less rapidly with an AQ detector than a normal quadrant detector as the orientation varies from $\varepsilon = 0$ to $\varepsilon = \pi/4$. Particularly, when assuming an AQ detector with a high value of $R_d \approx 0.8$, the curves are very similar

for both orientations in the range of $\Lambda > 1.2$ nm. This means that the DPC transfer function and signal-to-noise ratio are less dependent on the specimen orientation in this case. For instance, at $\Lambda = 1.5$ nm variation of the orientation from $\varepsilon = 0$ to $\varepsilon = \pi/4$ causes both I_m/I_p and $(S/N)_m$ to be reduced by a factor of $\sim 18\%$ with a normal quadrant, but only $\sim 10\%$ using an AQ detector with $R_d = 0.8$.

4.4. Summary and conclusion

- The use of a segmented annular detector leads to high efficiency DPC imaging modes and has attractive features which cannot be realized when $R_d = 0$.
- When $R_d = 0.2$ the I_m/I_p value using an AS detector is very close to that with a normal split detector, whilst the maximum $(S/N)_m$ is slightly higher.
- A near-constant DPC transfer function and signal-to-noise ratio can be obtained at higher R_d values; the stability is more significant in the case where AQ detectors are employed.
- When using a quadrant detector, both I_m/I_p and $(S/N)_m$ are reduced monotonically as the specimen orientation varies from $\varepsilon = 0$ to $\varepsilon = \pi/4$ and the minimum values are obtained with $\varepsilon = \pi/4$; normally the reduction is less using an AQ detector than with a normal quadrant detector.

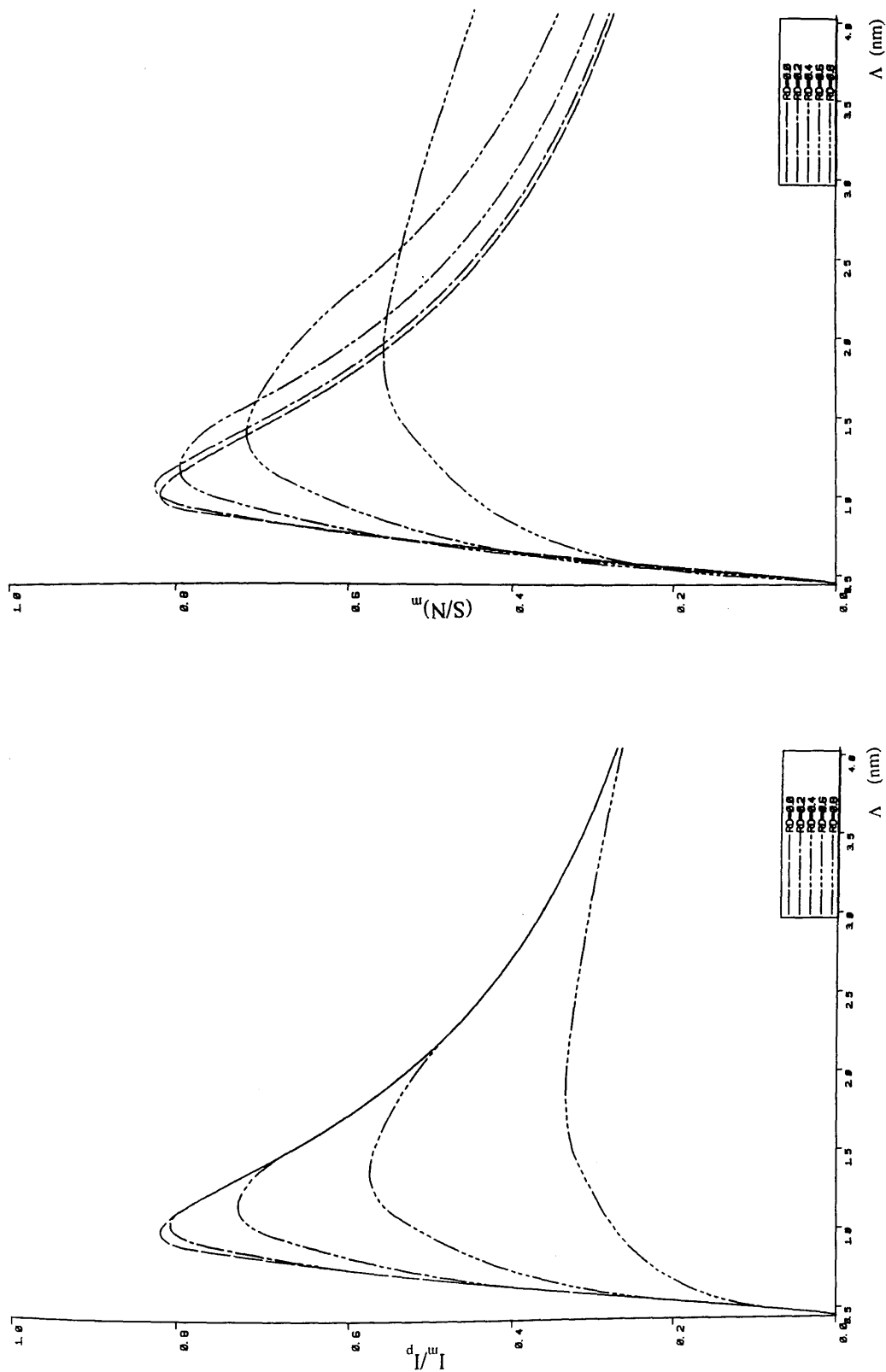


Fig.4.2. Calculated DPC transfer and signal-to-noise ratio with different detector configurations. (AS detectors, $\alpha_s = 4.16$ mrad, $d_z = -26$ nm)

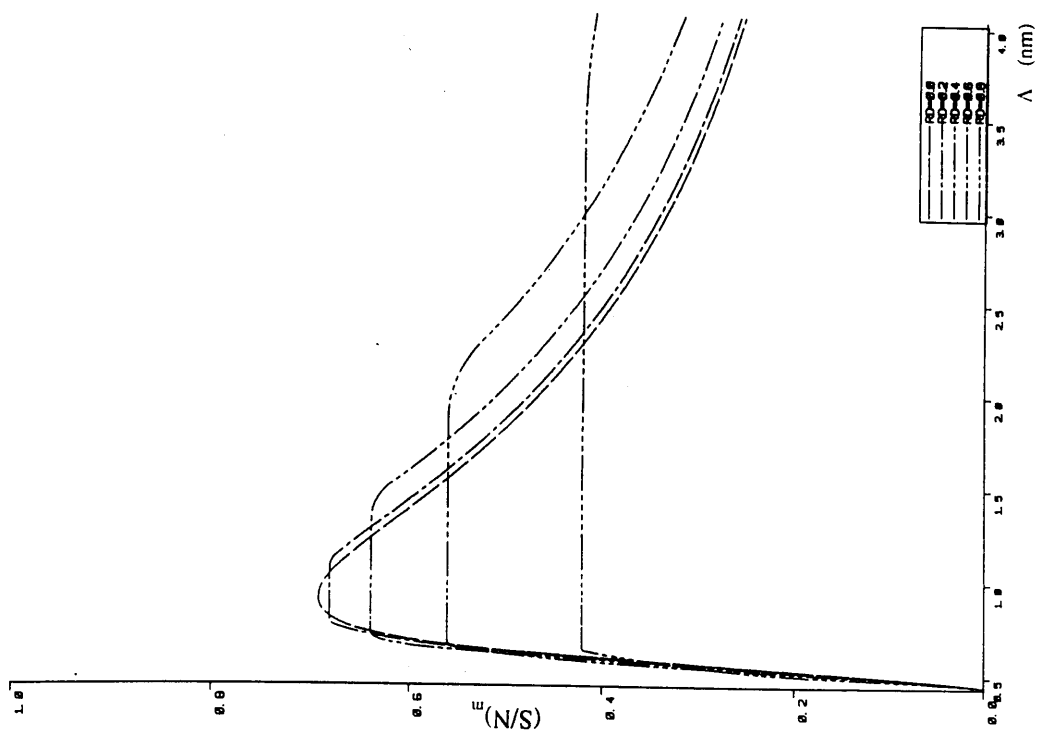
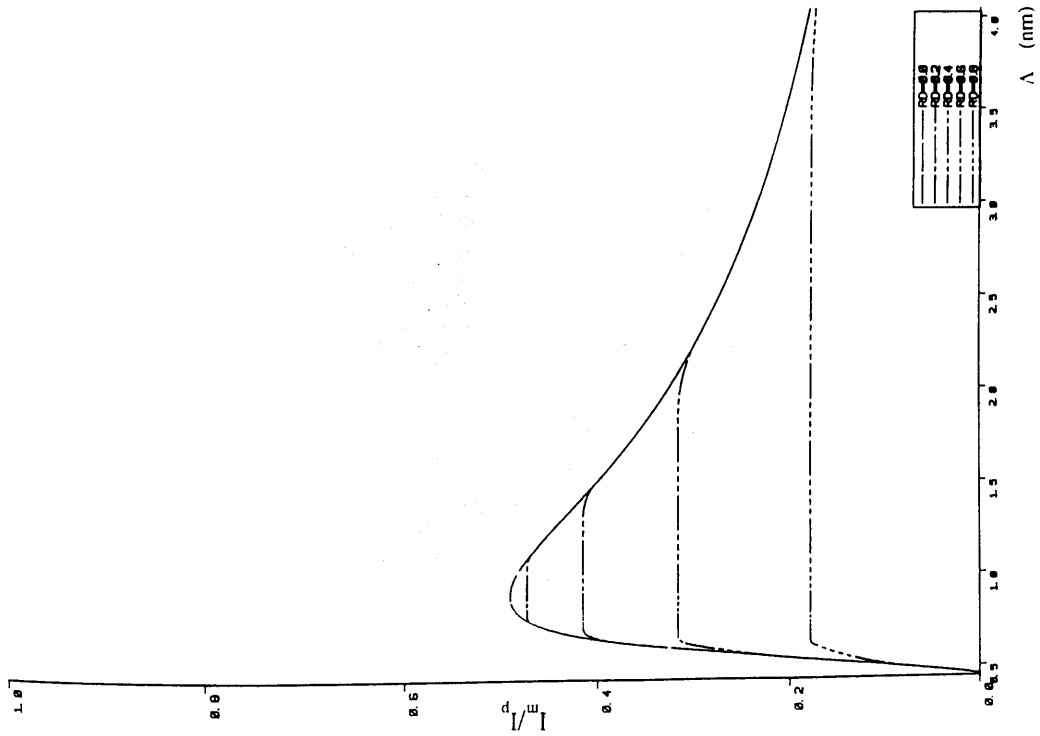


Fig.4.3. Calculated DPC transfer and signal-to-noise ratio with different detector configurations. (AQ detectors, $\alpha_s = 4.16$ mrad, $d_z = -26$ nm)

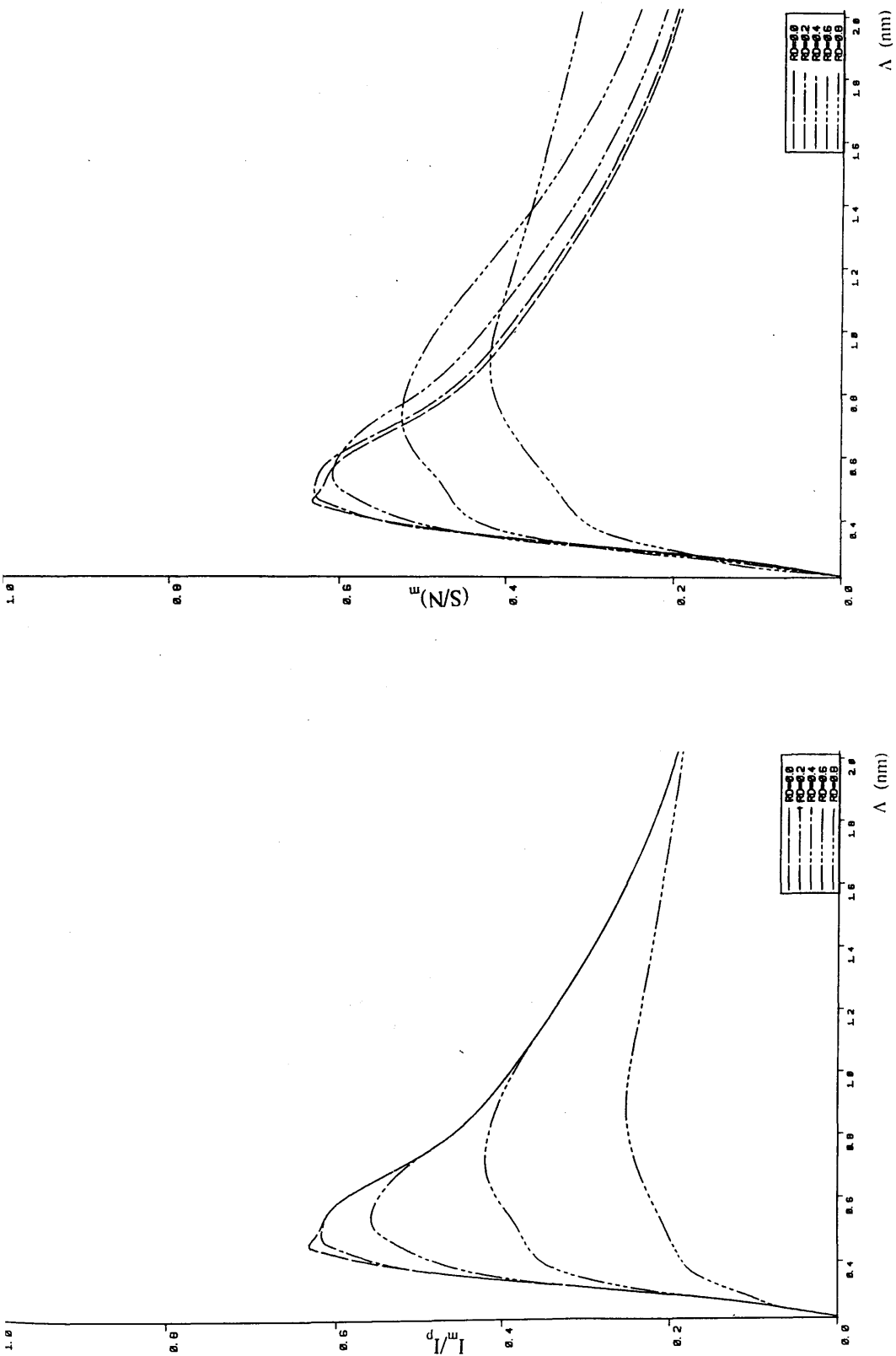


Fig 4.4. Calculated DPC transfer and signal-to-noise ratio with different detector configurations. (AS detectors, $\alpha_s = 8.32$ mrad, $d_z = -110$ nm)

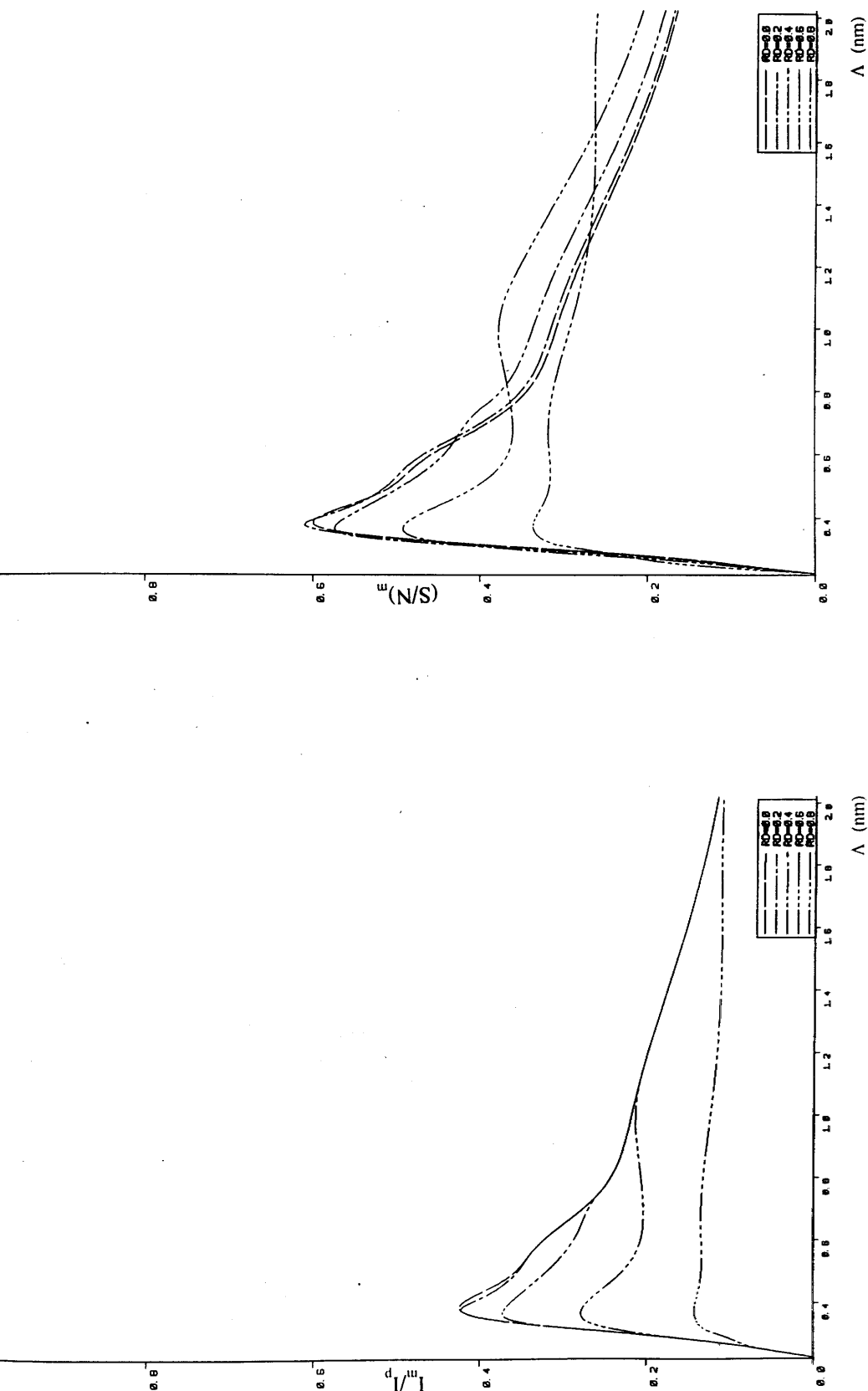


Fig.4.5. Calculated DPC transfer and signal-to-noise ratio with different detector configurations. (AQ detectors, $\alpha_s = 8.32$ mrad, $d_z = -110$ nm)

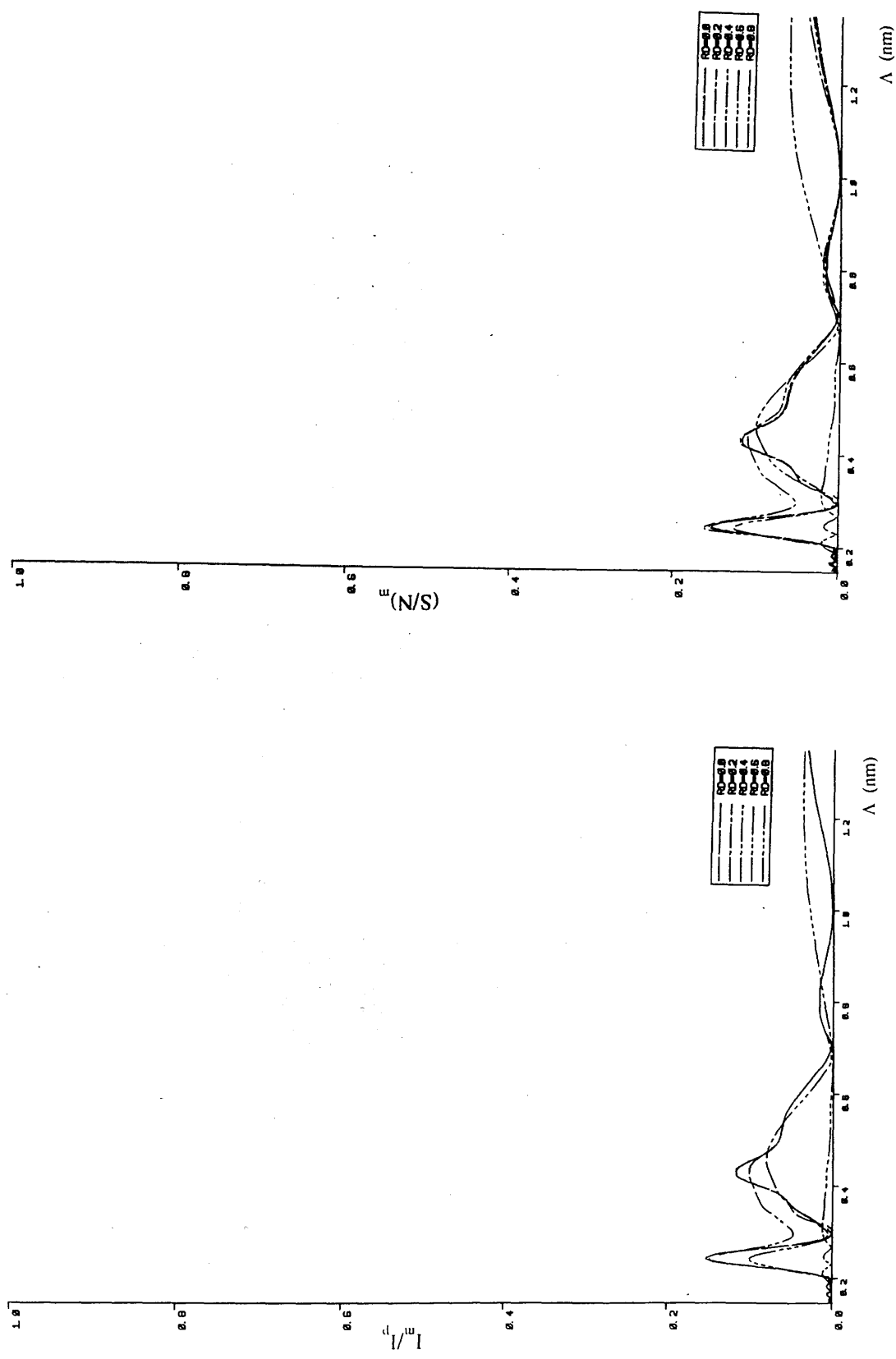


Fig.4.6. Calculated DPC transfer and signal-to-noise ratio with different detector configurations. (AS detectors, $\alpha_s = 12.48$ mrad, $d_z = -230$ nm)

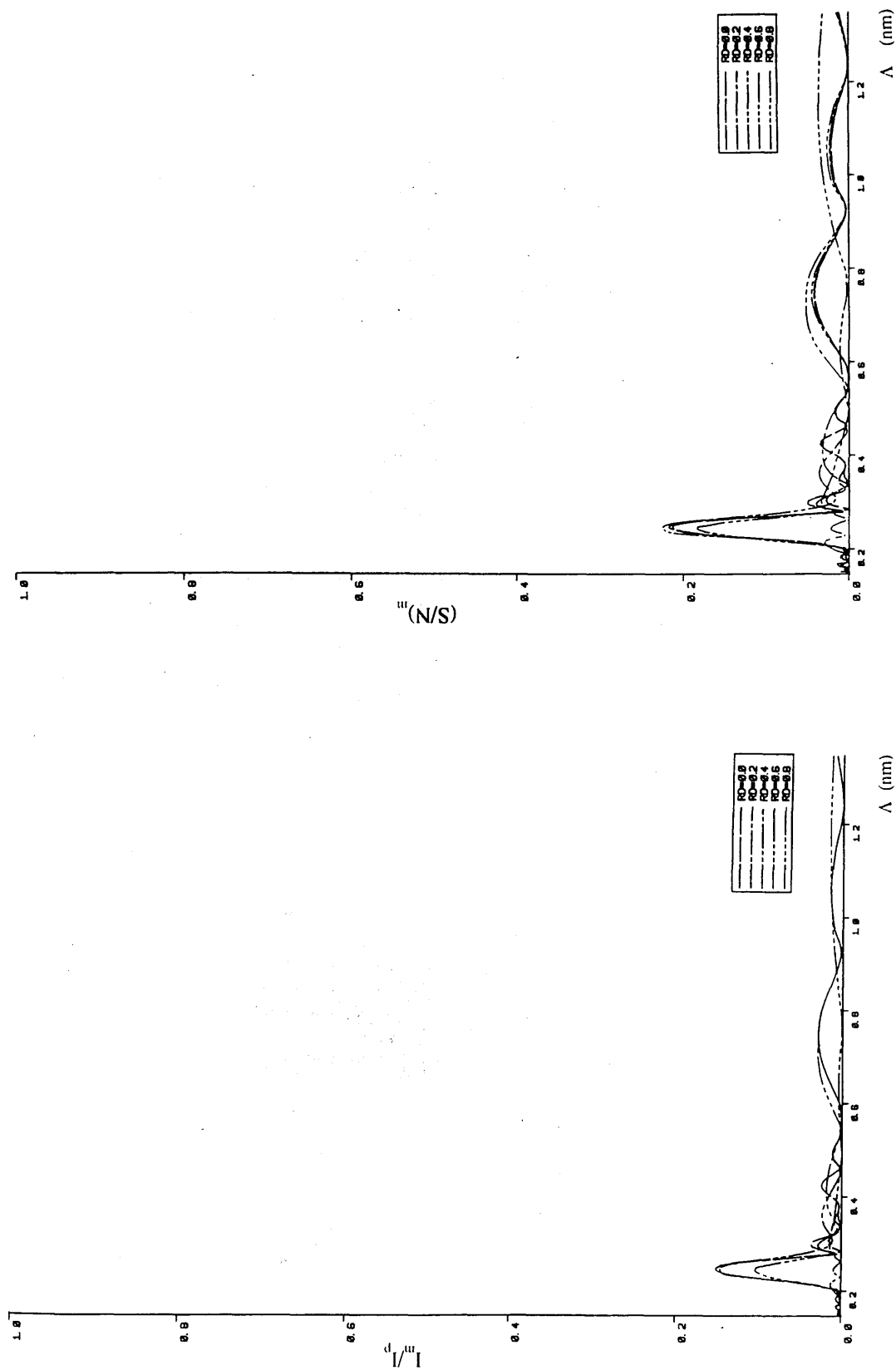


Fig.4.7. Calculated DPC transfer and signal-to-noise ratio with different detector configurations. (AQ detectors, $\alpha_s = 12.48$ mrad, $d_z = -230$ nm)

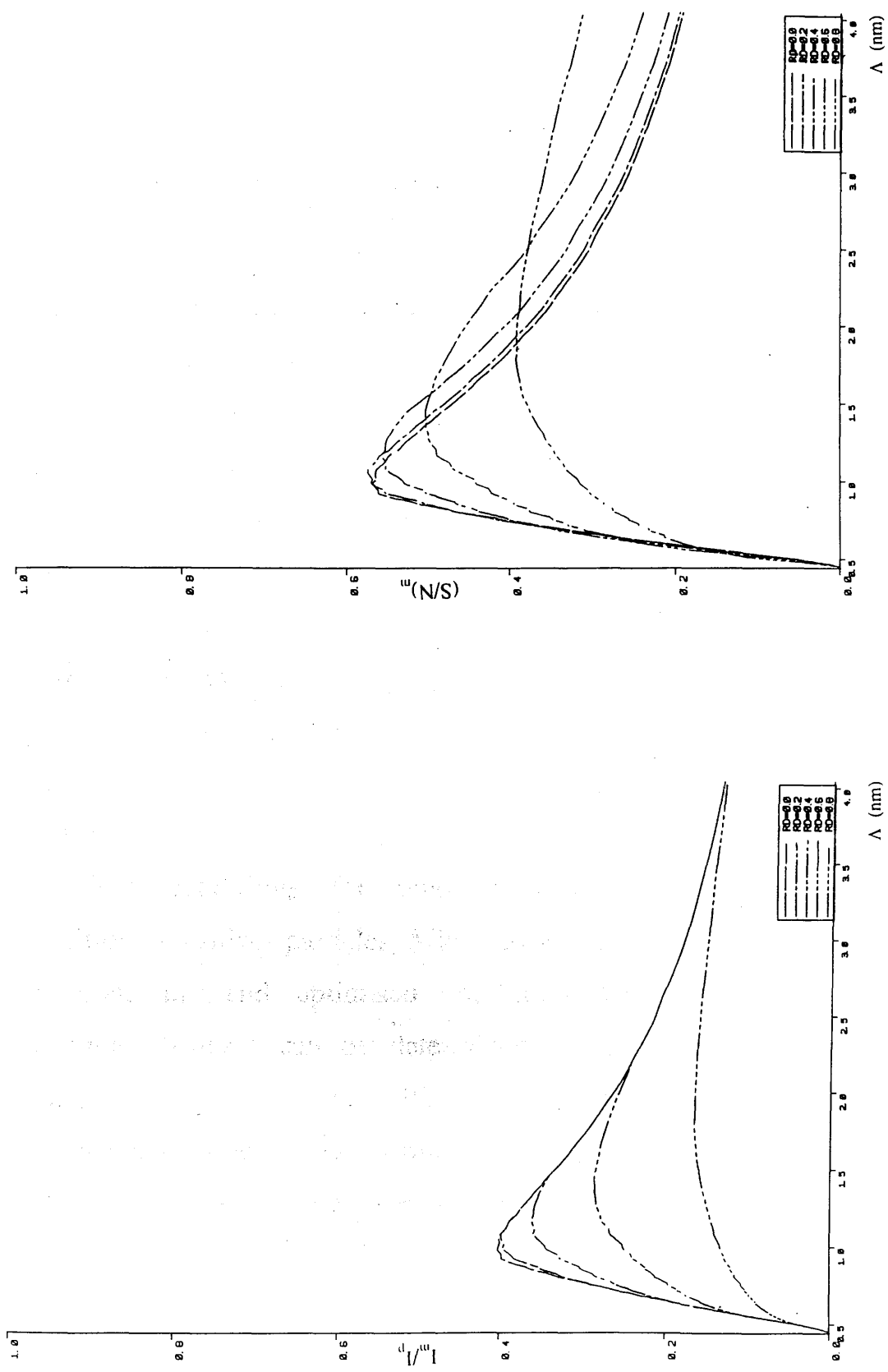


Fig.4.8. Calculated DPC transfer and signal-to-noise ratio in the orientation of $\epsilon = \pi/4$, with different detector configurations. (AQ detectors, $\alpha_s = 4.16$ mrad, $d_z = -26$ nm)

Chapter 5

Simulation of DPC and Modified DPC Images

5.1. Introduction

Radiation damage to beam sensitive particles is obviously a major obstacle when trying to image them. Many techniques have been developed to reduce the effect of radiation damage; these were outlined in Chapter 2. Among these techniques, those based on increasing the efficiency of electron utilization are of concern here. In the preceding chapters differential phase contrast imaging modes were introduced, and the detector configurations varied in a search for modes with a high signal-to-noise ratio and a suitable phase contrast transfer function. We now further explore these modes with the help of computer image simulations.

Computer image simulation techniques provide an attractive way to select conditions for imaging such difficult specimens as radiation sensitive particles. Microscope parameters can be varied systematically, and optimised conditions for revealing particular specimen features can be determined. A computer programme for image simulation in the DPC imaging mode, based on a two-dimensional Fourier transform, has been set up by Morrison (1985); it was simplified later to be a one-dimensional calculation suitable for imaging one-dimensional objects but still maintaining a two-dimensional probe forming system. Thus a lot of computing time was saved. (Gong, 1987).

The main study presented in this chapter is the adaptation and application of this one-dimensional image simulation programme for small pigmentary particle image simulation. The particles with which we are particularly concerned, and which are under current investigation at Glasgow University, are the halogenated copper phthalocyanine (Cl-Cu PC) particles. Particle sizes are typically ~ 50 nm whilst the detailed topography varies markedly with the degree of halogenation and the nature of the halogen atoms. We require as detailed a description as possible of the topography (edge acuity, faceting, porosity etc.). In addition, the relation of the internal structure to the external habit is important and so lattice fringe imaging must be considered. The models used in the simulations thus required variable habit and internal structure.

All electron optical parameters were selected to be applicable to the VG HB5 STEM at Glasgow University. In general images were calculated using both the DPC modes of Chapter 3 and the modified DPC modes of Chapter 4.

5.2. Mathematical treatment

In the STEM, the coherent probe image signal generated on a detector with a response function $D(\mathbf{r}_d)$ is given by Eqn.(1.29). It can be written in the form

$$S(\mathbf{r}_0) = \int D(\mathbf{r}_d) d\mathbf{r}_d \int T(\mathbf{k}) \exp(-2\pi i \mathbf{k} \mathbf{r}_0) d\mathbf{k} \int h(\mathbf{r}) \exp[-2\pi i \mathbf{r}(\mathbf{r}_d / \lambda R - \mathbf{k})] d\mathbf{r}^2 \quad (5.1)$$

in which R is the distance between detector and the specimen; $T(\mathbf{k})$ is the transfer function; $h(\mathbf{r})$ is the specimen transmittance and \mathbf{r}_0 is the position about which the probe is centred.

The formula above represents a two-dimensional image calculation. Fourier transforms are very frequently used during the evaluation to obtain the final simulated images and more than half of the total computing time is used in forming the transforms. However, if our interest is concentrated on a one-dimensional feature of the small particles with which we are concerned, the problem may be simplified. We note that Eqn.(5.1) can have an alternative form under these conditions

$$S(x_0, y_0) = \int D(x_d, y_d) dx_d dy_d \left| \int T(k_x, y_d/\lambda R) \exp(-2\pi i k_x x_0) dk_x \int h(x) \exp[-2\pi i x (x_d/\lambda R - k_x)] dx \right|^2 \quad (5.2)$$

Thus one-dimensional transforms only need be taken. The computer programme used in the image profile simulation of the small particles is based on this.

5.3. Computer image simulation

The computer program used has been written in Fortran 77, whilst the Fast Fourier transform subroutine using the Cooley-Tukey algorithm is provided by the standard subroutine package on the IBM-6361-5 mainframe computer at Glasgow University. The experimental parameters which must be specified include the accelerating voltage, the defocus, the spherical aberration

coefficient of the objective lens and the aperture size. Of particular importance here are the detector response functions for both normal and annular segmented detector configurations. Other aspects which must be included pertain to the specimen itself. Broadly speaking they include the particle length and thickness together with the periodicities of principal lattice planes. For Cl-Cu PC we have $\Lambda_{110} = 1.3$ nm and $\Lambda_{001} = 0.38$ nm. Further details are given in section 5.4.

For the simulations undertaken here, we represent the specimen as a one-dimensional phase object, $h(x) = \exp [i\phi(x)]$. As electrons pass through a specimen, they have to cross an electrostatic potential 'well' because the mean potential inside the specimen is slightly lower than that of the surroundings. Denoting the thickness variation of the specimen by $t(x)$ and the inner potential function of the crystalline specimen by $V(x,z)$, the phase excursion is then given by

$$\phi(x) = \pi \left[\int_0^{t(x)} V(x,z) dz \right] / (\lambda E_0) \quad (5.4)$$

in which z is the coordinate along the optic axis. Assuming the potential variation along the z direction is negligible, which is true when investigating a very thin specimen, we have

$$\phi(x) = \pi V(x) t(x) / \lambda E_0 \quad (5.5)$$

The inner potential function of a periodic structure can be expressed as

$$V(x) = V_0 + V_1 \sin(2\pi x / \Lambda) \quad (5.6)$$

The first term of this equation represents the mean inner potential energy of the object and is related to the structure factor, F_{000} , of the unit cell of the object under consideration. The second term represents a particular internal periodic structure in the unit cell and is related to F_{hkl} . The relationship can be expressed by

$$F_{hkl} = 2\pi m_0 e V_{hkl} / h^2 \quad (5.7)$$

in which m_0 is the rest mass of the electron, and h is Planck's constant. The structure factor of a specific unit cell can be calculated from the scattering vector, \mathbf{K} , and the position vectors, \mathbf{r}_i , of the atoms by

$$F(\mathbf{K}) = \sum_i f_i(\mathbf{K}) \exp(-2\pi i \mathbf{K} \cdot \mathbf{r}_i) \quad (5.8)$$

For Cl-Cu PC crystalline particle, V_0 is associated with the structure factor of F_{000} and V_1 with F_{110} or F_{001} . Using data from Hirsch^{et.al} (1965) values for V_{000} , V_{110} and V_{001} are found to be 9.88 V, 1.78 V and 9.0 V respectively.

5.4. Background information on Cl-Cu PC particles

As stated, in the observation of small pigmentary particles by TEM both topography and internal structure are of interest, and either of them may dominate a particular investigation. The specimen preparation of such insoluble pigmentary particles

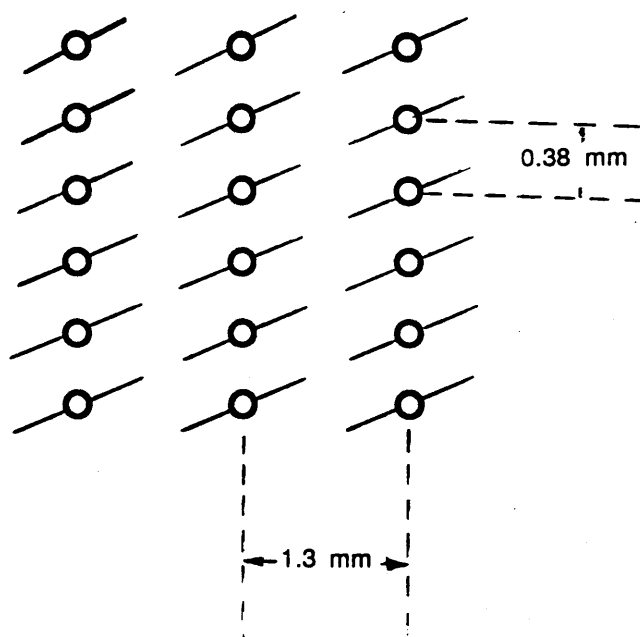


Fig. 5.1 Stacking of Chlorinated copper phthalocyanine

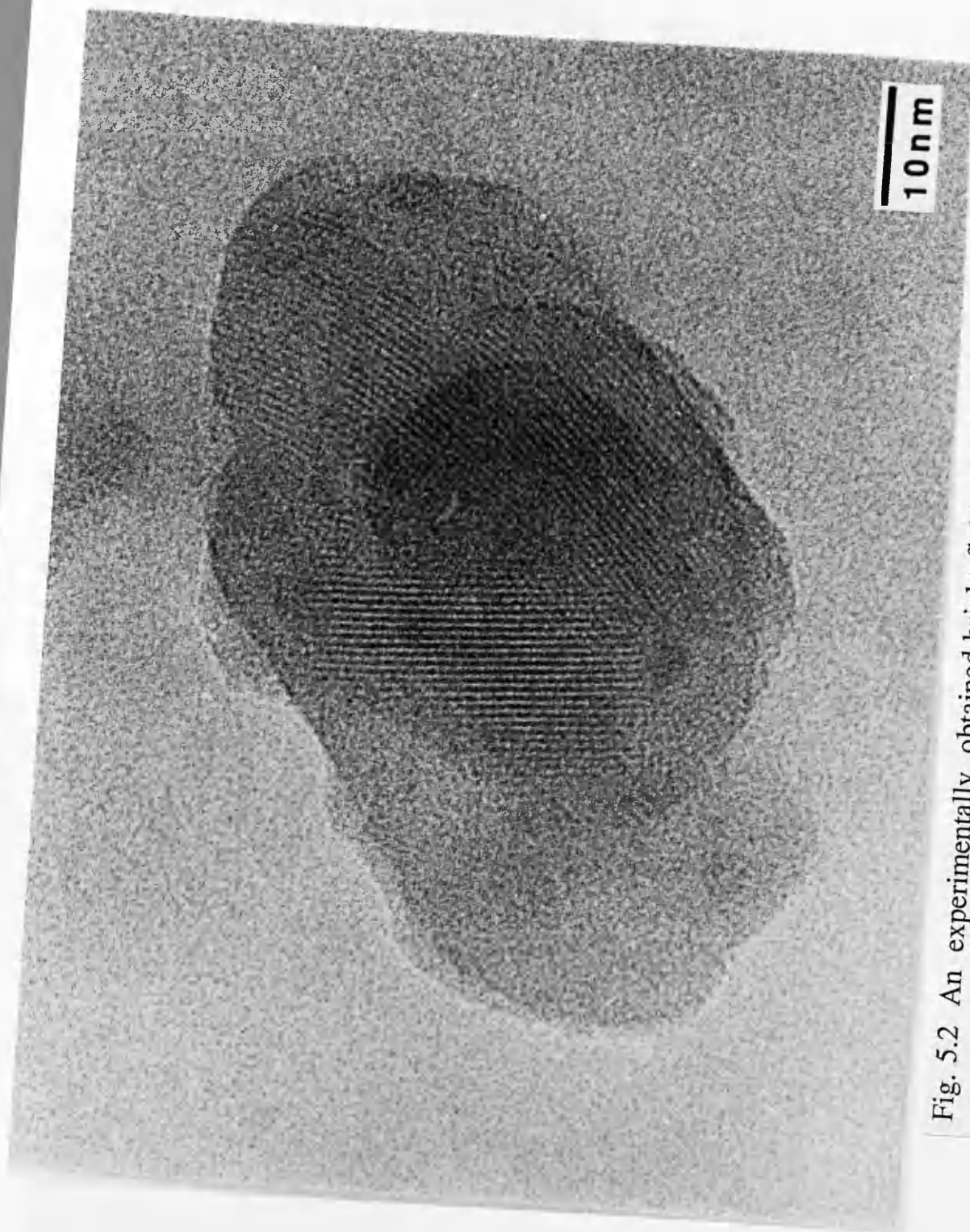


Fig. 5.2 An experimentally obtained bright-field image of Cl-Cu PC particles taken using a JEOL-1200 CTEM

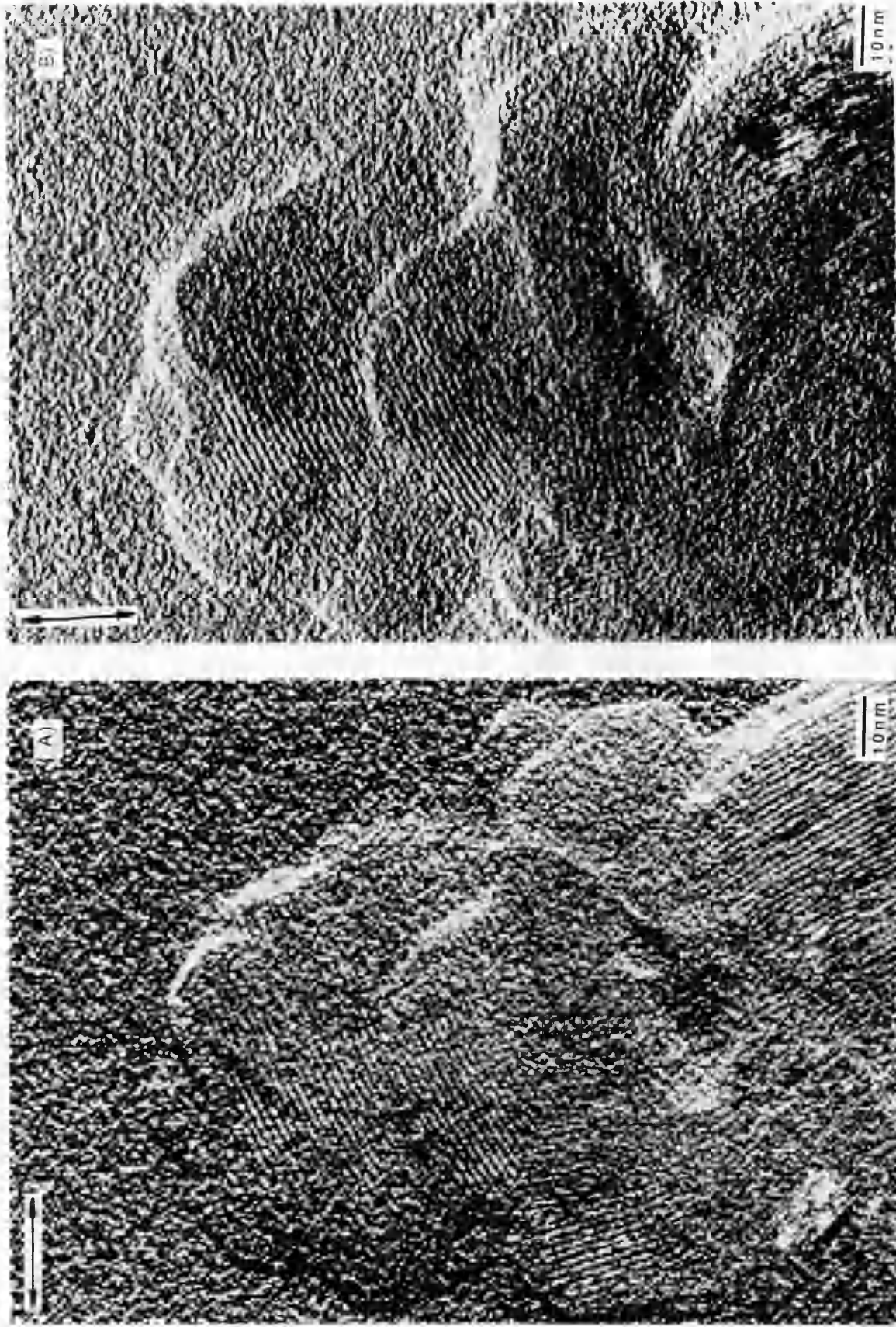


Fig. 5.3 Experimentally obtained images of Cl-Cu PC particles using standard DPC imaging mode on the VG-HB 5 STEM at Glasgow University

involves dispersion of the pigment powder in a liquid medium, and then the mixture is sprayed by a low pressure air flow onto carbon coated copper grids used for support. Using this procedure a specimen with suitable particle density on the support film can be obtained.

The atomic arrangement in a phthalocyanine molecule has been shown in Fig.2.1, and some general properties of the phthalocyanine pigments were described in section 2.4. In our study, the interest is concentrated on the 16 Cl-Cu PC particles. In a single crystal its stacking sequence is as shown in Fig.(5.1). The crystal lattice of the particle is found to be monoclinic c-face centred, and two major sets of lattice planes: $\Lambda = 1.3$ nm from the (110) reflection and $\Lambda = 0.38$ nm from the (001) reflection, can be identified.

Fig.5.2* shows an experimentally obtained bright-field image of Cl-Cu PC particles taken using a JEOL-1200 CTEM. The lattice fringes are clear but little information of the particle topography is available. Fig.5.3* shows images of the same material using the standard DPC imaging mode on the VG-HB 5 STEM equipped with a Centronic QD-100 quadrant photodiode detector at Glasgow University. In this figure, image (a) and (b) representing two specimen orientations perpendicular to each other, can be obtained simultaneously. These preliminary results imply that the technique of DPC imaging is viable for revealing both the edges and internal structure, these being much clearer than in bright field CTEM images. Our further study of the DPC

* given by P. McColgan

mode is concerned with optimizing conditions by systematic image simulations.

5.5. Image simulation of "model" Cl-Cu PC particles

5.5.1 Edge images of a particle

Edge acuity is one important aspect associated with the topography of the particle. In this case the phase shift is caused simply by the thickness function $t(x)$ and the mean inner potential V_0 . Thus, initially, no internal structure in the particle is assumed. A number of one-dimensional edge models of the particles with different values of edge width E_w and thickness T_c are shown in Fig.(5.4a - f). Model (f) reflects the case when a step exists in the particle. The corresponding simulated images of these edge models are shown in Fig.(5.4g - l). It is noted that the image signal corresponding to the particle edge is to a good approximation proportional to the thickness gradient, $\nabla t = T_c / E_w$ as expected. Thus, for example, the images (i) and (k) give approximately the same signal magnitude due to the same T_c/E_w ratio. Two objective semiangles, 4.16 mrad and 8.32 mrad, are used to simulate images for model (f), and the images are shown in (l') and (l'') in Fig.(5.4). We note that when using $\alpha_s = 4.16$ mrad the edge images are wider than their real width to some extent, and the step image is influenced by this broadening effect and not as clear as that using $\alpha_s = 8.32$ mrad. This is as expected as the current density distribution in the probe is close to the optimum for the latter probe angle, as shown in Fig.(5.5). Fig.5.6 shows

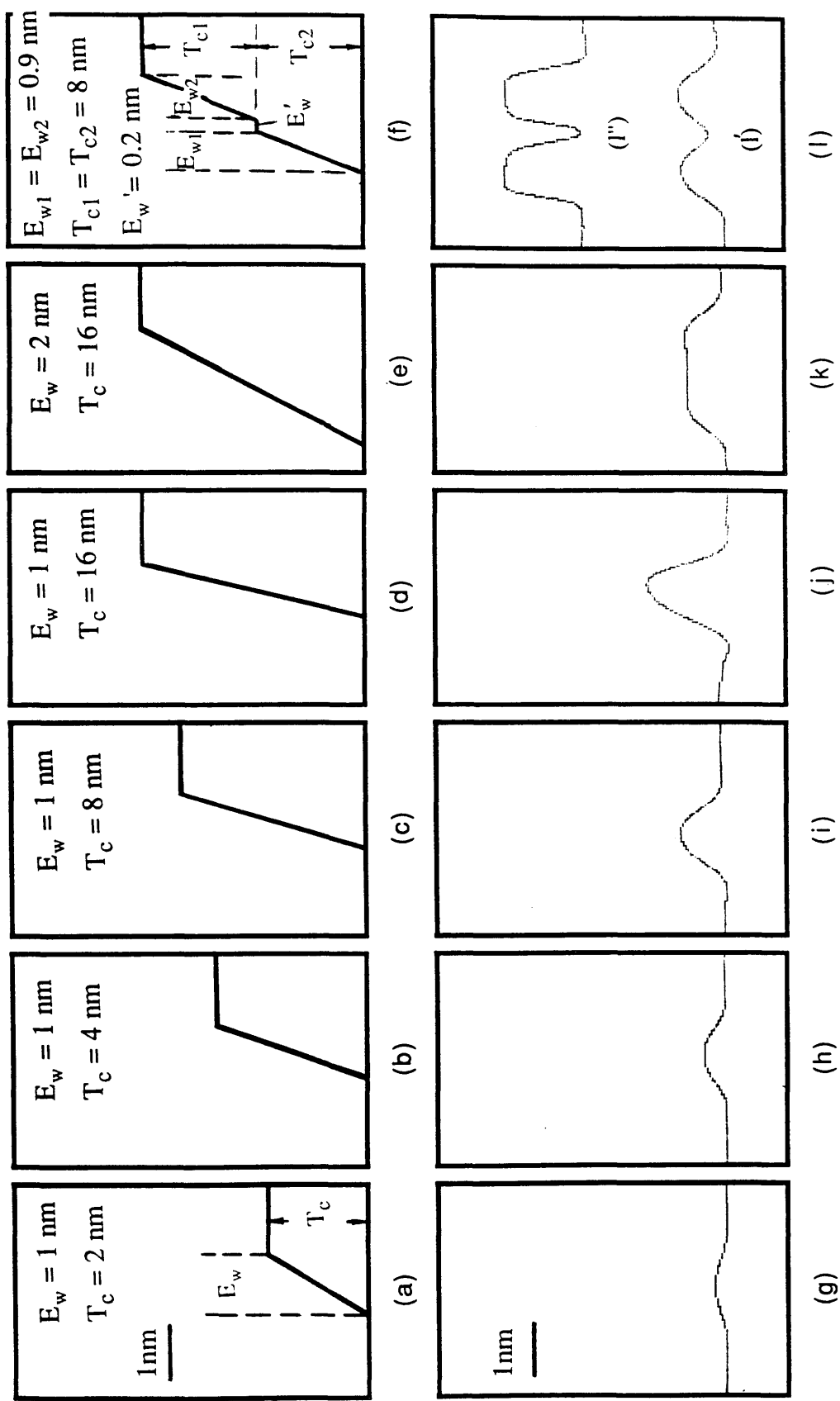


Fig. 5.4 The plots of (g) ~ (l) are the simulated images of the edge models of the particle shown in (a) ~ (f). T_c is the thickness of a particle and E_w is the width of a edge. $V_0 = 9.88 \text{ V}$, $\lambda = 3.7 \text{ pm}$, $\alpha_s = 4.16 \text{ mrad}$, and $d_z = -26 \text{ nm}$, except in (l'') where $\alpha_s = 8.32 \text{ mrad}$, and $d_z = -110 \text{ nm}$.

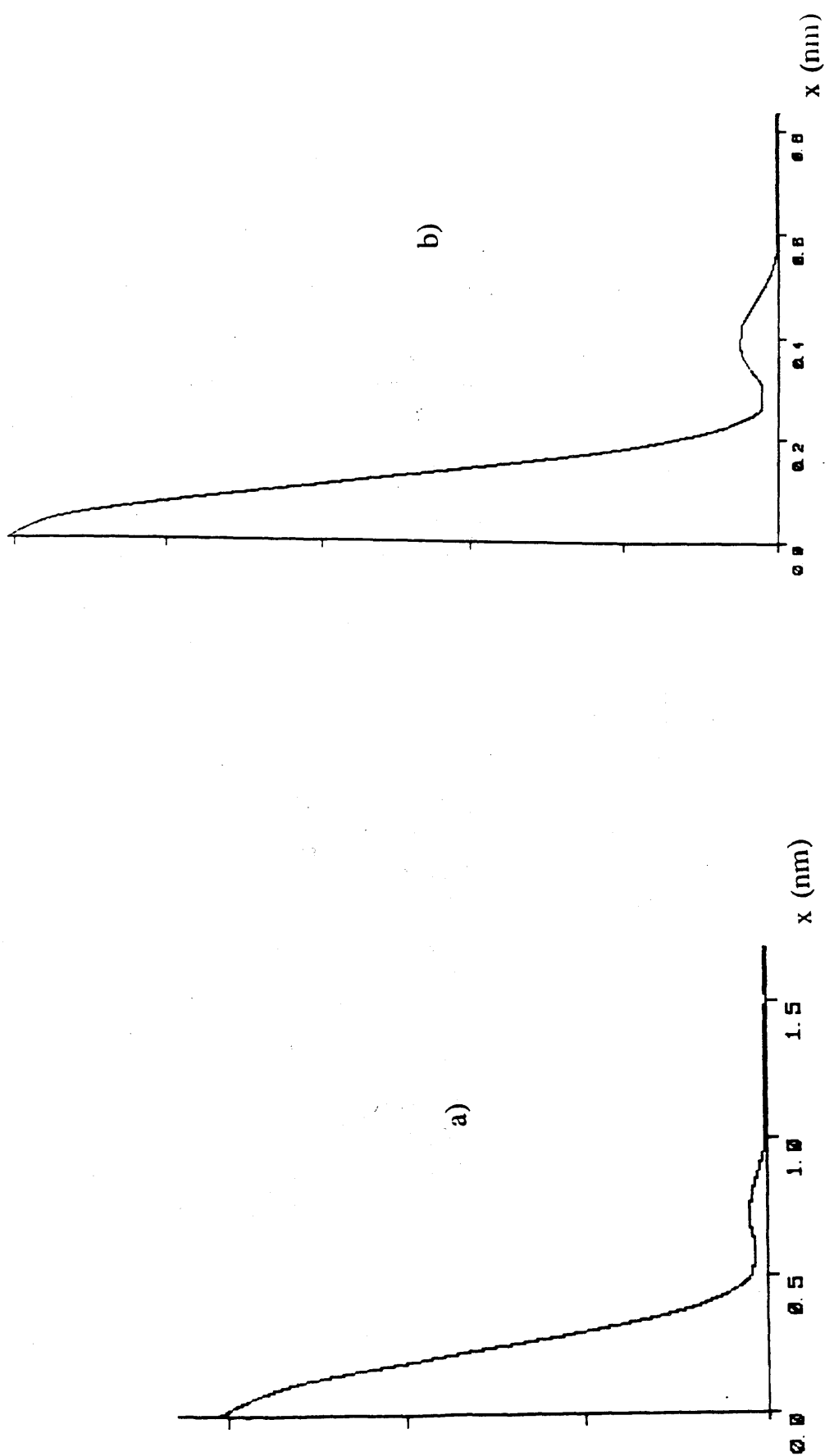


Fig.5.5 Computer simulated coherent probe profile in specimen plane for (a) $\alpha_s = 4.16$ mrad, $d_z = -26$ nm, and (b) $\alpha_s = 8.32$ mrad, $d_z = -110$ nm,

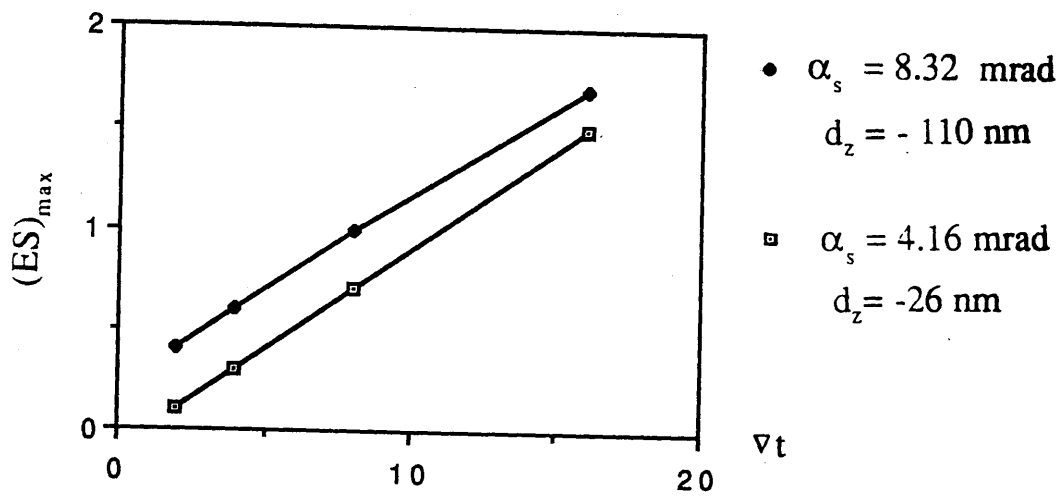


Fig.5.6 The variation of signal amplitude at a particle edge with the thickness gradient

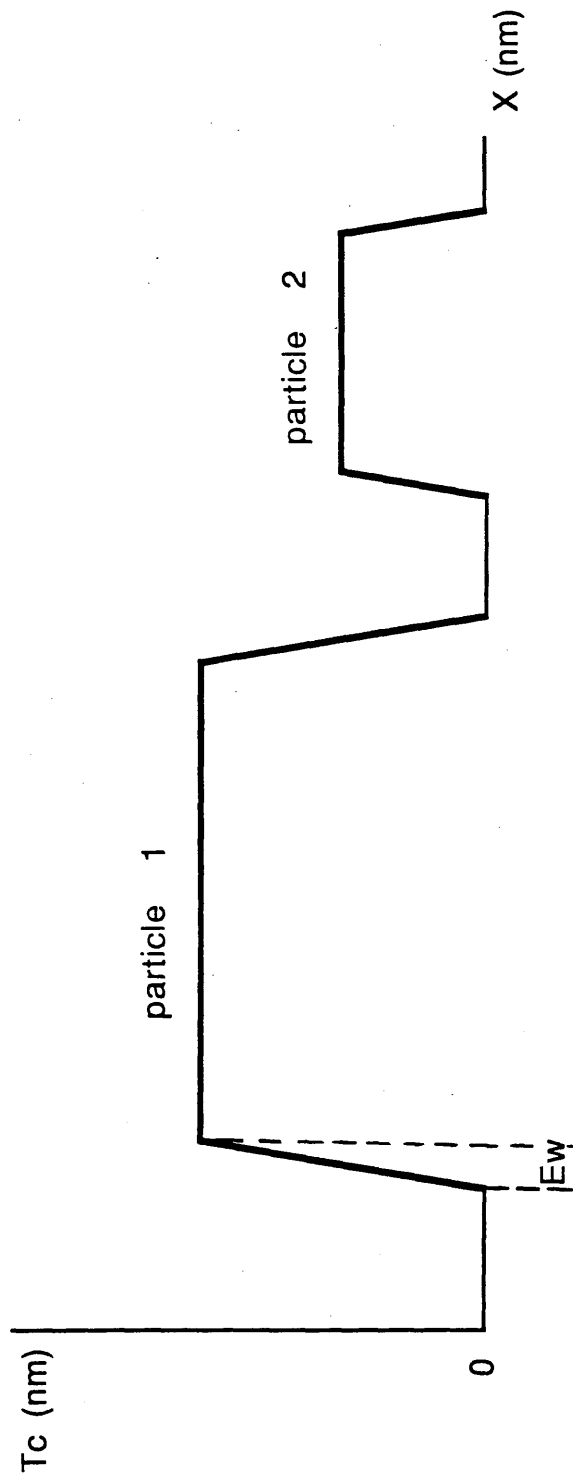


Fig.5.7 Schematic of the particle models, with
 $T_c = 20$ nm, $E_w = 1$ nm in particle 1, and
 $T_c = 10$ nm, $E_w = 0.5$ nm in particle 2

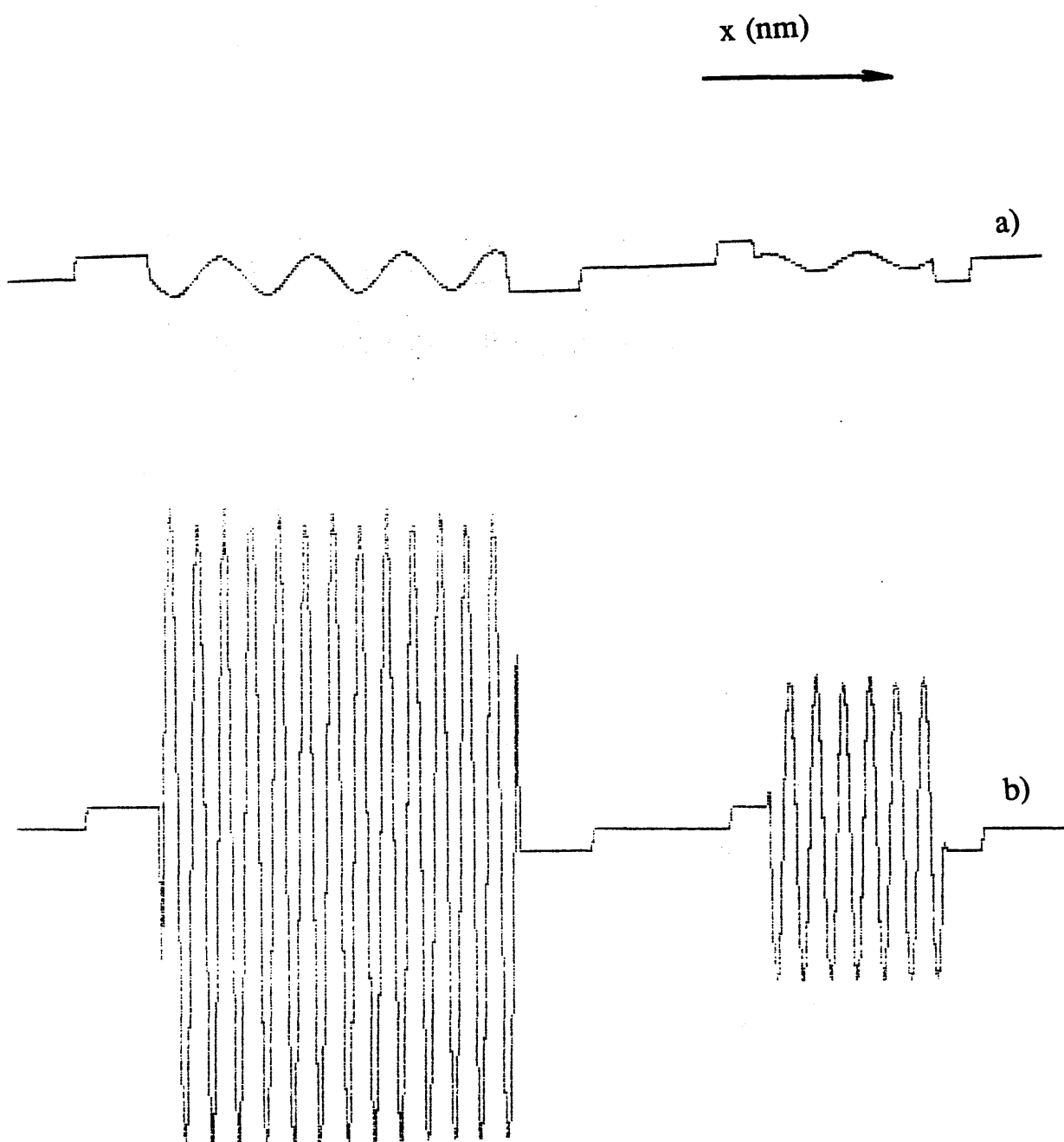


Fig.5.8 Plots of phase gradients for (a) $\Lambda = 1.3 \text{ nm}$, (b) $\Lambda = 0.38 \text{ nm}$ of the particle

Table.5.1 Values of parameters used in the fringes images
simulation of Cl-Cu PC particle

λ (pm)	3.7
C_s (mm)	3.3
dz (nm)	- 26, -110
α_s (mrad)	4.16, 8.32
α_d / α_s	2
V_{000} (V)	9.88
V_{001} (V)	9.0
V_{110} (V)	1.78

the linearity of the variation of maximum image signals, $(ES)_{\max}$ (arbitrary unit), with ∇t using two different probe.

5.5.2. Lattice fringe images of the particle

In the previous discussion in Chapter 3, we have shown that suitable DPC transfer functions are obtained when using objective apertures which subtend semiangles of 4.16 mrad and 8.32 mrad in the VG-HB5 STEM at Glasgow University. Thus in the particle image simulation, and particularly in the lattice fringe image simulation for Cl-Cu PC, probes so defined are of most interest. The basic instrumental parameters we used in the simulation are listed in Table.5.1 and the habit of two particles is shown in Fig.5.7. The plots of $d\phi/dx$ for two lattice periodicities within the particle are given in Fig.5.8.

We have noted in Chapter 3 that differential phase contrast is produced when the scattering angle satisfies the condition $0 < \theta < 2\alpha_s$. For a lattice periodicity of $\Lambda = 0.38$ nm and 100 keV electrons we have $\theta = 9.74$ mrad so that no lattice fringe images with this periodicity can be obtained using a probe with $\alpha_s = 4.16$ mrad. Simulated images of the particles shown in Fig.5.7 with different values of α_s and Λ are shown in Fig.5.9, and as predicted no phase information is given in Fig.5.9a. However, a probe of semiangle 4.16 mrad is perfectly suitable for imaging a periodic structure with $\Lambda = 1.3$ nm and clear fringe images are seen in Fig.5.9b. This is in accordance with the DPC transfer function we have calculated in section 3.4.2, where

the value of I_m/I_p is high for $\Lambda = 1.3$ nm but zero for $\Lambda = 0.38$ nm.

Fig.5.9 also shows the effect of a bigger objective aperture subtending a semiangle of $\alpha_s = 8.32$ mrad. This is clearly necessary to obtain lattice images from periodicities of both the higher spatial frequency ($\Lambda = 0.38$ nm) as shown in Fig.5.9c, and the lower spatial frequency ($\Lambda = 1.3$ nm) as shown in Fig.5.9d.

In practice the detector aperture semiangle, α_d , is usually greater than the objective aperture semiangle, α_s to ensure the potential of the detector is fully exploited. Simulation by the variation of α_d/α_s are shown in Fig.5.10. There are no significant changes in the signals from the edges and the fringes of the particle.

5.6. Simulated images using annular detectors

The transfer functions for modified DPC imaging modes using a series of annular detector configurations has been discussed in Chapter 4. It was found that for low spatial frequencies high signal-to-noise ratios could be obtained with an acceptable I_m/I_p value. Such a high efficiency imaging mode is well suited to the investigation of radiation sensitive specimens. Thus image simulation is again taken for model one-dimensional Cl-Cu PC particles using these imaging modes. Some results are presented below for the particle model shown in Fig.5.7.

In Fig.5.11 the images are for three annular split detectors with different values of R_d which was defined in section 4.2; a

coherent probe with $\alpha_s = 4.16$ mrad is used for imaging the crystalline structure with a periodicity of 1.3 nm. The signals are scaled to the same total detected current so that the noise content in each would be the same. We note that the image with $R_d = 0.2$ is very close to that with $R_d = 0$ in Fig.5.9b as expected from the plot of $(S/N)_m$ against Λ in Fig.4.2; here the curve for $R_d = 0.2$ almost overlaps with that for $R_d = 0$, meaning that there is little effect on the DPC transfer function when a small portion of area is removed from the detector centre. As R_d further increases, both edge and lattice fringe image intensities are reduced monotonically, but even when $R_d = 0.8$ (Fig. 5.11c) phase information of the structure remains clear. However, images obtained using detectors with $R_d > 0$ appear to offer no advantage in this instance and in general representation of what is happening near the particle edge is limited by use of a smaller than optimal value of α_s .

Fig.5.12. shows the case when using a probe with $\alpha_s = 8.32$ mrad to image the particle with $\Lambda = 0.38$ nm. Comparing the images with $R_d = 0$ in Fig.5.9c, we note the signal intensity of the image has been significantly affected by varying R_d . As shown in Fig.4.4 all the values of $(S/N)_m$ rise rapidly in the range of $\Lambda = 0.3 - 0.4$ nm; thus any little change in R_d can lead to a great variation in $(S/N)_m$. This can be used most advantageously to emphasise either the lattice fringes ($R_d = 0$) or the particle edge ($R_d = 0.8$). Alternatively, use of an intermediate value ($R_d = 0.4$) allows both to be seen with approximately equal contrast. If the alternative periodic structure of $\Lambda = 1.3$ nm is imaged in these same conditions the effect of varying R_d is different. The results

are shown in Fig.5.13, where there is little variation in the image signal as R_d increases. These also can be explained with $(S/N)_m$ in Fig.4.4, where the values obtained by annular detectors are very close to or slightly higher than those obtained by a normal detector used to image structures with $\Lambda > 1.0$ nm.

In Fig. 5.14 the simulations also show that the use of annular quadrant detectors yield similar results to those obtained using annular split detectors. This is as expected given the similarities of the DPC transfer function and signal-to-noise ratio.

We now compare the simulation results described above with the plots of $d\phi/dx$ shown in Fig.5.8 for the models used. These should be identical in a perfect DPC imaging system. In reality, we note

1) In all cases differences exist. Using $\alpha_s = 4.16$ mrad edge effects are broadened somewhat and small lattice spacings cannot be imaged; with $\alpha_s = 8.32$ mrad both lattice spacings of interest can be revealed but the effect of spherical aberration is apparent near the edges of the particles.

2) By varying R_d considerable advantages can be gained in that emphasis can be given to either the edge or lattice fringe image as required.

3) Despite departures from ideality, examination of images recorded under different conditions allows an accurate picture of the specimen to be obtained..

5.7. Summary and conclusion

The study by computer image simulation of small particles, related to Cl-Cu PC crystalline particles, using DPC STEM and modified DPC STEM shows

- The image signal of the particle edge is to a good approximation proportional to the thickness gradient $\nabla t = T_c / E_w$ when the mean inner potential V_0 remains the same.

- When assuming there is no internal structure in a specimen an objective aperture semiangle of $\alpha_s = 8.32$ mrad is suitable to obtain clear edge images, especially when steps exist in the edge.

- For the lattice imaging in Cl-Cu PC particles, an angle of $\alpha_s = 4.16$ mrad is satisfactory for obtaining the image for the structure with $\Lambda = 1.3$ nm, but not for that with $\Lambda = 0.38$ nm; the use of an angle of $\alpha_s = 8.32$ mrad allows images for both structures to be obtained although spherical aberration effects are apparent.

- Pronounced differences to the fringe images result by varying R_d in an annular detector. For $\alpha_s = 8.32$ mrad, increase in R_d causes a significant reduction in image signals for $\Lambda = 0.38$ nm fringes, but the signal remains almost the same for $\Lambda = 1.3$ nm fringes. Controlled variation of R_d can thus be used to emphasise either local topographic or internal structural detail.

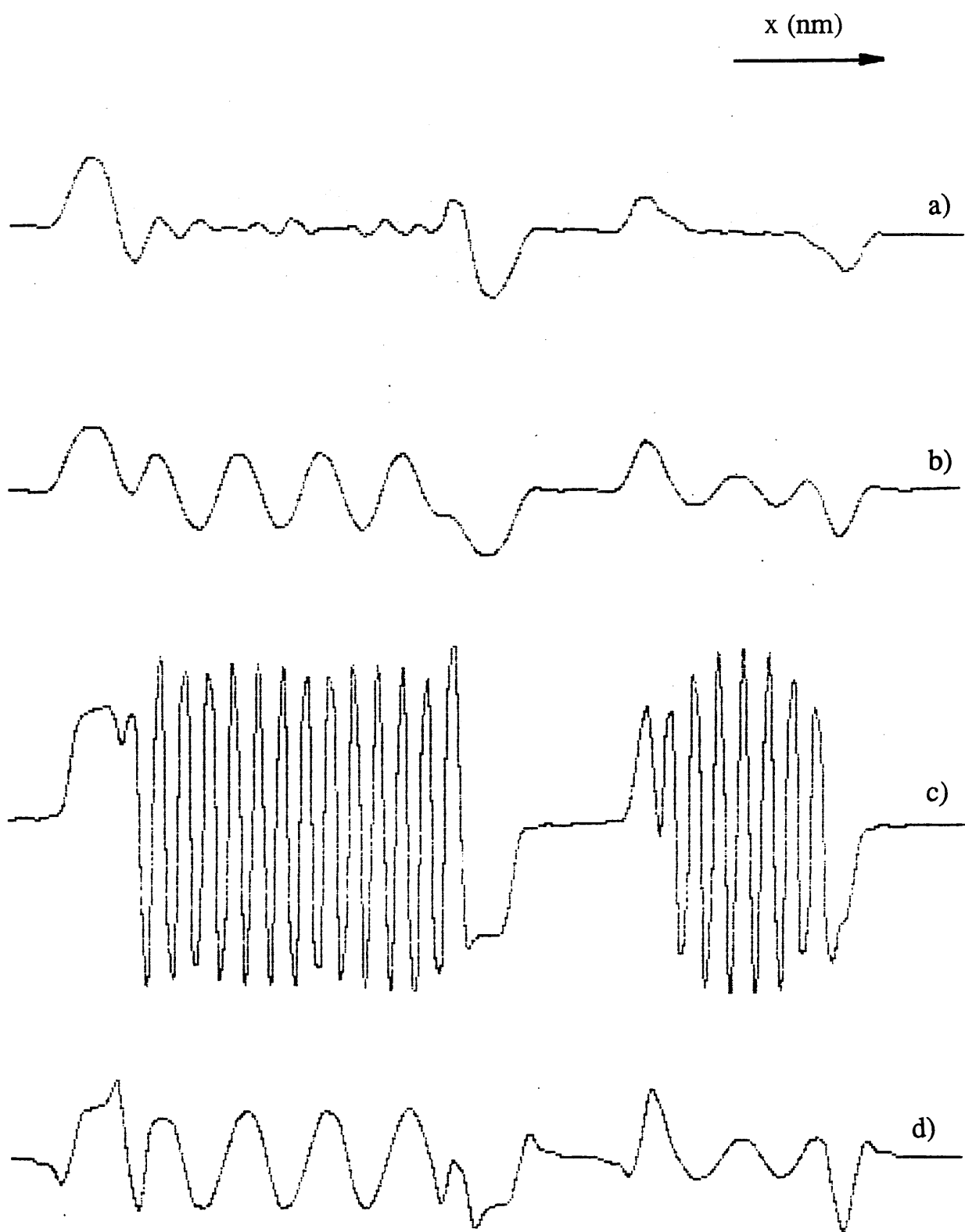


Fig. 5.9 Simulated profile images of the particles using a split detector, with (a) $\Lambda = 0.38 \text{ nm}$, $\alpha_s = 4.16 \text{ mrad}$, $d_z = -26 \text{ nm}$; (b) $\Lambda = 1.3 \text{ nm}$, $\alpha_s = 4.16 \text{ mrad}$, $d_z = -26 \text{ nm}$; (c) $\Lambda = 0.38 \text{ nm}$, $\alpha_s = 8.32 \text{ mrad}$, $d_z = -110 \text{ nm}$; (d) $\Lambda = 1.3 \text{ nm}$, $\alpha_s = 8.32 \text{ mrad}$, $d_z = -110 \text{ nm}$.

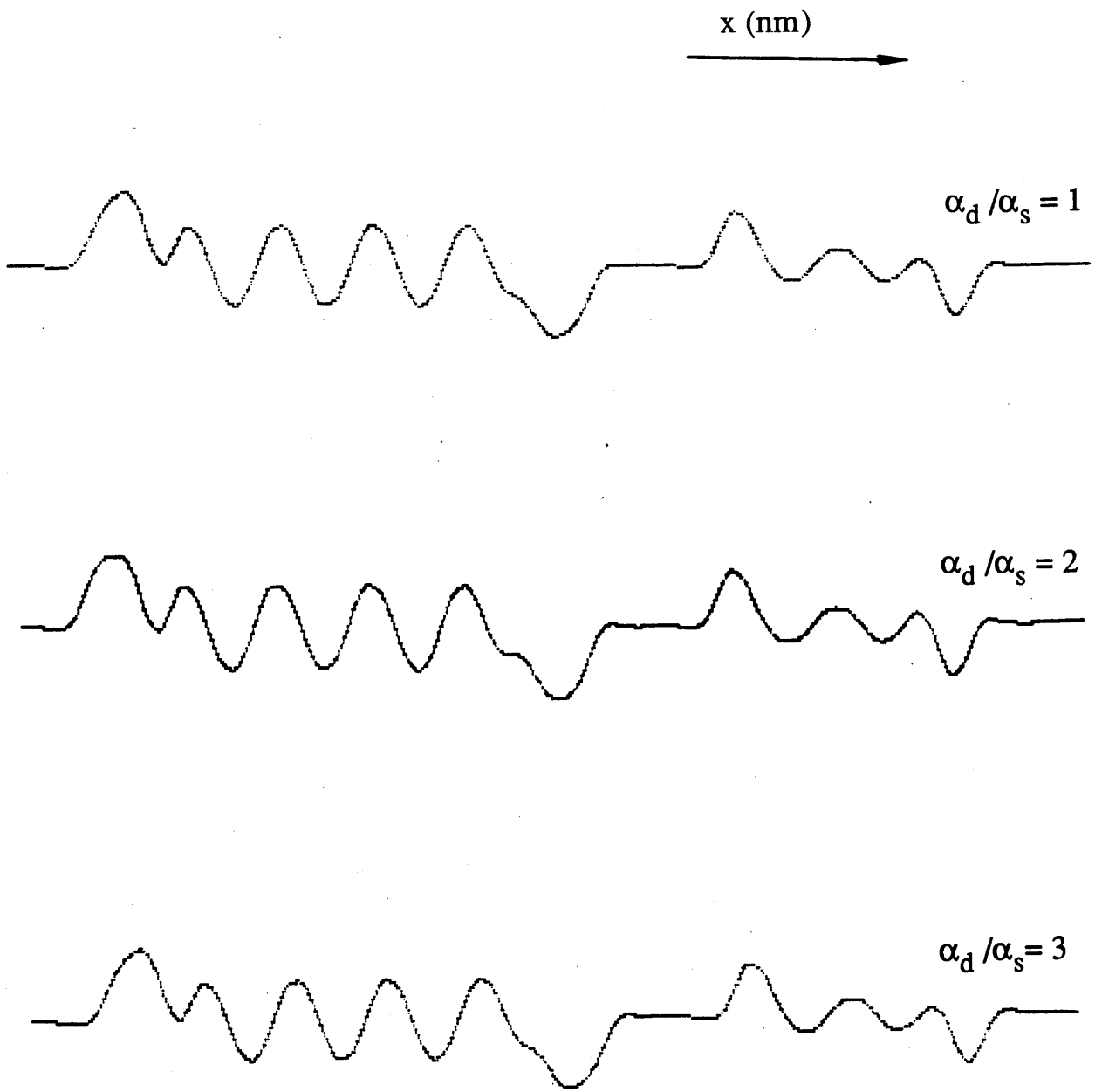


Fig.5.10 Simulated profile images of the particles for $\Lambda = 0.38 \text{ nm}$ using a split detector, with $\alpha_s = 4.16 \text{ mrad}$, $d_z = -26 \text{ nm}$ and indicated α_d/α_s ratio.

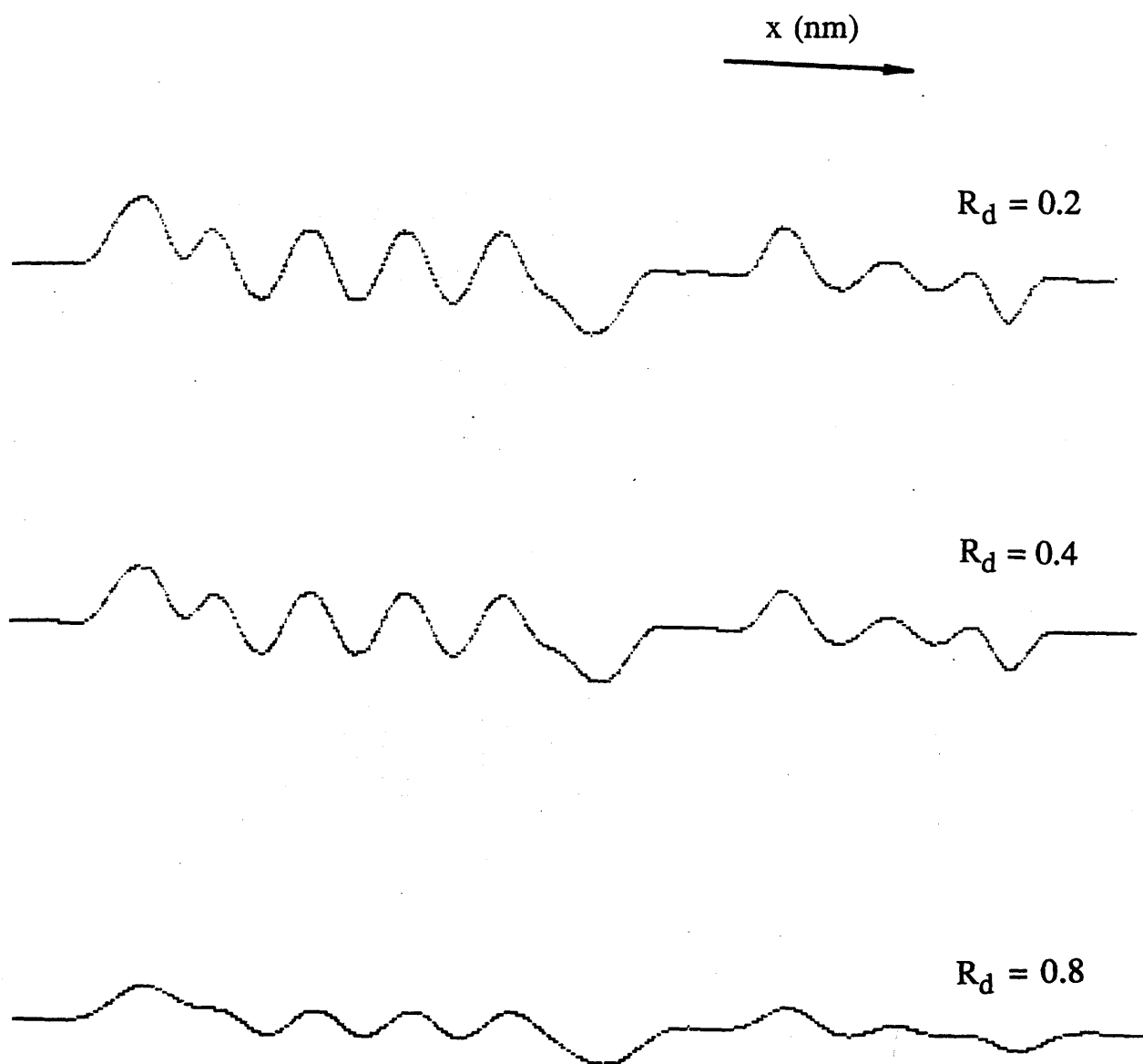


Fig.5.11 Simulated profile images of the $\Lambda = 1.3$ nm structure particles using $\alpha_s = 4.16$ mrad and annular split detectors with the indicated values of R_d .

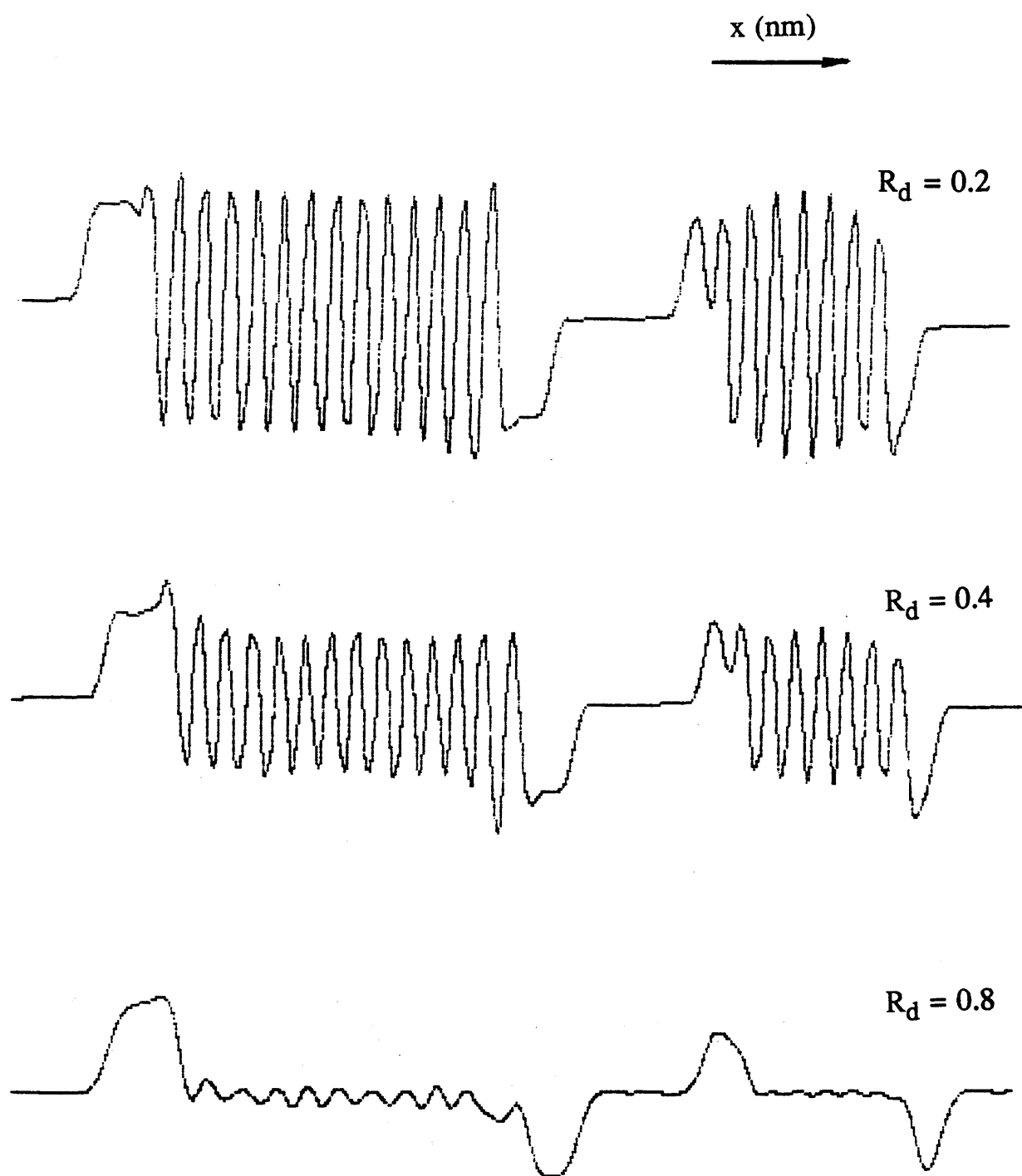


Fig.5.12 Simulated profile images of the $\Lambda = 0.38 \text{ nm}$ structure particles using $\alpha_s = 8.32 \text{ mrad}$ and annular split detectors with the indicated values of R_d .

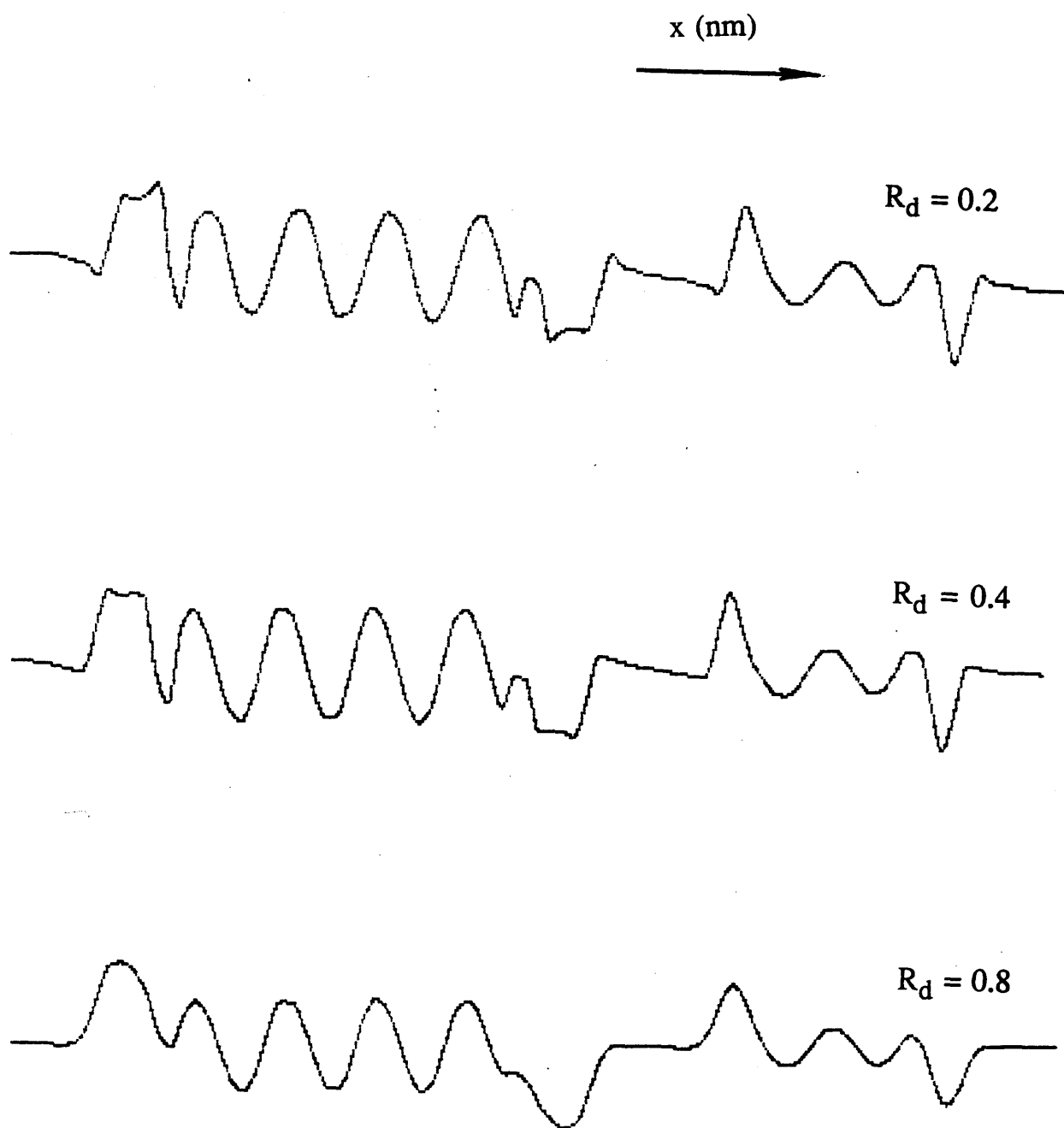


Fig.5.13 Simulated profile images of the $\Lambda = 1.3 \text{ nm}$ structure particles using $\alpha_s = 8.32 \text{ mrad}$ and annular split detectors with the indicated values of R_d .

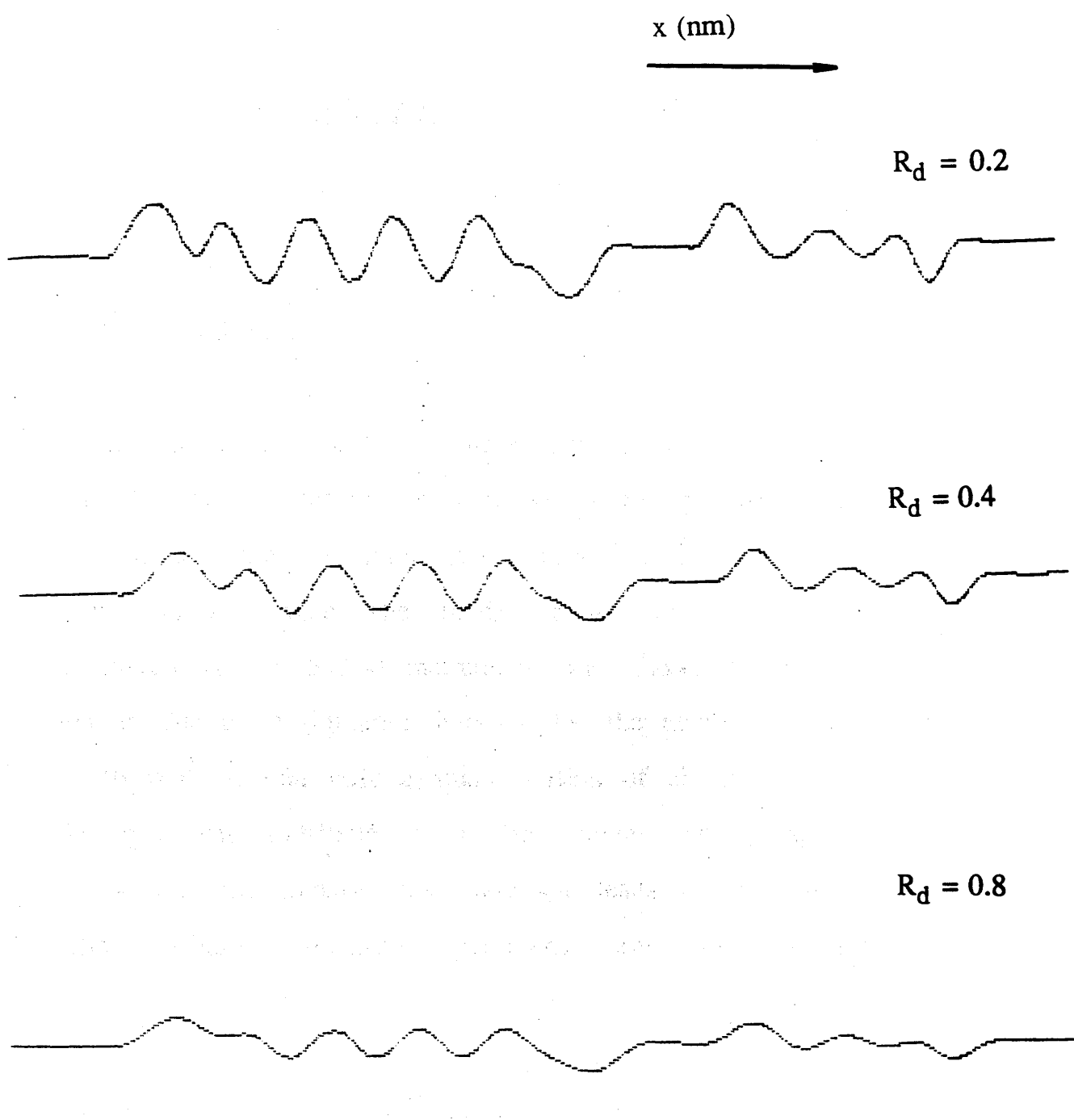


Fig.5.14 Simulated profile images of the $\Lambda = 1.3$ nm structure particles using $\alpha_s = 4.16$ mrad and annular quadrant detectors with the indicated values of R_d .

Chapter 6

Conclusions and suggestions for further work

1. Conclusion

In this thesis the basic phase contrast imaging modes in the transmission electron microscope were discussed and an assessment based on their efficiencies of transmitted electron utilization was made. The standard phase contrast imaging mode employed in the STEM instruments was shown to be inefficient mainly due to a limitation imposed by the instrumental condition of $(\beta_s/\alpha_s)^2$ so that only a small portion of electrons incident on the specimen contribute to the final image. This imaging mode provides a low signal-to-noise ratio and leads to a serious problem when radiation sensitive specimens are under investigation. Specifically, if an imaging mode with low efficiency is used, due to the effect of radiation damage, significant changes to the molecular structure usually occur before statistically significant signals carrying useful phase information are obtained. Much of the thesis is concerned with alternative imaging modes and particular attention is given to seeking ones suitable for providing information on the topography and internal structure of small radiation sensitive particles. Differential phase contrast (DPC) imaging modes in the STEM seem suitable. They provide a

number of useful characteristics, namely (i) phase contrast is present even in the absence of lens aberrations; (ii) no oscillation in the sign of the transfer function for spatial frequencies in the range of $0 < k_{xr} < 2$ occur provided the defocus is correctly chosen, and (iii) the efficiency of the DPC imaging mode is much higher and more resistant to non-linearities (Morrison and Chapman, 1982) than that of the standard phase contrast imaging mode in STEM.

The results of two-dimensional calculations of the DPC transfer function for an aberrated STEM imaging system were also presented. They show that the transfer function is strongly affected by the spherical aberration of the objective lens especially when using a large objective aperture. The Scherzer defocus, d_{zs} , is the optimum value for the imaging system when the semiangle of the objective aperture satisfies $\alpha_{opt} = 1.41(\lambda/C_s)^{1/4}$; if other values of α_s are chosen the optimum defocus will be approximately $(\alpha_{opt}/\alpha_s)^2 d_{zs}$. The maximum DPC transfer for a given set of instrumental parameters is normally obtained around the spatial frequency of $k_{xr} = 0.9$. No phase information is obtainable with a specimen orientation of $\varepsilon = \pi/2$ using a split detector; transfer of phase information and the signal-to-noise ratio are a minimum with $\varepsilon = \pi/4$ using a quadrant detector.

Further calculations involve modified DPC imaging modes where annular split/quadrant detectors are used. These show that a carefully chosen annular detector geometry can lead to either

a high signal-to-noise ratio or flat DPC transfer and signal-to-noise ratio bands.

Finally the results from computer simulations of the coherent probe images for small particles, relevant to 16 Cl-Cu PC pigmentary particles, using DPC STEM were presented. Useful information can be conveniently obtained by one-dimensional image simulation techniques involving modest computing time. The image signal from a particle edge is found to a good approximation to be proportional to the thickness gradient when the mean inner potential in the structure remains the same. For conditions pertaining to an HB5 STEM an objective aperture semiangle of 8.32 mrad is clearly necessary to obtain images for both 0.38 nm and 1.3 periodic structure in Cl-Cu PC although the effect of spherical aberration exists to some extent. Variation in R_d value for annular detector has little effect on $\Lambda = 1.3$ nm lattice fringe images but leads to a reduction for $\Lambda = 0.38$ nm fringe images when $\alpha_s = 8.32$ mrad is used.

2. Suggestions for further work

It is obvious in the calculations of DPC transfer functions that we used advantageously the split and quadrant detectors in the imaging mode to obtain signals which well represented the phase gradient of a weak object structure. In this procedure the amplitude contrast signals were completely cancelled. To fully explore the potential of a non-rotationally symmetric detector

system, it is possible to produce undifferentiated amplitude images simultaneously using the system by adding the signals from each individual segment. Although the transfer function for this is independent of the orientation of the object, calculation of the transfer function is significant in understanding the overall potential for image formation using a particular detector. (Dekkers and de Lang, 1977)

The idea of using non-rotationally symmetric detector systems has allowed us to design detectors for more flexible purposes. In the DPC imaging mode the use of annular split/quadrant detector systems is promising. Particularly the opportunity arises for obtaining equally-weighted phase information from a specimen comprising a range of spatial frequencies by using a quadrant detector with a high value of R_d . A development of an annular quadrant detector would consist of an array made up of many narrow concentric rings so that variable detector geometry in term of R_d can be obtained without the replacement of detectors. The output of the resulting signals from the separate areas of the detector would be processed by an arithmetic logical unit after the end of each pixel dwell time.

REFERENCES

Chapter 1

- Born M. and Wolf E., in 'Principles of optics (Pergamon Press, Oxford,1959).
- Burge R.E. and van Toorn P.V., in ' Multiple images and image processing in STEM ', Vol.I,1980,(SEM Inc., AMF O'Hare, IL, 60666), pp. 81.
- Colliex C. and Mory C., ' Quantitative aspects of scanning transmission electron microscopy', in ' Quantitative electron microscopy', ed. by Chapman J.N. and Craven A.J. (SUSSP Publications, 1984).
- Cowley J.M., Appl. Phys. Letters. No.15, 1969, pp.58.
- Crewe A.V. and Wall J., 1970, Optik, Vol. 30, Ch.13, pp.461.
- Hawkes P.W., in 'Electron optics and electron microscopy', 1972, pp. 65 - 82.
- Hawkes P.W., in ' Advances in optical and electron', Vol. 7 (Academic press, 1978), pp. 117-9
- Misell D.L., in 'Advances in optical and electron', Vol.2, (Academic press, 1978), pp. 185 - 228.

Chapter 2

- Cosslett V.E.J. Microsc., Vol. 113, Pt. 2, 1978a, pp. 113.
- Cosslett V.E., 'Radiation damage in the high resolution electron microscopy of biological materials: a review', J. Microsc., Vol.113, Pt. 2, July 1978b, pp. 113-129.

- Fryer J.R., 'Transmission electron microscopy of organic pigments', J.Microsc., Vol. 120, Pt.1, Sept. 1980, pp.1-14.
- Hobbs L.W., 'Radiation effects in analysis by TEM', in 'Quantitative electron microscopy', ed. by Chapman J.N. and Craven A.J. (SUSSP Publications, 1984).
- Isaacson M., 'Electron beam induced damage of organic solids: implications for analytical electron microscopy', Ultramicroscopy, Vol. 4, 1979, pp.193-199.
- Reimer L., 'Transmission electron microscopy', (Springer-Verlag, 1984). pp. 135 -176, pp.185 - 228.
- Salih S, Cosslett V.E., 'Reduction in electron irradiation damage to organic compounds by conducting coatings', Phil. Mag., Vol. 30, pp.225

Chapter 3

- Burge R.E. and van Toorn P.V., in ' Multiple images and image processing in STEM ', Vol.I,1980,(SEM Inc., AMF O'Hare, IL, 60666), pp. 81.
- Butler J.H. and Cowley J.M., 'Phase contrast imaging using a scanning transmission electron microscope', Ultramicroscopy, Vol.12,1983, pp.39-50
- Cowley J.M., Appl. Phys. Letters, Vol.15,1969, pp. 58.
- Cowley J.M., and Au A.Y., in 'Scanning electron microscopy', Vol.I, 1978, Ed.O.Johari (STEM Inc., AMF O'Hare,IL,1978), pp.53.
- Dekkers N.H. and de Lang H., ' Differential phase contrast in a STEM', Optik, Vol. 41, No.1,1974, pp.452-456.

- Dekkers N.M. and de Lang H., 'A detection method for producing phase and amplitude images simultaneously in a scanning transmission electron microscope', Philips technical review, Vol.37, 1977, No.1, pp.1-9.
- Dekkers N.H. and de Lang H., 'A calculation of bright field single-atom images in STEM with half plane detectors', Optik, Vol.51, 1978, No.1, pp.83-92.
- Hawkes P.W., 'Half-plane apertures in TEM, split detectors in STEM and ptychography', J.Optics (Paris), Vol.9, No.4, 1978, pp.235-241.
- Morrison G.R. and Chapman J.N., 'A comparison of three differential phase contrast systems suitable for use in STEM', Optik, Vol.64, 1983, No.1, pp.1-12.
- Mory C. and Colliex C., 'Optimum defocus for STEM imaging and microanalysis', Ultramicroscopy, Vol.21, 1987, pp.171-178.
- Rose H., 'Nonstandard imaging methods in electron microscopy', Ultramicroscopy, Vol. 2, 1977, pp. 251-267.
- Waddell E.M. and Chapman J.N., 'Linear imaging of strong phase objects using asymmetrical detectors in STEM', Optik, Vol.54, No.2, 1979, pp.83-96.

Chapter 4

- Burge R.E., Browne M.T., Lackovic S., and Ward J.F.L., 'STEM imaging at high resolution: the influence of detector geometry', in 'Scanning electron microscopy', Vol.I, 1979, (SEM Inc., AMF O'Hare, IL 60666, USA), pp.127-136.
- Burge R.E. and van Toorn P., 'Multi-signal detection and processing in STEM', Inst. Phys. Conf. Ser., No.52, 1980, Ch. 4, pp.249-252.

- Cowley J.M. and Au A.Y., 'Image signal and detector configurations for STEM', in 'Scanning electron microscopy', Vol.I,1978(STEM Inc., AMF O'Hare, IL 60666,USA), pp.53-60.
- Haider M, Boulin Ch., and Epstein A. Inst. Phys. Conf. Ser. No. 93, Vol. 1, Ch. 1, pp. 123-4.
- Huizer A.M.J. and van Toorn P., 'Optimal detection in scanning electron microscopy', J.Phys. D:Appl.Phys.,Vol.15,1982, pp.747-755.
- Rose H., 'Nonstandard imaging methods in electron microscopy', Ultramicroscopy, Vol. 2, 1977, pp. 251-267.

Chapter 5

- Fryer J.R., 'Transmission electron microscopy of organic pigments', J. Microsc., Vol. 120, Pt.1, Sept. 1980, pp.1-14.
- Gong H., M.Sc Thesis, Glasgow University,1987.
- Hillebrand R., Neumann W., and Heydenreich J., 'On the calculation of electron optical high resolution images', Ultramicroscopy, Vol.4, 1979, pp.305-316.
- Hirsch P.B. et.al., 'Electron microscopy of thin crystals',1965
- Morrison G.R., Ph.D Thesis, Glasgow University ,1985.

Chapter 6

- Dekkers N.M. and de Lang H., ' A detection method for producing phase and amplitude images simultaneously in a scanning transmission electron microscope', Philips technical review, Vol.37, 1977, No.1, pp.1-9.

Appendix 1

FIGURES 1:

DPC transfer function

FIGURE 1

The contour plots
(A) and (D)
correspond to
the plots
(A) and (D)
in Fig.3.11

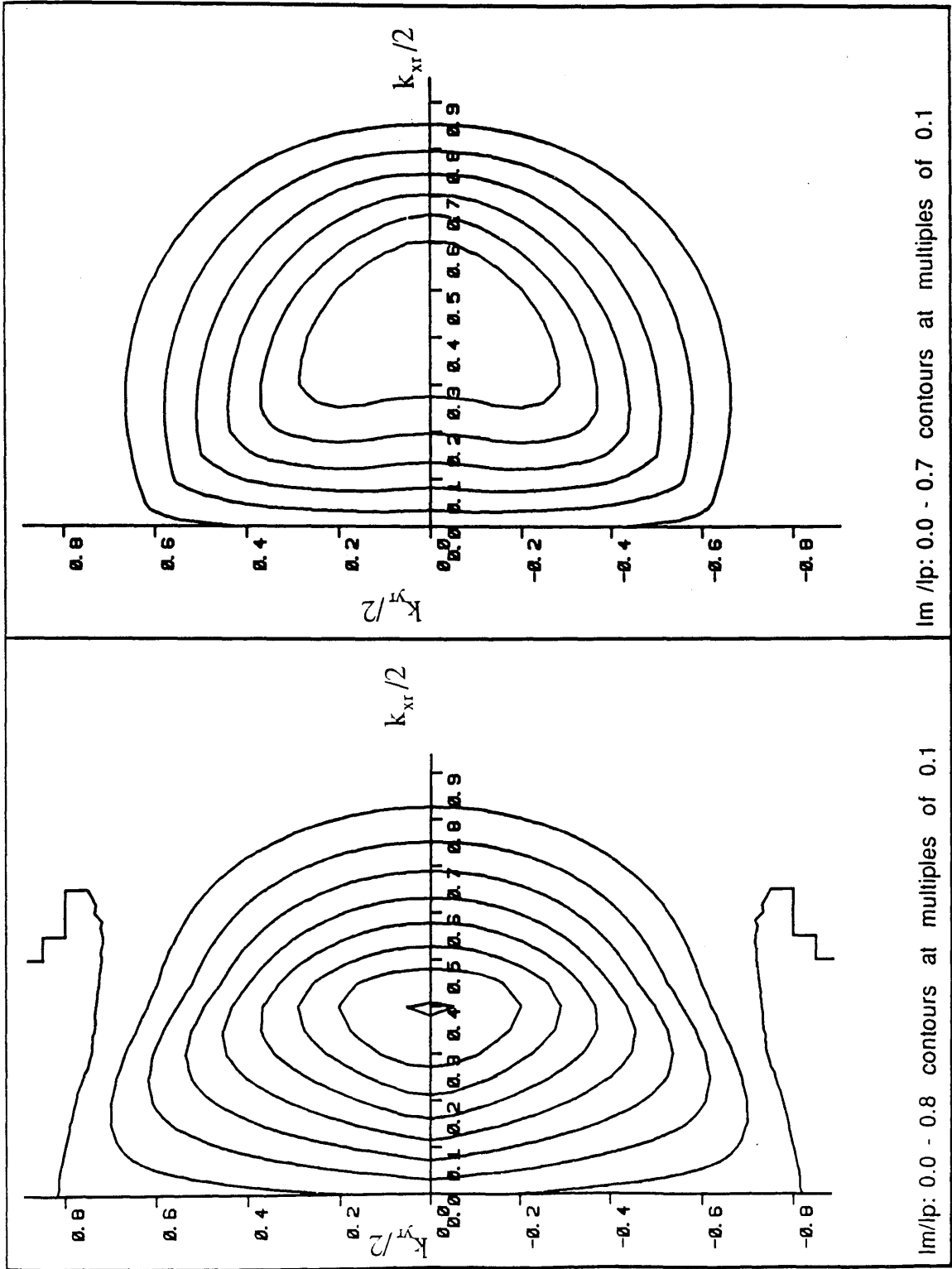


FIGURE 2

The contour plots
(B) and (E)
correspond to
the plots
(B) and (E)
in Fig.3.11

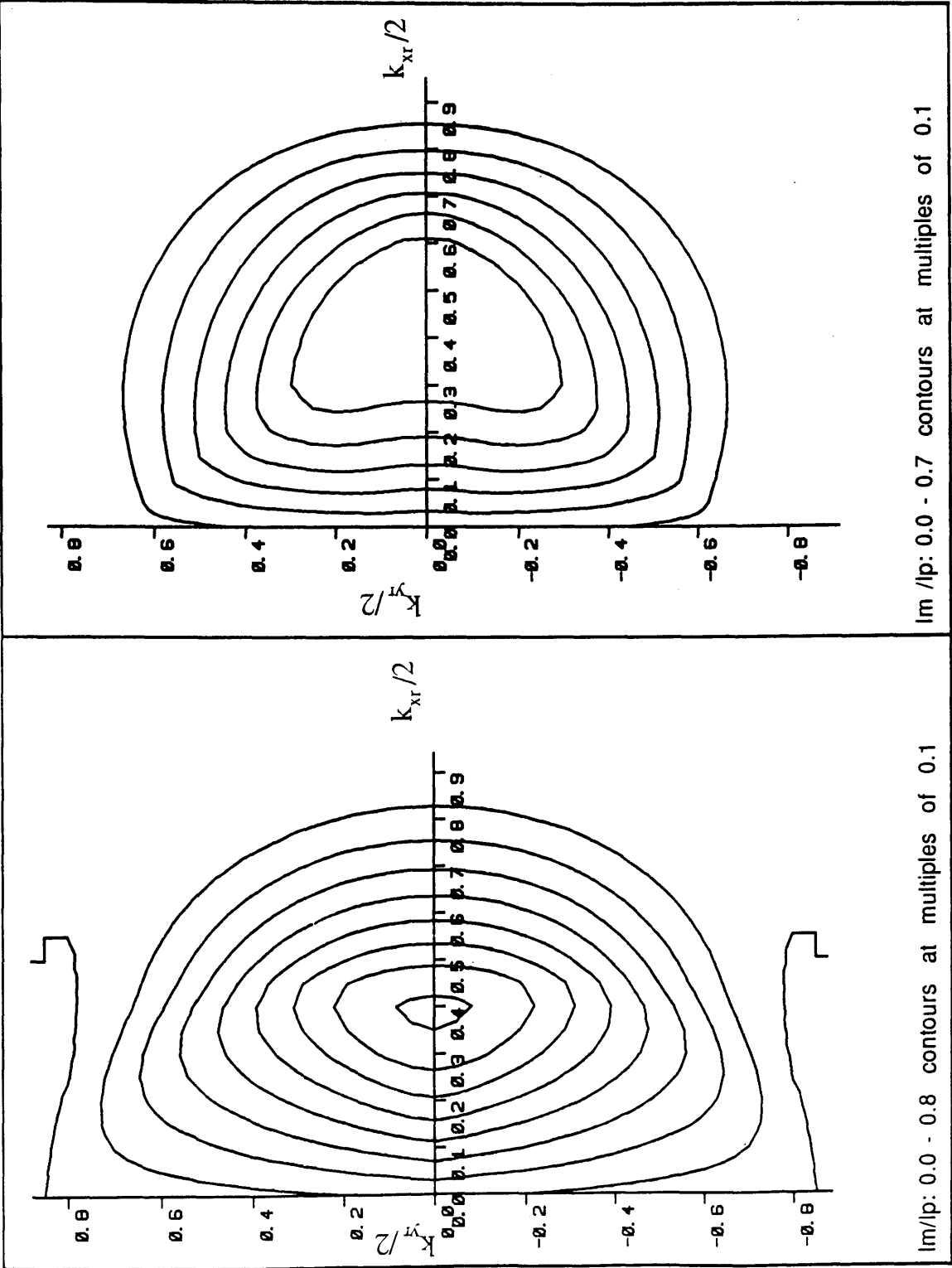


FIGURE 3

The contour plots
(C) and (F)
correspond to
the plots
(C) and (F)
in Fig.3.11

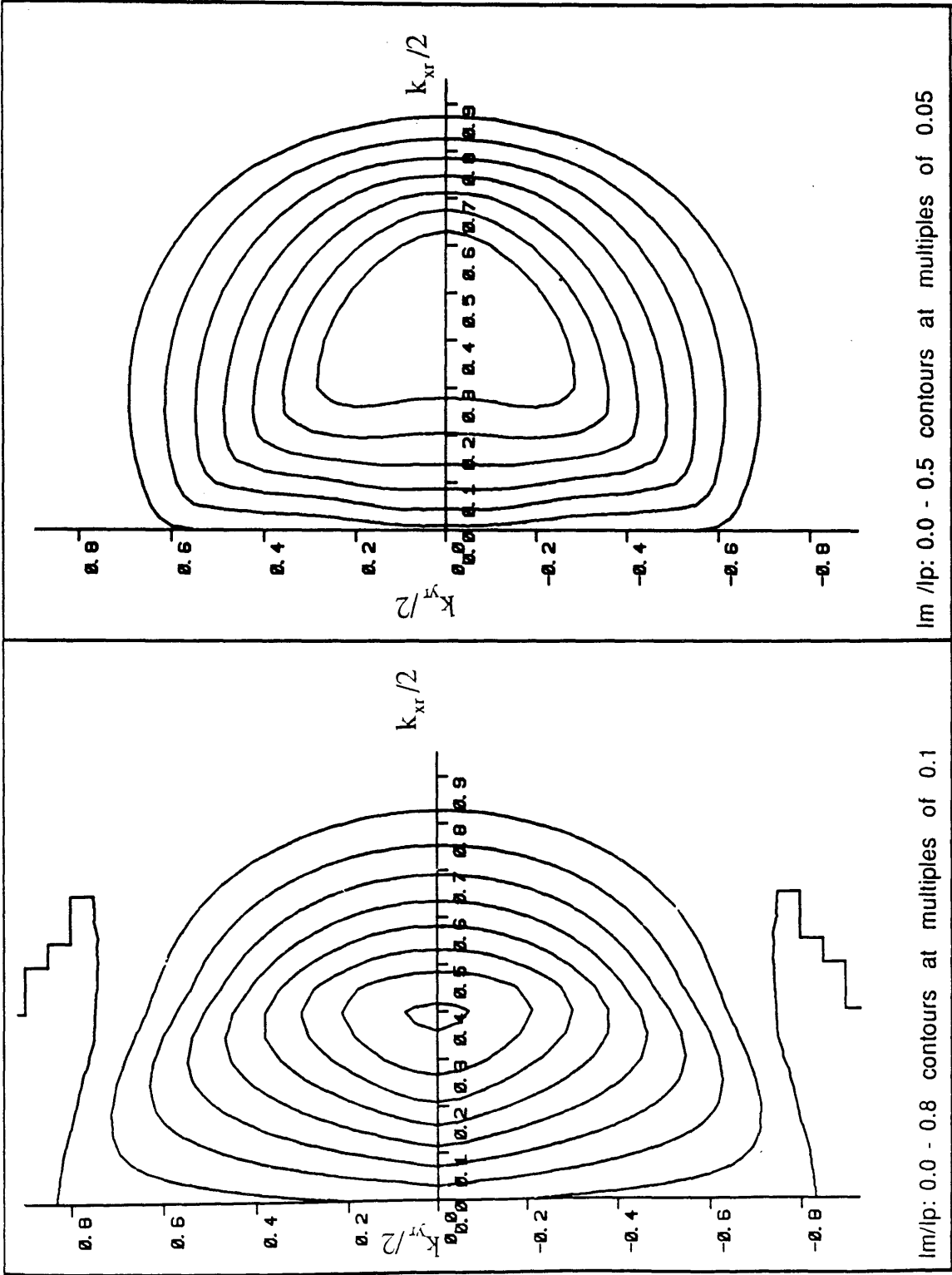


FIGURE 4

The contour plots
(A) and (D)
correspond to
the plots
(A) and (D)
in Fig.3.12

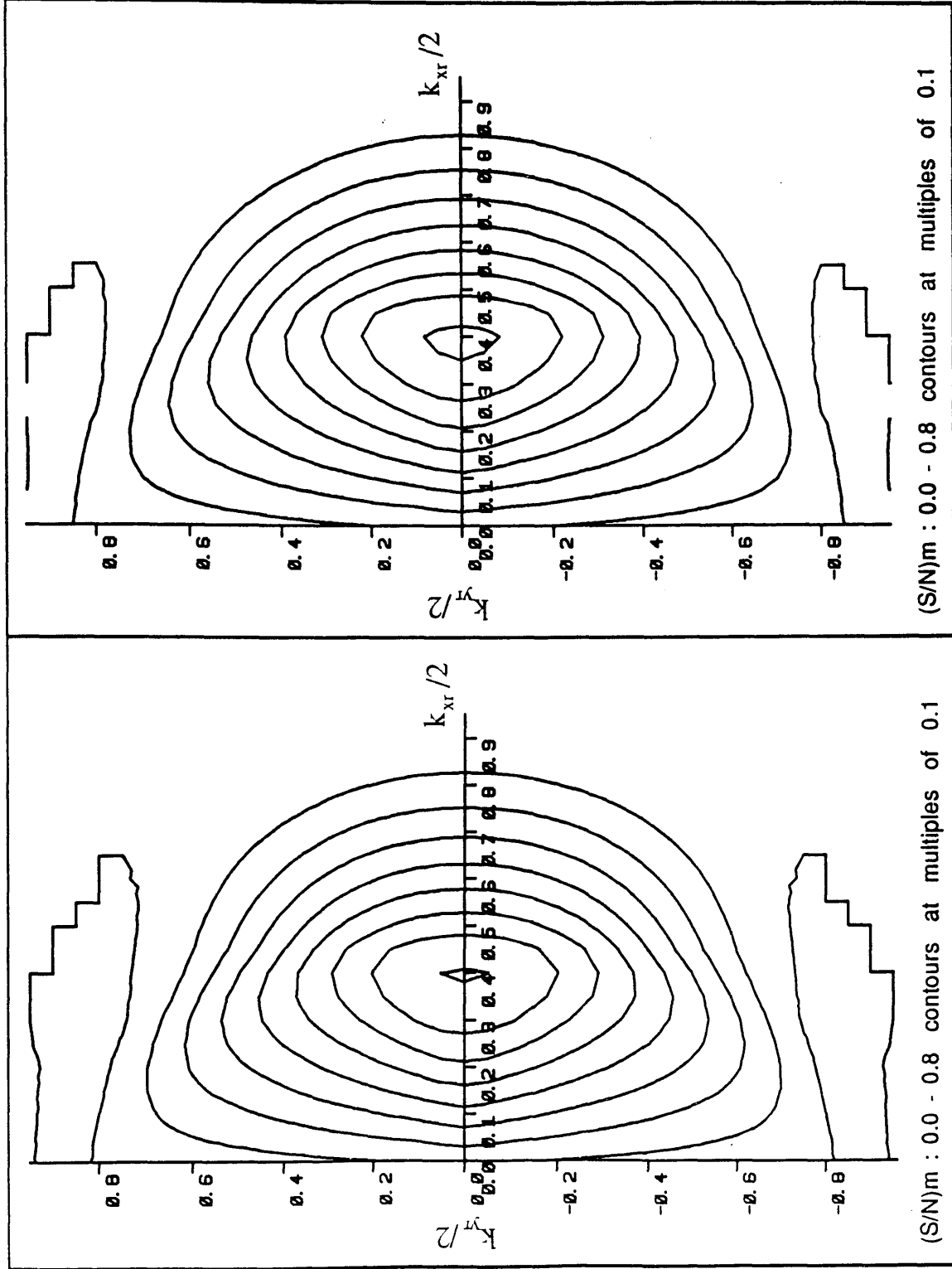


FIGURE 5

The contour plots
(B) and (E)
correspond to
the plots
(B) and (E)
in Fig.3.12

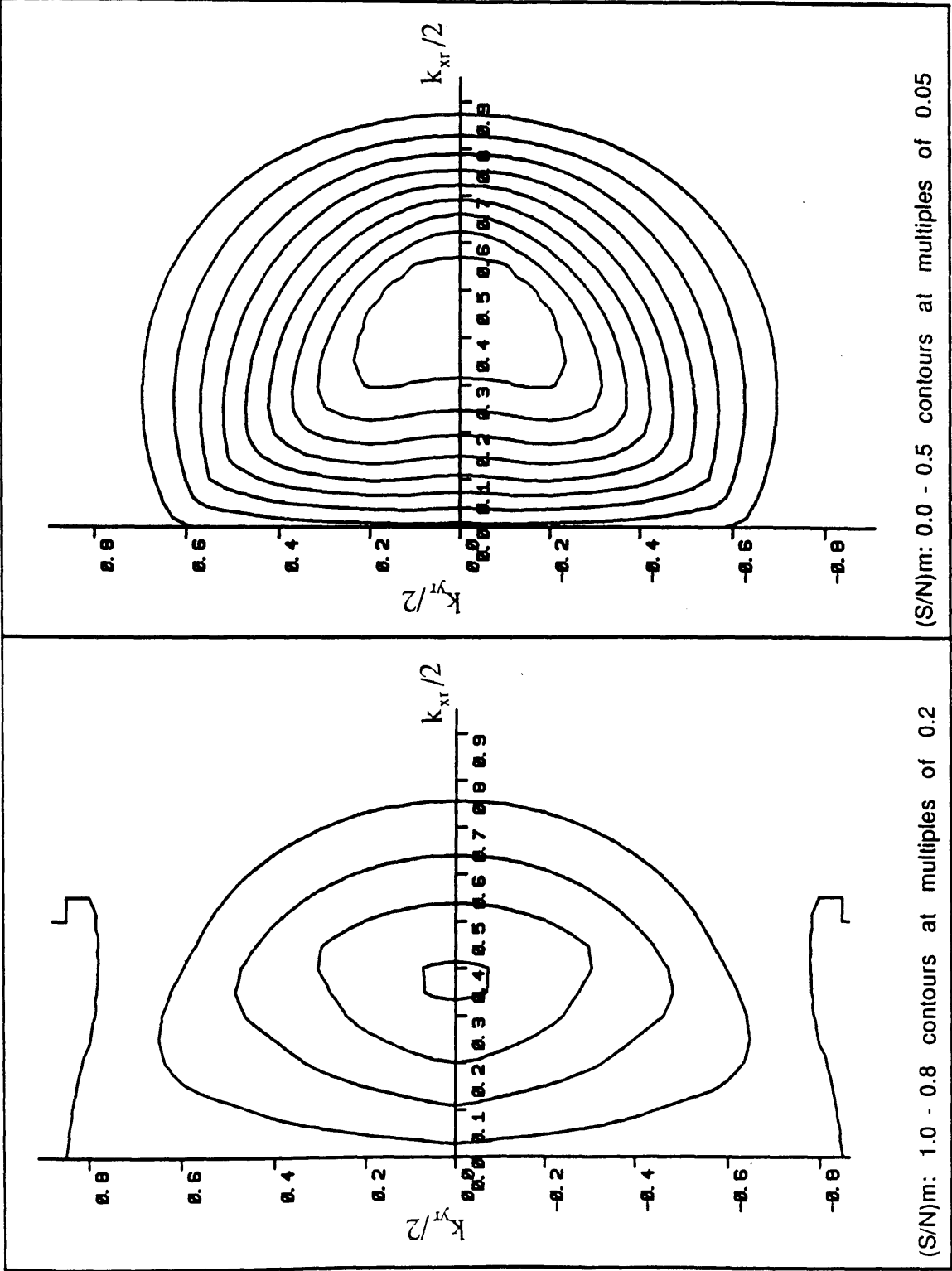
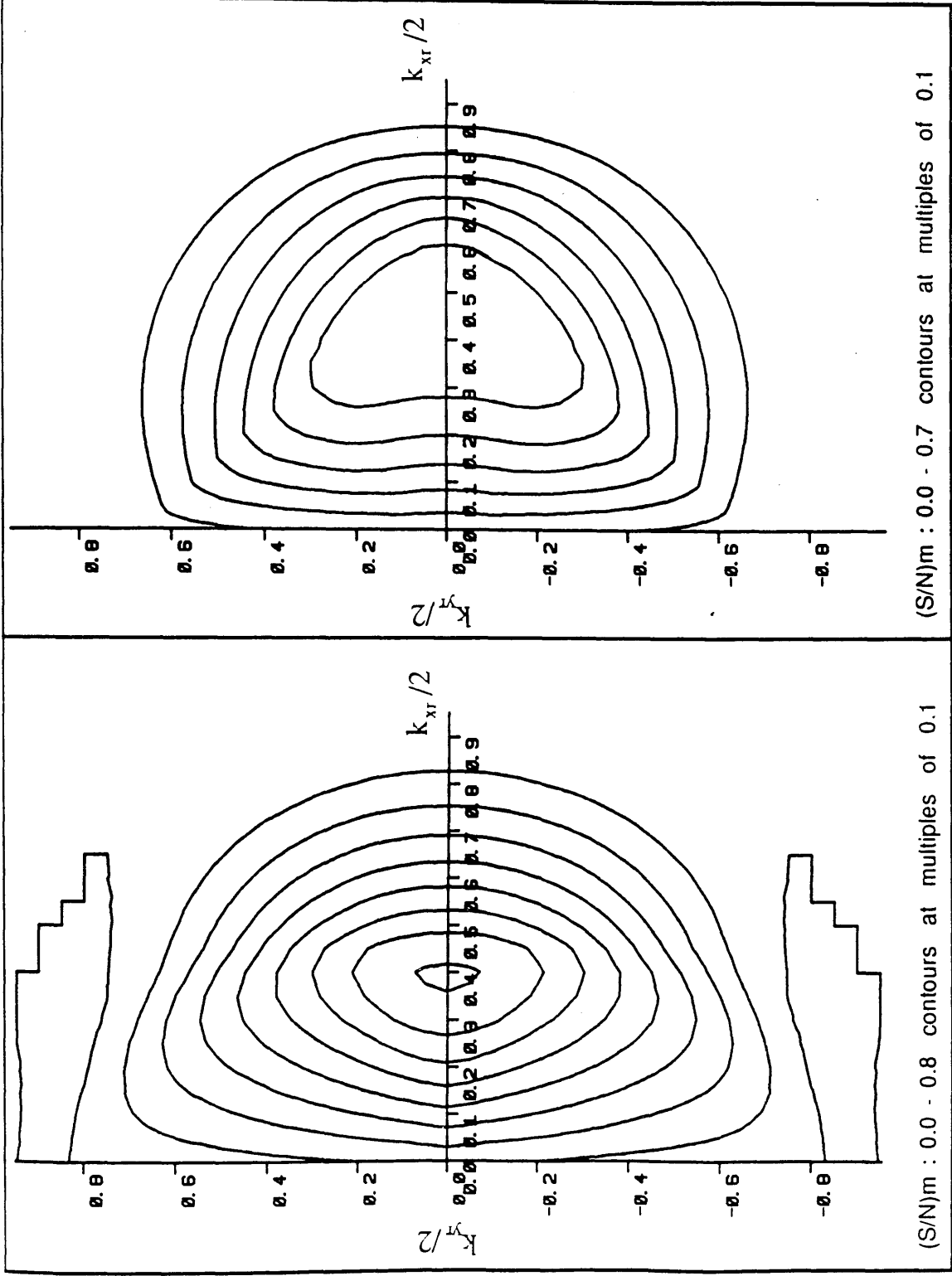


FIGURE 6

The contour plots
(C) and (F)
correspond to
the plots
(C) and (F)
in Fig.3.12



(C)

(F)

FIGURE 7

The contour plots
(A) and (D)
correspond to
the plots
(A) and (D)
in Fig.3.13

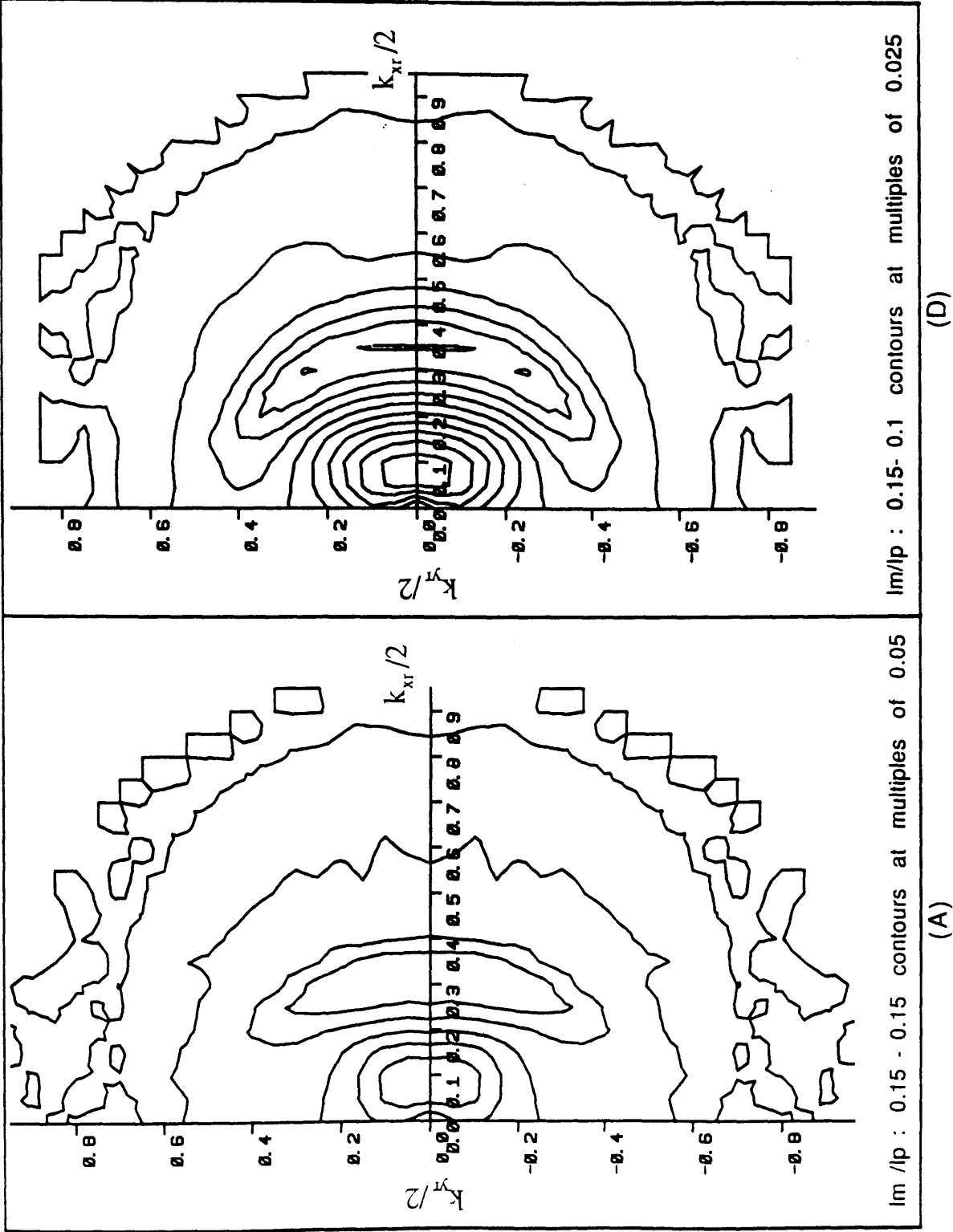


FIGURE 8

The contour plots
(B) and (E)
correspond to
the plots
(B) and (E)
in Fig.3.13

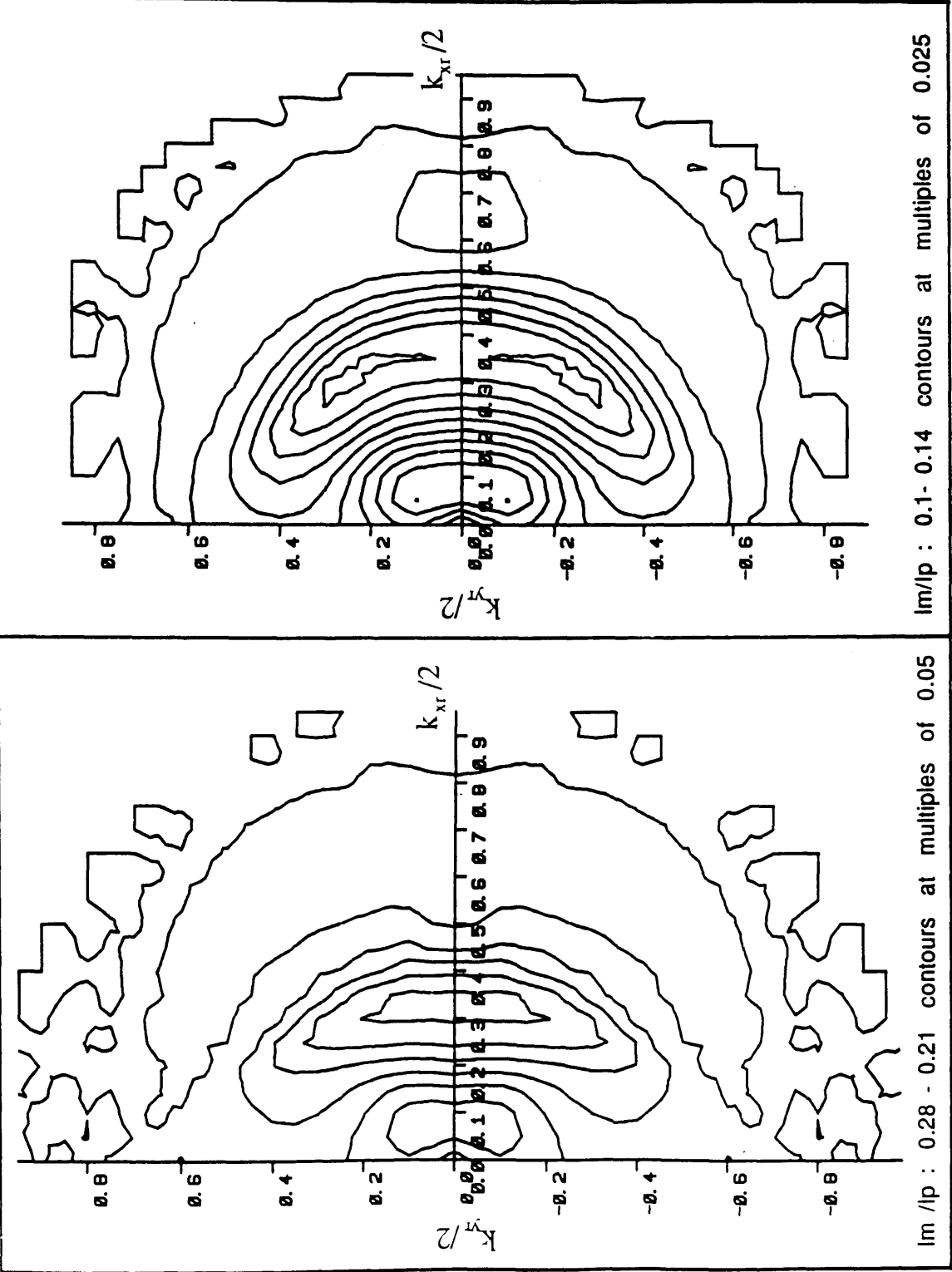
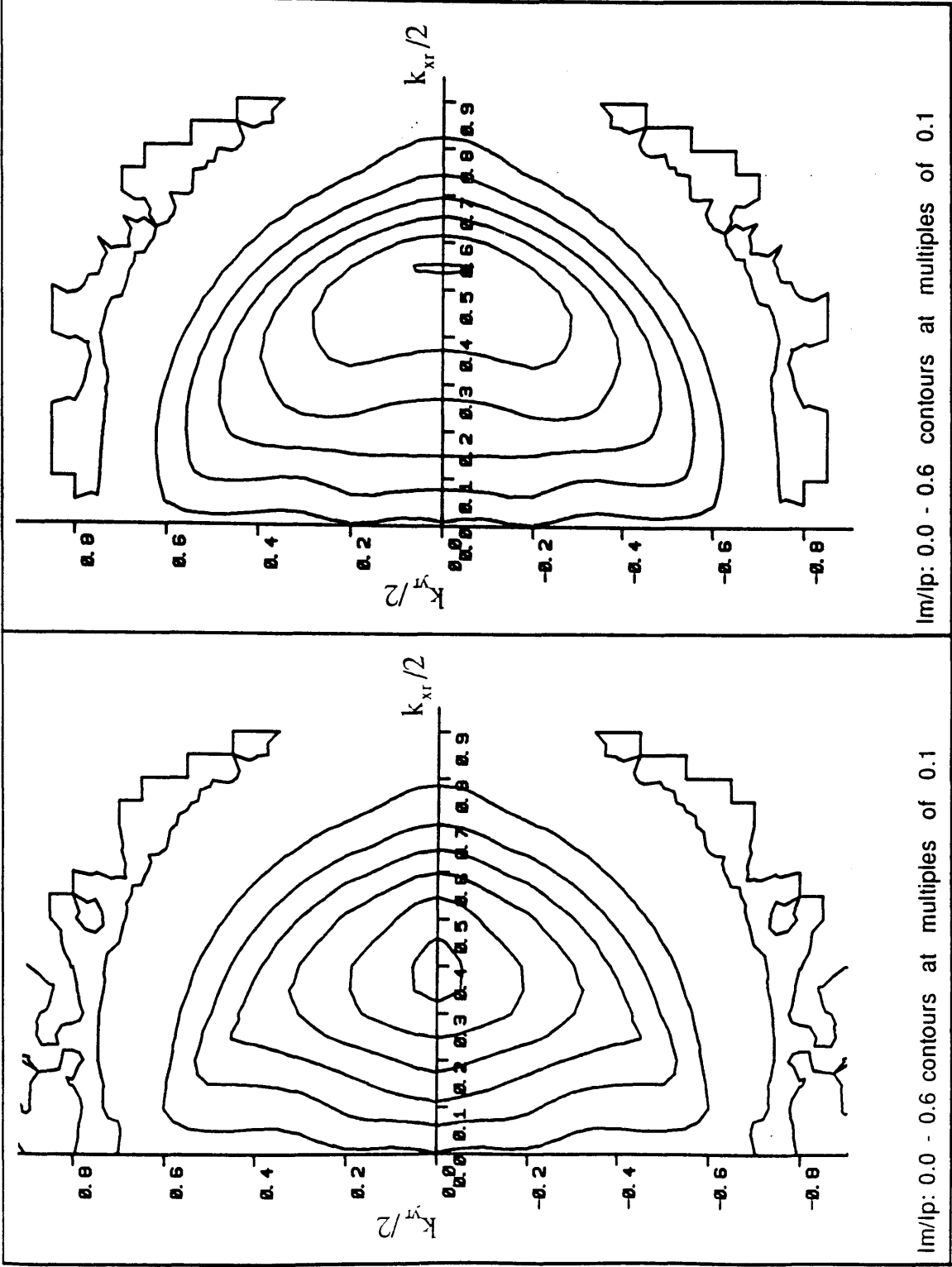


FIGURE 9

The contour plots
(C) and (F)
correspond to
the plots
(C) and (F)
in Fig.3.13



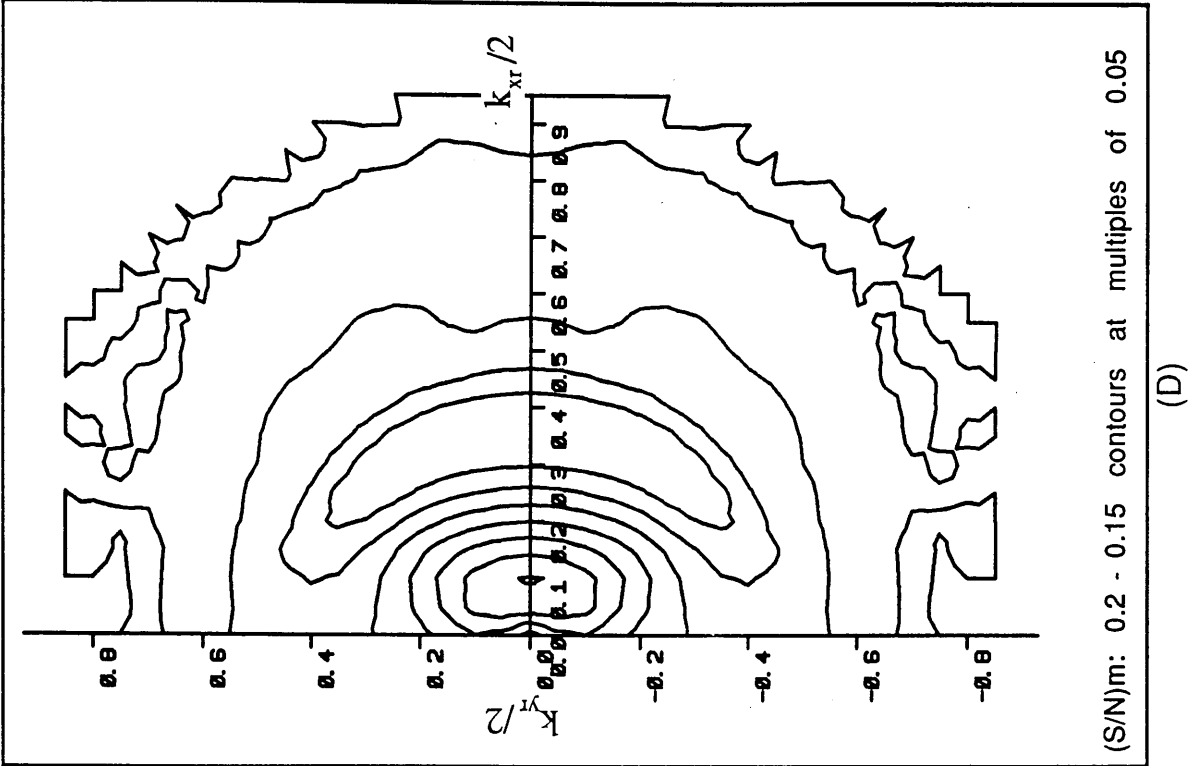
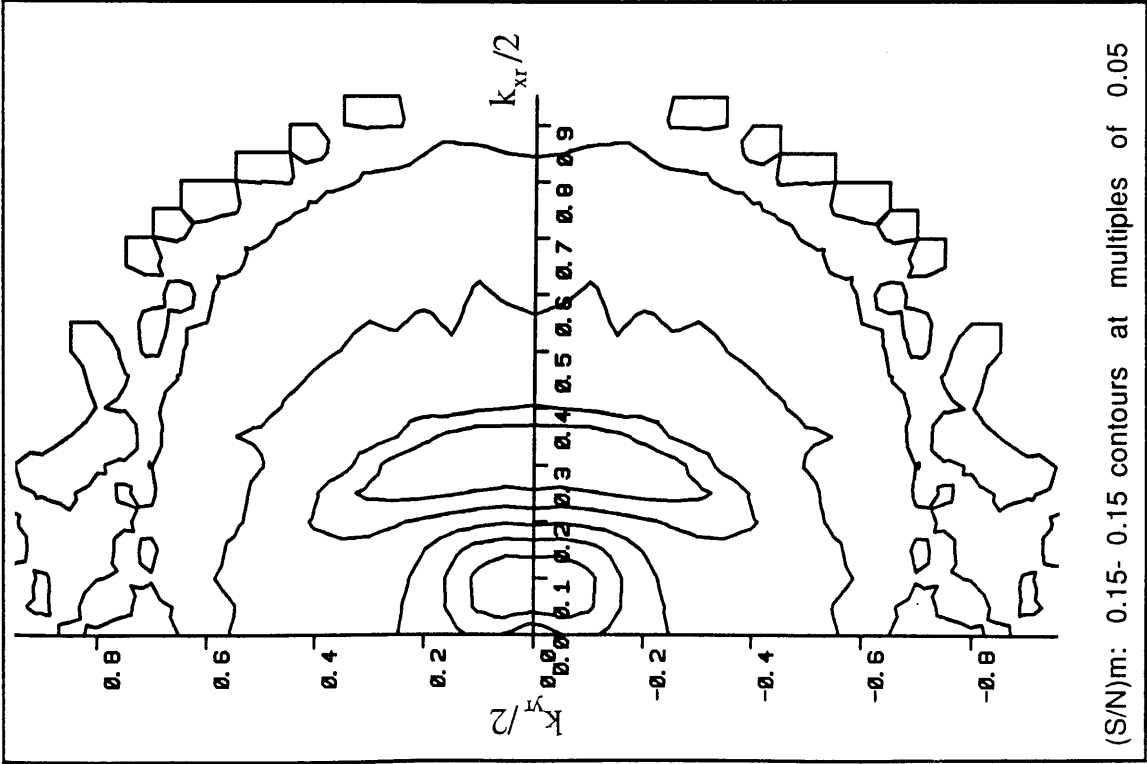


FIGURE 10

The contour plots
(A) and (D)
correspond to
the plots
(A) and (D)
in Fig.3.14

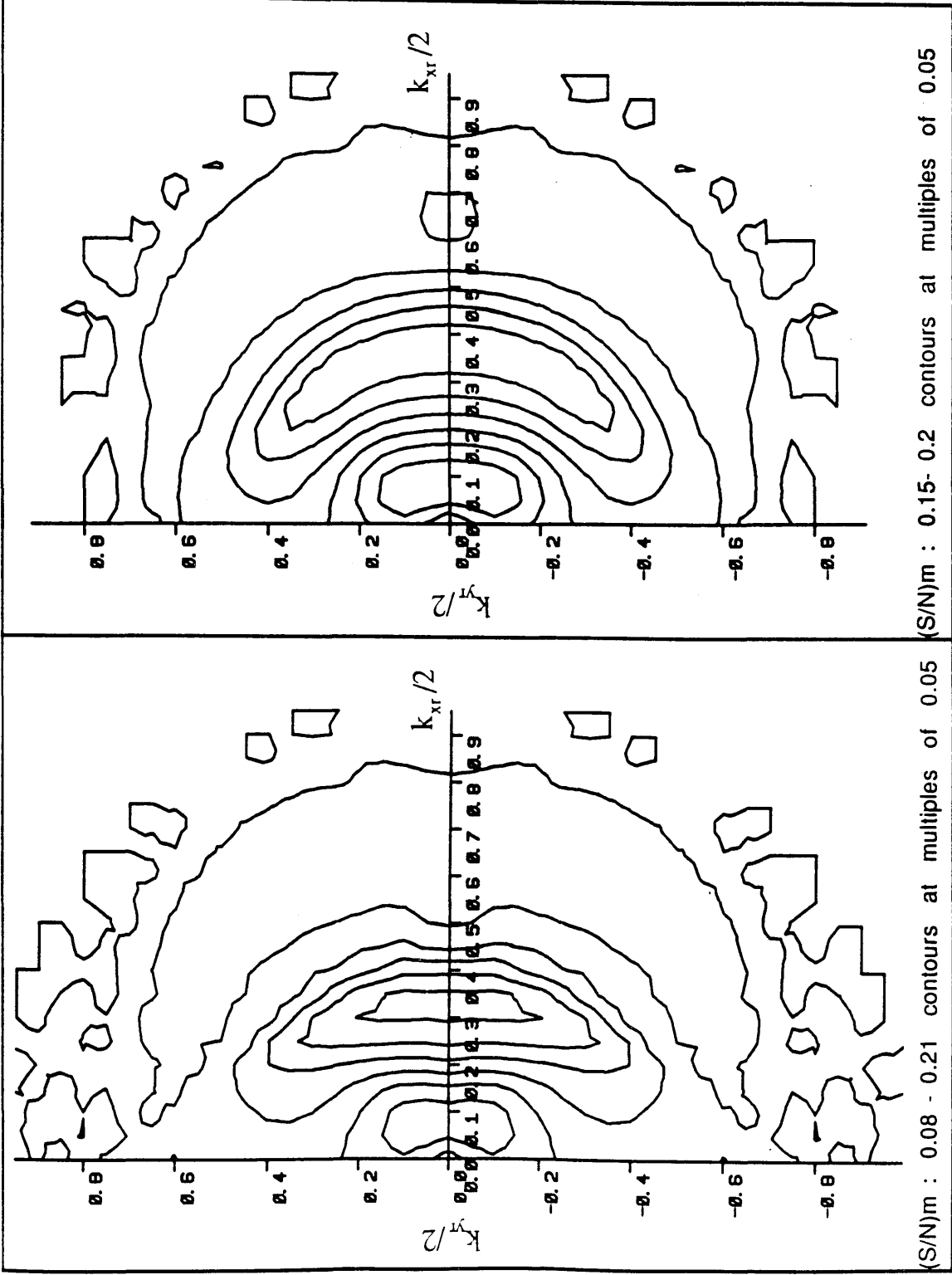


FIGURE 11

The contour plots
(B) and (E)
correspond to
the plots
(B) and (E)
in Fig.3.14

FIGURE 12

The contour plots
(C) and (F)
correspond to
the plots
(C) and (F)
in Fig.3.14

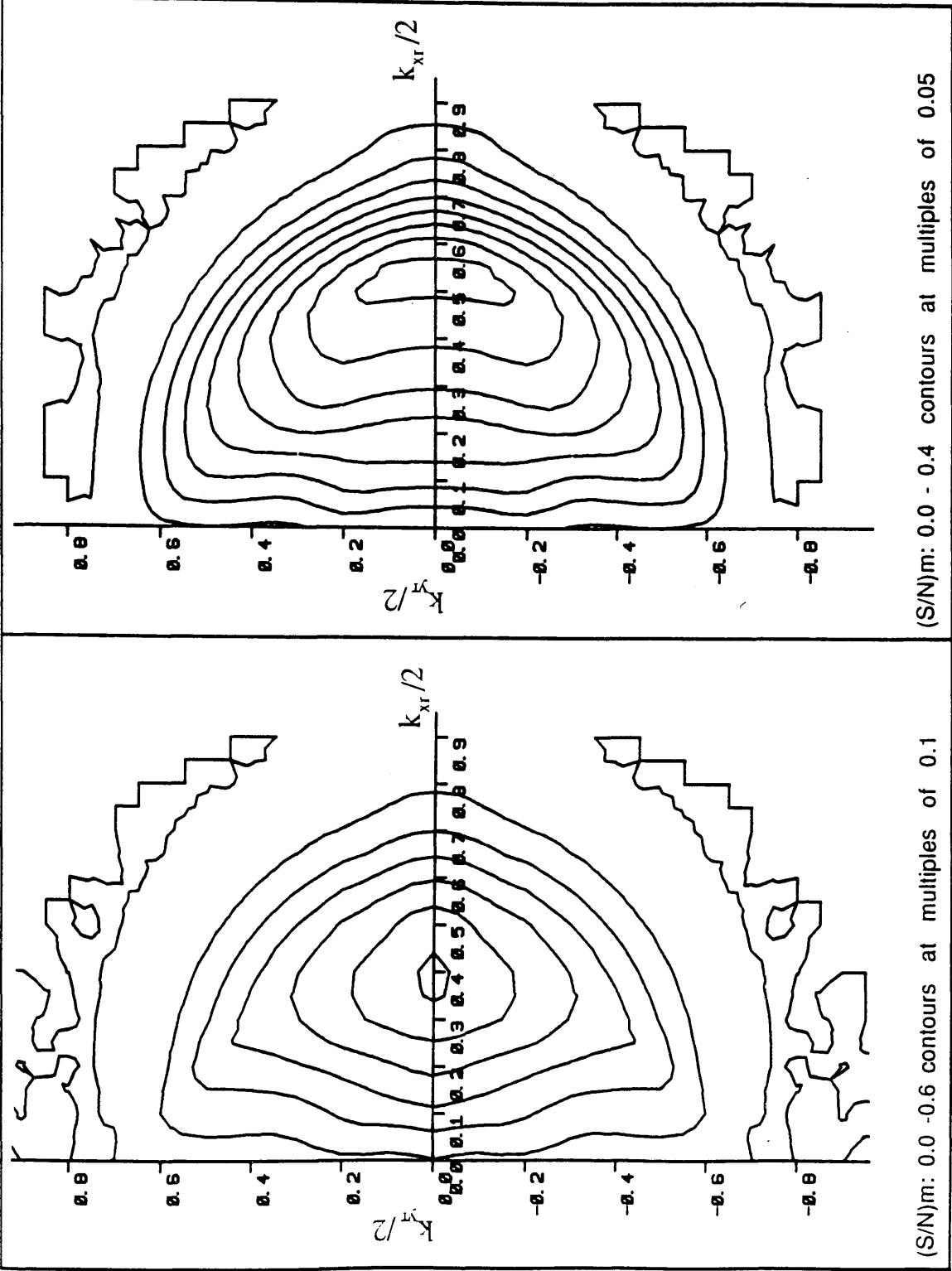


FIGURE 13

The contour plots
(A) and (D)
correspond to
the plots
(A) and (D)
in Fig.3.15

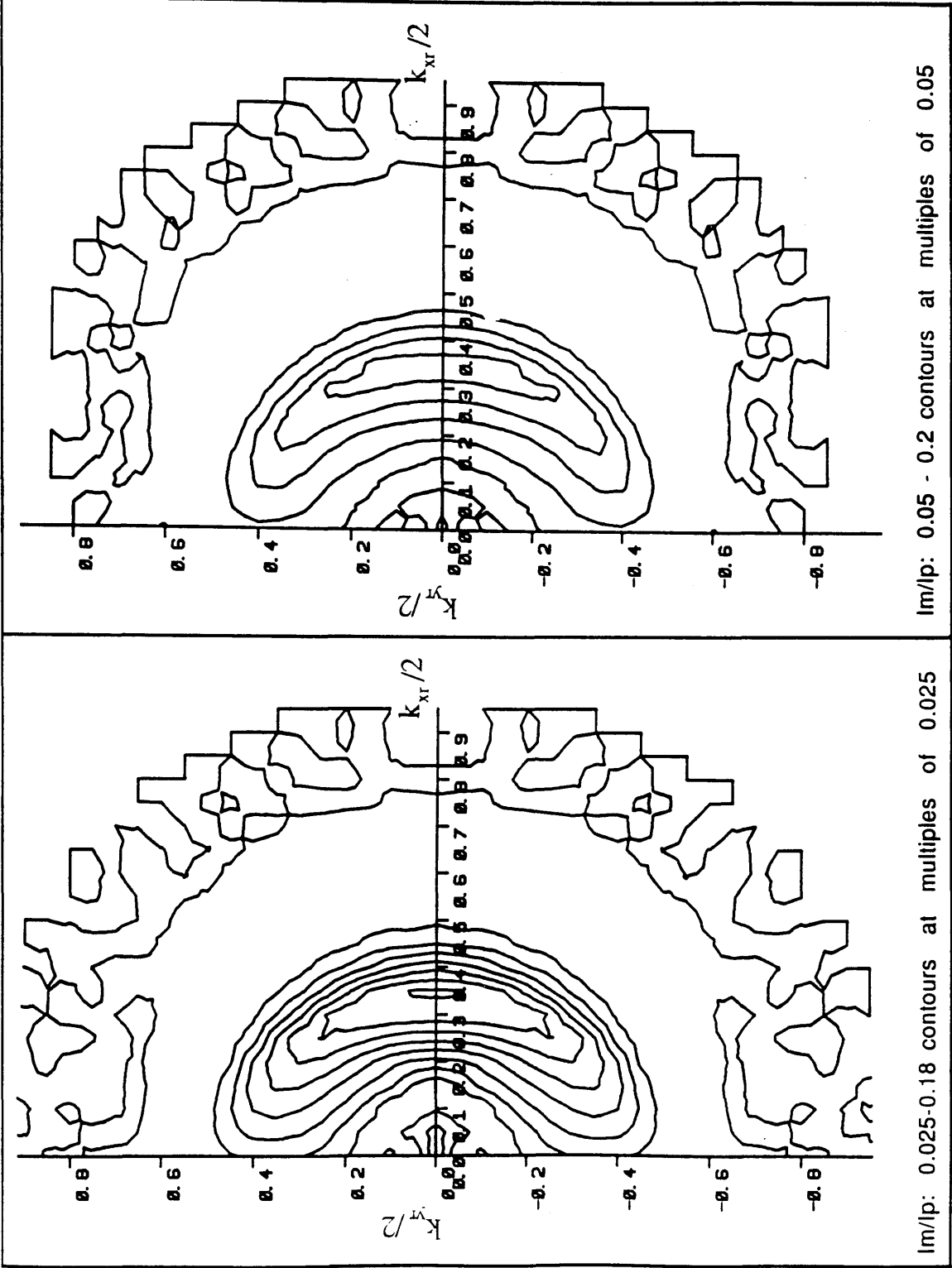


FIGURE 14

The contour plots
(B) and (E)
correspond to
the plots
(B) and (E)
in Fig.3.15

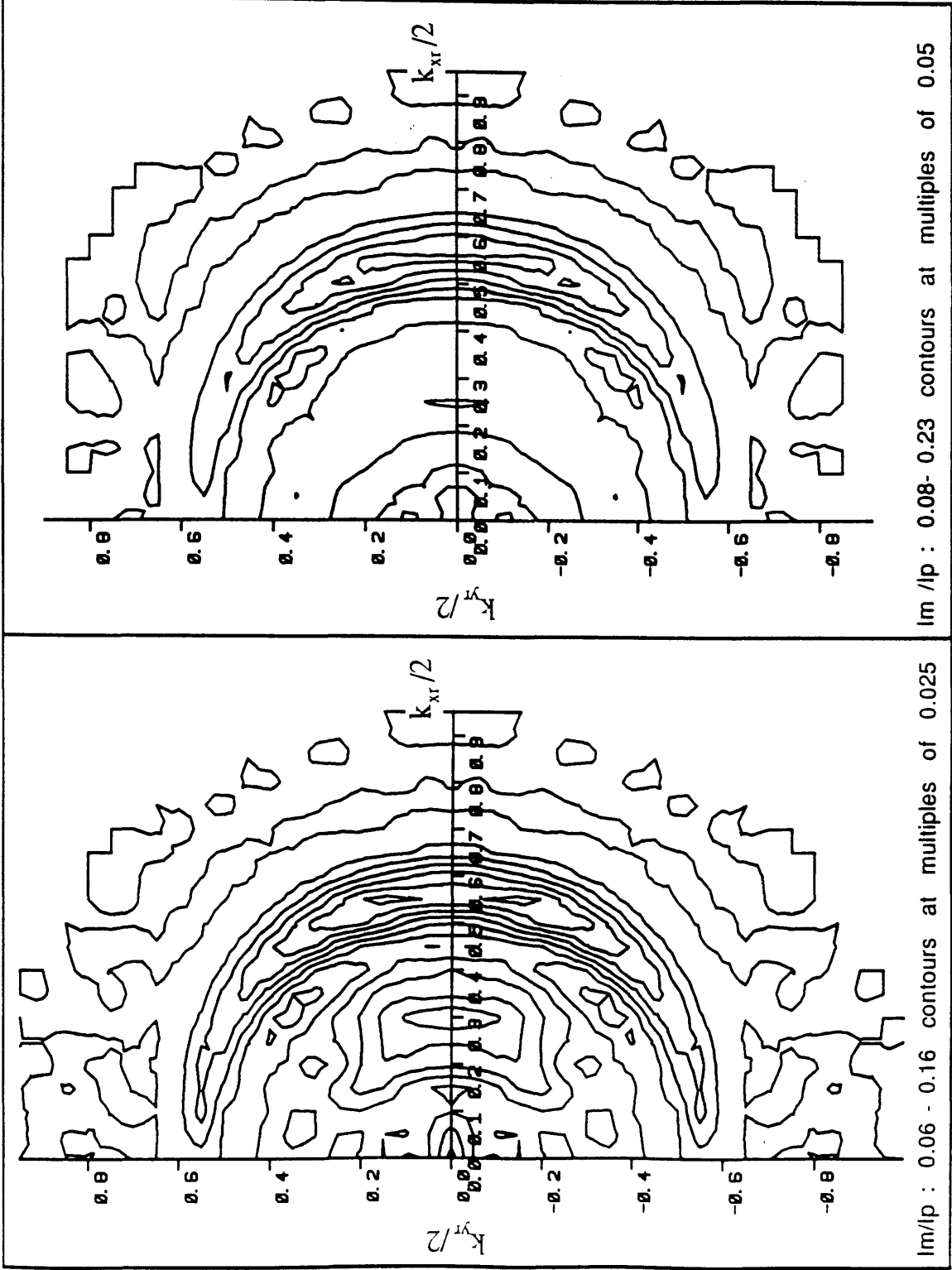


FIGURE 15

The contour plots
(C) and (F)
correspond to
the plots
(C) and (F)
in Fig.3.15

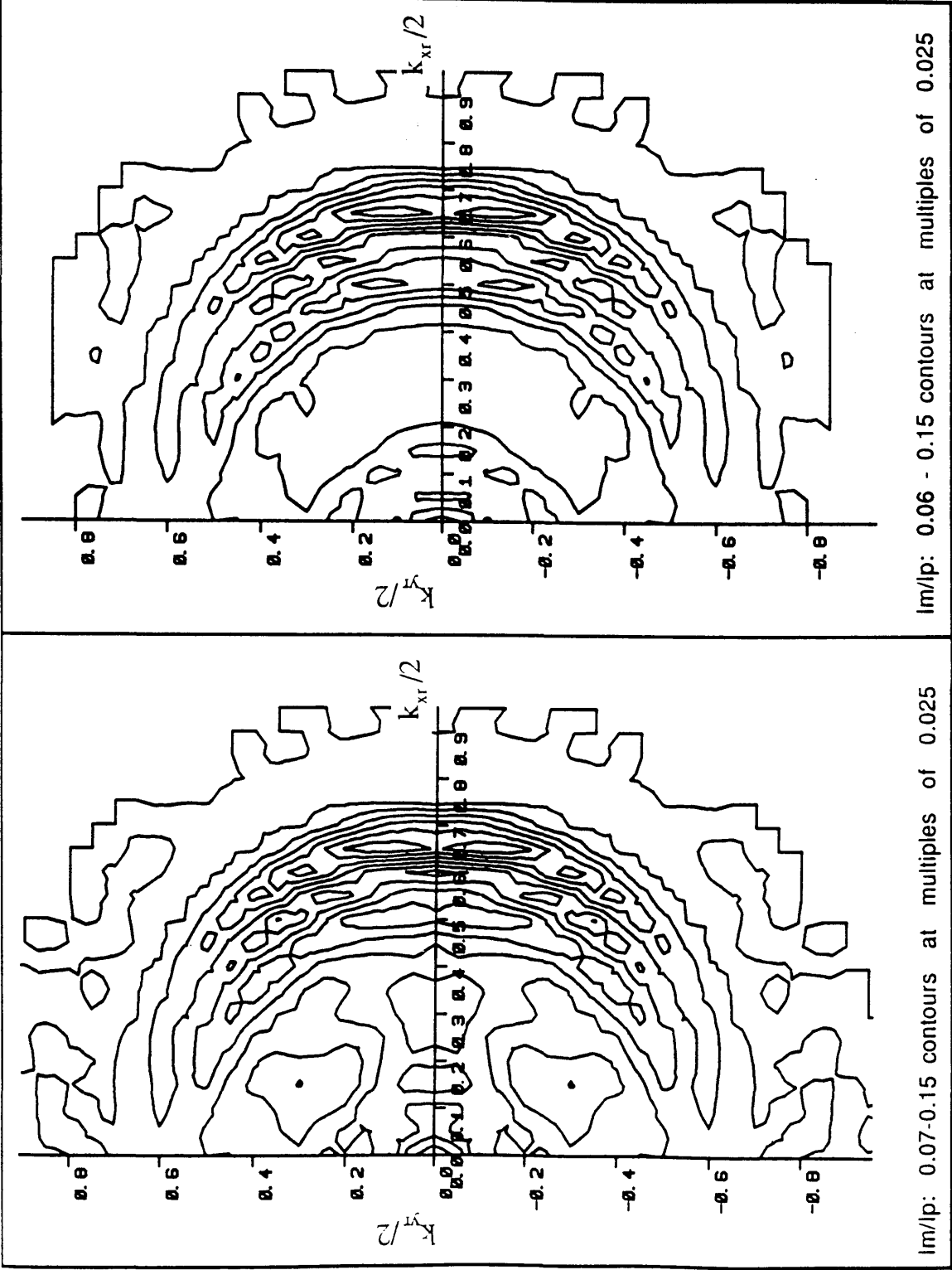


FIGURE 16

The contour plots
(A) and (D)
correspond to
the plots
(A) and (D)
in Fig.3.16

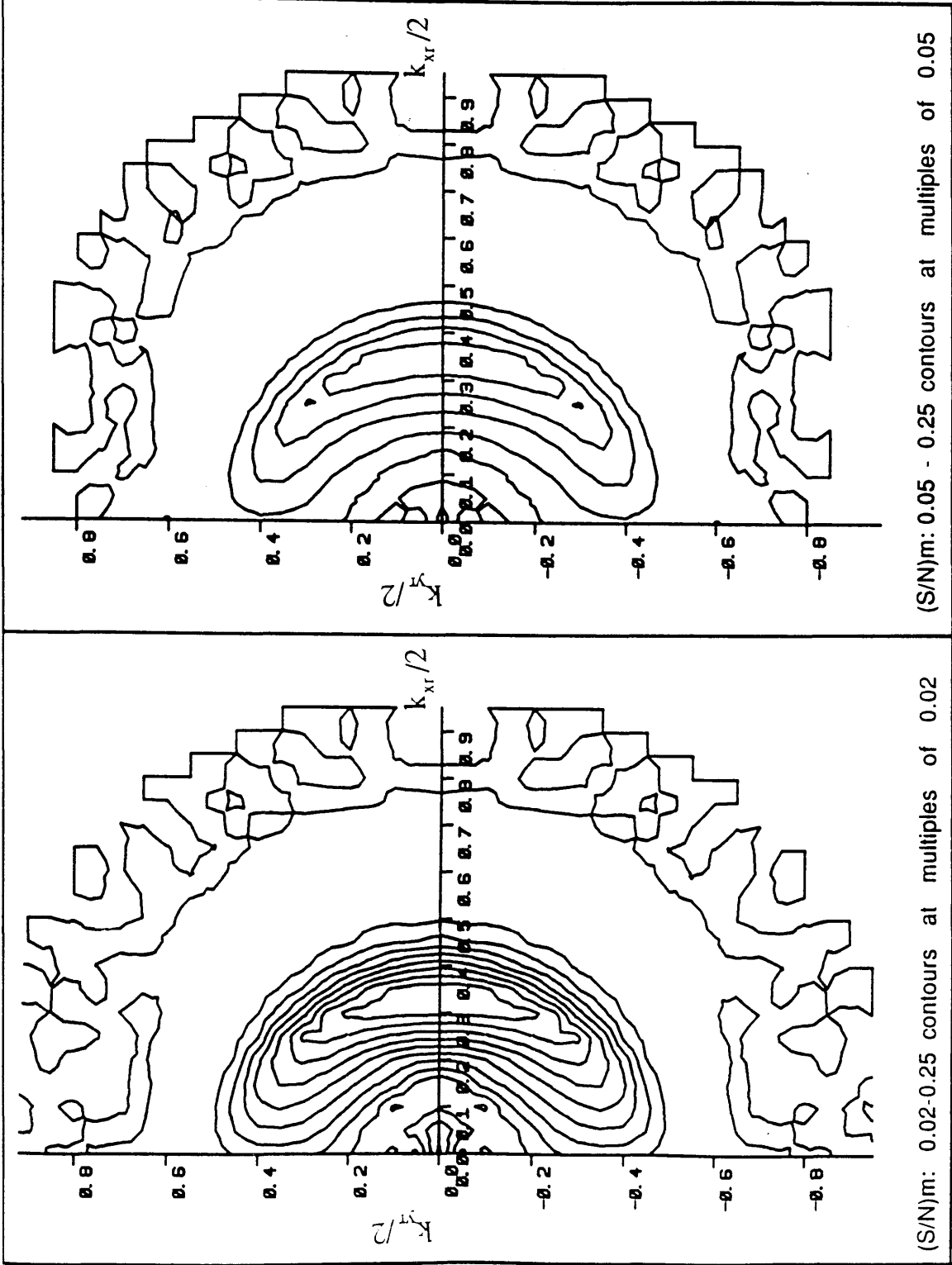


FIGURE 17

The contour plots
(B) and (E)
correspond to
the plots
(B) and (E)
in Fig.3.16

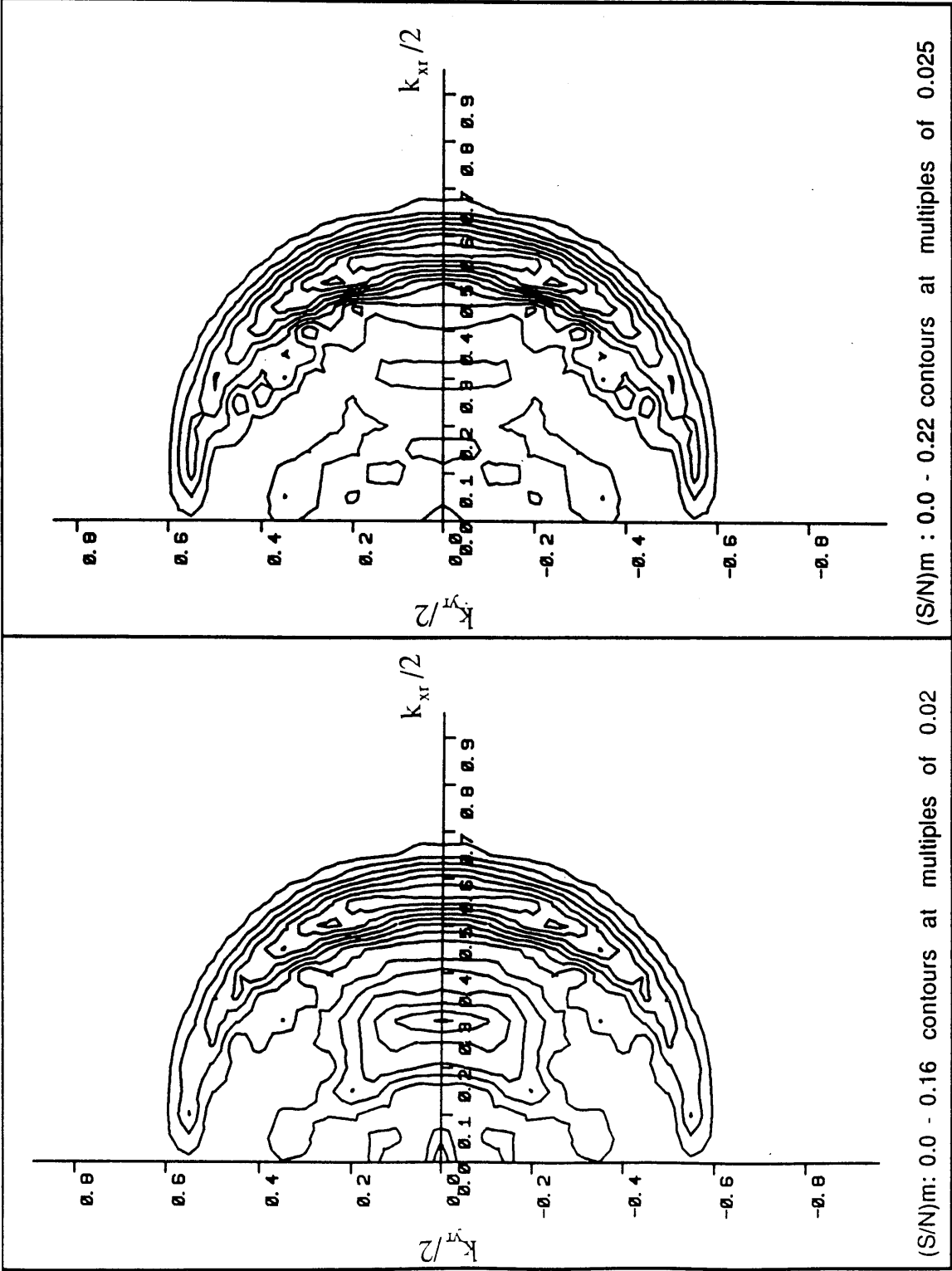


FIGURE 18

The contour plots
(C) and (F)
correspond to
the plots
(C) and (F)
in Fig.3.16

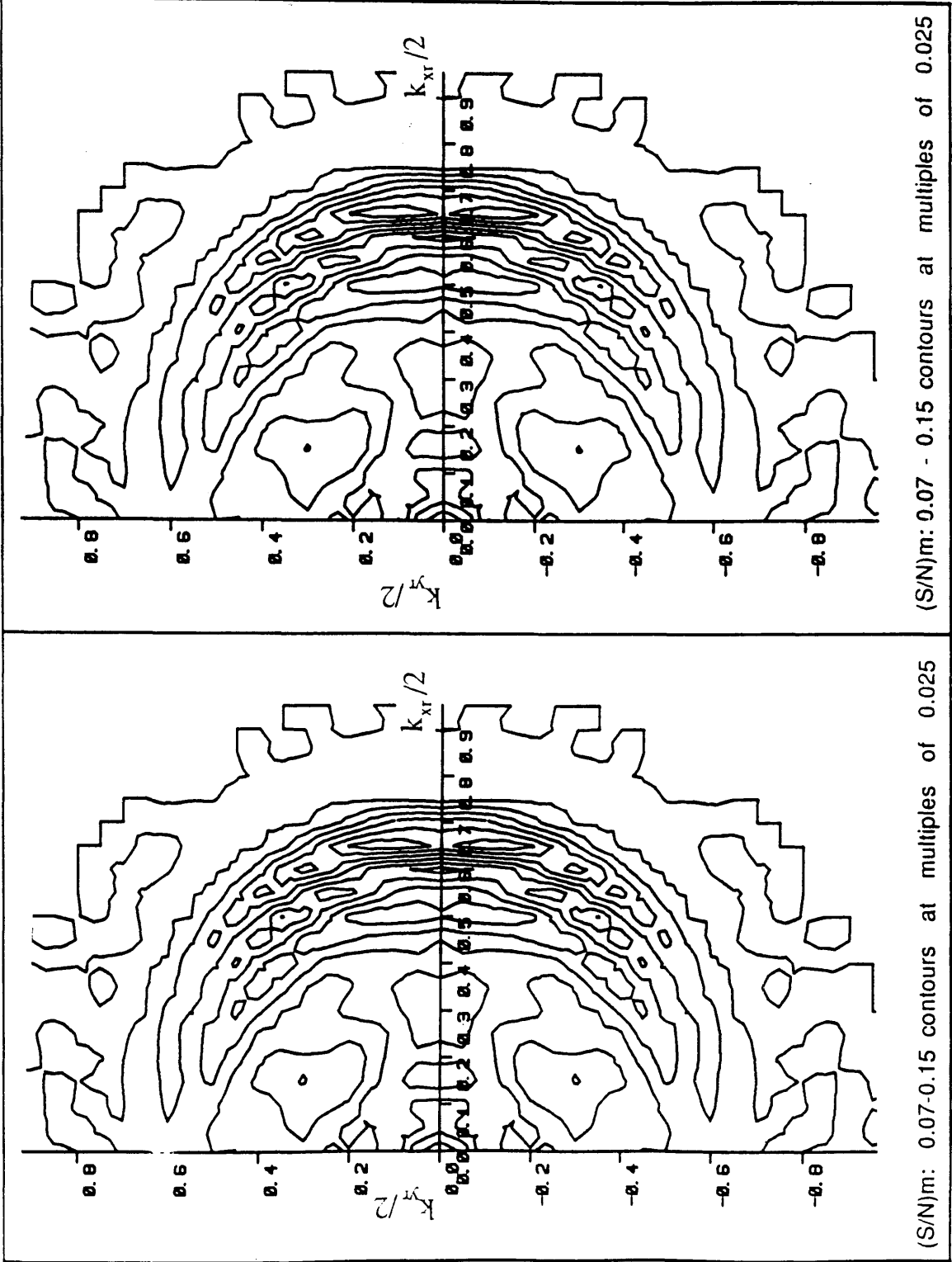


FIGURE 19

The contour plots
(A) and (D)
correspond to
the plots
(A) and (D)
in Fig.3.17

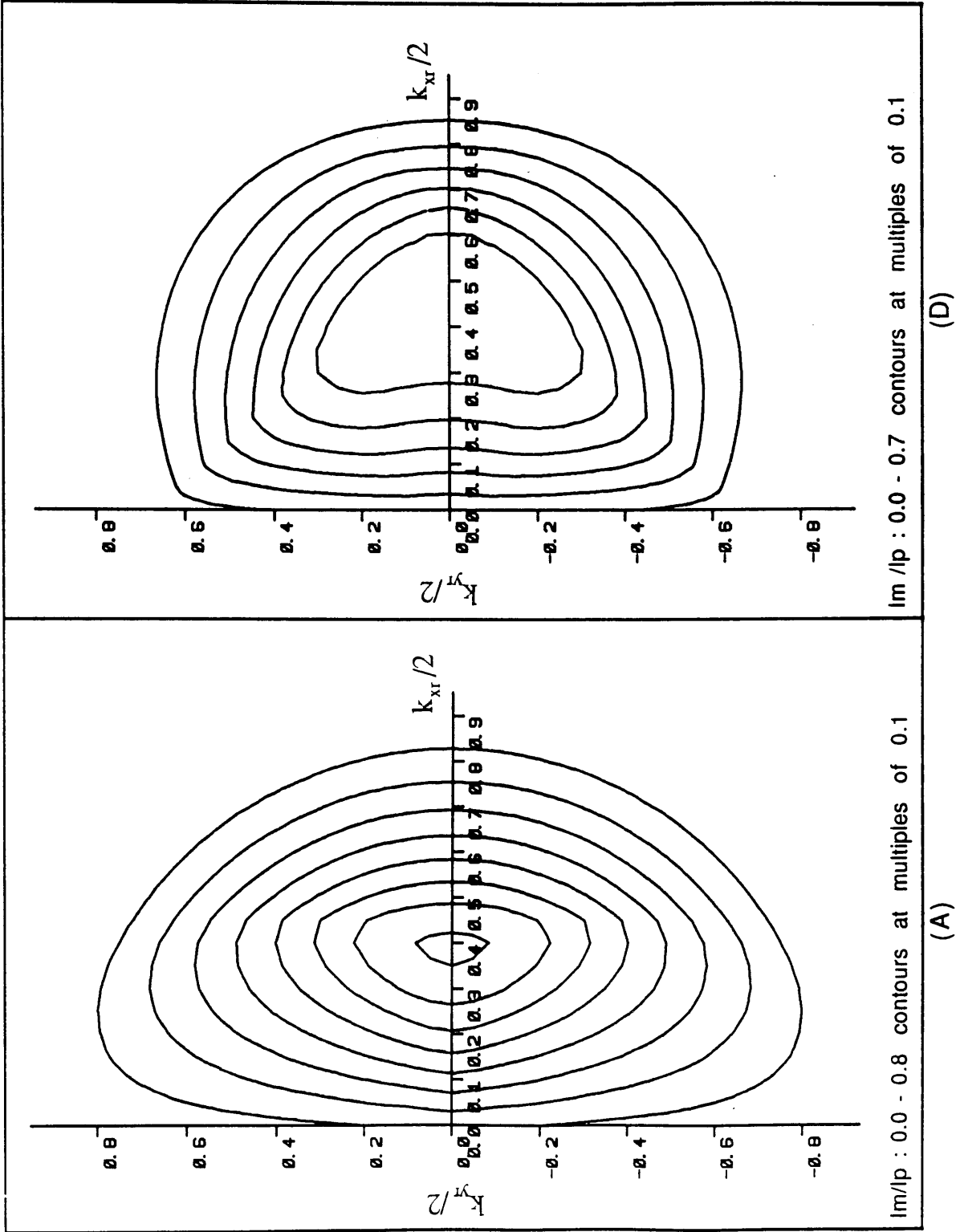


FIGURE 20

The contour plots
(B) and (E)
correspond to
the plots
(B) and (E)
in Fig.3.17

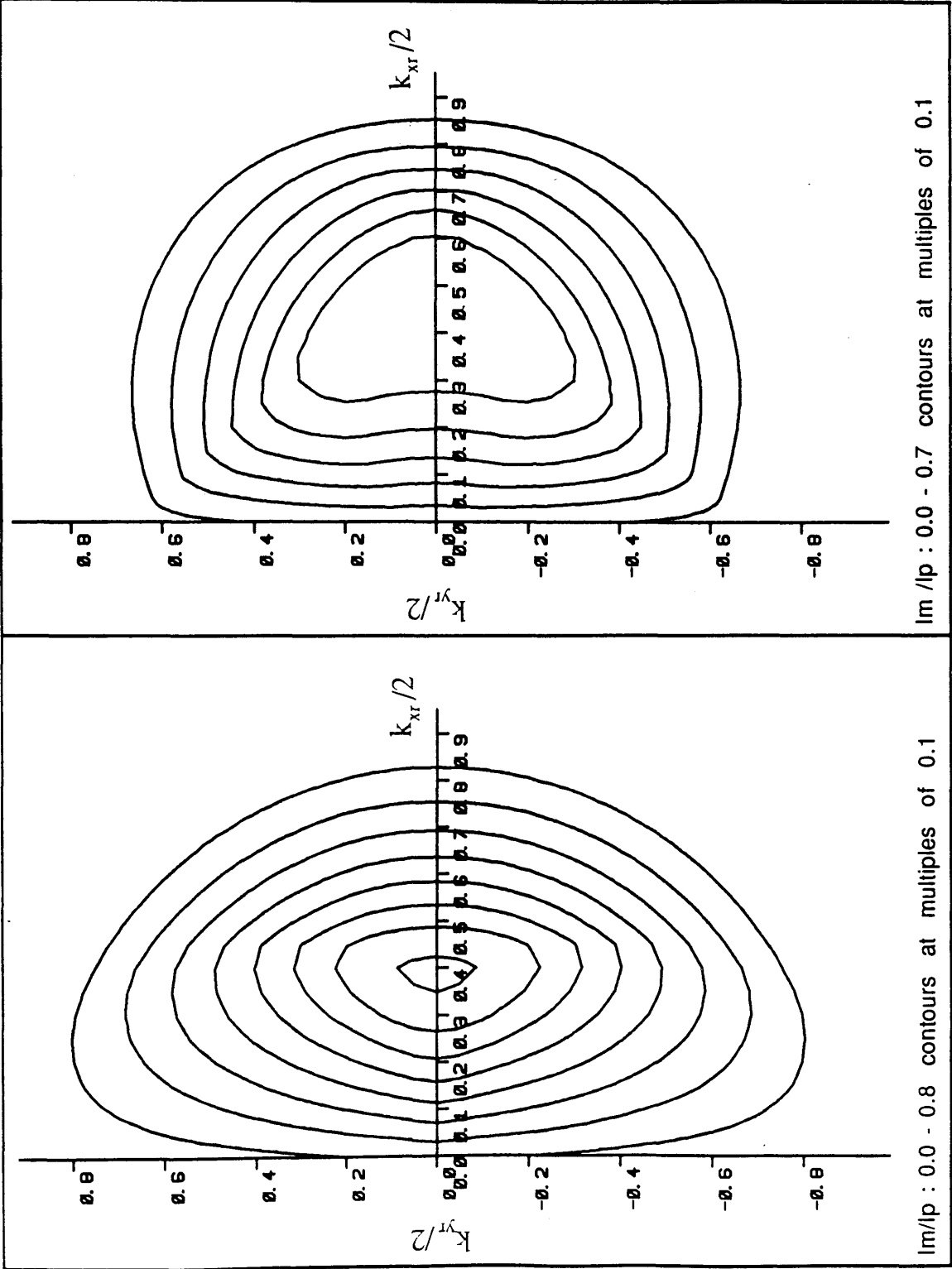


FIGURE 21

The contour plots
(C) and (F)
correspond to
the plots
(C) and (F)
in Fig.3.17

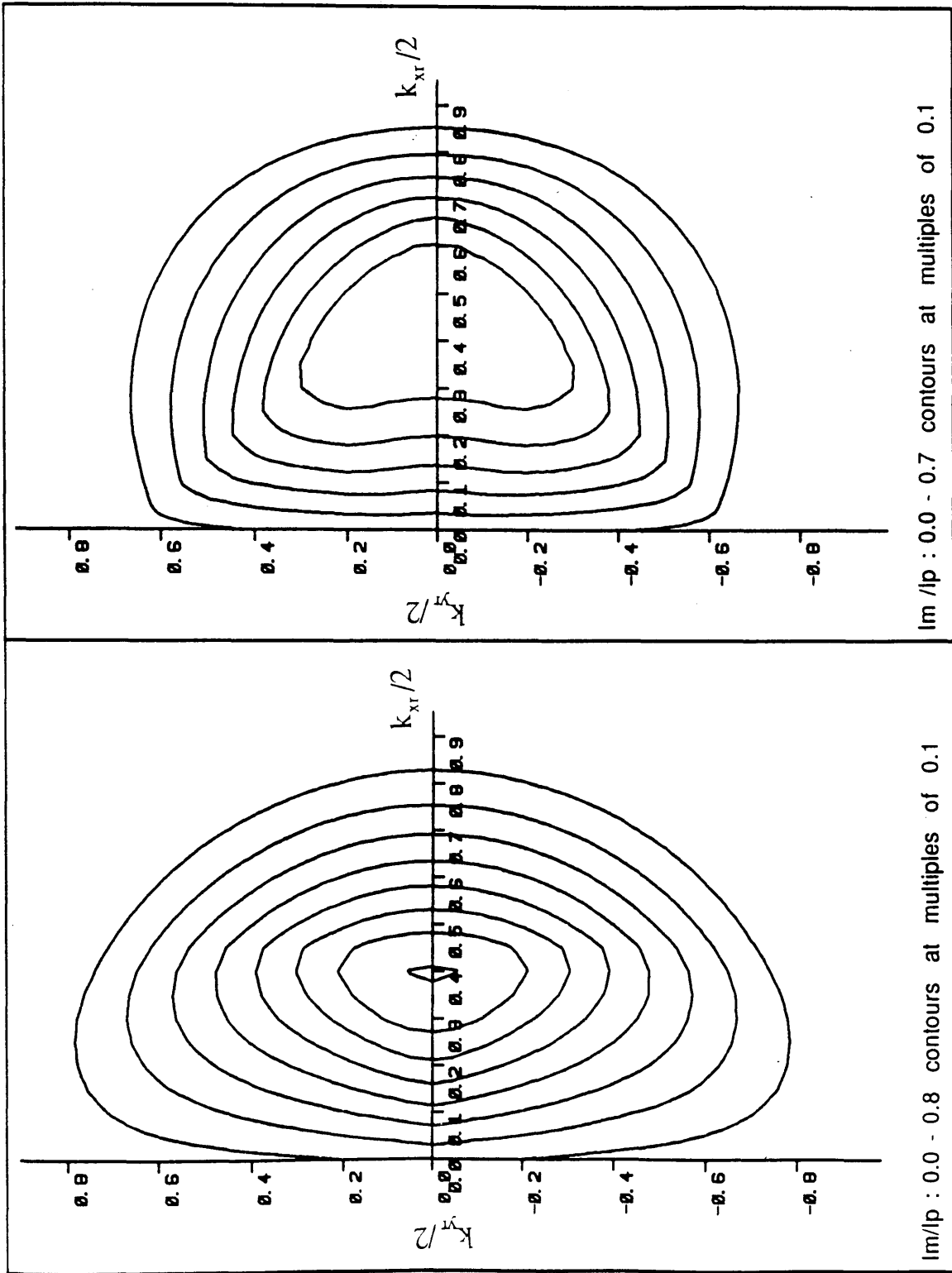


FIGURE 22

The contour plots
(A) and (D)
correspond to
the plots
(A) and (D)
in Fig.3.18

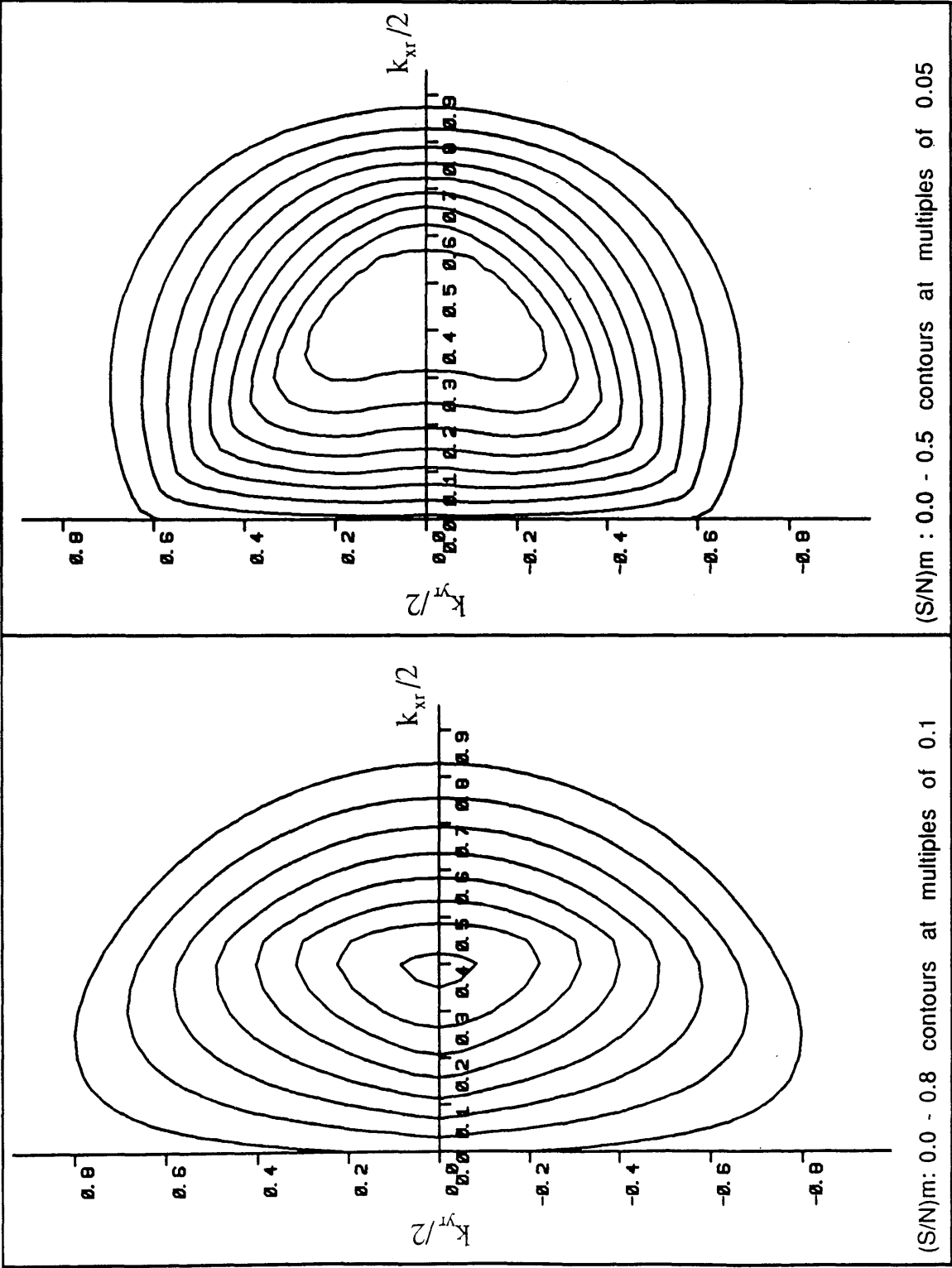


FIGURE 23

The contour plots
(B) and (E)
correspond to
the plots
(B) and (E)
in Fig.3.18

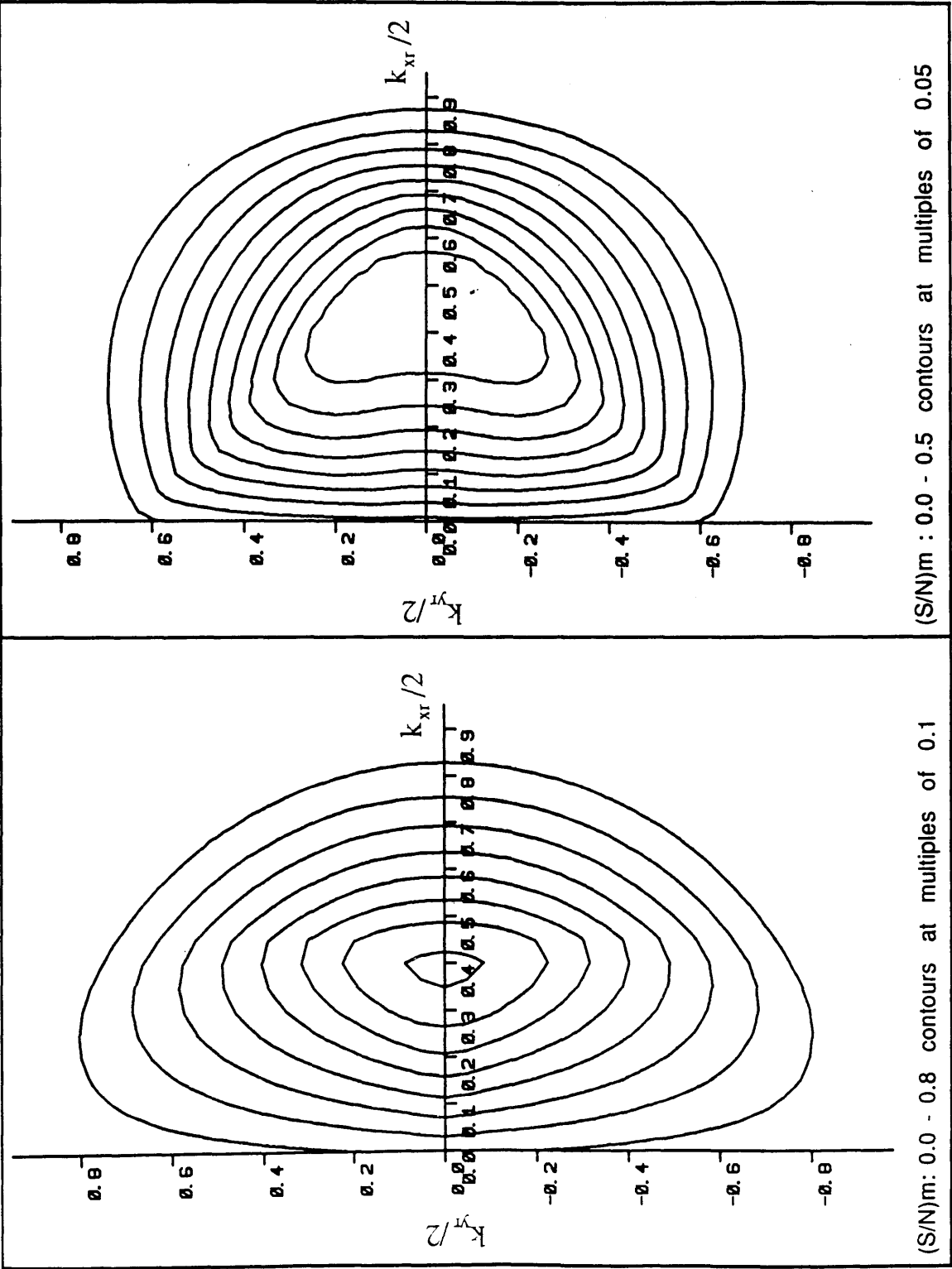
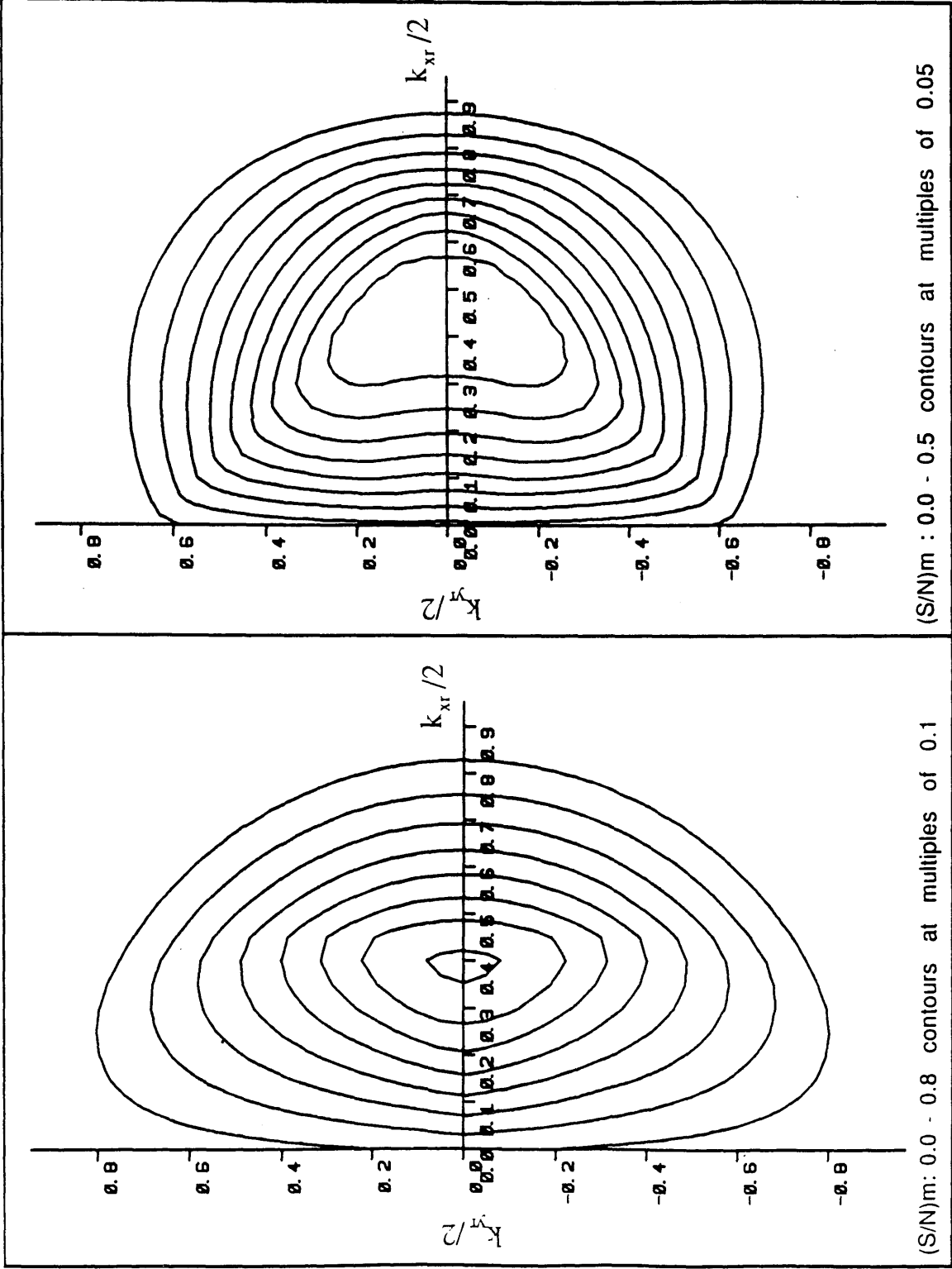


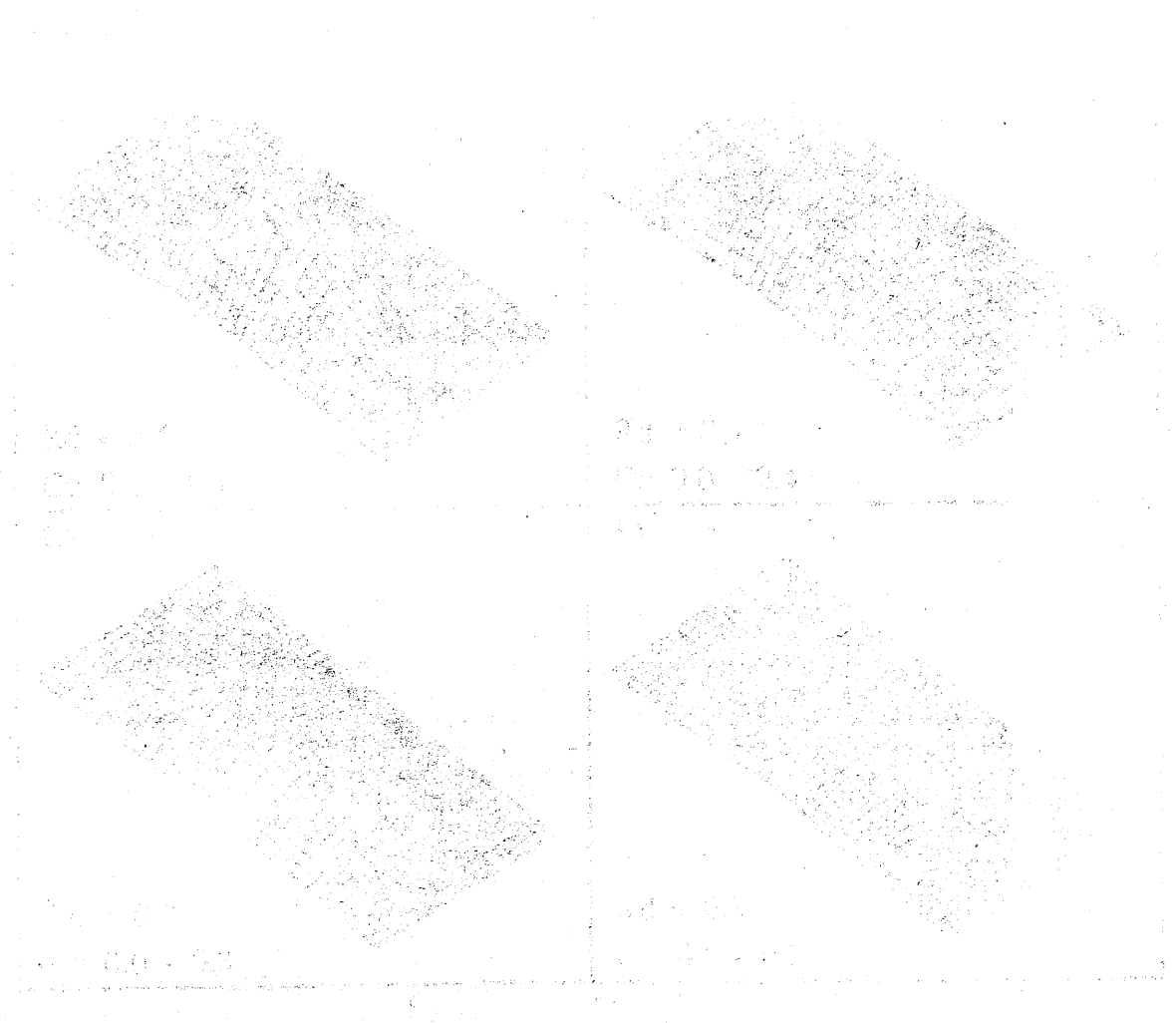
FIGURE 24

The contour plots
(C) and (F)
correspond to
the plots
(C) and (F)
in Fig.3.18



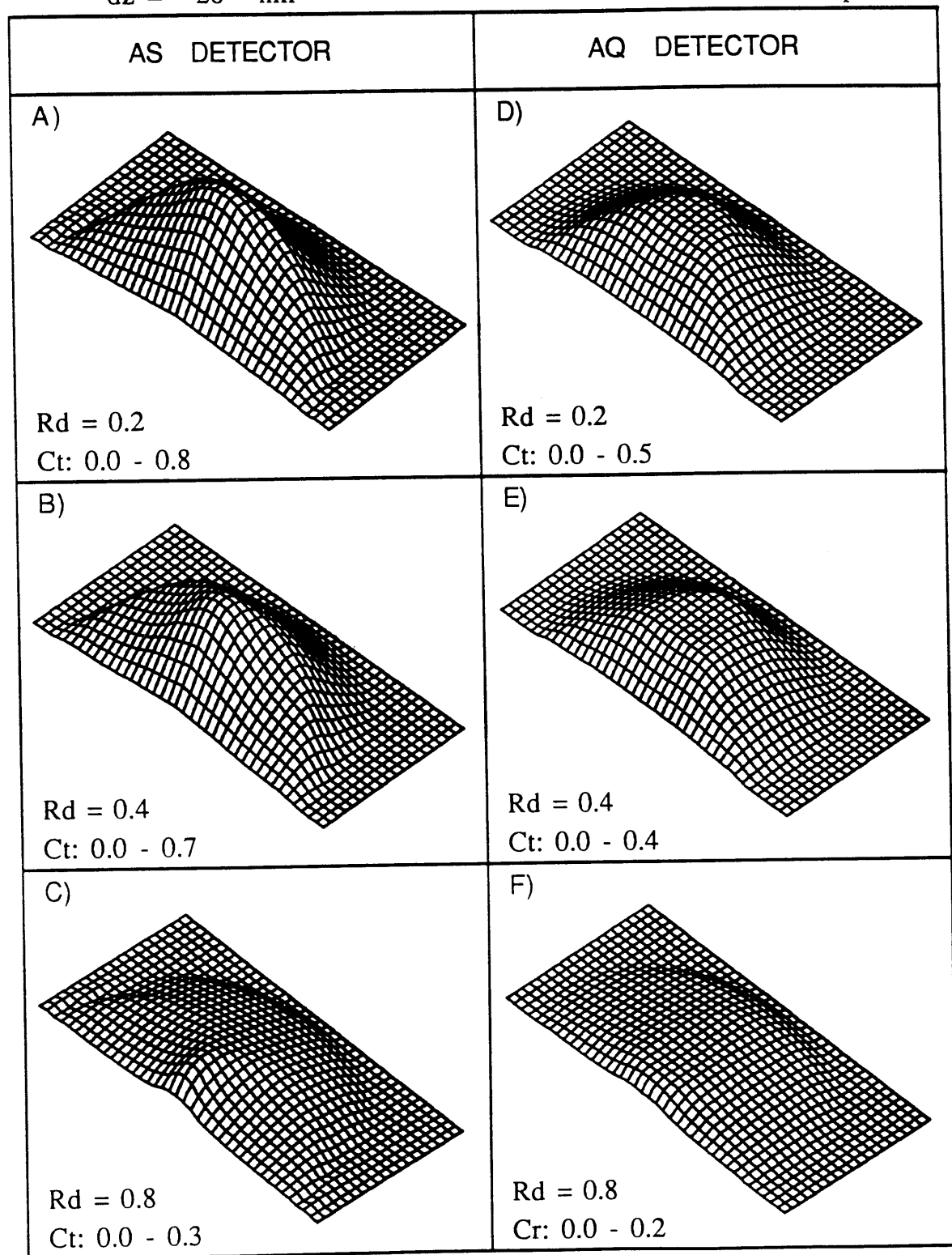
Appendix 2

FIGURES 2:
The modified DPC transfer function



$\alpha_s = 4.16 \text{ mrad}$
 $dz = -26 \text{ nm}$

$C_t = I_m/I_p$




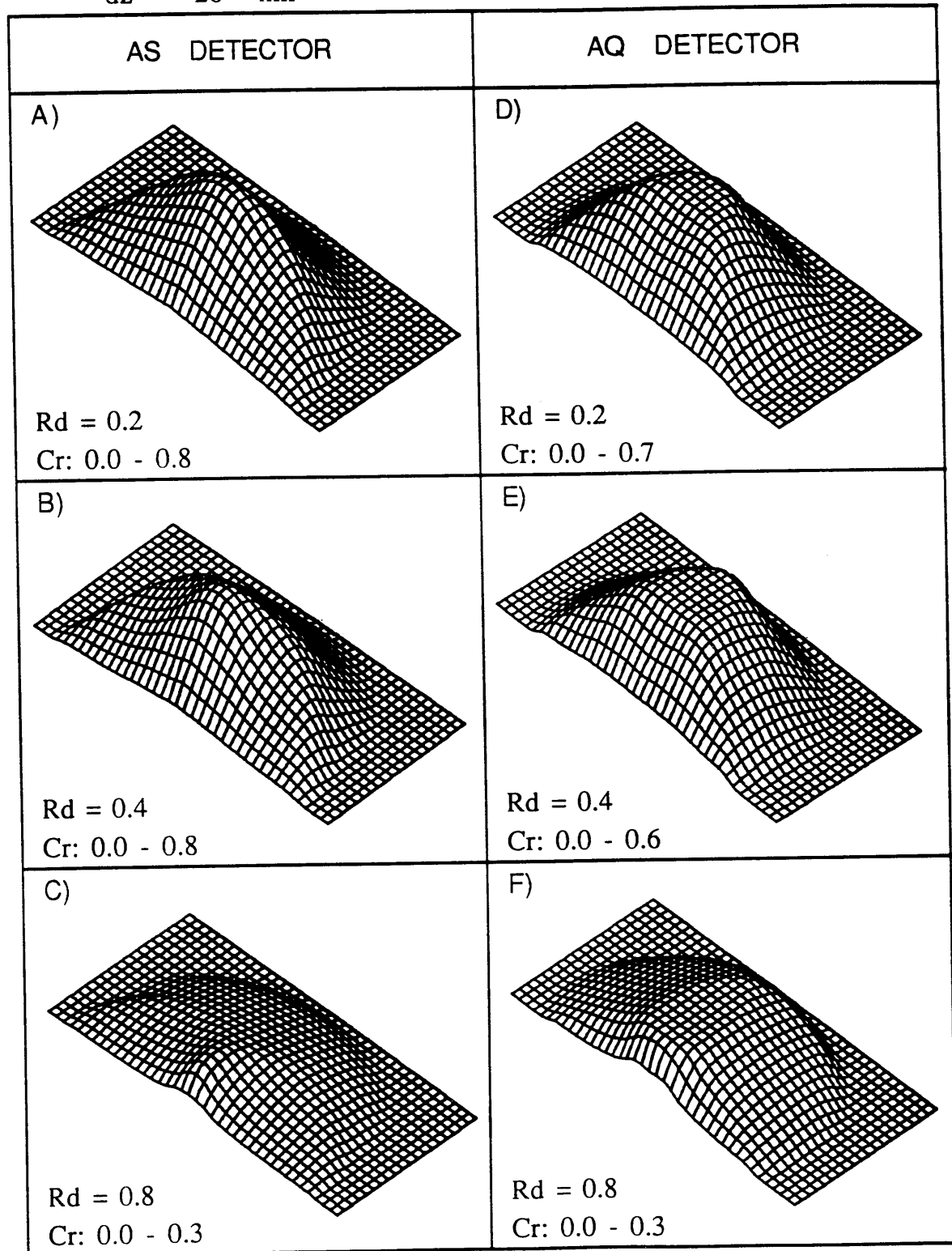
$k_y r$ C_t $k_x r$


FIGURE 1. Three-dimensional plots of modified DPC transfer

$$\alpha_s = 4.16 \text{ mrad}$$

$$dz = -26 \text{ nm}$$

$$Cr = (S/N)m$$



$\begin{matrix} & Cr & \\ k y r & \downarrow & k x r \end{matrix}$

FIGURE 2. Three-dimensional plots of signal-to-noise ratio in the modified DPC transfer

$$\alpha_s = 8.32 \text{ mrad}$$

$$dz = -110 \text{ nm}$$

$$C_t = I_m/I_p$$

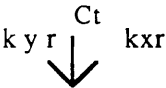
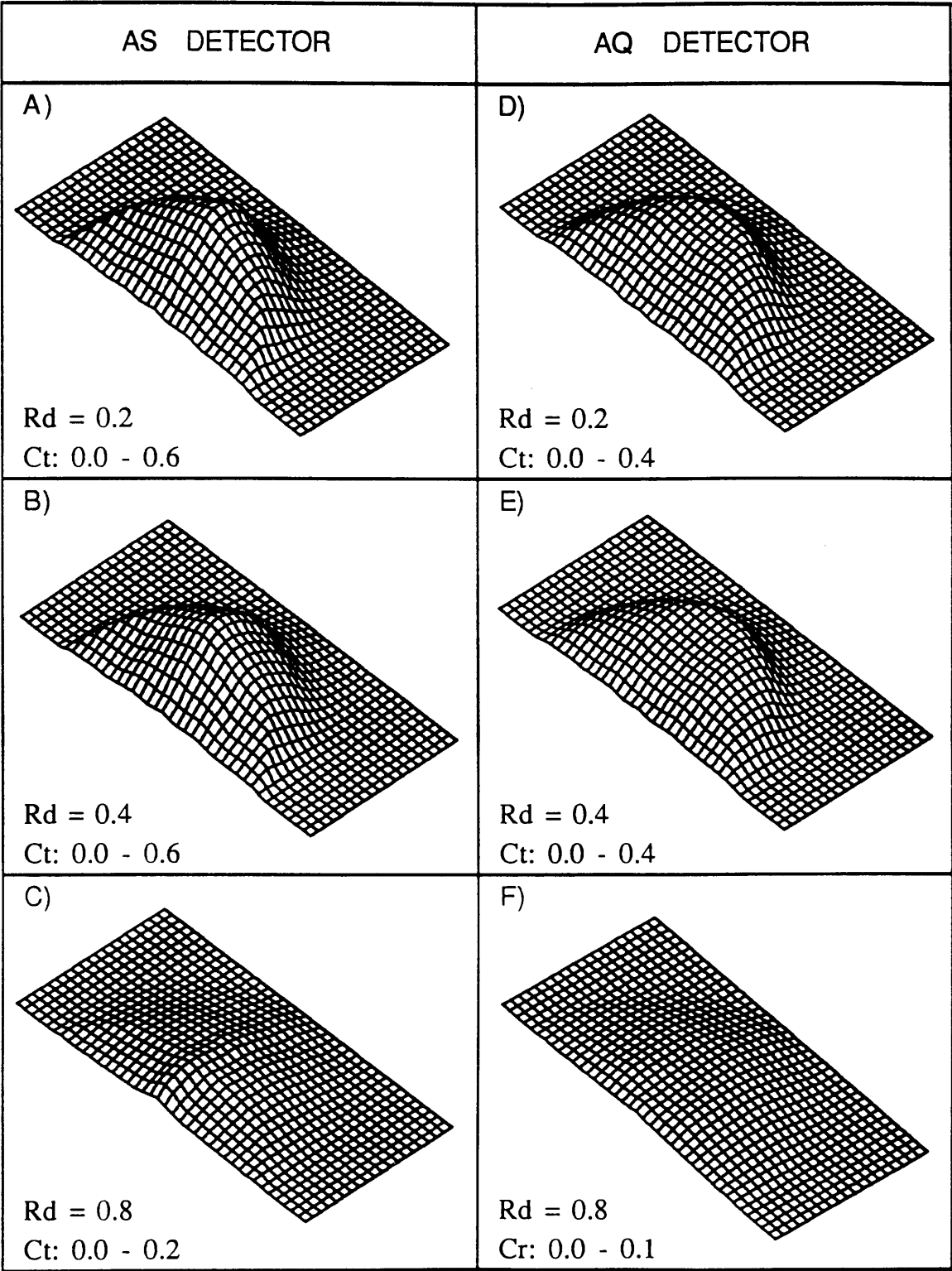
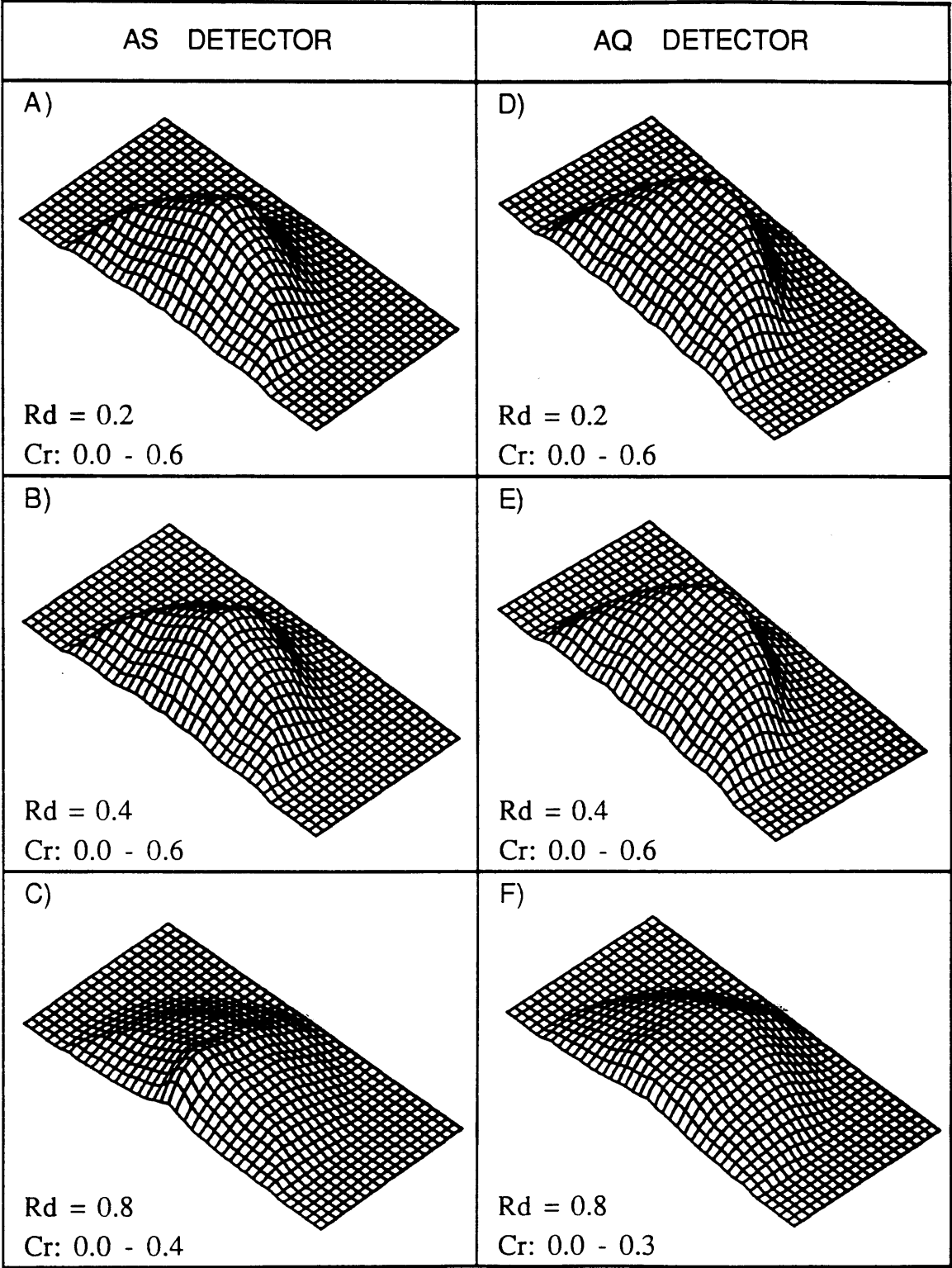


FIGURE 3. Three-dimensional plots of modified DPC transfer

$$\alpha_s = 8.32 \text{ mrad}$$

$$dz = -110 \text{ nm}$$

$$Cr = (S/N)m$$



Cr
 \downarrow
 $k_y r$ $k_x r$

FIGURE 4. Three-dimensional plots of signal-to-noise ratio in the modified DPC transfer

FIGURE 5

The contour plots
(A) and (D)
correspond to
the plots
(A) and (D)
in Figure 1

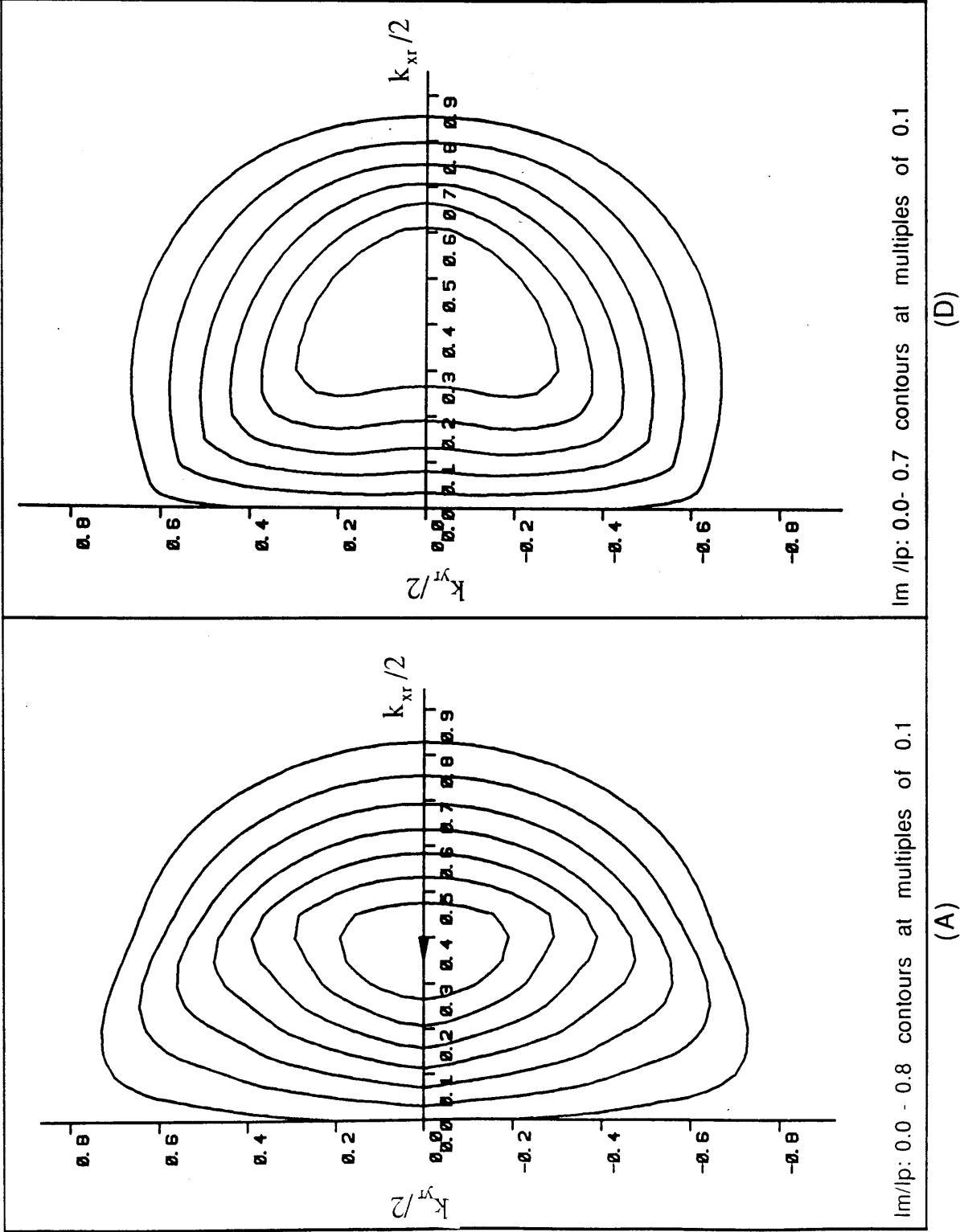


FIGURE 6

The contour plots
(B) and (E)
correspond to
the plots
(B) and (E)
in Figure 1

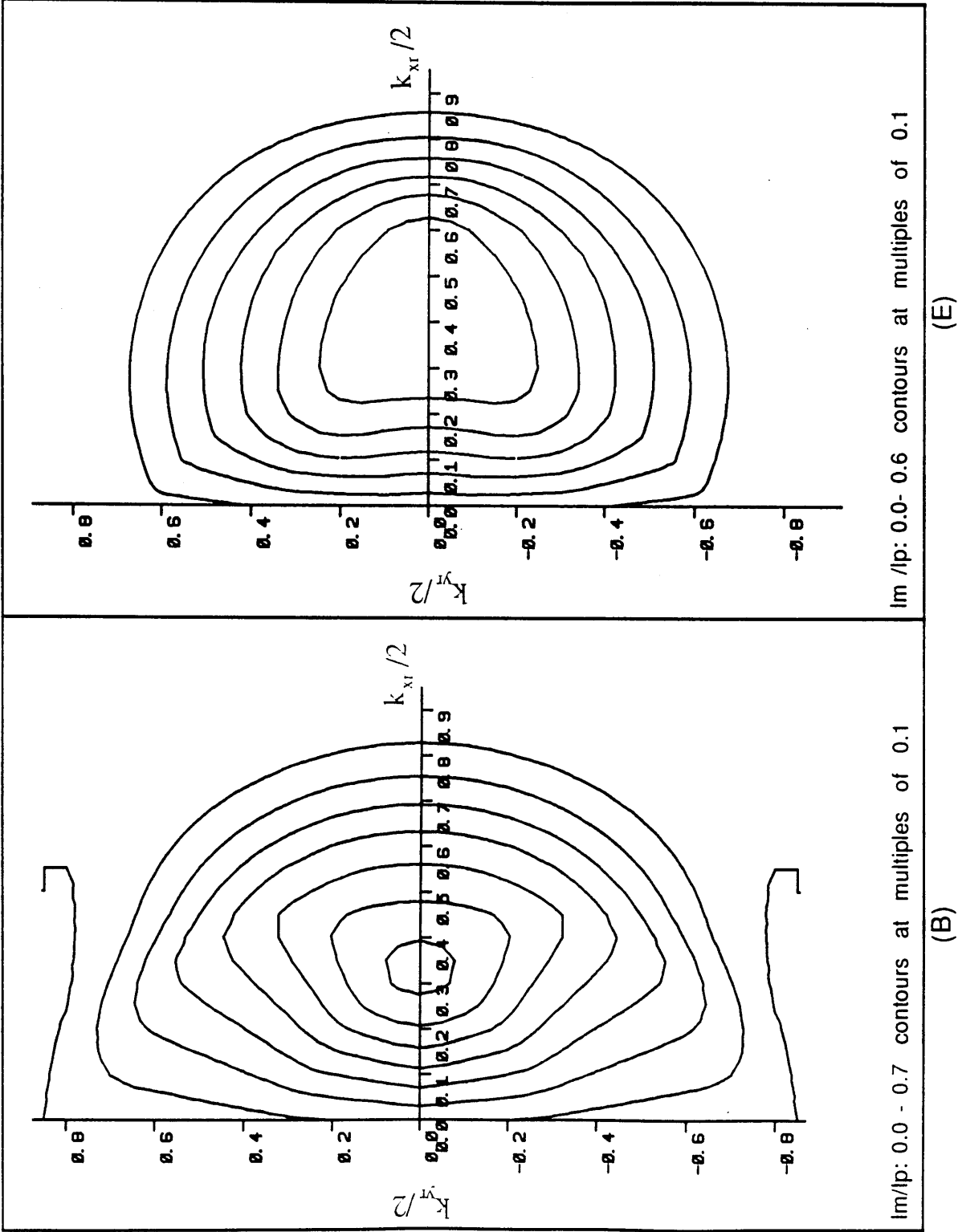


FIGURE 7

The contour plots
(C) and (F)
correspond to
the plots
(C) and (F)
in Figure 1

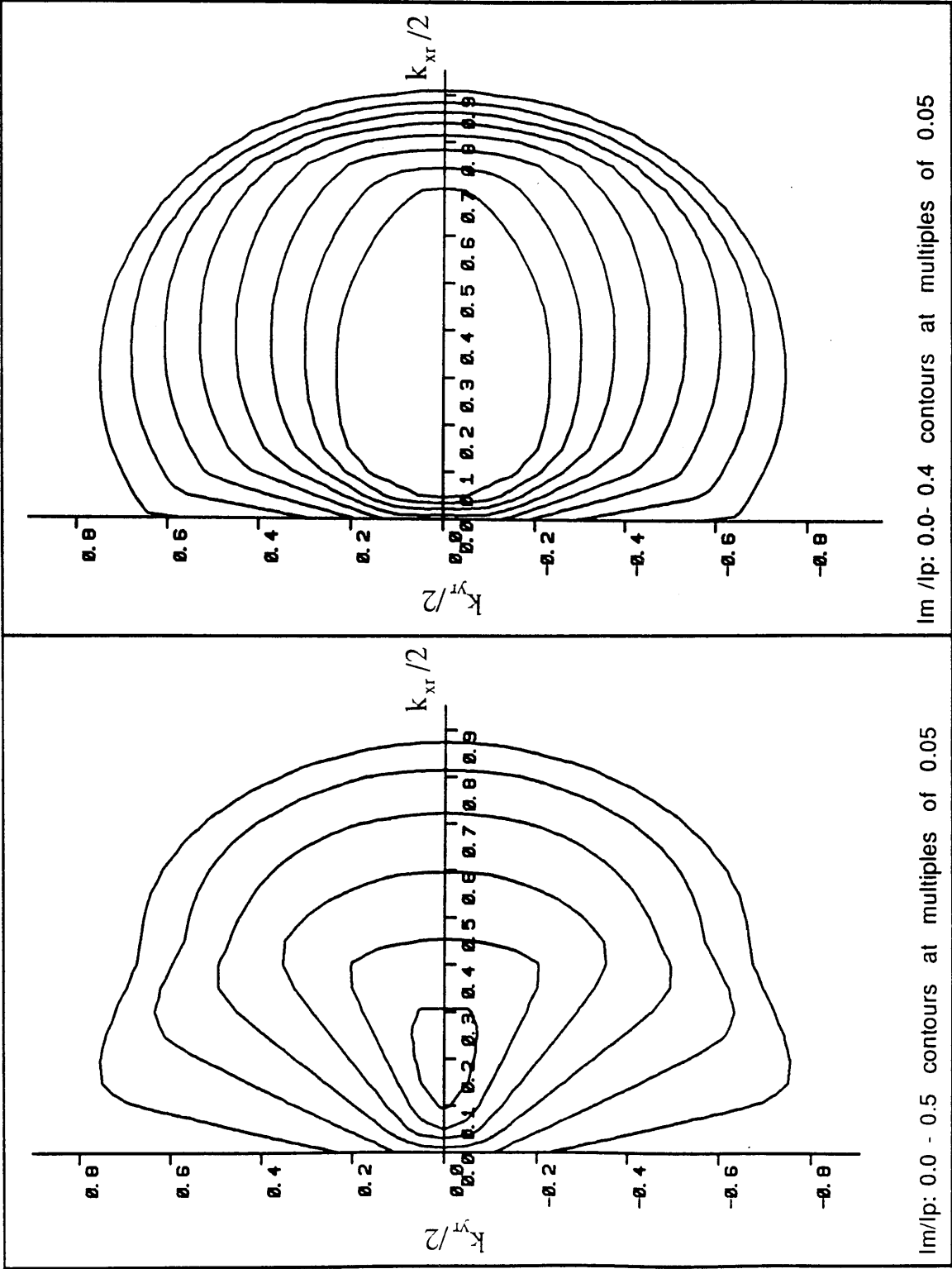


FIGURE 8

The contour plots
(A) and (D)
correspond to
the plots
(A) and (D)
in Figure 2

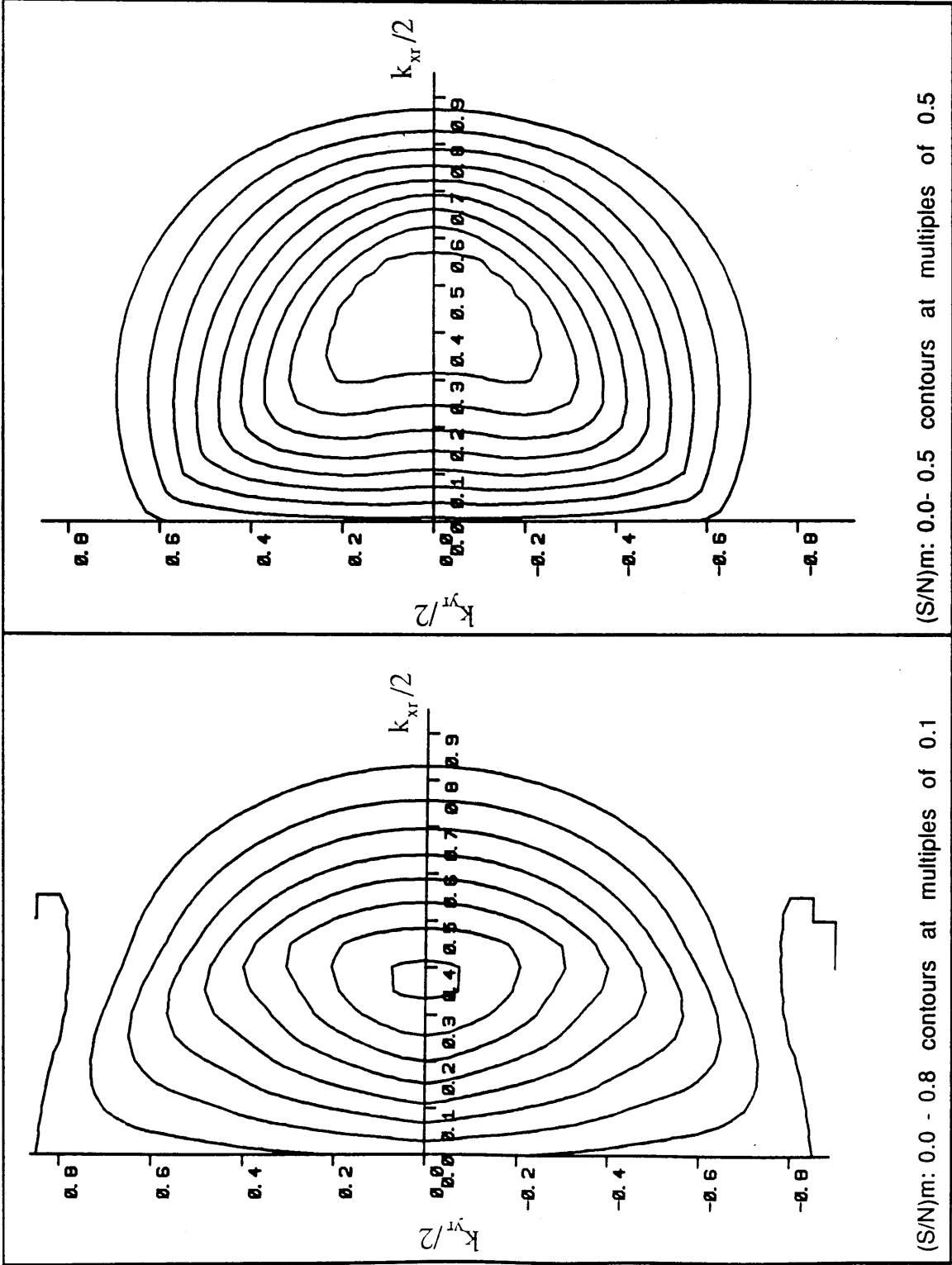


FIGURE 9

The contour plots
(B) and (E)
correspond to
the plots
(B) and (E)
in Figure 2

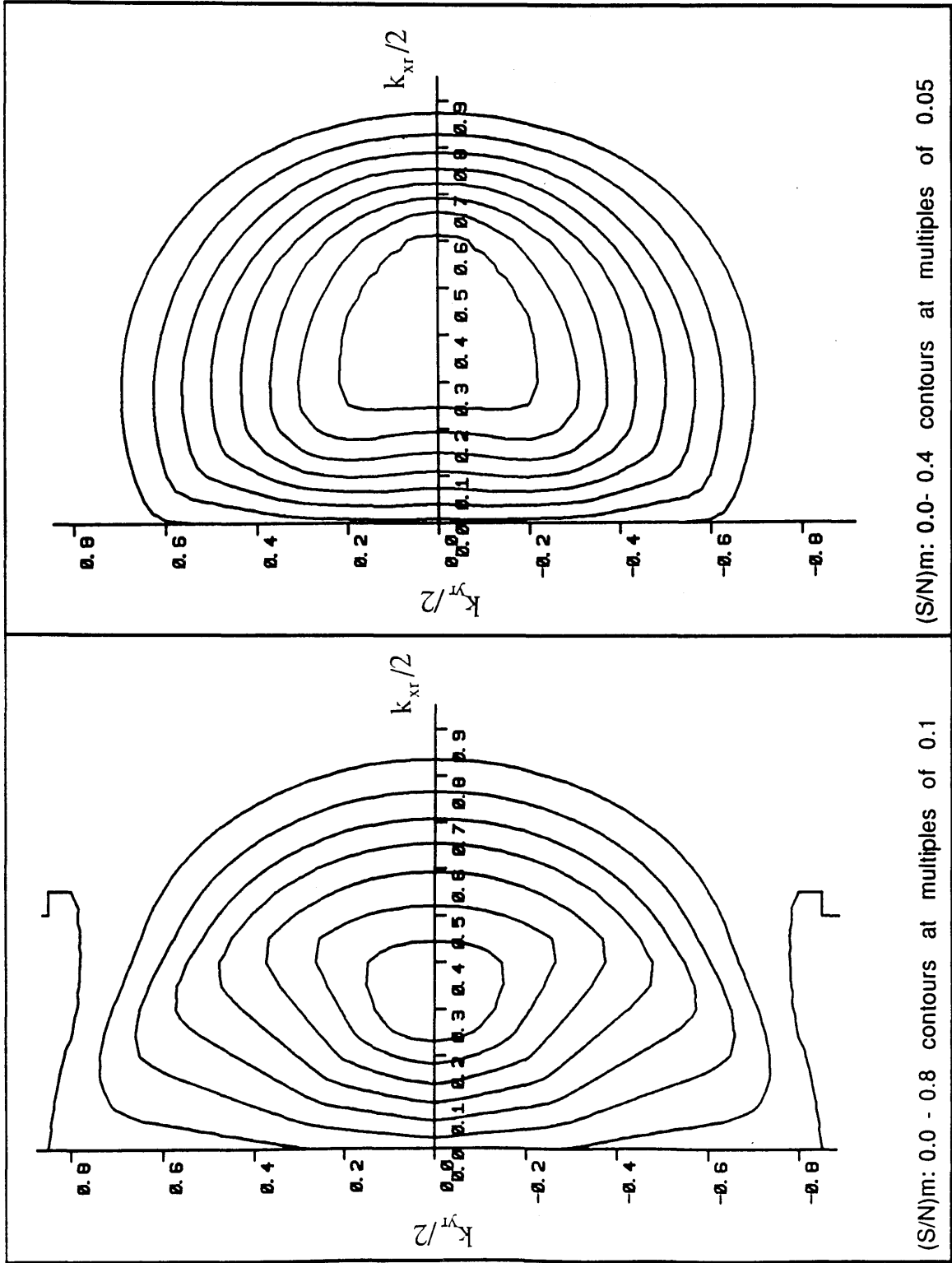


FIGURE 10

The contour plots
(C) and (F)
correspond to
the plots
(C) and (F)
in Figure 2

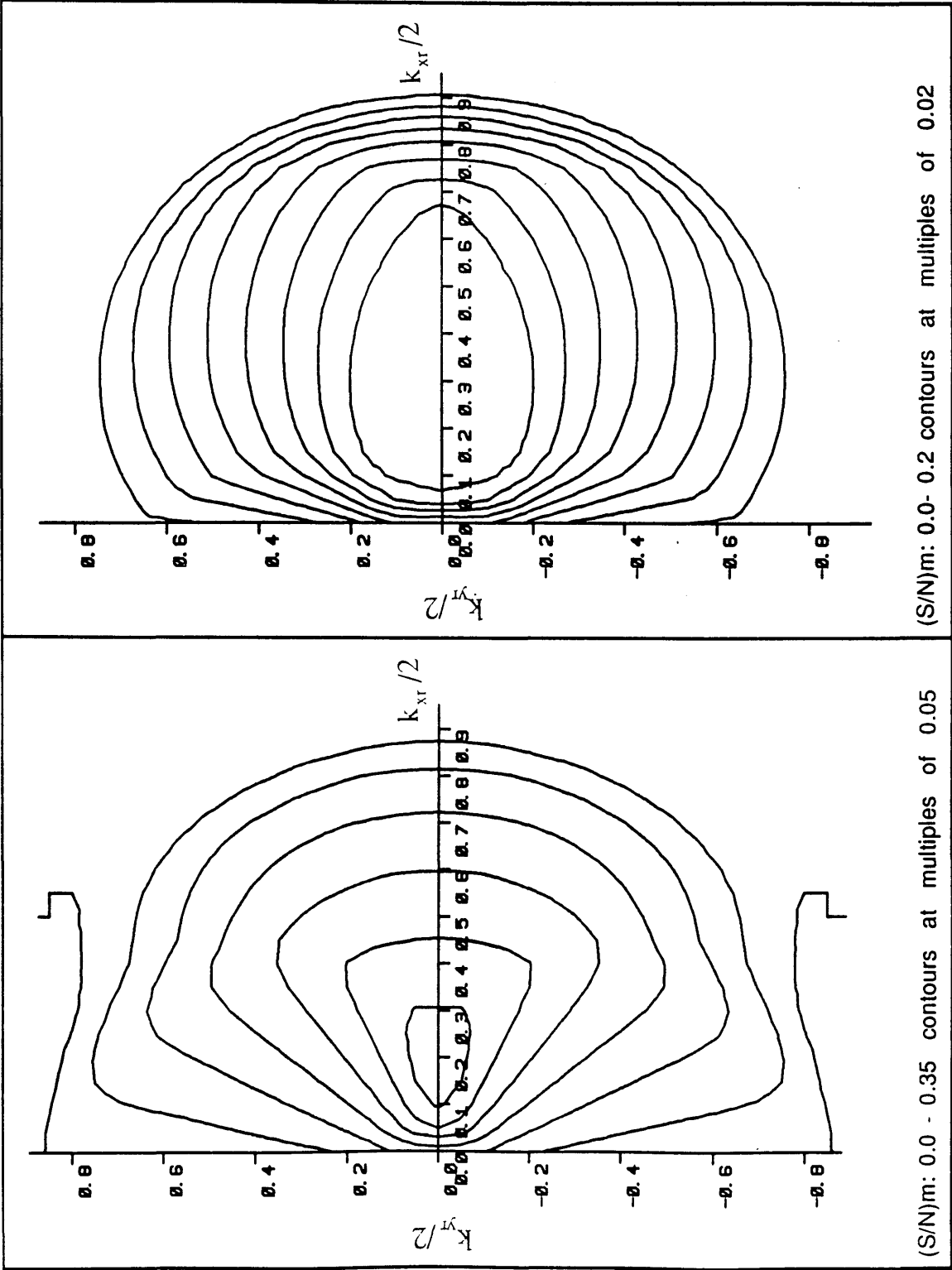


FIGURE 11

The contour plots
(A) and (D)
correspond to
the plots
(A) and (D)
in Figure 3

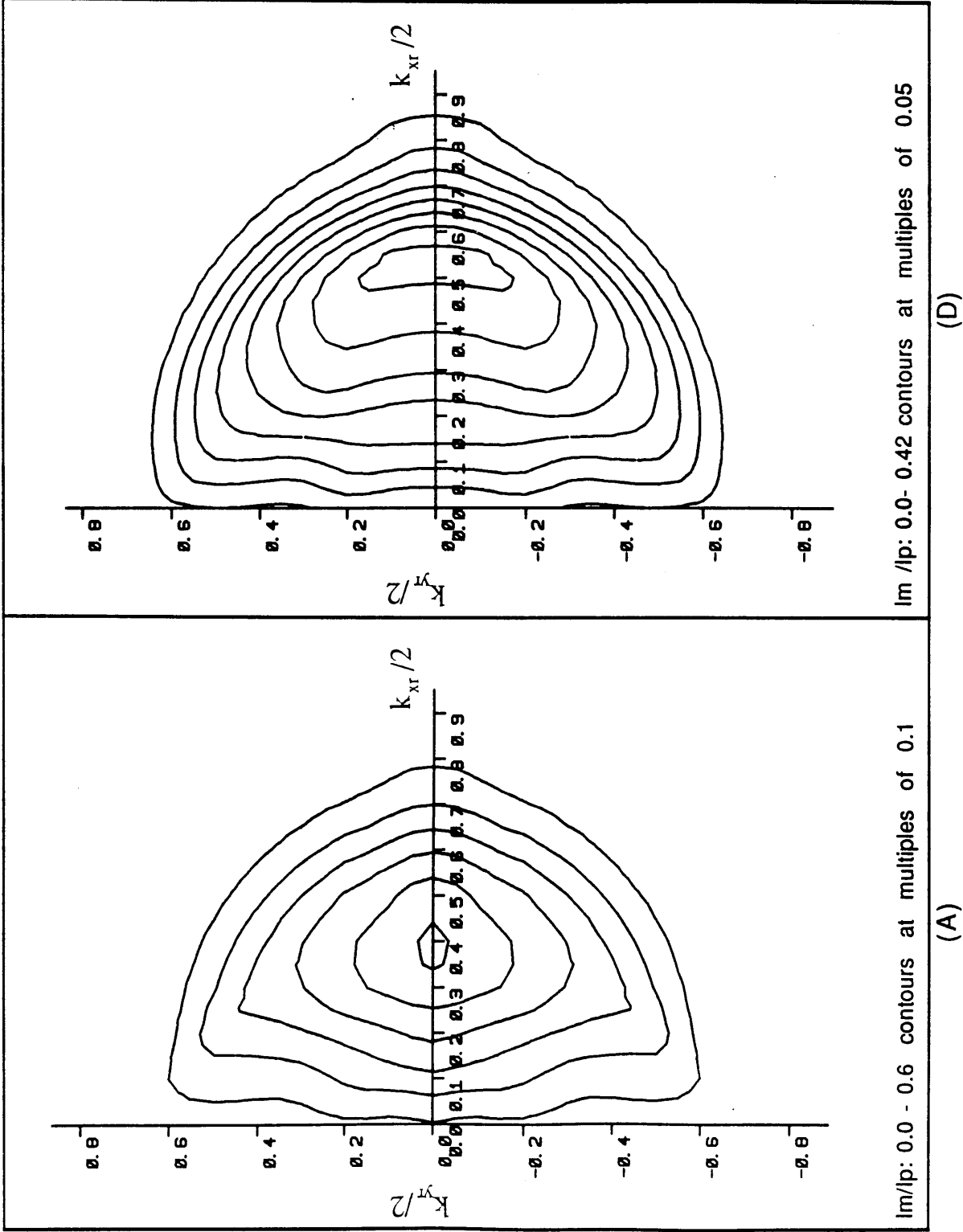


FIGURE 12

The contour plots
(B) and (E)
correspond to
the plots
(B) and (E)
in Figure 3

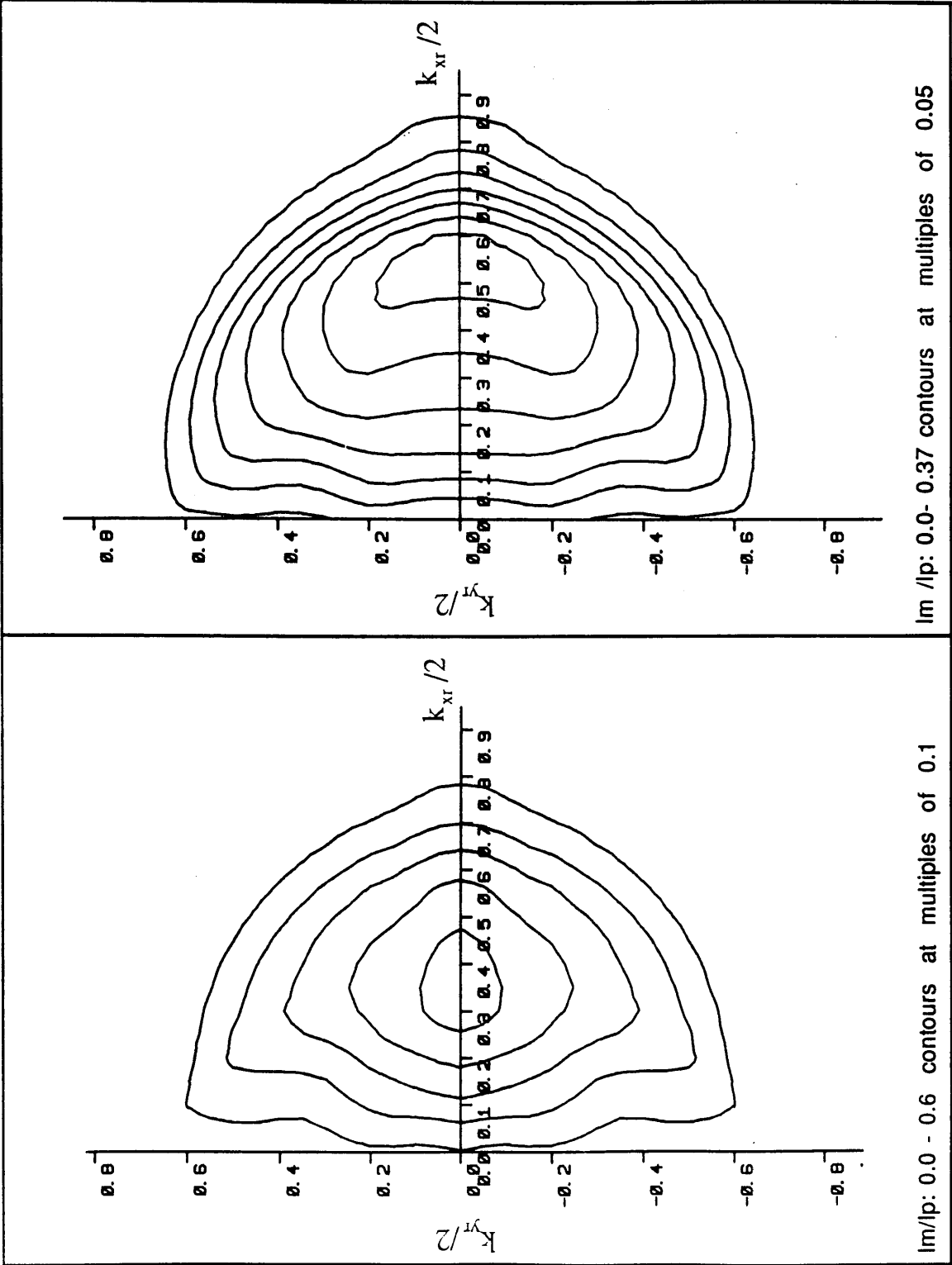


FIGURE 13

The contour plots
(C) and (F)
correspond to
the plots
(C) and (F)
in Figure 3

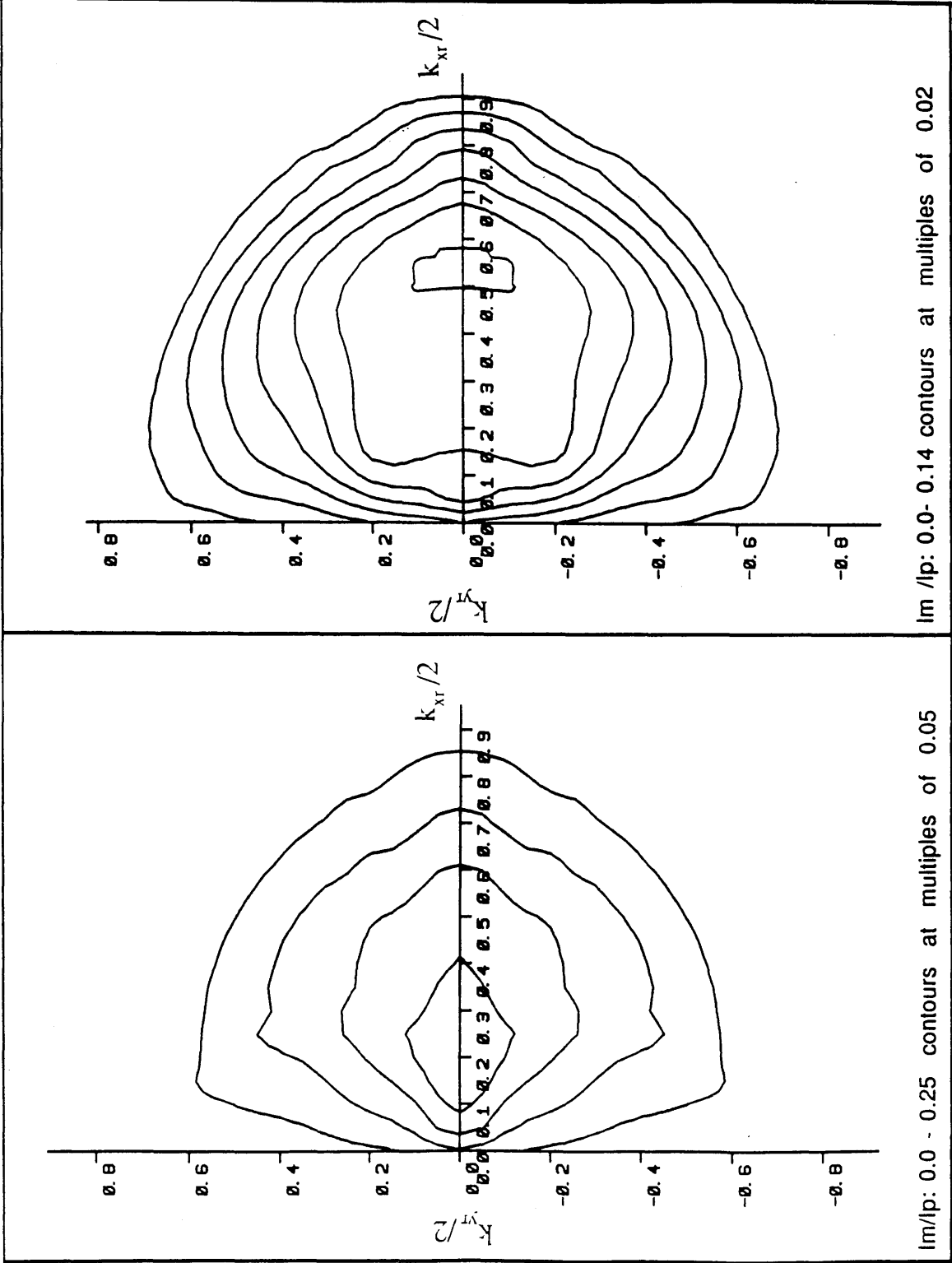


FIGURE 14

The contour plots
(A) and (D)
correspond to
the plots
(A) and (D)
in Figure 4

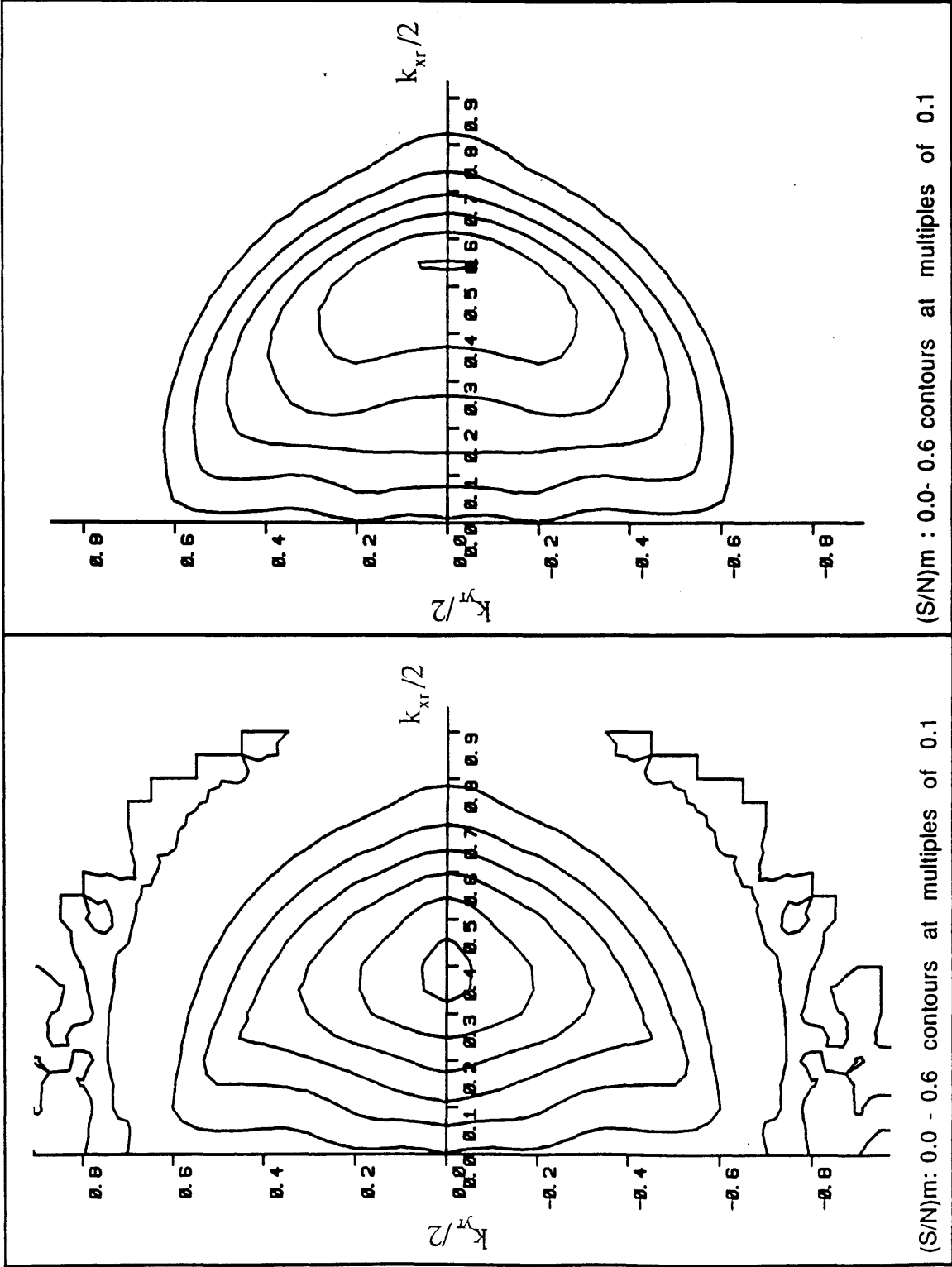


FIGURE 15

The contour plots
(B) and (E)
correspond to
the plots
(B) and (E)
in Figure 4

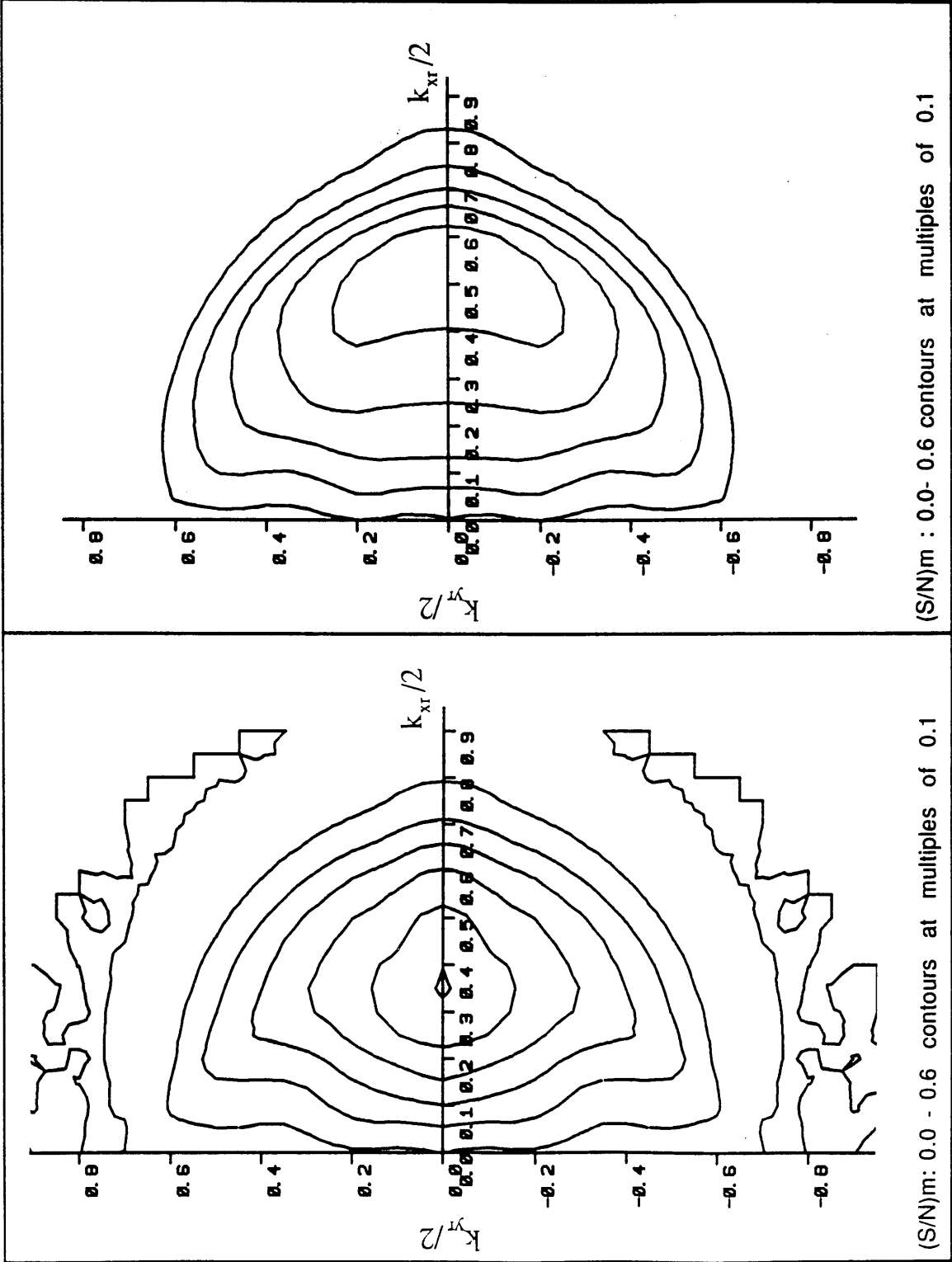
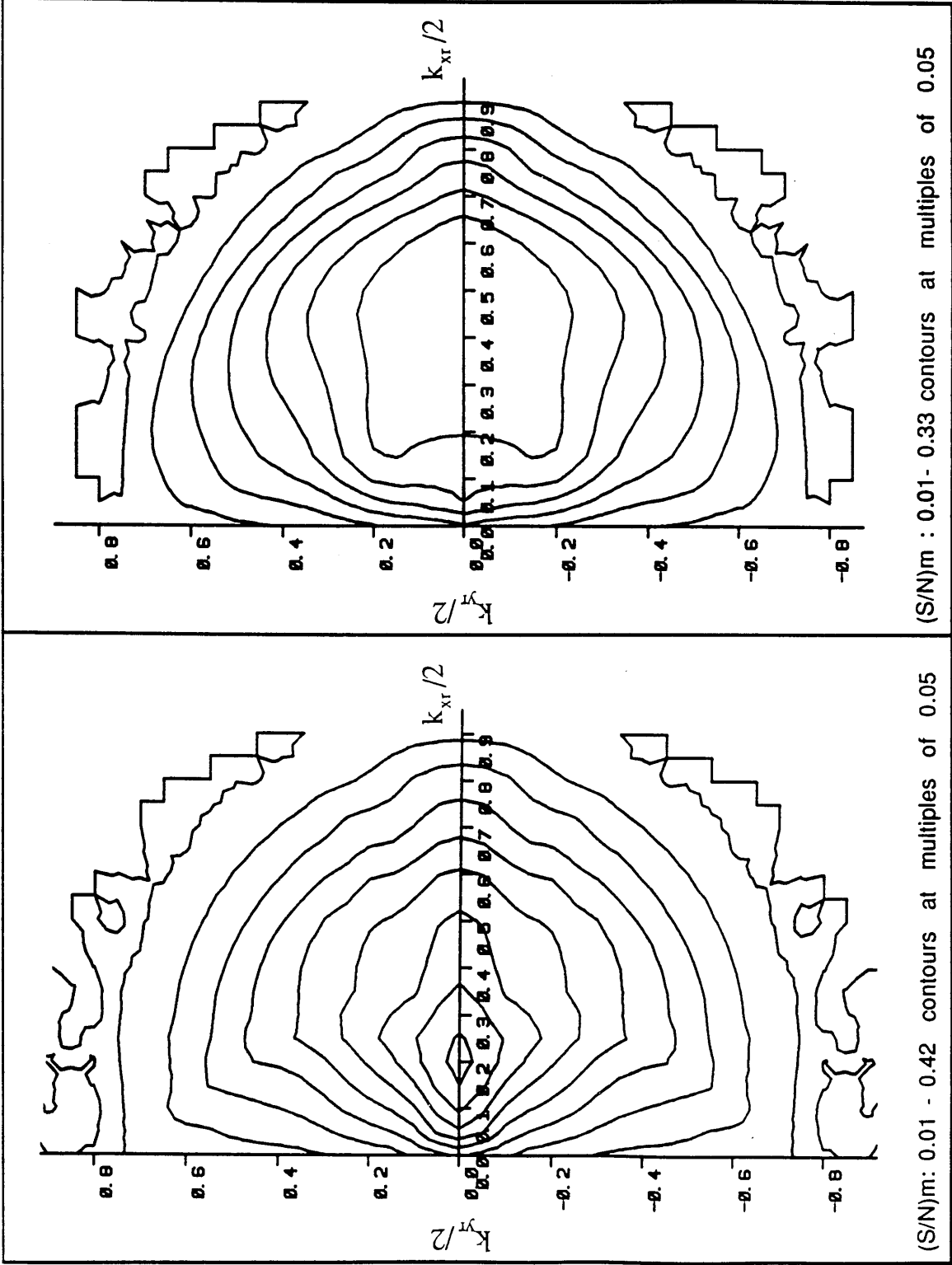


FIGURE 16

The contour plots
(C) and (F)
correspond to
the plots
(C) and (F)
in Figure 4



Appendix 3

Computer programme

```

CCCCCCCCCCCCCCCCCCCCCCCCCCCCCCCCCCCCCCCCCCCCCCCCCCCCCCCCCCCCCCCC
C
C | THIS IS FOR CALCULATING DPC TRANSFER AND SIGNAL-TO-NOISE RATIO
C   USING ANNULAR SPLIT (AS) OR ANNULAR QUADRANT (AQ) DETECTORS |
C
CCCCCCCCCCCCCCCCCCCCCCCCCCCCCCCCCCCCCCCCCCCCCCCCCCCCCCCCCCCCCCCC
C
C   SPH ---- COEFFICIENT OF THE 3RD ORDER SPHERICAL ABERRATION (M)
C   DEF ---- DEFOCUS (M)
C   WAVELN ---- WAVE LENGTH (M)
C   HANGL ---- HALF ANGLE OF THE PROBE FORMING APERTURE (RAD)
C   RD ---- THE RATIO OF SEMIANGLE SUBTENDED BY HOLLOW CONE ON THE
C           DETECTOR PLANE TO THAT BY PROBE-FORMING APERTURE
C   PHI ---- THE ORIENTATION OF SPECIMEN WITH DETECTOR
C
C-----
C
C   PARAMETER (SPH=3.3E-3,WAVELN=3.7E-12)
C   PARAMETER (HANGL=8.32E-3,DEF=-1.1E-7)
C   COMMON/GRAD/ALPHA,ELAMDA,PI,MODEEP,DEGEP
C   COMMON/SU/C,D,P
C
C       CS=SPH
C       DZ=DEF
C       ALPHA=HANGL
C       ELAMDA=WAVELN
C       PI=3.14159
C
C       C=CS*PI*ALPHA**4/(2.0*ELAMDA)
C       D=DZ*PI*ALPHA**2/ELAMDA
C
C-----
C   NEXT BLOCK WILL SELECT THE DETECTOR CONFIGURATION, MODEEP=0
C   FOR SPLIT DETECTOR, AND MODEEP=1 FOR QUADRANT DETECTOR
C-----
C
C   MODEEP=0
C
C   IF (MODEEP.EQ.0) THEN
C       DEGEP=0.0
C   ELSE
C       DEGEP=PI/4.0
C   ENDIF
C
C   CALL PCTF
C   CALL PROFL
C   CALL CONTO
C   CALL END PLT
C   STOP
C   END
C   END OF MAIN PROGRAM
CCCCCCCCCCCCCCCCCCCCCCCCCCCCCCCCCCCCCCCCCCCCCCCCCCCCCCCCCCCCCCCC
C
C   SUBROUTINE PROFL
C
C-----
C>>>> THIS SUB WILL CALCULATE DPC TRANSFER WITH A SERIES OF ANNULAR
C       DETECTORS WHICH ARE VARIED WITH THE VALUE, RD
C
C>>>> AN ORIENTATION CAN BE FIXED BY THE PARAMETER, 'ORIENT', WHICH
C       RANGES FROM 0.0 TO 0.5, AND CORESPONDS TO THAT FROM 0 TO PI/2
C-----
C
C   PARAMETER(N=100,NI=90,NJ=6,ORIENT=0.0)

```

```
C      REAL DLS(NI), AINT(NI,NJ), SNR(NI,NJ)

COMMON/GRAD/ALPHA, ELAMDA, PI, MODEEP, DEGEP
COMMON/PAN/AI, AP, PHI, RCH, DEG, MODE, SUM1, SUM2
COMMON/SU/C,D,P

C      MODE=MODEEP
        DEG=DEGEP
        PHI=PI*ORIENT
        AP=N/2.0

C-----
C      RD NOW IS ARRANGED TO HAVE 5 VALUES: 0.0, 0.2, 0.4, 0.6, 0.8
C
C      AINT ---- THE DPC TRANSFER, IM/IP(SEE.THESIS:CH.3)
C      SNR ---- THE SIGNAL-TO-NOISE RATIO
C      DLS ---- REAL SPACE PERIODICITY (NM)
C-----
C
DO 20,J=1,NJ-1
    RD=(J*2.0-2.0)/10.0
    RCH=RD*AP
DO 10,I=1,NI
    AI=I+10
    P=AI/AP
    SUM1=0.0
    SUM2=0.0
CALL COUNT
    DLS(NI+1-I)=ELAMDA*1.0E11/(2.0*ALPHA*AI)
    AINT(NI+1-I,J)=(SUM1-SUM2)*0.819/3215.0
IF(MODE.EQ.0) THEN
    SNR(NI+1-I,J)=AINT(NI+1-I,J)/SQRT(1.0-RD**2)
ELSE
    SNR(NI+1-I,J)=AINT(NI+1-I,J)*SQRT(2.0/(1.0-RD**2))
ENDIF
    AINT(NI+1-I,NJ)=1.0
    SNR(NI+1-I,NJ)=1.0
10 CONTINUE
20 CONTINUE
C
    CALL PLMCV(DLS,AINT,MODE)
    CALL PLMCV(DLS,SNR,MODE)
C
RETURN
END
CCCCCCCCCCCCCCCCCCCCCCCCCCCCCCCCCCCCCCCCCCCCCCCCCCCCCCCCCCCCCCCCCC
C
SUBROUTINE CONTO
C
C>>> THIS SUB WILL CALCULATE THE DPC TRANSFER OVER TWO-DIMENSIONAL
SPATIAL FREQUENCY (ORIENTATION FROM -PI/2 TO PI/2)
C
C>>> THE CONFIGURATIONS OF ANNULAR DETECTOR MAY BE VARIED BY CHANGING
THE VALUE OF RD
C-----
C
PARAMETER(N=100,K1=20,K2=40,RD=0.0)
REAL AINT(K1,K2), SNR(K1,K2)
C
COMMON/GRAD/ALPHA, ELAMDA, PI, MODEEP, DEGEP
COMMON/PAN/AI, AP, PHI, RCH, DEG, MODE, SUM1, SUM2
COMMON/SU/C,D,P
```

```
MODE=MODEEP
DEG=DEGEP
AP=N/2
RCH=RD*AP
```

```

Y=-K1
DO 20,J=1,K2
  X=0.0
DO 10,I=1,K1
  X=X+1.0
  PHI=ATAN(ABS(Y)/X)
  AI=5.0*SQRT(X*X+Y*Y)
IF(AI.GT.100.0)THEN
  AINT(I,J)=0.0
ELSE
  P=AI/AP
  SUM1=0.0
  SUM2=0.0
CALL COUNT
  AINT(I,J)=(SUM1-SUM2)*0.819/3215.0
IF(MODE.EQ.0)THEN
  SNR(I,J)=AINT(I,J)/SQRT(1.0-RD**2)
ELSE
  SNR(I,J)=AINT(I,J)*SQRT(2.0/(1.0-RD**2))
ENDIF
ENDIF
CONTINUE
  Y=Y+1.0
CONTINUE

```

```
CALL PLCON (AINT,MODE)
CALL PLCON (SNR,MODE)
```

RETURN
END

[illegible]

SUBROUTINE PCTF

C-----

C WITH THE PRESENT INSTRUMENTAL PARAMETERS

```

PARAMETER(M=100,N=2)
REAL TF(M,N),SF(M)
COMMON/SU/C,D,P

```

```
DO 20,J=1,N-1
DO 10,I=1,M
    AI=I/100.0
    TF(I,J)=-SIN(C*AI**4+D*AI**2)
    TF(I,N)=1.0
    SF(I)=AI
```

10 CONTINUE

20 CONTINUE

CALL PLCV(SF,TF)

RETURN
END

C

SUBROUTINE COUNT

[illegible]


```
C      SUBROUTINE UUP(CRB)
C
COMMON/PAN/AI,AP,PHI,RCH,DEG,MODE,SUM1,SUM2
COMMON/MID/IY,XPS
C
      ITOP=AI*SIN(PHI)-CRB
      ICRB=CRB+1.0
DO   10,IY=ICRB,ITOP
      SKY=IY/AP
      CALL JUDGE
C
      XP1=RIGHT(AI,IY,AP,PHI,-1)
      XP2=CENTRE(IY,AP)
      CALL EDGE(SKY,XP1,XPS,XP2,1)
10   CONTINUE
      RETURN
END
CCCCCCCCCCCCCCCCCCCCCCCCCCCCCCCCCCCCCCCCCCCCCCCCCCCCCCCCCCCCCCCCCCCCCC
C
SUBROUTINE COMS(RBL,RUP,CRB)
C
COMMON/PAN/AI,AP,PHI,RCH,DEG,MODE,SUM1,SUM2
COMMON/MID/IY,XPS
C
      ITOP=AI*SIN(PHI)-CRB
      ICRB=CRB
DO   10,IY=ICRB,ITOP
      SKY=IY/AP
      CALL JUDGE
C
      XP2=CENTRE(IY,AP)
IF(IY.LE.RBL.OR.IY.GT.RUP)THEN
      XP1=RIGHT(AI,IY,AP,PHI,-1)
ELSE
      XP1=0.0
ENDIF
      CALL EDGE(SKY,XP1,XPS,XP2,1)
10   CONTINUE
      RETURN
END
CCCCCCCCCCCCCCCCCCCCCCCCCCCCCCCCCCCCCCCCCCCCCCCCCCCCCCCCCCCCCCCCCCCCCC
C
SUBROUTINE COMA(RBL,BOT,CRB)
C
COMMON/PAN/AI,AP,PHI,RCH,DEG,MODE,SUM1,SUM2
COMMON/MID/IY,XPS
C
      IBOT=BOT+1.0
      IAP=AP
DO   10,IY=IBOT,IAP
      SKY=IY/AP
      CALL JUDGE
C
IF(IY.LE.RBL)THEN
      XP1=RIGHT(AI,IY,AP,PHI,-1)
      XP2=RIGHT(AI,IY,AP,PHI,1)
ELSEIF(IY.LE.CRB)THEN
      XP1=0.0
      XP2=RIGHT(AI,IY,AP,PHI,1)
ELSE
      XP1=0.0
      XP2=CENTRE(IY,AP)
ENDIF
      CALL EDGE(SKY,XP1,XPS,XP2,1)
```

```

10    CONTINUE
      RETURN
      END
CCCCCCCCCCCCCCCCCCCCCCCCCCCCCCCCCCCCCCCCCCCCCCCCCCCCCCCCCCCCC
C
      SUBROUTINE COMB(RBL,BOT,CRB)
C
      COMMON/PAN/AI,AP,PHI,RCH,DEG,MODE,SUM1,SUM2
      COMMON/MID/IY,XPS
C
      IBOT=BOT+1.0
      IAP=AP
      DO 10,IY=IBOT,IAP
        SKY=IY/AP
        CALL JUDGE
C
      IF(IY.LE.CRB) THEN
        XP1=RIGHT(AI,IY,AP,PHI,-1)
        XP2=RIGHT(AI,IY,AP,PHI,1)
      ELSEIF(IY.LE.RBL) THEN
        XP1=RIGHT(AI,IY,AP,PHI,-1)
        XP2=CENTRE(IY,AP)
      ELSE
        XP1=0.0
        XP2=CENTRE(IY,AP)
      ENDIF
      CALL EDGE(SKY,XP1,XPS,XP2,1)
10    CONTINUE
      RETURN
      END
CCCCCCCCCCCCCCCCCCCCCCCCCCCCCCCCCCCCCCCCCCCCCCCCCCCCCCCCCCCCC
C
      SUBROUTINE NEGTS(RBL,RUP)
C
      COMMON/PAN/AI,AP,PHI,RCH,DEG,MODE,SUM1,SUM2
      COMMON/MID/IY,XPS
C
      ILBL=-RUP
      ILUP=-RBL
      DO 20,IY=ILBL,ILUP
        SKY=IY/AP
        CALL JUDGE
        XP1=0.0
        XP2=SLEFT(AI,IY,AP,PHI)
        CALL EDGE(SKY,XP1,XPS,XP2,-1)
20    CONTINUE
      RETURN
      END
CCCCCCCCCCCCCCCCCCCCCCCCCCCCCCCCCCCCCCCCCCCCCCCCCCCCCCCCCCCCC
C
      SUBROUTINE NEGTCRB(RBL,CRB)
C
      COMMON/PAN/AI,AP,PHI,RCH,DEG,MODE,SUM1,SUM2
      COMMON/MID/IY,XPS
C
      CLB=CRB-AI*SIN(PHI)
      ILUP=- (RBL+0.5)
      IAP=AP
      DO 20,IY=-IAP,ILUP
        SKY=IY/AP
        CALL JUDGE
C
        XP1=0.0
        IF(IY.LE.CLB) THEN

```

```

      XP2=CENTRE(IY,AP)
ELSE
      XP2=SLEFT(AI,IY,AP,PHI)
ENDIF
      CALL EDGE(SKY,XP1,XPS,XP2,-1)
20    CONTINUE
      RETURN
END
CCCCCCCCCCCCCCCCCCCCCCCCCCCCCCCCCCCCCCCCCCCCCCCCCCCCCCCCCCCCCCCCC
C
      SUBROUTINE JUDGE
C
      COMMON/PAN/AI,AP,PHI,RCH,DEG,MODE,SUM1,SUM2
      COMMON/MID/IY,XPS
C
      SX=RCH*COS(DEG)
      IF(ABS(IY).GE.SX) THEN
        IF(MODE.EQ.0) THEN
          XPS=0.0
        ELSE
          XPS=ABS(IY)
        ENDIF
      ELSE
        XPS=SMALL(IY,RCH)
      ENDIF
      RETURN
END
CCCCCCCCCCCCCCCCCCCCCCCCCCCCCCCCCCCCCCCCCCCCCCCCCCCCCCCCCCCCCCCCC
C
      SUBROUTINE EDGE(SKY,XP1,XPS,XP2,ISIGN)
C
      COMMON/PAN/AI,AP,PHI,RCH,DEG,MODE,SUM1,SUM2
C
      IAP=AP
      DO 20,IX=1,IAP
        SKX=IX/AP
        IF (IX.LE.XP1) GOTO 20
        IF (IX.GT.XP2) GOTO 10
        IF(IX.LE.XPS) THEN
          COEF=0.0
        ELSE
          COEF=1.0
        ENDIF
        IF(ISIGN.EQ.1) THEN
          CALL SUPAN(COEF,SKX,SKY,SUM1,NTH)
        ELSE
          CALL SUPAN(COEF,SKX,SKY,NTH,SUM2)
        ENDIF
20    CONTINUE
10    RETURN
      END
CCCCCCCCCCCCCCCCCCCCCCCCCCCCCCCCCCCCCCCCCCCCCCCCCCCCCCCCCCCCCCCCC
C
      FUNCTION SMALL(IY,RCH)
        SMALL=SQRT(RCH*RCH-IY*IY)
        RETURN
      END
      FUNCTION SLEFT(AI,IY,AP,PHI)
        SLEFT=SQRT(AP*AP-(IY+AI*SIN(PHI))**2)-AI*COS(PHI)
        RETURN
      END
      FUNCTION RIGHT(AI,IY,AP,PHI,IGNR)
        RIGHT=AI*COS(PHI)+IGNR*SQRT(AP*AP-(IY-AI*SIN(PHI))**2)
        RETURN

```



```

RETURN
END
CCCCCCCCCCCCCCCCCCCCCCCCCCCCCCCCCCCCCCCCCCCCCCCCCCCCCCCCCCCC
C
SUBROUTINE PLCV(X,Y)
C
PARAMETER(M=100,N=2)
REAL X(M),Y(M,N)
C
CALL JBAXES(X,M,12.0,'KXR',3,Y,M*N,8.0,'-SIN(U)',6)
CALL DRAW CV(X,Y(1,J),M)
CALL TITLE('T','L','PHASE CONTRAST TRANSFER FUNCTION',34)
RETURN
END
CCCCCCCCCCCCCCCCCCCCCCCCCCCCCCCCCCCCCCCCCCCCCCCCCCCCCCCCCCCC

```

